Comprehensive Validation of Numerical Predictions for Liquefaction-Induced Lateral Spreading

（液状化による地盤の側方流動に対する数値解析予測の包括的な妥当性確認）

VARGAS TAPIA RUBEN RODRIGO

Abstract

Soil liquefaction is a complex geotechnical phenomenon that occurs under cyclic loading, causing the soil to experience a sudden loss of strength and stiffness, resulting in significant damage to buildings, infrastructure, and other critical structures. Accurate modeling of soil liquefaction is essential in geotechnical engineering research and design, as it enables the prediction of soil behavior during seismic events, allows the assessment of potential ground failure and structural damage, and contributes in the development of effective mitigation strategies.

Over the last decades, computational modeling of geomaterials has experienced significant advancements; however, in order to gain credibility and be integrated into design practices, rigorous Verification and Validation (V&V) exercises are required to ensure that the models are a “true” representation of the physical behavior of the soil and can be used to predict the behavior of soils during seismic events.

In the fields of Solid and Fluid Mechanics, V&V typically involves developing physical models or conducting field observations, along with their corresponding numerical models. The capabilities of the numerical models are then assessed by comparing the simulation results with those obtained from physical models or field observations. This comparison allows for the identification of model limitations, uncertainty quantification, and facilitates informed decision-making and risk assessment.

The primary objective of this study is to propose a novel and comprehensive probabilistic validation methodology for numerical models used to predict liquefaction phenomena. Although several validation methodologies/exercises have been proposed, most of them employ qualitative approaches or simple comparisons between mean values obtained from experimental results and numerical simulations. In recent years, some exercises have incorporated probabilistic approaches, but they are still based on limited amounts of non-crosschecked experimental data.

It has been observed that even when conducted under controlled laboratory conditions, "identical" physical models performed in different facilities can yield significant differences in results; factors such as facility and machine characteristics, as well as the skills and experience of the experimenters, contribute to these variations. This highlights the need to use cross-checked data to verify the accuracy of experimental data and allow a proper uncertainty quantification for a comprehensive validation of numerical models. The novelty of this study lies in proposing a fully probabilistic validation methodology based on the estimation of mean trends and associated variability using cross-checked experimental results, in accordance with the recommendations of state-of-the art validation standards.

The proposed methodology is applied specifically to assess the capabilities of the "Strain Space Multiple Mechanism Model" in simulating the lateral spreading phenomenon across a wide range of densities and input motions. The mean trends and associated variability of the physical models are characterized using a

large and internationally cross-checked database of Centrifuge Experiments developed as part of the LEAP Project. State-of-the-art Hollow Cylinder Shear Tests performed under various Relative Densities (Dr) and Cyclic Stress Ratio (CSR) values are utilized to characterize the mean trends and associated variability of the soil's mechanical behavior. Based on the ground's mechanical characterization, numerical simulations are then developed to replicate the physical models. These simulations cover the range of relative densities (Dr50% - Dr85%) and input motions (0.1g – 0.35g) in which the physical models were characterized.

The validation process demonstrates that the "Strain Space Multiple Mechanism Model" successfully predicts displacements within the median trend and the 95% probability confidence bounds for Dr=50%-85% and PGA<0.25g. The incorporation of state-of-the-art validation procedures and uncertainty quantification using internationally cross-checked data, allowed a comprehensive evaluation of the model`s capabilities to simulate the liquefaction-induced lateral spreading phenomena; this enhances the model's reliability and contributes to its integration into common geotechnical engineering design practices/standards. Furthermore, the methodology proposed on this study have important implications for the improvement of numerical models for predicting soil liquefaction, and it can be used as a basis for future research by applying the validation methodology to other models and datasets.

Acknowledgments

I express my deepest gratitude to my supervisors, Ryosuke Uzuoka Sensei and Kyohei Ueda Sensei, for their support and constant guidance. I was fortunate to be accepted in their laboratory, and receive comprehensive and insightful guidance during and after my stay in the laboratory; their encouragement has been a cornerstone of my development as a researcher and individual; I look forward for their continuous guidance, and will be in debt of them for the rest of my life.

I also extend my heartfelt thanks to the professors at Kyoto University, particularly Hideaki Yasuhara Sensei and Yosuke Higo Sensei, for their invaluable advice and support during the writing of this manuscript; and Kiyoshi Kishida Sensei and Yasuo Sawamura Sensei for their insightful feedback throughout the process.

My gratitude extends to all participants and institutions involved in the LEAP program, including, but not limited to Prof. Tetsuo Tobita, Prof. Koji Ichii, Prof. Mitsu Okamura, Prof. Jiro Takemura, Prof. Gopal SP Madabhushi, Prof. Majid Manzari, Prof. Sandra Escoffier, Prof. Mourad Zeghal, Prof. Bruce Kutter, and Prof. Yan-Guo Zhou. Their suggestions and contributions have been invaluable.

I would like to extend a special acknowledgment to my colleagues at Penta-Ocean Construction. I am grateful to Mr. Tomohiro Kariyama, Mr. Toru Yamashita, and Mr. Takehiko Sato, who provided invaluable guidance and support during the early stages of my career in the Civil Engineering Design Department. To Mr. Keisaku Takae, Mr. Toshikatsu Ide, Mr. Kenta Suyama, Mr. Satoshi Amano, and Mr. Koki Nagata, who offered invaluable guidance, mentorship, and instilled confidence in me during my first construction project in Japan, at the Tokyo Branch Office. I am particularly in debt to Mr. Masahito Tsuru, Dr. Takahiro Kumagai, Dr. Tomohiro Tanaka, and Dr. Kunihiko Uno, who provided invaluable support, gave me the opportunity to embark on a research career at the Research Institute, and supported the drafting of this manuscript. Special thanks are due to Dr. Katsuya Ikeno, for his patience, invaluable guidance, encouragement, and support in the completion of this manuscript.

To my former lab partners and friends in Japan, your friendship, support, and the warm, welcoming atmosphere you created have been a source of immense joy and comfort. The memories we made and the times we shared will always hold a special place in my heart.

The most heartfelt portion of my gratitude is reserved for my family. To my beloved wife, Sayaka, your unconditional love, support, and motivation have been my guiding light; your smile has the power to brighten even my darkest days, and I am endlessly grateful for your presence in my life. To the fruit of our love, for being our hope and bringing light to our lives, even though we can`t see you yet.

To my dear parents Ruben and Gladys, for always supporting me, for correcting my mistakes with love, for getting me up in my defeats, and for educating me always through their example; I hope to be one day at least half as good as they are. Dad, your physical absence leaves a huge void, but your spirit and teachings continue to guide and inspire me daily.

To my brothers and life partners Danny and Miguel, for being always unconditional, and for providing strength in times of weakness. To Alicia, for joining our family and bringing happiness. To Rafa, for being the symbol of a new generation in the family.

I am also immensely grateful to my extended family, Satoshi, Emi, and Takahiro, for welcoming me with open arms, providing unwavering support, and teaching me invaluable life lessons.

Lastly, to my uncles, cousins, and the entire family, your presence in my life has been a constant source of strength and happiness.

Thank you all for being part of my journey.

Contents

List of Tables

List of Figures

1 Introduction

1.1 Background

Soil liquefaction is a complex geotechnical phenomenon that can occur under cyclic loading, causing the soil to experience a sudden loss of strength and stiffness, resulting in significant damage to buildings, infrastructure, and other critical structures. Therefore, intensive research and development efforts have been dedicated to understand the phenomena and prevent future losses/damages. Due to its complexity, the liquefaction phenomenon has been studied mainly through field investigation, physical modeling, and numerical modeling.

While case studies resulting from large earthquake field investigations have been used to study the mechanisms of failure (or success after a good performance of certain structures), aiming to relate them to the key features of the soil stress-strain-strength behavior [1]; the availability of information may be limited due to the lack of existing instrumentation, pre-earthquake data, etc. Therefore, the development of research alternatives such as physical and numerical models has become necessary to improve the understanding of soil liquefaction phenomenon, and to enable more accurate predictions of soil behavior during seismic events.

Accurate modeling of soil liquefaction is essential in geotechnical engineering research and design, as it enables the prediction of soil behavior during seismic events, assessment of potential ground failure and structural damage, and the development of effective prevention and mitigation measures.

Physical models, such as centrifuge experiments or 1-g shaking table tests, have been widely used to simulate soil behavior during earthquakes and have provided valuable insights into the factors that influence the occurrence of soil liquefaction. Also, computational modeling of geomaterials has advanced significantly over the past few decades, leading to more sophisticated simulations of soil behavior. The use of numerical models to simulate the liquefaction phenomenon enabled significant advancements in the field, allowing researchers and practitioners to investigate complex soil behavior and simulate the effects of seismic events. Nonetheless, despite the advancements, significant discrepancies between numerical models and physical models still exist.

To ensure the reliability and accuracy of numerical models, rigorous verification and validation against physical models or field observations are necessary [2]. This validation process ensures that the numerical models are a “true” representation of the physical behavior of the soil and can be used to predict the behavior of soils during seismic events.

1.2 Verification and Validation Background and reference standards/guidelines

Verification and Validation (V&V) are defined as the processes by which evidence is generated, and credibility is thereby established, that computational models have the appropriate accuracy and level of detail for their intended use [2]. In the fields of Solid and Fluid Mechanics, V&V generally involves developing physical models or conducting field observations alongside their corresponding numerical models.

The capabilities of the numerical models are then evaluated and assessed by comparing their results with those obtained from the physical models.

Through the comparison of model predictions with experimental data and field observations, the validation process enables the assessment of a model's ability to capture the complex behavior of the phenomena being modeled. This validation also helps identify model limitations, providing feedback for further improvement in representing the underlying physical mechanisms. Additionally, it allows for the quantification of uncertainties associated with the predictions, facilitating informed decision-making and risk assessment.

1.2.1 Base V&V guidelines/standards used in the thesis manuscript

As it will be later introduced, this thesis manuscript aims to propose a comprehensive probabilistic validation methodology for numerical models used in the prediction of the liquefaction phenomena; consequently, “QC V&V” is not be covered, “Model V&V” is referred as “V&V” for brevity purposes, and “Verification” procedures are not covered hereinafter.

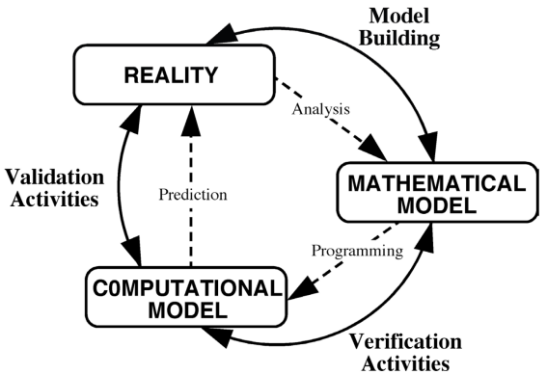

Figure 1-1 Initial illustration of the interaction of verification and validation in the numerical modelling process [3]

Figure 1-1 illustrates the steps involved in verification and validation (V&V), which are typically followed by most V&V standards/guidelines for numerical modelling. The steps shown in this figure can be summarized as follows [4]:

- The starting point, labeled as "Reality," represents the physical system/phenomenon intended for numerical modeling.
- The physical system is analyzed and conceptualized, leading to a “Mathematical Model”. This mathematical model is usually a system of partial differential equations, derived by considering the aspects of the physical system/phenomena aimed to be numerically modeled.
- The system of partial differential equations is converted via programming into a numerical algorithm, which along with boundary conditions, material properties, etc., form the “Computational Model”. Verification activities then involve testing and assessing the computational model to provide confidence that the mathematical model has been properly converted into a correct computational model (i.e., verify that the equations are being solved correctly).
- After verifying that the “Computational Model” properly solves the equations described by the “Mathematical Model”, it must be assessed whether the “Computational Model” properly simulates the phenomena under interest. Validation activities consist of assessing that the model is appropriate; in the field of solid/fluid mechanics, it is common to develop physical models and compare the results with those of the “Computational Model”.

While several validation standards/guidelines/recommendations have been established following the above main steps, important variations among them could be identified. Therefore, to perform repeatable and meaningful V&V exercises, appropriate validation procedures must be established.

Although different guides and recommendations regarding the validation procedures have been published [2] [5] [6] [7] [8] [9] [10] [11] [12] [13] [14] [15] (a review of the state of the art of V&V guides/standards is included in Section 2.4), the ASME Guides/Standards, and the JSCE Guidelines are recognized as international standards in the field of solid and fluid mechanics. These standards have been successfully applied in numerous applications and fields, making them suitable as a foundation for this thesis manuscript.

The ASME has developed validation standards/guidelines under different committees, tailored to specific target fields (refer to Section 2.4.1.2). While there are no specific committees addressing geotechnical engineering or liquefaction, it is important to note that the model intended to be validated in this thesis simulates the liquefaction phenomenon by solving equations of motion and water flow balance (refer to Appendix 3). Therefore, the use of either “ASME V&V 10” [2] (Standard for Verification and Validation in Computational Solid Mechanics), “ASME V&V 20” [5] (Standard for Verification and Validation in Computational Fluid Dynamics and Heat Transfer), along with the “JSCE V&V” [14] (Verification and Validation Methods for Nonlinear Ground/Structures Simulations - Guidelines and Practical Examples) would be applicable. A summary of these standards is included in Section 2.4.2.

1.2.2 Importance of Uncertainty Quantification and Cross-Checked experimental results

As it will be shown on Section 2.5, several efforts have been undertaken to validate specific models, not only in the context of soil liquefaction, but also in a wide range of fields.

While the V&V guidelines/standards emphasize the significance of quantitative validation exercises and uncertainty quantification (refer to Section 2.4); historically, the majority of validation efforts for numerical models have predominantly employed qualitative validation approaches (refer to Section 2.5.1). However, qualitative assessments of model validity are often subjective and rely on the author's observations when comparing numerical results with test or observation data; therefore the inclusion of a quantitative methodology for validation becomes crucial (refer to Section 2.5.2).

Along with the implementation of qualitative validation methodologies, quantifying uncertainty in model validation is essential to understand the limitations, reliability, and confidence of the analysis. Although experimental/observation data used for validation often lack sufficient information for accurately quantifying uncertainty in the evaluation of structure and material characteristics [14], in recent years, efforts have been made towards the development of quantitative validation exercises including uncertainty quantification (refer to Section 2.5.3).

Although the recent efforts towards the quantitative validation including uncertainty quantification provide valuable insights, they still often rely on a limited number of non-crosschecked experimental data. As it will be introduced in Section 2.5.4, it was found that even when conducted under controlled laboratory conditions, "identical" experiments performed in different facilities can yield significant differences in results due to various factors such as facility and machine characteristics, as well as the skills and experience of the experimenters. In the absence of noticeable errors or deviations in the experiments, it may not be possible to judge whether the differences between the “identical” experiments are due to one of them being correct or incorrect. Recognizing that none of the experiments provide the "correct values," the differences should be acknowledged as inherent variability in modeling the phenomenon.

Therefore, to adequately assess main trends and inherent variability, it becomes necessary to conduct cross-checked experiments/tests that compare test results from different facilities and experimenters; such cross-checked experiments/tests provide a robust foundation for the validation of numerical models

1.3 Objectives and novelty of the study

The primary objective of this thesis manuscript is to introduce a comprehensive probabilistic validation methodology for numerical models used in the prediction of the liquefaction phenomena. The methodology is based on state-of-the-art validation standards, and it is presented through the implementation of an actual validation exercise that explores the capabilities of the “Strain Space Multiple Mechanism Model” [16] for

liquefaction predictions. Specifically, the study focuses on assessing the final displacement caused by the lateral spreading phenomenon in a sloping ground under a diverse range of densities and input motions, using internationally cross-checked physical models, and high-quality element tests.

As it will be shown in Section 2.5, existing validation methodologies/exercises either rely on simple comparisons between mean values obtained from experimental results and numerical simulations, without considering uncertainty, or are based on limited and non-cross-checked experimental data. The novelty of this study is that it proposes a fully probabilistic validation methodology, based on a comprehensive comparison between the mean trends and associated variability observed in cross-checked experimental results and those in numerical simulations derived from high-quality element tests, in accordance with the recommendations of state-of-the art validation standards ([2] [17] [14]).

To achieve the main goal of this manuscript, the following specific objectives have been identified:

1. Define the validation procedures based on the latest validation standards.
2. Develop centrifuge tests as part of the LEAP Framework.
3. Process data of all the centrifuge tests under LEAP Framework (forty-eight tests) to characterize the response (i.e., the outcomes, expressed by the median response and its associated variability) of the sloping ground deposit under a wide range of densities (Dr50% - Dr 85%), and peak accelerations (0.1 – 0.35g)
4. Conduct high-quality Cyclic Hollow Cylinder Torsional Shear Tests under a wide range of densities and "Cyclic Stress Ratio" (CSR) to characterize the mechanical behavior (mean trends its and associated variability) of Ottawa F-65 Sand.
5. Calibrate the "Strain Space Multiple Mechanism Model" [16] parameters based on the Hollow Cylinder Torsional Shear Tests, and define/estimate the input uncertainty for the Numerical Modeling.
6. Develop numerical simulations based on the calibrated parameters, and uncertainty propagation.
7. Validate the numerical simulation implementation by comparing the outcomes (characterized by the mean trends and associated variability) of both the experimental results and numerical simulations, in accordance with the probabilistic validation methodology proposed in this study.
8. Assess the differences between the simulation results and individual centrifuge tests, and analyze the reasons for any discrepancies.

1.4 Proposed Validation Procedures

As mentioned, in Section 1.2.1, the ASME Guides/Standards (V&V 10, and V&V 20), and the JSCE Guidelines are intended to be used as a basis in this thesis manuscript.

Regarding the ASME Guides/Standards, the main differences between the V&V-10 and V&V-20 standards are summarized as follows [18] (detailed information of each guide/standard is included in Section 2.4.2):

1. Although the V&V-10 and V&V-20 standards share the same definition for “Validation”, the need to make decisions about the model adequacy in the hierarchical validation procedure proposed in the V&V-10 standard requires the definition of validation requirements, and validation comparisons to accept/reject the model. This pass/fail aspect of validation incorporated in the V&V-10 standard is not included in the V&V-20 standard.
2. The V&V-10 standard formulate a comparison of validation variables defined by probability distributions, whereas the V&V-20 standard formulates the comparison of validation variables by a scalar (which can represent the mean value or any other property as the median, variance, etc.) of the distributions used by V&V-10 [18].
3. The V&V-20 standard contain specific equations for the validation exercise, whereas the V&V-10 standard provide guidelines, and illustrations.

Since the validation procedures described in the V&V-10 standard allow a comprehensive assessment of the numerical model (both for the main trend and the associated variability) and provides conclusive metrics to assess the model's suitability (whereas the validation procedure described in the V&V-20 standard comprises only an assessment of the model error δ_{model} of specific scalar values), its validation procedures/recommendations, as well as the recommendations included in the JSCE Guidelines are used as the basis for the validation methodology/exercise described in this manuscript.

1.4.1 Methodology

As described in the V&V-10 standard [2], prior continuing with a Validation Exercise (refer to Section 2.4.2.1.3), three prerequisites are required. The conditions/assumptions under which these prerequisites are met in this study are described below.

1. Having a clear definition of the model's intended use.

   The model is intended to simulate the lateral spreading phenomenon of clean sands under a diverse range of densities (Dr50% - Dr 85%), and input motions (0.1g – 0.35g). Details of materials, model geometry, loading conditions, boundary conditions, etc., are provided in Section 3.1.

   In accordance with the V&V-10 standard described in Section 2.4.2.1.1, a hierarchical approach is recommended for dividing complex systems into smaller sub-systems to facilitate the validation process. However, this approach, as outlined in the JSCE Guidelines, is primarily intended for large-scale systems such as plants and aircraft. Given that the target validation system in this manuscript focuses specifically on a submerged sloping ground of Ottawa F-65 sand, and considering the recommendations of the JSCE Guidelines, subdivision of the system into additional sub-systems was not performed.

Additionally, as outlined in Section 2.4.2.3, the JSCE Guidelines propose a two-step validation procedure: the "Linear Behavior Range" and the "Non-Linear Behavior Range". The objective of conducting a validation step within the "Linear Behavior Range" is to establish the "optimal analytical model," which serves as the foundation for the subsequent validation within the "Non-Linear Behavior Range". However, considering previous studies [19] that have successfully replicated individual experiments on the target system (i.e., submerged sloping ground of Ottawa F-65 sand), the characteristics of the numerical implementation in this study are defined based on their recommendations; therefore, the validation in the “Linear Behavior Range” was not performed.

2. Having already conducted code verification.

   The model intended to be validated has been implemented in the commercial finite element program “FLIP ROSE”, and it has been widely used for evaluating the seismic performance of soil-structure systems in the research and engineering practice fields [20] [21] [22] [23], hence, the verification step is considered out of the scope.

3. Quantifying uncertainties in both the simulation results and the experimental results.

   As specified by the V&V-10 standard, the mean trends and associated variability of the system response of interest can be quantified when multiple (repeat) experiments have been performed. Therefore, the uncertainty quantification of the experimental results is analyzed by means of the observed variability in the results of a large database of centrifuge models. Additionally, the uncertainty quantification of the numerical simulation results is estimated based on the observed variability of the liquefaction resistance curve (LRC), obtained by a series of torsional hollow cylinder cyclic shear tests.

Considering the V&V processes according to the V&V-10 standard (refer to Figure 2-5 in Section 2.4.2.1.2), the V&V processes according to the JSCE Guidelines(refer to Figure 2-6 in Section 2.4.2.3.1), and the conditions/assumptions in which the validation prerequisites are met (see lines above), the flow for the validation exercise developed in this manuscript is summarized in Figure 1-2.

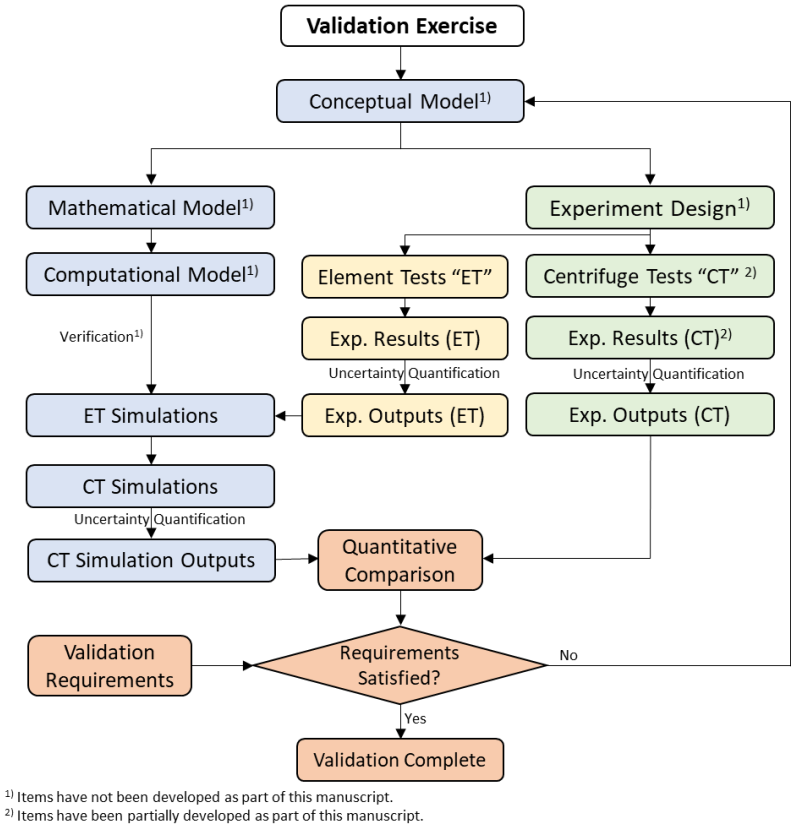

Figure 1-2 Schematic diagram of the main steps of the validation exercise

1.4.2 Conceptual Model, Mathematical Model, and Computational Model

The model selected for the validation exercise is the "Strain Space Multiple Mechanism Model" [16]. In this model, the behavior of granular materials is idealized on the basis of a multitude of virtual simple shear mechanisms oriented in arbitrary directions [19].

The Conceptual Model, Mathematical Model, and the Computational model are described in Appendix 3.

1.4.3 Experimental Design and Centrifuge Tests

In order to properly assess the main trends and variability of the physical models, large and cross-checked databases of high-quality experiments are required; for which large-scale testing campaigns through international collaborative efforts are considered appropriate.

In this sense, the Experimental Design, and Centrifuge Tests developed as part of the LEAP Project Exercises (refer to Section 2.5.5.2 and 3.1) have been used.

- The experimental specifications were developed by an international panel of experts [24] [25]; the experimental geometry, preparation method, and test conditions were designed to be replicable in multiple facilities around the world. The test specifications are described in Section 3.1.
- Forty-eight centrifuge tests were developed following the same specifications in ten different

centrifuge facilities around the world, as part of LEAP-UCD-2017 and LEAP-ASIA-2019 exercises.

- Among the forty-eight centrifuge tests, eight centrifuge tests were developed by the author in the geotechnical centrifuge at the Disaster Prevention Research Institute, Kyoto University. The model preparation, and test results are described in Sections 3.2 and 3.3.
- Based on the results of the forty-eight centrifuge tests, the database of the Physical Models was constructed, and its consistency was evaluated to estimate the mean response and the associated variability (uncertainty quantification) of the quantities under interest (i.e. estimate the "Experimental Output"). A description of the test results and the data processing is included in Section 3.4; and the uncertainty quantification (through hybrid MCMC-based Bayesian estimation) is described in Section 3.5.

1.4.4 Element Tests

Element tests were developed to study/characterize the mechanical behavior of Ottawa F-65 sand. As part of this step, twenty-three Hollow Cylinder Cyclic Torsional Shear Tests were performed for four different relative densities (Dr=50%, 60%, 70%, and 85%), under a wide range of Cyclic Stress Ratio (CSR) values [26]. To ensure consistency, sand from the same batches used in the numerical model was used.

The test specifications are described in Section 4.2, the test results are summarized in Section 4.3, and an assessment of the repeatability is provided in Section 4.4. Furthermore, the uncertainty quantification of the achieved Liquefaction Resistance Curve (by hybrid MCMC-based Bayesian estimation) is described in Section 4.5.

1.4.5 Element Tests Simulations, and Centrifuge Tests Simulations

Element Tests Simulations were conducted following the element-test experiments. As part of this step, the model parameters of the "Strain Space Multiple Mechanism Model" [16] were calibrated based on the results of the Torsional Shear Tests. The calibration of the model parameters for both the mean trend and the associated variability is described in detail in Section 5.1.

Based on the calibrated parameters, the Centrifuge Tests Simulations were developed to replicate the actual test conditions, and covering the range of relative densities (Dr50% - Dr 85%), and input motions (0.1g – 0.35g). In this process, the variability of the numerical model was estimated by propagating the variability established in the previous process (i.e., parameters calibration process). The characteristics of the Centrifuge Tests Simulations are described in detail in Section 5.2.

1.4.6 Quantitative comparison, and model assessment

As a final step in the validation exercise, the outcomes of the numerical and physical models were compared, taking into account the median trends and their associated variability; also, the suitability of the model was

assessed by means of validation metrics. The quantitative comparison, and model assessment is detailed in Section 6.1 and 6.2. In addition, the importance of Type B simulations, and the repeatability in physical models is discussed in Sections 6.3, and 6.4.

1.5 Structure of the manuscript

As previously introduced, the primary objective of this thesis manuscript is to propose a comprehensive probabilistic validation methodology for numerical models used in the prediction of the liquefaction phenomena, through the implementation of a complete validation exercise. To meet this objective, the manuscript has been organized as follows:

Section 1 – Introduction: This section provides an introduction to the manuscript, outlining the background and issues that will be addressed, along with the definition of the objectives, the novelty of the study and the methodology.

Section 2 – Literature Review: This section provides a description and advancements of the elements included in the study (liquefaction and lateral spreading, centrifuge models, effective stress models, V&V, etc.); including a description of the related existing studies, describing its advancements and limitations.

Section 3- Physical Modeling: This section provides a detailed description of the physical models used in the validation exercise, including a description of the specifications, testing process, data processing, and uncertainty quantification.

Section 4 – Element Tests: This section presents in detail the element tests conducted to study the mechanical properties of the target soil, required to calibrate the numerical model in the validation exercise. The section includes a detailed description of the specifications, testing process, data processing, and the uncertainty quantification.

Section 5 – Numerical Modeling: This section presents the numerical modeling process in detail, including the element simulations, model parameter estimations, definition and propagation of the uncertainty, and simulations of the physical models.

Section 6 – Numerical Model Assessment: This section presents the final step of the validation exercise, including a probabilistic assessment of the Numerical Model Outcomes based on the Physical Model Outcomes.

Section 7 – Conclusions and Future Works: This section summarizes the conclusions of the study, and identifies the future works required to continue/enhance the research.

2 Literature Review

2.1 Literature Review – Liquefaction, and Lateral Spreading caused by Liquefaction

One of the most dramatic causes of damage to structures during earthquakes is the occurrence of liquefaction in saturated sand deposits. When subjected to cyclic loading (such as an earthquake), loose sand tends to contract and transfer normal stress from the sand matrix onto the pore water if the soil is saturated and unable to drain during shaking. This results in a reduction in the effective confining stress within the soil, and an associated loss of strength and stiffness that contributes to deformations of a soil deposit [27].

The occurrence of soil liquefaction has been documented in numerous major earthquakes; however, it was the 1964 Niigata earthquake and the Alaska earthquake that provided clear and compelling examples of the devastating effects of liquefaction on civil infrastructure. These events served as a wake-up call to the earthquake engineering community, bringing liquefaction to the forefront as a major concern. As a result, efforts to understand the phenomenon of liquefaction intensified, with a view towards mitigating its effects on critical infrastructure. Following these earthquake events, extensive damage caused by liquefaction has been reported in the 1985 Mexico City earthquake, the 1995 Kobe earthquake, the 2007 Pisco earthquake, the 2011 Tohoku earthquake, the 2011 Christchurch earthquake, the 2016 Kaikoura earthquake, the 2018 Sulawesi earthquake, etc.

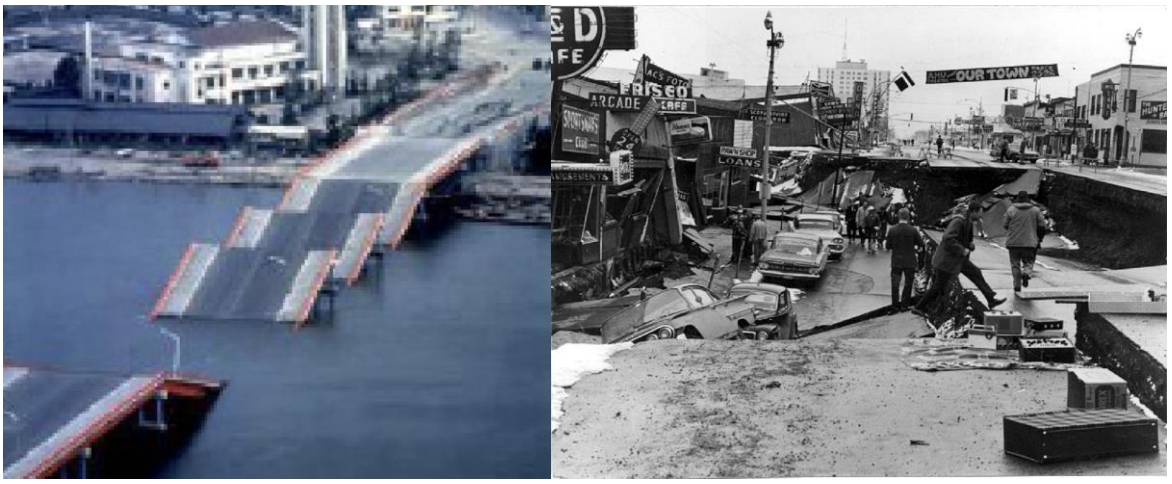

(a) (b)

Figure 2-1 (a) Liquefaction-triggered Showa Bridge collapse – 1964 Niigata Earthquake (NISEE), (b) Liquefaction-triggered damage – 1964 Alaska Earthquake (US Army)

2.1.1 Definition of Liquefaction or cyclic softening

As described by Ishihara [28], the basic mechanism of onset of liquefaction is elucidated from observation of the behavior of a sand sample undergoing cyclic stress application in the laboratory triaxial test apparatus. Seed and Lee [29] conducted the first cyclic triaxial test on samples of saturated sand to determine their resistance to liquefaction. The sand samples were consolidated under a certain confining pressure and subjected to a series of cyclic axial stresses under undrained conditions until they deformed to a certain amount of peak-to-peak axial strain. This loading procedure creates stress conditions on a plane of 45° through the sample which is the same as those produced on the horizontal plane in the ground during earthquakes.

Ishihara [28] observed that, in a typical cyclic triaxial test (see Figure 2-2), the pore water pressure builds up steadily as the cyclic stress is applied and eventually approaches a value equal to the initially applied confining pressure (i.e., 100% pore water pressure build up), producing an axial strain of about 5% in double amplitude, defining this state as initial liquefaction or simply liquefaction.

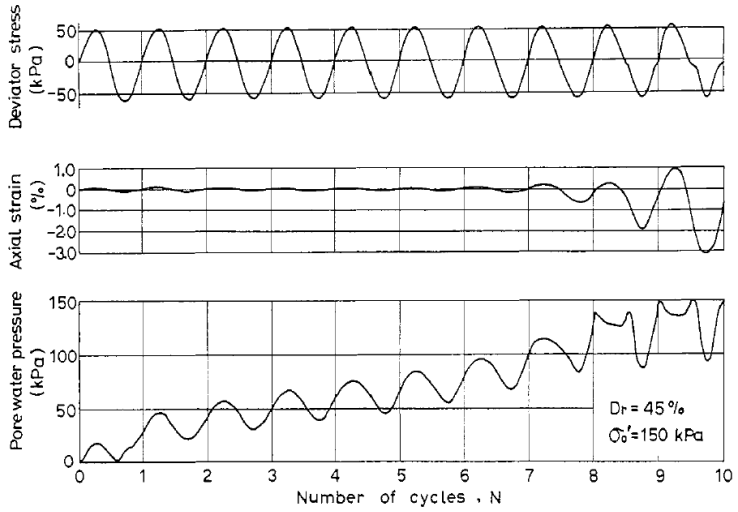

Figure 2-2 Axial strain and pore water pressure buildup in a cyclic triaxial test [28]

Subsequent experiments have revealed that certain types of samples (such as silty sands) exhibit considerable cyclic strain without 100% pore water pressure build up. Therefore, the occurrence of 5% double-amplitude (D.A.) axial strain in the cyclic triaxial test has been taken as a criterion to define the state of liquefaction by several researchers.

2.1.2 Liquefaction Research and Estimation Methods

Various methods have been developed to study soil liquefaction, including empirical methods, element tests, physical modeling, and numerical modeling.

- Empirical methods typically involve the use of field data, such as in-situ testing, to develop relationships between soil properties, earthquake characteristics, and the likelihood of liquefaction [27] [30]. These methods are useful for preliminary assessments and screening of potential liquefaction hazards. Examples of empirical methods include:
    - Empirical methods based on case histories: These methods use the observed performance of structures during past earthquakes to estimate the liquefaction potential. Examples include the HAZUS and NCEER methods.
    - SPT-based methods: These methods use Standard Penetration Test (SPT) data to estimate the liquefaction potential. Examples include the Seed and Idriss (1971) method [31], the Boulanger and Idriss (2014) method [32], the JRA (2019) method [33], etc.
    - CPT-based methods: These methods use Cone Penetration Test (CPT) data to estimate the liquefaction potential. Examples include the Robertson method (2021) [34], the Boulanger and Idriss (2014) method [32], etc.
    - Shear wave velocity-based methods: These methods use measurements of shear wave velocity (Vs) to estimate the liquefaction potential. The most representative example is the Andrus and Stokoe (2000) method [35].
- Element tests involve laboratory testing of soil samples, such as cyclic triaxial tests, cyclic simple shear tests, cyclic torsional tests, etc., to investigate the elemental behavior of soils under cyclic loading conditions. These tests can provide valuable insights into the soil's response to loading and its susceptibility to liquefaction. The tests are used primarily for: (1) study the liquefaction potential at a specific location, (2) to further study the mechanisms of liquefaction phenomena, and (3) to serve as a base for the development/validation of constitutive models.
- Physical modeling, such as 1-g tests, and centrifuge testing, has also been utilized to study soil liquefaction. In specific, centrifuge tests involve the scaling of soil samples and structures to simulate the behavior of full-scale systems under earthquake loading [28] [36].
- Numerical modeling; advanced numerical models can simulate the complex behavior of soils during liquefaction, however, prior its use in research and in engineering practice, these models require to be validated, usually based on reliable data from element tests and centrifuge experiments, providing a powerful tool for understanding and predicting the behavior of soils and structures during liquefaction-induced events.

2.1.3 Lateral Spreading Phenomenon

Lateral spreading is the finite, lateral movement of a sloping-saturated soil deposits caused by earthquake-induced liquefaction. The movement of soil deposits undergoing lateral spreading can range from a few centimeters to a few meters [37], causing significant damage to infrastructure elements such as buildings, bridges, lifelines, etc. Lateral spreading often occurs along riverbanks and shorelines where loose, saturated sandy soils are commonly encountered at shallow depths [38].

Several factors can influence the occurrence and magnitude of lateral spreading, including the slope angle, the presence of a free face, earthquake magnitude and direction, distance to the seismic source, the characteristics of the liquefiable layer (relative density, thickness, fines contents, grain size, etc.), soil stratigraphy, and others [37]. Due to this, actual deformation patterns are very complex and can be challenging to predict, as the one shown in Figure 2-3.

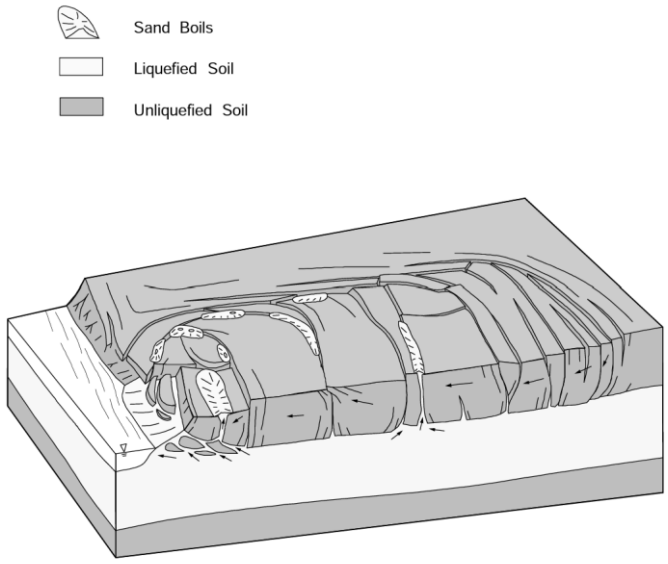

Figure 2-3 Schematic depiction of a lateral spread resulting from soil liquefaction in an earthquake [39]

2.1.4 Approaches for Estimating Lateral Spreading Displacements

Due to the complex nature of lateral spreading phenomena, various approaches have been proposed to estimate the resulting displacements [27]. These approaches can be broadly classified into the following categories:

- Estimation of displacements through regressions derived from past observations, including empirical regressions [37] [40], and machine learning [41] [42] [43].
- Newmark sliding block analysis, which predicts that displacements occur whenever the inertial forces from shaking cause the factor of safety against instability to temporarily drop below unity [27].
- Integration of estimated shear strains expected within liquefied zones [27].
- Estimation through non-linear dynamic analyses.

2.2 Literature Review – Centrifuge Models

Regarding physical modeling techniques, although other techniques (such as 1-g models) have been extensively used, centrifuge modeling has been identified as a reliable research tool for studying the behavior of geo-materials in a wide range of boundary value problems, mainly due to its ability to capture the correct stress-strain behavior of the materials under study [36].

2.2.1 Principles of Centrifuge Modeling

Centrifuge modeling is a powerful technique for studying geotechnical problems, including soil liquefaction, by replicating full-scale behavior in small-scale models [44]. The basic principle of centrifuge modeling involves scaling down the dimensions of the soil and structure while maintaining the same stress levels as in the full-scale prototype; this is achieved by subjecting the model to a centrifugal acceleration field (typically between 30g to 100g).

Geotechnical materials such as soil and rock have nonlinear mechanical properties that depend on the effective confining stress and stress history. By applying an increased gravitational acceleration to physical models, the centrifuge produces "identical" self-weight stresses in both the model and prototype. This one-to-one scaling of stress enhances the similarity of geotechnical models, making it possible to obtain accurate data for solving complex problems such as earthquake-induced liquefaction, soil-structure interaction, and the underground transport of pollutants like dense non-aqueous phase liquids [45].

By simulating real-world conditions and studying geotechnical behavior on a reduced timescale, centrifuge testing has become a crucial tool in advancing the field of geotechnical engineering.

2.2.2 Key Findings and Advances in Centrifuge Modeling of Soil Liquefaction

Centrifuge experiments have significantly advanced our understanding of soil liquefaction and its effects on structures. Some of the key findings and advances in centrifuge modeling of soil liquefaction are as follows [36]:

- Integration with numerical modeling: The combination of centrifuge experiments and advanced numerical simulations has led to a more comprehensive understanding of soil liquefaction and its effects on structures. Centrifuge model testing provides data to improve our understanding of basic mechanisms of deformation and failure and provides benchmarks useful for verification of numerical models [45].
- Influence of soil properties: Centrifuge experiments have helped to prove that soil properties, such as permeability, relative density, and initial effective stress, play a critical role in the initiation and development of liquefaction. These properties affect the generation of excess pore water pressure and the subsequent strength degradation of the soil.

- Effects on infrastructure: Centrifuge studies have demonstrated the impact of soil liquefaction on various types of infrastructure, including shallow foundations, piles, retaining walls, caissons, etc.
- Role of countermeasures: Centrifuge experiments have also been used to investigate the effectiveness of various liquefaction mitigation techniques, such as ground improvement methods, the use of reinforcements, etc., to enhance the performance of structures subjected to static and dynamic loading conditions.
- Advancements in instrumentation and data interpretation: Centrifuge experiments on soil liquefaction have benefited from advancements in instrumentation and data interpretation techniques, allowing for more accurate and detailed measurements of soil response and structural performance. These advancements have facilitated a better understanding of the underlying mechanisms of soil liquefaction and the factors that influence its development and consequences.

2.2.3 Centrifuge models and numerical models

Centrifuge modeling and numerical simulations are two prominent approaches used in geotechnical engineering to study complex soil behavior, such as liquefaction. As stated by Madabhushi [36], some of the advantages of centrifuge modeling include:

- It allows the investigation of complex problems by constructing small-scale physical models and testing them in the enhanced gravity field of a geotechnical centrifuge.
- Use of miniature instruments (inside the model), to capture the soil behavior before, during, and after the events being studied.
- Geotechnical laboratories can create accurate models to ensure the repeatability, in order to increase confidence in their results.
- Soil models with well-known and well-controlled stress history can be simulated.
- Extreme/rare events can be simulated (such as earthquake loading) can be modeled in-flight using customized actuators.
- Complex construction sequences can be modeled in flight.
- Plane strain models, or fully three-dimensional models can be developed based on test conditions.

Regarding the numerical modeling of geomaterials, during the last decades, important efforts and developments in computational modeling have contributed to the understanding of the phenomena, and allowed to increase the accuracy of prediction of the dynamic response of soil systems. Although computational models are not yet able to capture/model all the details and the complex behavior of the geomaterials [8], important advantages of numerical simulations compared to physical modeling can be summarized as follows:

- Because of its low cost and speed, multiple models can be developed to investigate multiple scenarios, develop parametric studies, implement probabilistic approaches, etc.
- Large scale models can be developed.
- Detailed information can be obtained at any point in the system, such as deformations, stress values, etc.
- Modeling repeatability can be ensured.

If the outcomes of a numerical model can be shown to be reliable, it can be considered reasonable to prefer its use over centrifuge models (and other methods such as empirical methods, 1-g tests, etc.) due to its cost/time advantages. However, in order to increase their reliability, promote their development, and enable their incorporation into design practice, the numerical tools for liquefaction modeling must undergo verification and validation processes [1].

2.3 Literature Review – Effective stress models for modeling Soil Liquefaction

Although several efforts have been made in the development of computational models to simulate the behavior of geomaterials using discrete elements [46] [47], the computational models predominantly employed in research and engineering practice, including the model adopted in this thesis, are based on the assumption that geomaterials can be represented as continua, where, the main assumption is that geomaterials can be treated as a continuous media at the macroscopic scale, disregarding the discrete nature of their constituents.

In continuum mechanics, the fundamental laws provide the following nine equations: the mass conservation law (1), the conservation laws of linear momentum (3), the conservation laws of angular momentum (3), the conservation of energy (1), and the entropy production inequality (1). On the other hand, the following nineteen variables are contained in the fundamental laws: the mass density (1), velocity components (3), components of the stress tensor (9), temperature (1), components of the heat flow vector (3), internal energy (1), and entropy (1) [48].

The constitutive equations describe the material's inherent response to external actions, and include the eleven additional equations required to describe material behavior, such as: stress-strain relations (6), heat flux (3), internal energy (1), and entropy (1). These constitutive equations are derived based on actual experiments, satisfying the fundamental laws and objectivity (the constitutive equations shall be independent to changes in the coordinate frame).

2.3.1 Governing equations for multiphase geomaterials

One of the most important characteristics of geomaterials is that these are composed of solid, liquid, and gas phases in general. In order to model these materials within the framework of continuum mechanics, and

by considering the characteristics of each phase, the Porous-Media theory is generally used.

Porous-media theory is based on a representation of two or more species occupying the same space at the same time [49] (immiscible mixture of solids and fluids), as shown in Figure 2-4.

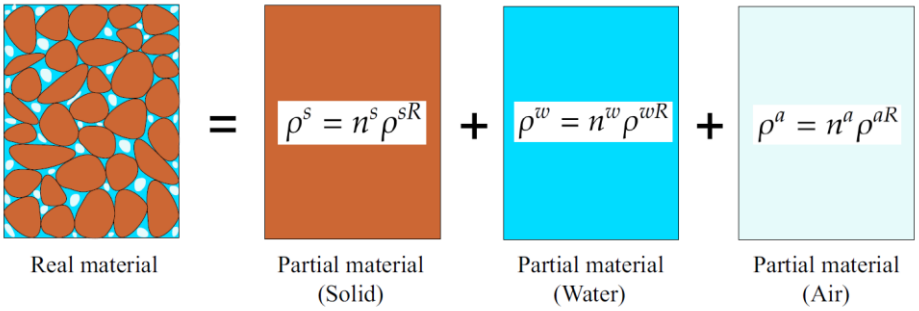

Figure 2-4 Porous-media theory representation [49]

As it will be later introduced, the models developed on this thesis manuscript are built on the assumption that the ground model is fully saturated, therefore, a brief description of the governing equations for water-soil (skeleton) materials is included.

2.3.1.1 u-p formulation

The governing equations for water-soil coupled problems can be derived from Biot's theory of water saturated porous media [50] [51]. Although various methods have been proposed for the Biot's two-phase mixture theory depending on the method of approximation and the choice of unknown variables, in many computer programs for liquefaction and consolidation analyses, the displacement (u) of the solid and pore water pressure (p) are used as the unknown variables (u-p formulation) [48]. However, it shall be noted that it has been found that this formulation provides a different solution in the high frequency range for high permeability values [52].

In the u-p formulation, the following assumptions are adopted [48]:

- An infinitesimal strain is used.
- The relative acceleration of the fluid phase to that of the solid phase is much smaller than the acceleration of the solid phase.
- The grain particles in the soil are incompressible.
- The effect of the temperature is disregarded.

2.3.1.2 Density of mixture

The relationship between the overall density ρ, and the densities of the solid phase $\bar{\rho}_s$, the fluid phase $\bar{\rho}_f$ is defined as follows:

$$\rho = \bar{\rho}_s + \bar{\rho}_f = (1-n)\rho_s + n\rho_f \quad (2\text{-}1)$$

Where:

- ρ : Overall density of the soil/water mixture
- $\bar{\rho}_s$: Density of the solid phase
- $\bar{\rho}_f$: Density of the fluid phase
- n : Porosity
- ρ_s : Density of the solid
- ρ_f : Density of the fluid

2.3.1.3 Effective stress and partial stresses of the fluid-solid mixture

The total stress is given by the sum of the partial stresses acting on the phases as:

$$\boldsymbol{\sigma} = \boldsymbol{\sigma}_s + \boldsymbol{\sigma}_f \quad (2\text{-}2)$$

$$\boldsymbol{\sigma}_f = -np\boldsymbol{I} \quad (2\text{-}3)$$

$$\boldsymbol{\sigma}_s = \boldsymbol{\sigma}' - (1-n)p\boldsymbol{I} \quad (2\text{-}4)$$

Where:

- $\boldsymbol{\sigma}$: Total stress tensor
- $\boldsymbol{\sigma}_s$: Partial stress tensor of the solid phase
- $\boldsymbol{\sigma}_f$: Partial stress tensor of the fluid phase
- p : Pore water pressure
- $\boldsymbol{\sigma}'$: Effective stress tensor
- $\boldsymbol{I}$: Second-order unit tensor

The total stress is described by the effective stress and the pore water pressure as:

$$\boldsymbol{\sigma} = \boldsymbol{\sigma}' - p\boldsymbol{I} \quad (2\text{-}5)$$

2.3.1.4 Equations of motion, and water flow balance

Considering the fundamental principles of conservation laws (mass, linear momentum, and angular momentum, etc.), the assumptions of the u-p formulation, and incorporating Darcy's Law, the equations of

motion and water flow balance for a fully saturated porous medium can be derived.

Detailed descriptions of the equations of motion and water flow balance (including its numerical implementation) that are used to solve the numerical models developed as part of this thesis manuscript are included in Appendix 3.

2.3.2 Constitutive equations for soil liquefaction

As previously described, constitutive equations are required to describe material responses to external actions. In the context of the development of constitutive models for soil liquefaction, elastoplastic theory is known as a representative tool for modeling the nonlinear and hysteretic behavior of soil. Within soil mechanics, an associated flow rule has been employed to model the behavior of soil, specifically soil exhibiting negative dilatancy, such as normally consolidated clay. Conversely, non-associated flow rules are commonly used to represent sand with positive-negative dilatancy [48].

Over the past decades, the development of constitutive equations for simulating liquefaction phenomena has led to the creation of several cyclic elastoplastic models for granular soils [16] [53] [54] [55] [56] [57] [58]. These models have been subsequently applied to design practice using suitable numerical methods, such as the finite element method.

It has been found that the "Strain Space Multiple Mechanism Model" has shown good performance in simulating the liquefaction phenomenon when compared to field observations [59] [22] [23], laboratory models [60], and specifically models simulating liquefaction-induced lateral spreading [19] [61]; therefore, it has been selected as the target model for validation.

A detailed description of the formulation of the "Strain Space Multiple Mechanism Model" 's constitutive equation has been included in Appendix 3.

2.4 Literature Review – Verification and Validation

2.4.1 State of the art of Validation Standards/Guidelines

Since mid-1960s, the importance of modeling and simulation dramatically increased as computer-controlled systems started to become widespread in commercial and public systems, particularly automatic flight-control systems for aircraft [2] [7].

As modeling and simulation advanced, concerns arose as to whether the simulations correctly reproduced the systems/phenomena under study, and whether the results could be reliably applied in practical applications. Consequently, efforts were initiated to establish standards and guidelines for V&V processes.

Although some works have been published earlier, the first formal definitions for V&V procedures were

published by the Society for Computer Simulation [3] on 1979 (refer to Figure 1-1). Although brief, they have served as a basis for further development of Guidelines/Standards in this area.

According to the “Verification and Validation Methods for Nonlinear Ground/Structures Simulations - Guidelines and Practical Examples” [14], published by the Japanese Society of Civil (JSCE), the V&V guidelines/standards can be classified in “QC (Quality Control) V&V”, and “Model V&V”.

- In “QC V&V”, the verification aims to confirm that the analysis has been performed correctly, adhering to the specifications and plans, while validation seeks to determine whether the analysis results adequately represent the entity to fulfill the purpose of the analysis.
- In “Model V&V”, verification is defined as the process of demonstrating that the model accurately represents the solution of the underlying mathematical (theoretical) model. Validation, on the other hand, is the process of determining the extent to which the model accurately represents the target phenomenon based on its intended use and other metrics.

2.4.1.1 “QC V&V” guidelines/standards

Regarding the development “QC V&V” guidelines/standards, initial standards for quality assurance of engineering simulations were developed by NAFEMS (a non-profit organization from the UK) since early 1990`s, resulting in the publication of the “SAFE Structural Analysis (SAFESA)” [62] Technical Standard for Structural Analysis Quality Assurance in 1995. SAFESA outlines detailed procedures and requirements for describing the target, creating models, performing calculations, and verifying appropriateness of the model. Following SAFESA, in 2020, NAFEMS published the “NAFEMS Engineering Simulation Quality Management Standard” [63], which is intended to interpret the quality standard ISO 9001:2015 in the particular context of the engineering simulation process.

In terms of Japanese National Standards/Guidelines for “QC V&V”, the Japan Society for Computational Engineering and Science (JSCES) organized the "Quality and Reliability Subcommittee on Simulation" in 2009. The subcommittee conducted investigations on international trends and industrial efforts, establishing practical quality management and standard procedures in 2015 and 2017 [64] [65].

Furthermore, the JSCE's V&V Concrete Engineering Committee organized the "Numerical Analysis Certification Subcommittee Based on Concrete Standard Specifications" in 2013; based on its findings, started implementing the JSCE Technical Evaluation System in 2015.

2.4.1.2 “Model V&V” guidelines/standards

Regarding the development of “Model V&V” guidelines/standards, the scientific and engineering communities have explored application-specific V&V since the 1990s [2]. In 1992, the AIAA Computational Fluid Dynamics Committee on Standards began a project to formulate and standardize the

basic terminology and methodology in the V&V of CFD simulations. A committee was composed of representatives from academia, industry, and government, with representation from six countries; and after six years of development, the committee published the “Guide for the Verification and Validation of Computational Fluid Dynamics Simulations” in 1998 (then revised in 2002) [66]. This guide is considered the initial internationally -accepted guideline for “Model V&V” processes, although it is tailored for Computational Fluid Dynamics Simulations. [7]

Following the AIAA's work, in August of 1999, the American Society of Mechanical Engineers (ASME), under the auspices of the United States Association of Computational Mechanics (USACM), proposed the formation of a verification & validation specialty committee to explore the possibility of developing V&V guidelines for computational solid mechanics, which would complement the already completed work of the AIAA CFD Standards Committee [4].

The ASME has since expanded its scope and formed the “V&V Standards Committee on Verification and Validation in Modeling and Simulation” in 2008, which aims to develop V&V standards under the following committees.

- V&V 10–Verification and Validation in Computational Solid Mechanics
- V&V 20–Verification and Validation in Computational Fluid Dynamics and Heat Transfer
- V&V 30–Verification and Validation in Computational Simulation of Nuclear System Thermal Fluids Behavior
- V&V 40–Verification and Validation in Computational Modeling of Medical Devices
- V&V 50–Verification and Validation of Computational Modeling for Advanced Manufacturing
- V&V 60–Verification and Validation of Computational Modeling in Energy Systems
- V&V 70 – Verification and Validation of Machine Learning

As of March 2023, the following Guidelines/Standards have been published by the “V&V Standards Committee on Verification and Validation in Modeling and Simulation”.

- V&V 10–2019, Standard for Verification and Validation in Computational Solid Mechanics [2]
- V&V 10.1–2012, An Illustration of the Concepts of Verification and Validation in Computational Solid Mechanics [17]
- V&V 20–2009 (R2021), Standard for Verification and Validation in Computational Fluid Dynamics and Heat Transfer [5]
- V&V 40–2018, Assessing Credibility of Computational Modeling through Verification and Validation: Application to Medical Devices [67]

In Japan, efforts to establish national standards and guidelines for "Model V&V" have also been made. The

Atomic Energy Society of Japan (AESJ) published the "Guide for the Assessment of Nuclear Simulation Credibility" in 2015 [15], targeting V&V for nuclear simulations. Additionally, the JSCE organized subcommittees to promote the generation of V&V Standards/Guidelines in 2014, resulting in the publication of the “Verification and Validation Methods for Nonlinear Ground/Structures Simulations - Guidelines and Practical Examples” [14] in 2022. This publication provides guidance on V&V methodologies for nonlinear ground and structural simulations, offering practical examples and outlining procedures for ensuring the credibility of such simulations in civil engineering applications.

2.4.2 Description of the base V&V guidelines/standards

As introduced in Section 1.2.1, the V&V ASME Guides/Standards (V&V 10, and V&V 20), and the JSCE Guidelines have been selected as base guides/standards to formulate the validation methodology proposal. The characteristics of “V&V 10” (based on [2]), “V&V 20” (based on [5]), and “JSCE V&V” (based on [14]) are included in Sections 2.4.2.1, 2.4.2.2, and 2.4.2.3 respectively.

2.4.2.1 Standard for Verification and Validation in Computational Solid Mechanics (V&V 10 - 2019)

The purpose of the V&V 10 Standard is to provide the Computational Solid Mechanics (CSM) community with a common language, a conceptual framework, and general guidance for implementing the process of V&V. To this end, the standard includes definitions, recommendation of the V&V approach activities, and discussion of factors that shall be considered when developing and executing a V&V program.

Also, the document V&V 10.1 (“An Illustration of the Concepts of Verification and Validation in Computational Solid Mechanics”) [17], is a follow-on publication that illustrates the steps in the V&V process described in the V&V 10 Standard.

The definitions of “Verification”, and “Validation” set by the V&V 10 are given as follows:

- Verification is the process of determining that a computational model accurately represents the underlying mathematical model and its solution.
- Validation is the process of determining the degree to which the model is an accurate representation of corresponding physical experiments from the perspective of the intended uses of the model.

2.4.2.1.1 Hierarchical approach to V&V

Many real-world physical systems subject to V&V are inherently complex; to address this complexity the system being modeled is considered as hierarchical in nature, and each separate section of the hierarchy is considered as a validation case (or instance that need to be validated).

Generally, a top-down decomposition of the physical system into its constituents is the basis for developing a model of a complex system, however, the recommended approach to V&V is to develop such a hierarchy

and then work from the bottom up, beginning at the lowest tier, to identify and describe the physical phenomena at each level that must be accurately simulated with the model.

2.4.2.1.2 V&V processes

Figure 2-5 illustrates the V&V processes recommended by the V&V-10 standard; in this Figure, prior assessing the validation requirements, 2 main branches (i.e., group of activities) are identified: (a) The Modeling and Simulation Branch, and (b) The Physical Experimentation Branch. In this section, a description of these branches is included.

The Modeling and Simulation Branch:

- Through idealization, the modeler constructs a mathematical interpretation of the conceptual model, which is composed of a set of equations and modeling data that describe physical reality, including the geometric description, governing equations, initial and boundary conditions, constitutive equations, and external forces.
- As part of the approximation, implementation, and input definition activity, the modeler develops the computational model, which is the software implementation of the mathematical model, which generally includes numerical procedures, such as finite element or finite difference, for solving the governing equations.
- In the code verification assessment activity, the modeler uses the computational model to assess a separate set of problems with known solutions. These problems typically have much simpler geometry, loads, and boundary conditions than the validation problems to identify and eliminate algorithmic and programming errors.
- In the calculation activity, the modeler runs the computational model to generate the simulation results for the validation case. The simulation results can also be post-processed to generate response quantities for comparison with experimental results.
- In the subsequent UQ activity, the modeler should quantify the uncertainties in the simulation results that are due to inherent variability in model parameters or lack of knowledge of the parameters or model form.
- Response quantities of interest extracted from simulation results and estimates of uncertainty combine to form the simulation outputs that are used for comparison with the experimental outputs.

The Physical Experimentation Branch:

- The experimental design is a set of material specifications, boundary conditions, initial conditions, and instrumentation requirements that are necessary to observe and measure the effect that changes to input variables have on the solid mechanics behavior of the validation case. The modeler and the experimenter should work together so that each is continually aware of assumptions in the models

or the experiments.

- Implementing the experiment design into a validation experiment involves setting up the physical model, installing instrumentation, and confirming the setup.
    - Instrumentation quality assurance is an assessment of whether the measurement system is acceptably accurate and repeatable for its intended purpose.
    - Data acquisition involves the collection of raw data from various instruments used in the experiment, and the generation of processed data.
- The experimental results can be transformed as necessary into experimental quantities that are more useful for direct comparison with simulation outputs. Multiple experiments are generally required to quantify uncertainty due to inherent variability. Data quality assurance (Data QA) is an assessment of whether data captured during a validation experiment are a reasonable representation of what occurred during the experiment.
- The UQ shall be performed to quantify the effects of various sources of uncertainty on the experimental results. These sources include measurement error, design tolerances, manufacturing and assembly variations, unit-to unit fabrication differences, and variations in performance characteristics of experimental apparatuses.

Once experimental and simulation outputs for the actual test conditions have been generated, the modeler and experimenter perform the validation assessment activity by comparing these two sets of outputs. The metrics for comparing experimental and simulation outputs as well as the criteria for meeting the requirements shall be defined during the formulation of the V&V plan.

It is important to remark that the diamond symbol asking “Requirements Satisfied?” provides an objective decision point for (a) Complete the Validation (or continue the next validation case in the hierarchy), or (b) Revise the Model/Experiments.

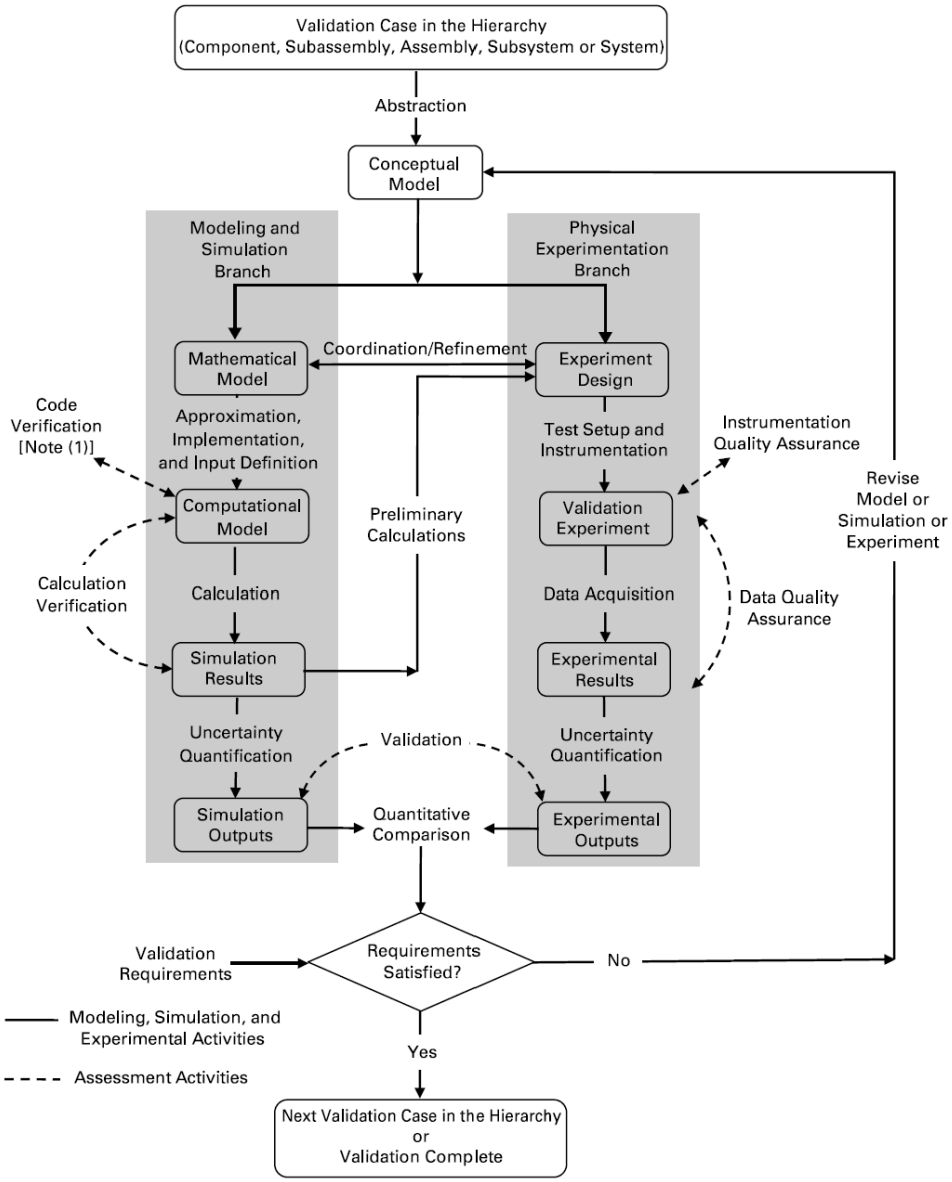

Figure 2-5 V&V Process as per the V&V 10 Standard [2]

2.4.2.1.3 Validation Process

Three prerequisites prior proceeding to the Validation Process are required:

1. Having a clear definition of the model's intended use
2. Completed code verification and calculation verification activities
3. Quantify uncertainties in both the simulation outputs and the experimental outputs

The approach of validation is to measure the agreement between the simulation outputs from a computational model and the experimental outputs from appropriately designed and conducted experiments. These outputs should incorporate the experimental and modeling uncertainties in dimensions, materials, loads, and responses.

2.4.2.1.4 Model Accuracy Assessment

Following UQ of the experimental results that produced the experimental outputs, the final steps in validation consist of:

1. Comparing values of the metrics chosen to measure the agreement between simulation outputs and experimental outputs.
2. Making an assessment of the accuracy of the computational model relative to the goals provided in the V&V plan for the model's intended use

A validation metric provides a method by which the simulation outputs and the experimental outputs can be quantitatively compared. The metric result is compared to the accuracy requirements defined in the V&V plan to determine whether acceptable agreement has been achieved.

Validation metrics should incorporate the uncertainties associated with the experimental outputs and the uncertainties associated with the simulation outputs (e.g., the input parameter uncertainties propagated through the computational model). When multiple (repeat) experiments have been performed, the mean and variance of the system response of interest can be quantified.

2.4.2.2 Standard for Verification and Validation in Computational Fluid Dynamics and Heat Transfer (V&V 20 - 2009(R2021))

The goal of the V&V-20 standard is the estimation of the accuracy of a mathematical model for specified validation variables at a specified validation point for cases in which the conditions of the actual experiment are simulated. A specified validation point means that the accuracy of the mathematical model is evaluated for simulations performed for the same domain, fluid properties, and boundary conditions of the experiment that provides the physical data [18].

The validation methodology applied in the V&V-20 standard applies to validation variables defined by a scalar; however, this shall not be misinterpreted as it is focused on deterministic simulation because the validation procedure can be applied to the mean, median, variance or any property (global or local) of a probabilistic distribution that can be defined by a scalar [18].

The starting point of the V&V-20 standard is the definition of the simulation error δ_S, and the experimental error δ_D of the validation variable, as follows:

$$\delta_S = S - T \tag{2-6}$$

$$\delta_D = D - T \tag{2-7}$$

Where:

- S : Simulation Value
- D : Experimental Value
- T : True value (unknown)

The difference between the simulation and experimental values (which is equivalent to the difference between the simulation and experimental errors), is the comparison error E, defined as follows:

$$E = S - D = \delta_S - \delta_D \tag{2-8}$$

The process of simulating the validation variable generates the simulation error δ_S, which includes the following three contributions:

- The model error δ_{model}, which is the consequence of the continuum modeling assumptions, and approximations.
- The numerical error δ_{num}, which is originated from the numerical solution of the mathematical model.
- The parameter/input error δ_{input}, which is the error caused by to inexact boundary conditions, fluid properties, etc.

The goal of the validation procedure established by the V&V-20 standard is the determination of δ_{model}, which, can be calculated as follows:

$$\delta_{model} = E - (\delta_{num} + \delta_{input} - \delta_D) \tag{2-9}$$

As stated in Eq. (2-9), the determination of δ_{model} requires the numerical, input, and experimental errors, which are not known, therefore, δ_{model} cannot be determined, but only estimated using Eq. (2-10).

$$\tilde{\delta}_{model} = E - (\tilde{\delta}_{num} + \tilde{\delta}_{input} - \tilde{\delta}_D) \tag{2-10}$$

Where $\tilde{\delta}_{model}$, $\tilde{\delta}_{num}$, $\tilde{\delta}_{input}$, and $\tilde{\delta}_D$ become the estimates of the unknown errors included in Eq. (2-9), under the following assumptions:

- Once the experiment and simulations have been performed to determine D and S, the effect of experimental error on D and numerical, input, and model errors on S are realized fixed quantities ("fossilized") of unknown magnitude.
- Any known signed biases in the experiments and simulations are assumed to be removed.
- Standard uncertainties u_{num}, u_{input} and u_D are estimated to obtain reasonable characterizations of

the numerical, input and experimental errors $\tilde{\delta}_{num}$, $\tilde{\delta}_{input}$, and $\tilde{\delta}_D$. The uncertainty for the combination of these three errors is defined as u_{val}.

Using a probabilistic description of $\tilde{\delta}_{num}$, $\tilde{\delta}_{input}$, and $\tilde{\delta}_D$ based on the mean and standard uncertainty, the expected value of the model error $\tilde{\delta}_{model}$ can be obtained by using Eq. (2-10), as follows (the expected values of the numerical, input and experimental are equal to zero because all known biases have been removed):

$$\hat{\delta}_{model} = \varepsilon[\tilde{\delta}_{model}] = E - \varepsilon\left[\tilde{\delta}_{num} + \tilde{\delta}_{input} - \tilde{\delta}_D\right] = E \tag{2-11}$$

Also, following the assumption that E is a fixed number, the variance of $\tilde{\delta}_{model}$ can be estimated as follows.

$$V[\tilde{\delta}_{model}] = V\left[\tilde{\delta}_{num} + \tilde{\delta}_{input} - \tilde{\delta}_D\right] \tag{2-12}$$

Although, the V&V-20 standard describes complex dependencies between the three different error sources ($\tilde{\delta}_{num}$, $\tilde{\delta}_{input}$, and $\tilde{\delta}_D$), in the simplest situation these error sources are assumed to be independent; in that case, Eq. (2-12) can be expressed as follows:

$$u_{val}^2 = V\left[\tilde{\delta}_{model}\right] = u_{num}^2 + u_{input}^2 + u_D^2 \tag{2-13}$$

Thus, the interval that characterizes the estimated model error is given in Eq. (2-14).

$$E - u_{val} \leq \delta_{model} \leq E + u_{val} \tag{2-14}$$

Then, the estimation of u_{val} (which require the evaluation of the numerical, input, and experimental uncertainties) is thus at the core of the methodology presented in the V&V-20 standard.

2.4.2.2.1 Expanded uncertainties and degree of confidence

The standard uncertainties u_{val} may be multiplied by a coverage factor k to obtain an expanded uncertainty $U_{val,\%}$, which provides a band at a given confidence level. The determination of the coverage factor k requires knowledge/assumption about the probability distributions that characterize $\tilde{\delta}_{num}$, $\tilde{\delta}_{input}$, and $\tilde{\delta}_D$; for typical distributions (such as uniform, triangular, Gaussian) the coverage factor k takes values in the range of 2-3 for a 95% of probability

2.4.2.2.2 Interpretation of the Validation Results in the V&V-20 standard

For a specific validation variable at specified conditions (the set point), the V&V 20 standard defines an interval that should contain the model error, as follows:

$$E - U_{val,\%} \leq \delta_{model} \leq E + U_{val,\%} \quad (2\text{-}15)$$

There are two main observations about the outcome of the procedure:

- The goal of the V&V20 standard is to estimate δ_{model}, not to obtain $E \leq U_{val,\%}$. Satisfying this inequality is always possible and trivial (increasing numerical and/or experimental uncertainties is sufficient to achieve it)
- $U_{val,\%}$ reflects the quality of the validation assessment and not the accuracy of the model (i.e. δ_{model}). $U_{val,\%}$ depends only on the numerical, input and experimental uncertainties and so its level reflects quality of the experiments and simulations not the quality of the model.

Eq. (2-15) estimates an interval that should contain δ_{model} (with a certain confidence level percentage), which means that it provides estimates of the lowest $\left(\tilde{\delta}_{model}\right)_{min}$ and largest $\left(\tilde{\delta}_{model}\right)_{max}$ values of δ_{model} at the set point (with a certain confidence level percentage). Based on the relative values of E and $U_{val,\%}$, the validation results can be interpreted as follows:

- $|E| \gg U_{val,\%}$ leads to $\delta_{model} \approx E$.
- $|E| \ll U_{val,\%}$ gives $|\delta_{model}| \leq U_{val,\%}$, which still gives a band for δ_{model}, but it does not identify the sign of the model error.
- If $|E|$ and $U_{val,\%}$ do not satisfy either of the two conditions above, it can only be said that $|\delta_{model}| \leq |E| + U_{val,\%}$.

From a Validation perspective, the first case is the desired result because the goal of the procedure is to estimate δ_{model}. On the other hand, the second case is a consequence of a poor-quality validation exercise that may be easily misinterpreted.

Finally, the outcome of the V&V-20 standard is an assessment of the model error δ_{model}, however, the decision of whether or not a given model error is acceptable for a specific application is not part of the standard.

2.4.2.3 Verification and Validation Methods for Nonlinear Ground/Structures Simulations - Guidelines and Practical Examples (JSCE V&V)

The "JSCE V&V" guideline outlines fundamental concepts and procedures to confirm the reliability of simulations using analytical models for permanent, variable, and contingent actions (such as earthquakes), in geotechnical and structural engineering. A summary of the validation procedures, and its differences with the ASME V&V10 Standard is presented.

2.4.2.3.1 Validation Procedures

The validation and verification procedures are summarized in Figure 2-6.

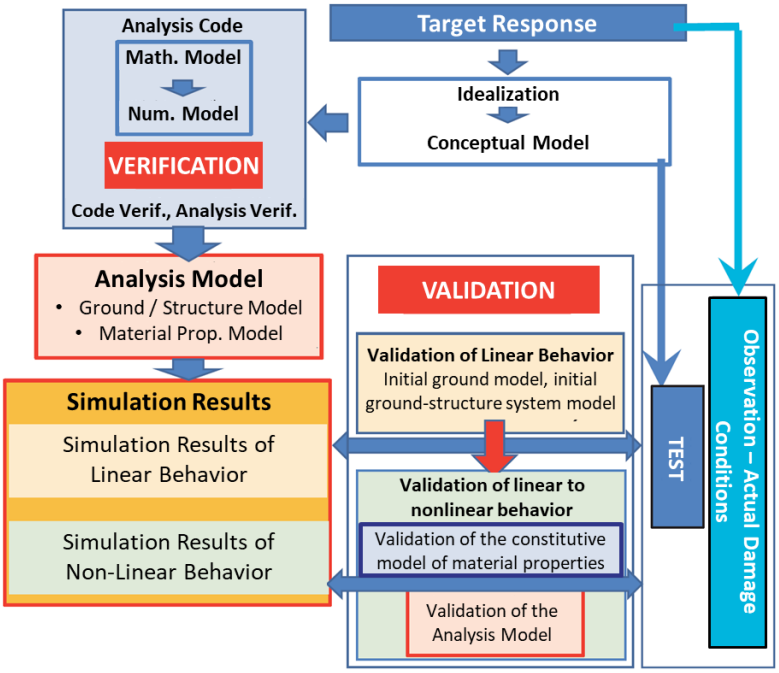

Figure 2-6 Flow of V&V Procedures - JSCE V&V (translated from Japanese) [14]

The procedure begins with the Verification of the code used in the target simulation. Following that, the Validation is performed using the verified analysis code through the following steps:

1. Validation is performed in two stages: (1) linear behavior of the target ground or ground-structure system, and (2) behavior transitioning from linear to nonlinear behavior. Here, "linear behavior" or "behavior transitioning from linear to nonlinear" is classified based on the main factors governing the overall performance of the target element/structure, such as ground deformation or the deformation of the materials constituting the ground-structure system.
    a. The model used for simulating the linear behavior of the target ground or ground-structure system is called the "initial ground model", or the "initial ground-structure system model". Multiple ground and ground-structure system models are then established from these "initial" models to estimate the "optimal analytical model". The estimation of the "optimal analytical model" is based on the reproducibility of the model in the linear to slightly-nonlinear behavior range.
    b. The model used for simulating the behavior transitioning from linear to nonlinear of the target ground or ground-structure system is called the "analysis model", which is based on the "optimal analytical model". The validation of the simulation results for the "analysis model" is based on first validating the constitutive model of the materials, and then

validating the analysis model of the ground or ground-structure system considering the constitutive model.

2. In the validation process, the evaluation of the certainty of the simulation can be performed by a comparison of the simulation results with: (1) models using actual materials, (2) experiments using a simple model to reproduce the behavior, (3) observations of the actual behavior of the ground or the ground-structure system, (4) or observations of actual damages of the ground or the ground-structure system.
3. The validation process is composed by two steps “reproducibility evaluation”, and “predictive performance evaluation”. The reproducibility evaluation is performed by evaluating the comparison performed in the previous step (comparison between simulation against tests, observations, etc.), taking into account the uncertainties by defining a metric based on the model's intended use.
4. The analytical model that produces reproducible simulation results is called the “best estimate model”, and is used for the predictive performance evaluation. The evaluation of the prediction performance is based on the variability of the evaluation-metric, which is estimated by conducting simulations that take into account the uncertainties associated with conditions that differ from the experiments/observations used in the previous steps (e.g., different actions, different material properties, etc.).

The purpose of dividing the target behavior into two domains (linear and non-linear) during the Validation process in the “JSCE V&V” guideline is summarized as follows:

1. The validation step targeting the linear domain aims to establish credible “initial ground models” and “initial ground-structure system models”. A credible model refers to an “initial ground model” and “initial ground-structure system model” with appropriate reproducibility, and is called the “optimal analytical model”. The criteria to judge “appropriate reproducibility” shall be set considering the uncertainty of basic characteristics of the ground and structures included in experiments or observations.
2. The validation step targeting the nonlinear domain, aims to validate the model, considering the constitutive model of the materials, using the “optimal analytical model. This step confirms both reproducibility and predictive performance of the model

2.4.2.3.2 Similarities and differences with the ASME V&V Standards

The "JSCE V&V" guideline and the ASME V&V10 standard share many similarities; however, there is one significant difference in the steps required during the validation process.

The "JSCE V&V" guideline validates the entire ground or ground-structure system and divides the target behavior into linear and non-linear domains, whereas the ASME V&V10 standard suggests a hierarchical approach that is more applicable for large systems such as plants, aircraft, etc.

2.4.2.3.3 Future challenges of the JSCE V&V Guidelines

A notable aspect of the "JSCE V&V" guideline is its clear identification of future challenges. This foresight facilitates the development of research that can serve as a foundation for future enhancements of the guidelines. By acknowledging the areas that require further investigation, researchers can focus on addressing these gaps and contributing to the ongoing refinement and evolution of the standard, ultimately leading to more robust and accurate guidelines for engineering practice. The most relevant future challenges described in the "JSCE V&V" guideline are summarized as follows:

- Experiments, observations, or actual damage situations used for validation comparisons often lack sufficient information needed to quantify the uncertainty of the structure and material characteristics required for accuracy evaluation. There is a significant challenge in constructing strategies to acquire such information, including information needed for accuracy evaluation of simulations related to the assessment of the impact on structures from the failure process, and sharing the obtained information.
- Existing testing methods for material characteristics, especially ground material characteristics, are insufficient for the information needed to set the parameters of constitutive models in the strong nonlinear domain.
- There is little experience in setting acceptable indexes as evaluation criteria for reproducibility predictive performance.

2.5 Literature Review - Examples of Validation Implementations

As presented in Section 2.4, significant advancements in the development of guidelines and standards that serves as the basis for the validation of numerical models. In parallel, numerous efforts have been undertaken to validate specific models, not only in the realm of liquefaction, but also in various phenomena within geotechnical engineering, including consolidation, slope stability, tunnels, and rock engineering. Moreover, validation efforts can be found among a wide variety of fields such as concrete technology, aviation, explosives, fuels, medicine, nuclear engineering, transportation, and others.

However, it is observed that the volume of Validation and Verification (V&V) activities in geotechnical engineering is relatively limited when compared to other engineering disciplines. Some causes that contribute to this disparity include: (1) The complexity of geomaterials and site-specific conditions, which are characterized by variability, heterogeneity, anisotropy, etc., necessitates multiple case scenarios for validation, thereby increasing the complexity of these exercises. (2) Regulatory and industry standards in geotechnical engineering may not be as stringent or focused on V&V compared to other fields, resulting in less formalized validation processes. (3) Lack of standardization; due to its complex behavior, geotechnical engineering often requires tailored approaches, which can hinder the development and adoption of standard V&V practices.

This section provides a review of these validation efforts, with particular emphasis on the key characteristics of the validation process. Special attention is given to aspects such as the Validation Criteria (qualitative validation, or quantitative validation) inclusion of Uncertainty Quantification techniques in both the tests and the model, and the crosschecking of results.

2.5.1 Examples of Qualitative Validation Implementations

Qualitative validations involve the comparison of test or observation results with those obtained from numerical models, without explicitly quantifying the degree of correspondence between the two. Typically, these validations rely on subjective assessments, such as statements like "as seen in the figure, the model is able to reproduce the experimental results."

Historically, the majority of validation efforts for numerical models, whether in geotechnical engineering(liquefaction [68] [69] [70], tunnel-engineering [71] , etc.) or other disciplines such as, concrete technology [72] [73] [74] [75], aviation [76] [77], fuels [78], medicine [79], and others [80], have predominantly employed qualitative validation approaches.

To illustrate this type of validation, the following examples are presented.

<u>Illustrative Example of a Qualitative Validation Implementation in Liquefaction Modeling</u>

Lopez-Querol and Blazquez [68] proposed a new liquefaction constitutive model, based on the endochronic theory applied to densification of sandy soil, and attempted to validate it based on a comparison of its results against a set of centrifuge tests modeling the seismic behavior of a submerged dike surrounded by loose sand (see Figure 2-7), performed in the University of British Columbia.

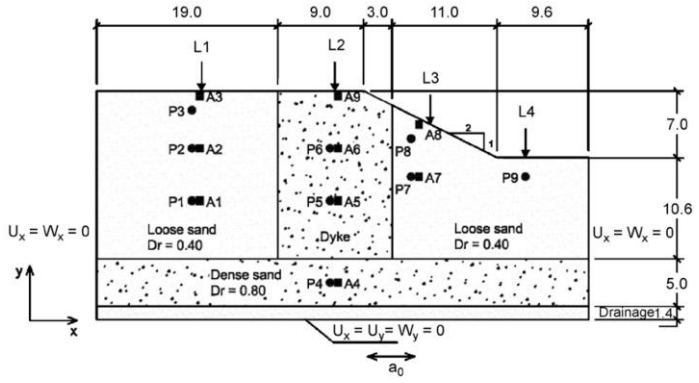

Figure 2-7 Characteristics of the centrifuge test used in the validation exercise performed by Lopez-Querol and Blazquez [68]

In this attempt, the sand properties are firstly calibrated by means of undrained cyclic simple shear stress test data (see Figure 2-8), and numeric models are created, simulating the seismic loading and geometry

conditions of the centrifuge test results (see Figure 2-9).

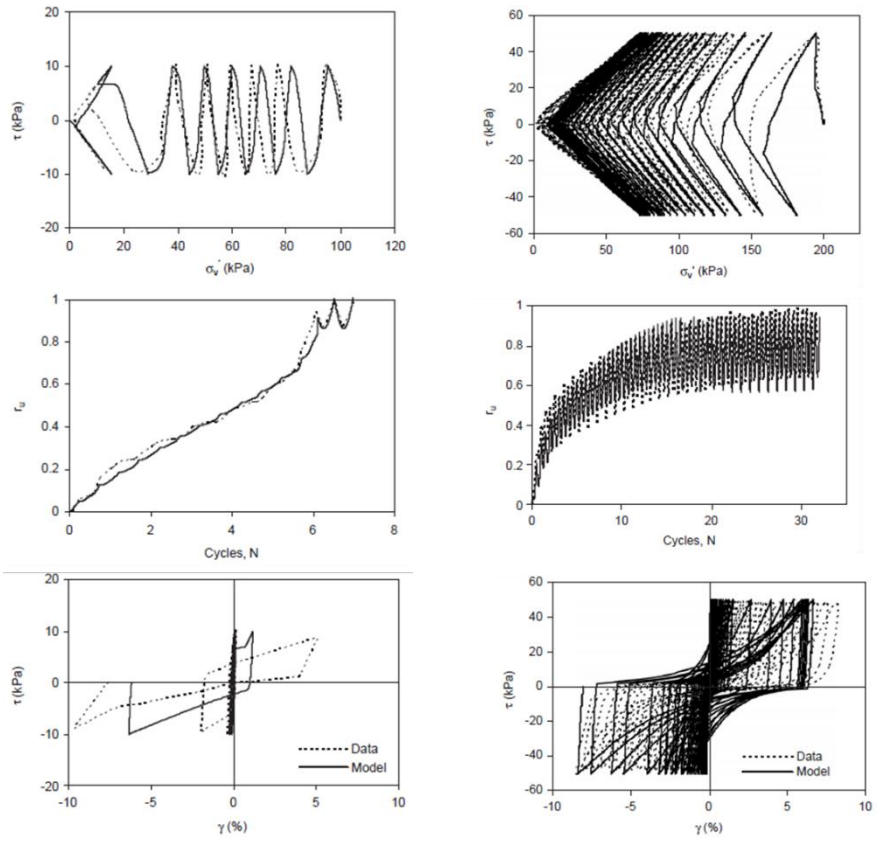

(a) (b)

Figure 2-8 Calibration of the sand properties in the validation exercise performed by Lopez-Querol and Blazquez. (a) Loose Fraser River Sand (Dr = 0.44, CSR = 0.10), (b) Dense Fraser River Sand (Dr = 0.81, CSR = 0.25) [68]

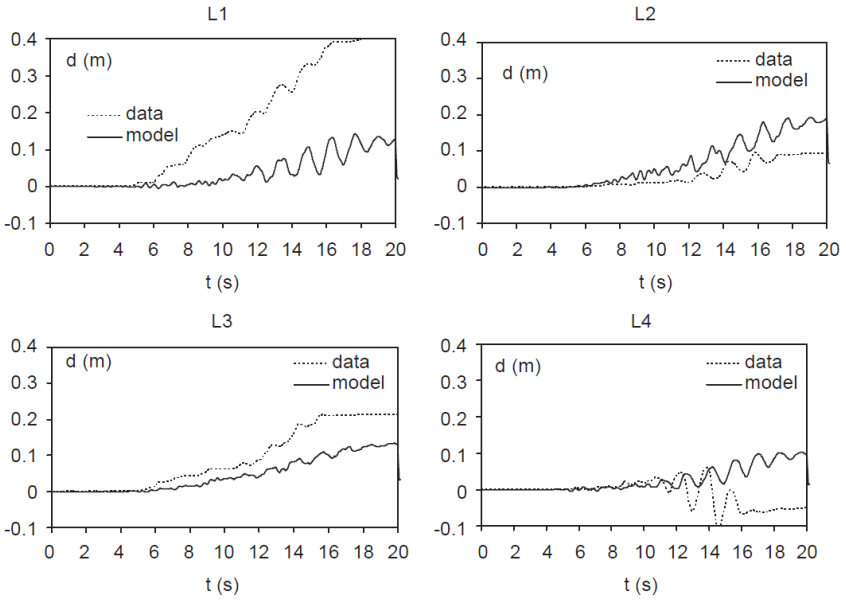

Figure 2-9 Comparison between the Centrifuge Experimental displacements, and the numerical results (test CT2) in the validation exercise performed by Lopez-Querol and Blazquez [68]

Illustrative Example of a Qualitative Validation Implementation in other areas

Duarte et.al., [76] presented the implementation and validation of a strongly coupled model of a fully passive flapping foil turbine operating at a high Reynolds number. In this validation exercise, the model is validated by comparing the simulation results with respect to experimental data of a lightweight turbine prototype tested in a confined channel.

The experimental setup is shown in Figure 2-10, and the comparison between the experimental results (flow velocity downstream from a lightweight fully passive flapping foil turbine), and the numerical model results is shown in Figure 2-11.

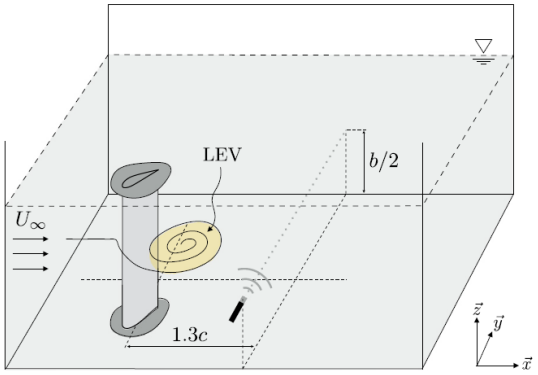

Figure 2-10 Experimental set-up of the test used in the validation exercise performed by Duarte et.al. [76]

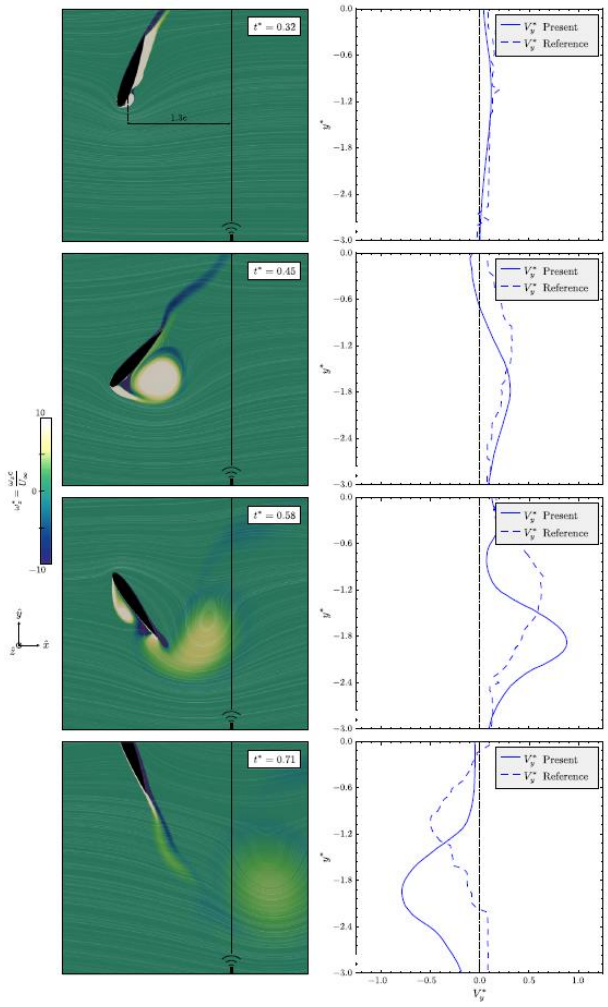

Figure 2-11 Comparison between the test results, and the numerical results in the validation exercise performed by Duarte et.al. [76]

2.5.2 Examples of Quantitative Validation Implementations without Uncertainty Quantification

As discussed in Section 2.5.1, qualitative assessments of model validity often rely on subjective "impressions" made by the author when comparing numerical results with test or observation data (refer to Figure 2-8, Figure 2-9, and Figure 2-11). Consequently, different individuals may draw different conclusions when evaluating such comparisons. To mitigate subjectivity and ensure more objective evaluations, it becomes crucial to quantify the differences in the comparisons, and establish indexes to evaluate the validity of the models.

Whie the V&V ASME Standards [2] [5], and the JSCE Guidelines [14] emphasize the importance of quantitative validation, including uncertainty quantification, it is worth noting that some examples in the existing literature primarily focus on qualitative validation exercises without incorporating uncertainty quantification [81] [82], These examples typically involve the use of defined indexes to assess the validity of numerical models through comparisons with tests or observations. This section includes an illustrative

example of qualitative validation, without uncertainty quantification, to provide insights (the significance of uncertainty quantification is addressed in Section 2.5.3).

Illustrative Example of a Quantitative Validation Implementation without Uncertainty Quantification

Eshraghi et.al. [82] conducted a validation exercise to assess the performance of a model designed to predict the behavior of tank car side impact simulations, including other crashworthiness simulations.

The validation process involved comparing the simulation results to experimental data obtained from full-scale dynamic shell impact tests conducted on railroad tank cars. Figure 2-12 illustrates the test setup employed in this study.

Figure 2-12 Experimental set-up of the test used in the validation exercise performed by Eshraghi et.al. [82]

In this study metrics recommended by the NCHRP 22-24, and CORA (ISO/TS 18571:2014) have been used to compare the simulation results against the test results. These metrics enabled a quantitative estimation of the differences between the simulation and test results. The estimated metrics are shown in Figure 2-13.

		CORA (ISO/TS 18571:2014)					RSVVP (NCHRP 22-24)				
No.	Signals	Corridor	Cross-Correlation Rating			Overall	Sprague-Geer			ANOVA	
			Phase	*Magnitude*	*Slope*		*Magnitude*	*Phase*	*Overall*	*Error*	*STDEV*
1	Impactor Acceleration	0.93	0.76	0.97	0.27	0.77	0.04	0.05	0.07	0.03	0.11
2	Impactor Change in Velocity	1.00	1.00	1.00	0.96	0.99	0.00	0.00	0.00	0.00	0.00
3	Impactor Displacement	1.00	0.90	1.00	0.99	0.98	0.02	0.01	0.02	0.01	0.03
4	Change in Air Pressure	0.87	0.68	0.89	0.53	0.81	0.18	0.03	0.18	0.05	0.09
5	String Pot 48" Offset A-End	0.87	0.68	0.89	0.53	0.77	0.08	0.04	0.09	0.02	0.09
6	String Pot 24" Offset A-End	1.00	0.90	1.00	0.81	0.94	0.04	0.01	0.04	0.03	0.02
7	String Pot 0" Offset	1.00	0.94	1.00	0.87	0.96	0.02	0.01	0.02	0.02	0.01
8	String Pot 24" Offset B-End	1.00	0.92	0.99	0.84	0.95	0.00	0.01	0.01	0.00	0.02
9	String Pot 48" Offset B-End	1.00	0.89	0.99	0.81	0.94	0.00	0.01	0.01	0.01	0.02
10	String Pot Vertical	0.99	0.86	0.99	0.68	0.90	0.01	0.02	0.02	0.01	0.03
11	String Pot Head A-End	0.87	0.62	0.97	0.93	0.85	0.04	0.04	0.06	0.04	0.07
12	String Pot Head B-End	0.83	0.63	1.00	0.93	0.85	0.10	0.04	0.11	0.07	0.07
13	String Pot Skid A-End	0.76	0.46	0.99	0.94	0.78	0.12	0.06	0.13	0.09	0.10
14	String Pot Skid B-End	0.70	0.44	0.99	0.75	0.71	0.18	0.07	0.19	0.12	0.11

Figure 2-13 Estimated validation metrics for the validation exercise performed by Eshraghi et.al. [82]

2.5.3 Examples of Quantitative Validation Implementations including Uncertainty Quantification

As mentioned previously, the incorporation of uncertainty quantification is a key aspect of the V&V ASME Standards [2] [5], and the JSCE Guidelines [14].

Quantifying uncertainty in model validation is essential to understand the limitations, reliability, and confidence of the analysis. In general, models simplify complex phenomena, and uncertainties arise from various sources. Through the quantification of uncertainties, sensitivity can be assessed, significant factors can be identified, and informed decisions can be made under uncertain conditions. Without incorporating uncertainty quantification, validation may lead to misleading conclusions, hindering accurate and reliable predictions; therefore, the quantification of uncertainty is indispensable for establishing valid and credible models in practical applications.

As stated in the JSCE Guidelines [14], experimental/observation data used for validation comparisons often lack sufficient information needed to quantify the uncertainty of the structure and material characteristics required for accuracy evaluation. However, in recent years, notable efforts have been made towards the development of quantitative validation exercises in the geotechnical engineering [14] [83], and other disciplines [84] [85].

To illustrate this type of validation, the following examples are presented.

Illustrative Example of a Quantitative Validation Implementation including Uncertainty Quantification in Liquefaction Modeling

As part of the "JSCE V&V" Guideline [14], a set of validation exercises has been incorporated as application examples. One specific example (Part 2 - Section 4.3 of the guideline) focuses on the validation of numerical models for liquefaction, which is summarized below.

The validation exercise primarily examines the seismic behavior of caissons founded on granular materials with liquefaction potential. Initially, the validity of the model is assessed by comparing the results of numerical simulations with observed displacements of caisson structures situated in the Kobe Port RF3 Quay, following the 1995 Kobe Earthquake. A representative cross-section of the target structures is presented in Figure 2-14.

The uncertainty quantification of the observed displacements was performed by measuring the displacements of the caissons within the aforementioned quay.

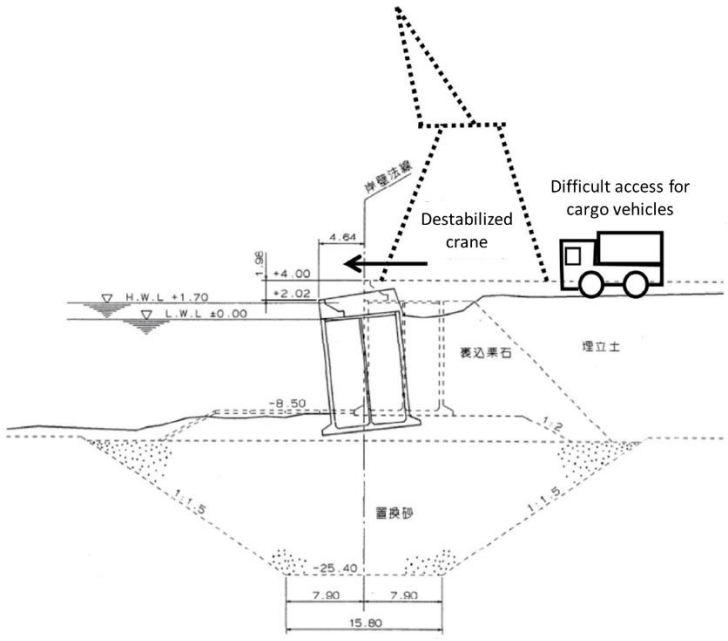

Figure 2-14 Target structure used in the validation example included in the JSCE [14]

For the numerical model, this validation exercise utilizes the "Multi-Spring Model" and the "Cocktail Glass Model," implemented in the commercial software FLIP Rose.

Following the numerical simulation process and uncertainty propagation, the validation exercise presents a quantitative comparison of the results between the field observations and the numerical models, including both the main response and the associated variability (see Figure 2-15). The evaluation also incorporates the estimation of validation indexes, with the adoption of the "Area Metric" (further details regarding this metric and its applicability are provided later in this thesis manuscript).

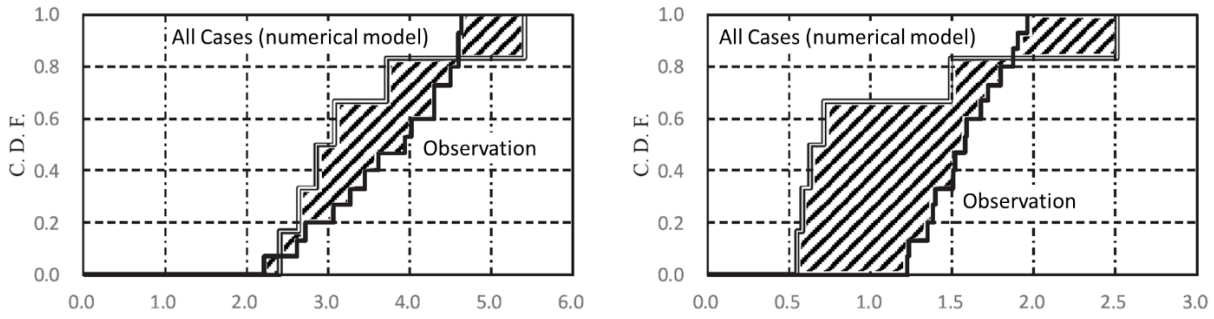

(a) (b)

Figure 2-15 Comparison of the main response, and associated variability of the results of the field observations, and the numerical models in the validation example included in the JSCE [14]: (a) Horizontal displacement at the crown, (b) Settlement at the crown

In addition to validation against the observed data, the validation example includes a comparison with

experimental data obtained from a 1/20 scale shaking-table experiment. However, as seen in Figure 2-16, the variability of the experimental results has not been quantified.

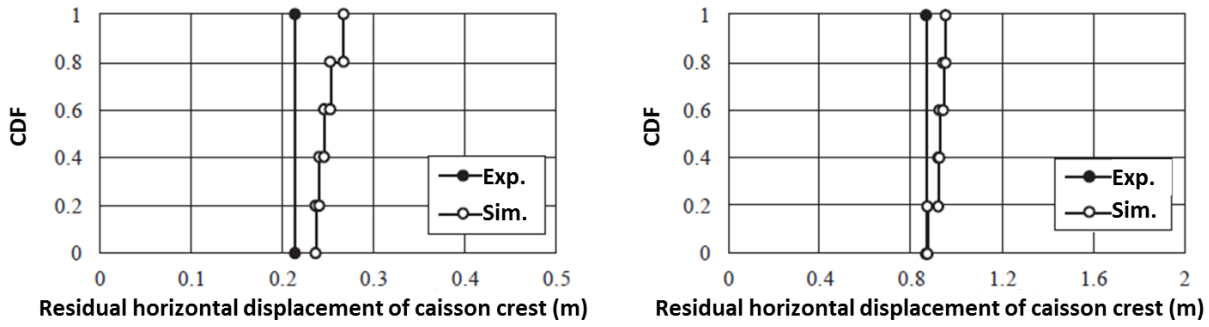

(a) (b)

Figure 2-16 Comparison of the main response, and associated variability of the results of the shaking-table tests, and the numerical models in the validation example included in the JSCE [14]: (a) Wave scenario 1, (b) Wave scenario 2

Illustrative Example of a Quantitative Validation Implementation including Uncertainty Quantification in Consolidation modeling

Hizen et.al., [83] conducted a verification and validation exercise to assess the numerical analysis of clay consolidation based on a series of triaxial tests, and centrifuge tests. The numerical implementation consisted in a soil-water coupled analysis (based on the porous media theory), considering finite deformation.

The characteristics and dimensions of the Centrifuge Model used to in the validation exercise are shown in Figure 2-17. To assess variability, the experiment was repeated eight times, and probability distributions were estimated based on the obtained displacements, assuming a Normal Distribution (see Figure 2-18).

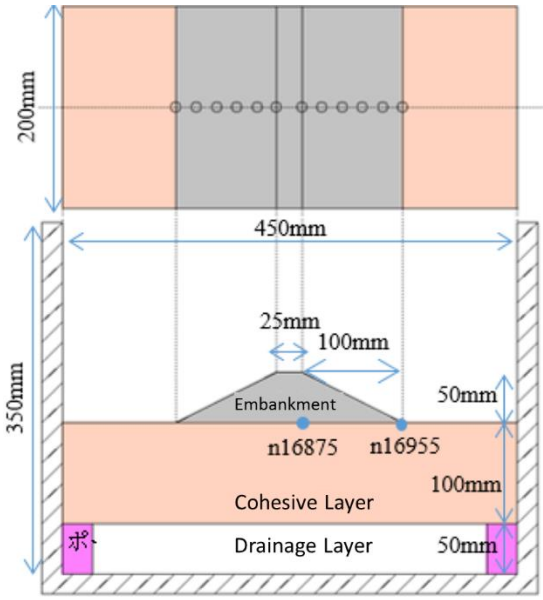

Figure 2-17 Characteristics of the Centrifuge Test used in the validation exercise performed by Hizen et.al. [83]

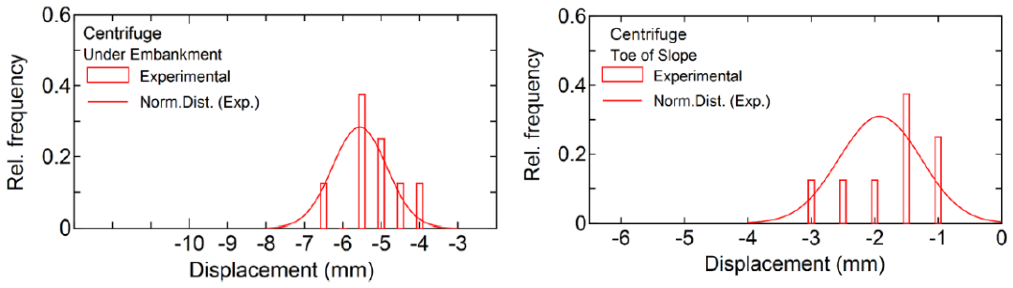

(a) (b)

Figure 2-18 Uncertainty quantification of the centrifuge test results in the validation exercise performed by Hizen et.al. [83]: (a) Displacements at the center of the embankment, (b) Displacements at the edge of the embankment

Regarding the uncertainty quantification of the numerical model, it has been estimated through the propagation of the uncertainty of the model parameters. The uncertainty associated with the model parameters was estimated by fitting probability distributions (assuming normal distributions) to certain elastoplastic parameters derived from several undrained triaxial tests, as seen in Figure 2-19.

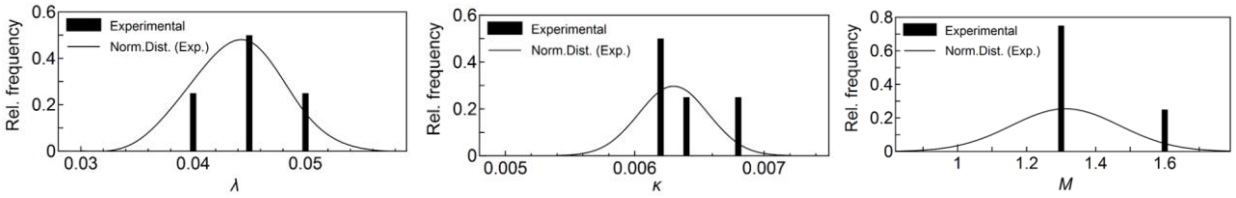

Figure 2-19 Uncertainty quantification of the model parameters in the validation exercise performed by Hizen et.al. [83]

The validation exercise concluded by quantitatively comparing the main response and the associated variability of the results between the centrifuge tests and the numerical models. Figure 2-20 and Figure 2-21 showcase the comparison, including the estimation of validation metrics.

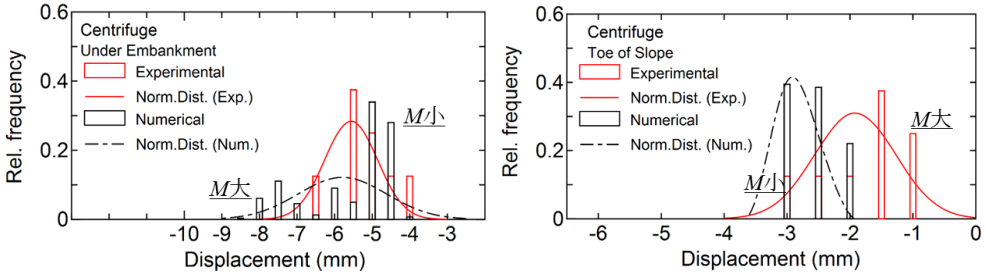

(a) (b)

Figure 2-20 Comparison of the main response, and associated variability of the results of the centrifuge tests, and the numerical models in the validation exercise performed by Hizen et.al. [83]: (a) Displacements at the center of the embankment, (b) Displacements at the edge of the embankment

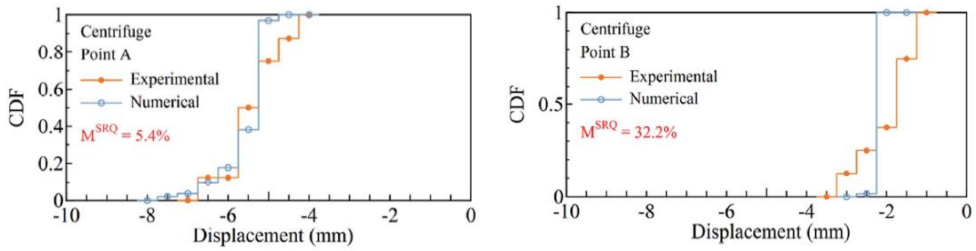

Figure 2-21 Estimation of the validation metrics (M^{SRQ}) validation exercise performed by Hizen et.al. [83]: (a) Displacements at the center of the embankment, (b) Displacements at the edge of the embankment

2.5.4 Importance of Cross-Checked experimental results

In the previous sections, it was observed that validation exercises of numerical models, due to their complexity and the significant resources required to develop reliable physical models, often rely on a limited number of non-crosschecked experimental data.

Since a V&V process evaluates the outcomes of a numerical model based on the outcomes of physical models, if the results of a physical model are not close to the "correct value", the conclusions drawn in the V&V process may lead to incorrect conclusions. Therefore, it becomes necessary to ensure that repeatable and high-quality physical models (which have higher probability of being close to the "correct value") are used in the V&V process. However, when experimental data is limited and not cross-checked, it may not be possible to ascertain the quality and repeatability of the physical models.

By way of illustration, Figure 2-22, Figure 2-23, Figure 2-24, and Figure 2-25 show a comparison of the results of two "identical" experiments that aim to simulate the lateral spreading in clean sands on a 5-degrees sloping deposit, conducted in two different laboratories, under identical specifications (full specifications of this tests are further provided in Section 3.1), using the sand from the same batch, and with the same target input wave.

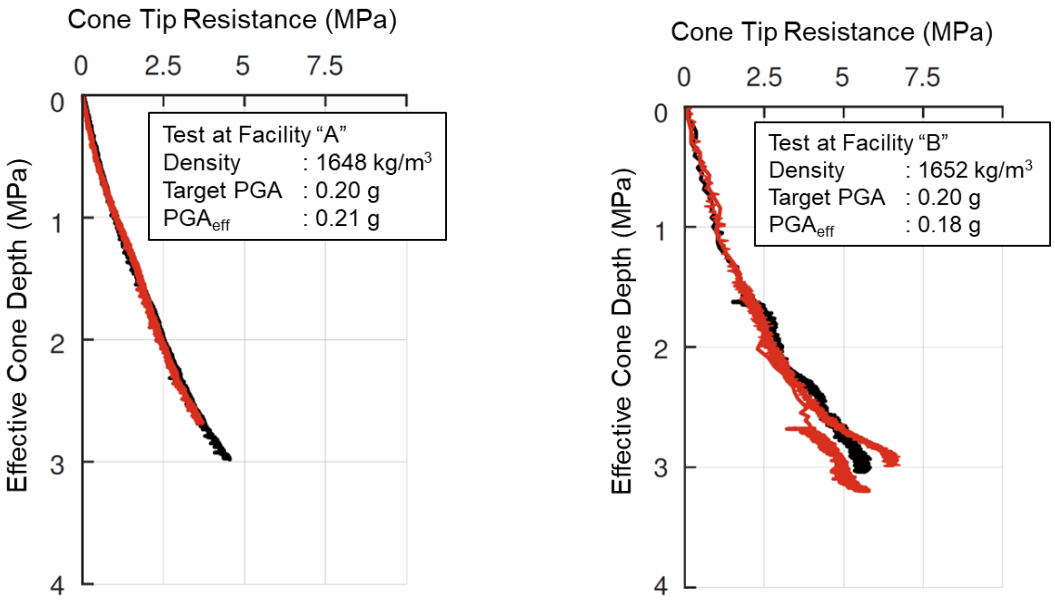

(a) (b)

Figure 2-22 Difference in the Cone Penetration Testing (CPT) Results in two "identical" experiments performed in two different laboratories (a) Test Facility "A", (b) Test Facility "B"

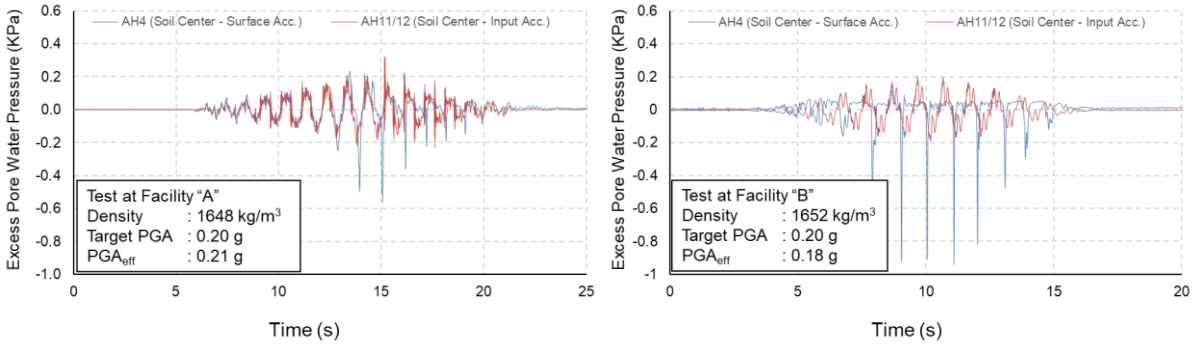

(a) (b)

Figure 2-23 Difference in the Input and Response acceleration in two "identical" experiments performed in two different laboratories (a) Test Facility "A", (b) Test Facility "B"

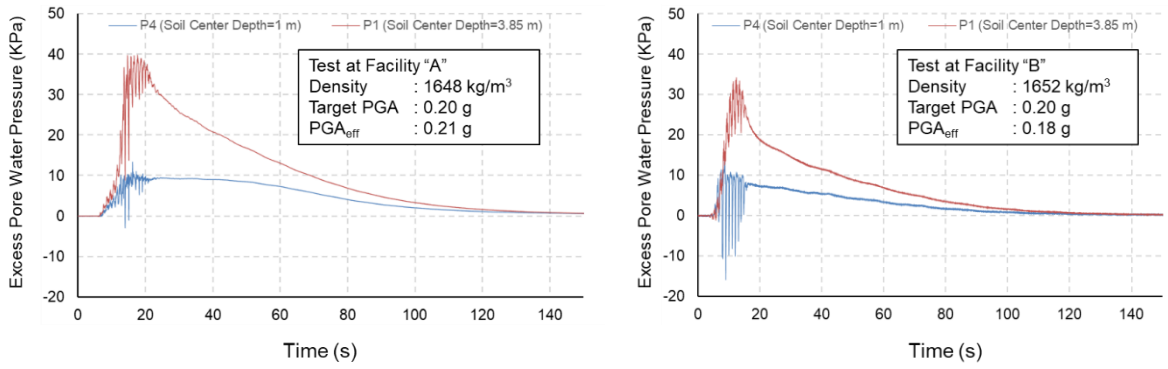

(a) (b)

Figure 2-24 Difference in the Excess Power Pressure in two "identical" experiments performed in two different laboratories (a) Test Facility "A", (b) Test Facility "B"

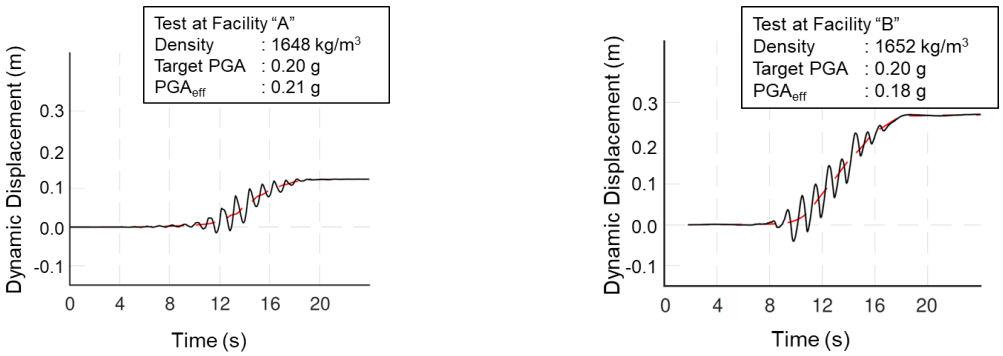

(a) (b)

Figure 2-25 Difference in the Mid-Slope Deformation in two "identical" experiments performed in two different laboratories (a) Test Facility "A", (b) Test Facility "B"

The comparison between these tests clearly demonstrates that even when conducted under controlled laboratory conditions, "identical" experiments can yield significant differences in results due to various factors such as facility and machine characteristics, as well as the skills and experience of the experimenters, etc. Consequently, if a model is validated based on a single experiment, it will inherently inherit the biases associated with that specific experiment.

In the absence of noticeable errors or deviations in the experiments, it may not be possible to judge whether the differences between the experiments are due to one of them being correct or incorrect. Often, none of the experiments will provide the "correct values", and the differences should be recognized as part of the variability inherent in modeling the phenomenon.

Although significant variations between "identical" the experiments could be attributed to the highly nonlinear responses of materials (such as saturated loose sand) and the dynamic testing conditions, studies

have indicated that variations also exist in tests performed on materials with less "complicated" stress-strain relationships, under static conditions. As an example, Kurumatani et. al. [86] conducted four-point bend tests on two types of reinforced concrete beams (see Figure 2-26) in five different laboratories at approximately the same time, with minor variations in boundary conditions (to minimize variability, all specimens tested were fabricated in the same laboratory, under the same conditions). Figure 2-27 shows the stress-strain results of the tests; and, although the differences in results between laboratories are smaller compared to the liquefaction tests, the presence of variability among laboratories is evident.

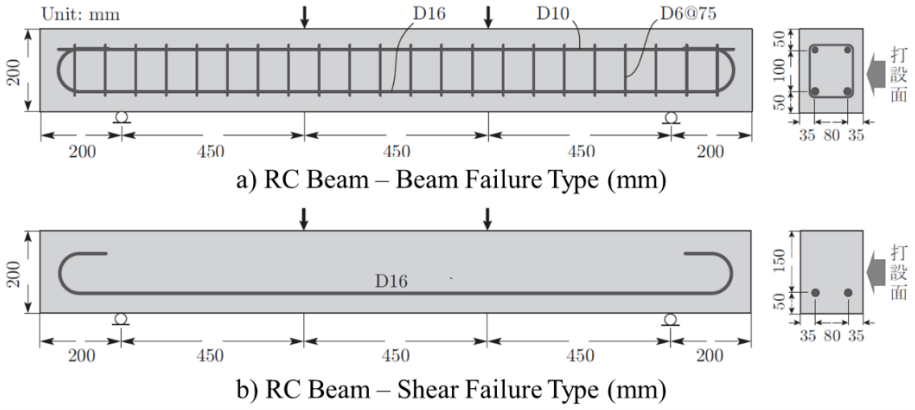

Figure 2-26 Reinforced concrete beams tested in the cross-checked experiments by Kurumatani et. al [86]

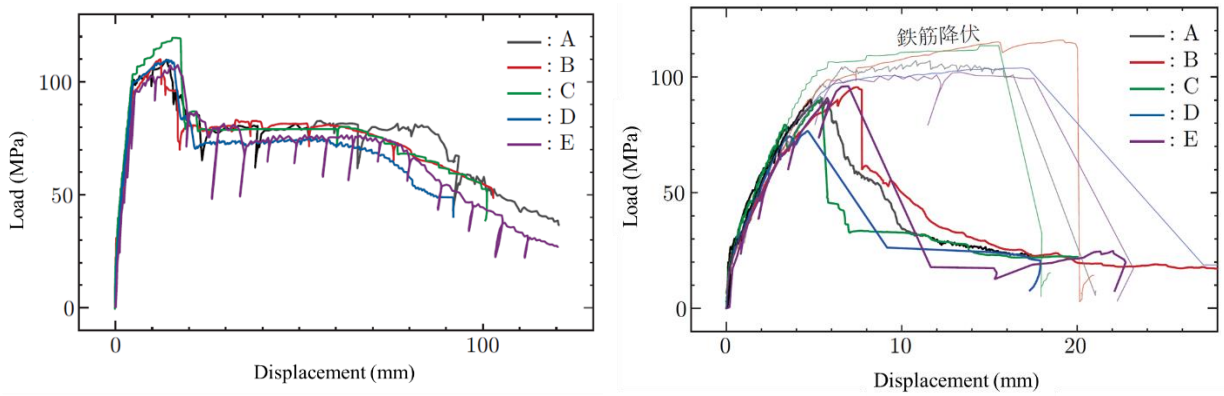

Figure 2-27 Stress-strain responses of reinforced concrete beams tested in five different facilities (A, B, C, D, and E) - Four-point bend cross-checked experiments by Kurumatani et. al [86] (a) Test results of "Beam Failure Type" experiments, (b) Test results of "Shear Failure Type" experiments (thick lines indicate brittle failure without yielding, and the thin line indicates failure after yielding.)

While validation exercises solely based on non-crosschecked experimental results are important, particularly in the early stages, they may not provide sufficient evidence for the complete validation of a numerical model. Main trends and inherent variability cannot be adequately assessed if the test results cannot be compared with similar tests conducted in different facilities by different experimenters; therefore, the performance of cross-checked experiments/tests, becomes necessary to provide a strong base for validation of numerical models, especially in cases in which significant validation between laboratories may be expected.

2.5.5 Examples of Cross-Checked experimental campaigns for liquefaction modeling

As discussed in the previous section, cross-checked experiments/tests are essential for comprehensive validation of numerical models. However, the resources required to perform extensive test campaigns can often be prohibitive. Therefore, an alternative approach to address this challenge is the establishment of international collaborative projects. These projects provide an opportunity to develop large-scale test campaigns at a relatively low cost and in a short timeframe (several teams work on the experiments in parallel).

This section outlines the major international collaborative projects that have been specifically designed to generate cross-checked experimental results for liquefaction modeling.

2.5.5.1 VELACS Project

The first “large” international effort to develop cross checked databases for numerical-model’s validation was “Verify Liquefaction Analysis by Centrifuge Studies” (VELACS Project - 1994). Its main objective was to provide the experimental data necessary to validate the efficiency of computer codes available for soil dynamics, by developing centrifuge models simultaneously at several universities in USA and UK. As part of this project, over 20 teams of numerical modelers developed predictions of the centrifuge experiments; and, two key lessons arose in that effort: (1) none of the numerical techniques available at that time were reliable to produce high-quality predictions of liquefaction problems, and (2) there was significant variability among the centrifuge results, highlighting the need for better and more reliable experimental data [1] [87] [88].

In the last decades (after VELACS Project), the physical and numerical modeling techniques have experienced remarkable progress. Advances in experimental research have led to the development of new, more precise, and smaller instrumentation, as well as the construction of new research facilities worldwide. As a result, the reliability of element tests, in-situ tests, 1g models, and centrifuge models has increased, providing valuable information to the community, and improving the understanding of geosystems under static and dynamic loading [1].

Similarly, the remarkable advances in computational power have provided a tremendous opportunity to the

development and use of sophisticated numerical techniques. Several constitutive models for granular soils have been being developed [16] [53] [54] [55] [56] [57] [58] and being improving along the time (such as the inclusion of "large deformations" theory, expansion to 3D models, sophisticated formulations of the dilatancy, etc.); moreover, various Finite Element Method (FEM), Finite Difference Method (FDM), and Material Point Method codes (such as FLIP, LIQCA, FLAC, OpenSees, etc.), provide nonlinear fully coupled effective stress capabilities for analysis of geomaterials. Additionally, new research trends, such as the Discrete Element Method (DEM) [46] [47], Smoothed Particle Hydrodynamics (SPH) [89] [90], and Moving Particle Simulation Method (MPS) [91], are gaining more attention due to computational advancements.

Given the recent advancements in experimental and numerical modeling techniques, a new international collaborative project (named "LEAP") was developed, aiming a re-assessment of the reliability of modern numerical techniques in the analysis of liquefaction related problems [1] [92].

2.5.5.2 LEAP Project Exercises

At the time this manuscript is elaborated, LEAP (Liquefaction Experiments and Analysis Projects) is an ongoing international joint project that pursues the verification, validation and uncertainty quantification of numerical liquefaction models, based on high-quality centrifuge experiments and element tests [92] [24]. As part of this project, three major validation exercises related to the dynamic response of a saturated sloping ground were developed.

The first LEAP Exercise was "LEAP-GWU-2015", in which six centrifuge facilities, including Kyoto University [93], tested a centrifuge model with a uniform, 4 m deep, 5 degrees slope sandy ground with the same target characteristics (in terms of relative density and input waves). Kutter et. al [94] found that, despite some variability, the experimental results were consisting among each other, demonstrating the feasibility of a next-generation validation database.

The second exercise, "LEAP-UCD-2017", in which nine centrifuge facilities, developed twenty-four centrifuge models with the same geometry as the previous exercise, considering this time different combinations of relative density (Dr) and Peak Ground Acceleration (PGA). The main objective was to perform a sufficient number of experiments to characterize the median response, and the uncertainty of a specific sloping deposit of sand. In this exercise, Kutter et. al [95] found consistency in the results and clear trends among the experiments.

Based on the consistency of the previous exercises, "LEAP-ASIA-2019" [96] was developed aiming to maintain the same model's geometry of the previous exercises. One of the main objectives was to develop of additional experiments that would fill the gaps of the "LEAP-UCD-2017"'s data (in terms of combinations of Dr and PGA), to extend, establish and confirm the observed trends. In this exercise, ten

facilities from all over the world developed another twenty-four centrifuge tests.

Section 3 of this manuscript provides detailed testing specifications, test results, and outcomes obtained as part of "LEAP-UCD-2017" and "LEAP-ASIA-2019.

2.6 Section Conclusions

This section provides a comprehensive overview of the key elements covered in the study, including liquefaction and lateral spreading, centrifuge modeling, effective stress models, and validation and verification (V&V). The objectives of this section are to provide a contextual understanding of the key elements described in the research, facilitate the comprehension of the presented content, and establish the state-of-the-art in related studies. The main points summarized in this section are as follows:

- The definition of soil liquefaction, and the general mechanism of the lateral spreading phenomenon caused by liquefaction, including the approaches for research and estimation is introduced, highlighting the importance of improving the understanding of the phenomena, and enable more accurate predictions of soil behavior during seismic events.
- The concept, and principles of centrifuge modeling are introduced, highlighting the importance of its use, and its advantages/disadvantages against numerical models.
- A brief review of the foundations of the effective stress models for modeling soil liquefaction is included, clearly identifying general model`s assumptions, describing the governing equations for multiphase geomaterials (focusing on the u-p formulation), and describing the main characteristics of some of the existing constitutive equations for modeling soil liquefaction.
- An introduction of the historical development, and the state of the art of V&V standards/guidelines is introduced, identifying, and describing in detail the most suitable standards/guidelines that serves as the basis (ASME Standards, and JSCE Guidelines) to propose the validation methodology for validating numerical models for liquefaction prediction.
- The state of the art of current actual validation implementations is introduced through the introduction of a series of published examples of validation exercises, highlighting that the majority of validation efforts for numerical models have predominantly employed qualitative approaches.
- As stated in the most recent V&V standards/guidelines, the development of quantitative validation implementations including uncertainty quantification, is indispensable for establishing valid and credible models in practical applications. It has been shown that although some examples of quantitative validation incorporating uncertainty quantification have been performed in the recent years, they are still based on a few amount of non-crosschecked experimental data.
- It has been shown that even when conducted under controlled laboratory conditions, "identical" experiments performed in different facilities can yield significant differences in results, due to various factors such as facility and machine characteristics, as well as the skills and experience of

the experimenters, etc. Therefore, the use of cross-checked data to verify the accuracy of the experimental data, and allow a proper uncertainty quantification, is essential for a comprehensive validation of numerical models.

- Cross-checked experiments/tests are essential for comprehensive validation of numerical models. However, the resources required to perform extensive test campaigns may limit its performance; therefore, an alternative approach to address this challenge is the establishment of international collaborative projects. In this context, the major international collaborative projects that have been specifically designed to generate cross-checked experimental results for liquefaction modeling (VELACS Project, and LEAP) is introduced.

3 Physical Modeling

3.1 "LEAP-UCD-2017" and "LEAP-ASIA-2019" - Test Specifications

To ensure that multiple high-quality experiments could be conducted, the experimental specifications for the "LEAP-UCD-2017" and "LEAP-ASIA-2019" exercises were designed to be replicable in numerous facilities worldwide. This included the experimental geometry, preparation method, and test conditions.

The experimental model was designed to be a uniform-density, 20 m long, 4 m deep at center, and 5 degrees sloping deposit inside a rigid container [24]. Figure 3-1 shows the geometry, dimensions, and instrumentation of the target models. As seen in this figure, 2 horizontal (AH11 and AH12) and 2 vertical accelerometers (AV1 and AV2) were placed outside the box to record the input motions; additionally, 6 horizontal accelerometers (AH1, AH2, AH3, AH4, AH6, AH9) and 8 pore pressure transducers (P1, P2, P3, P4, P6, P8, P9 and P10) were placed inside the ground to obtain the soil response in the central array, and assess the effects of the rigid boundaries.

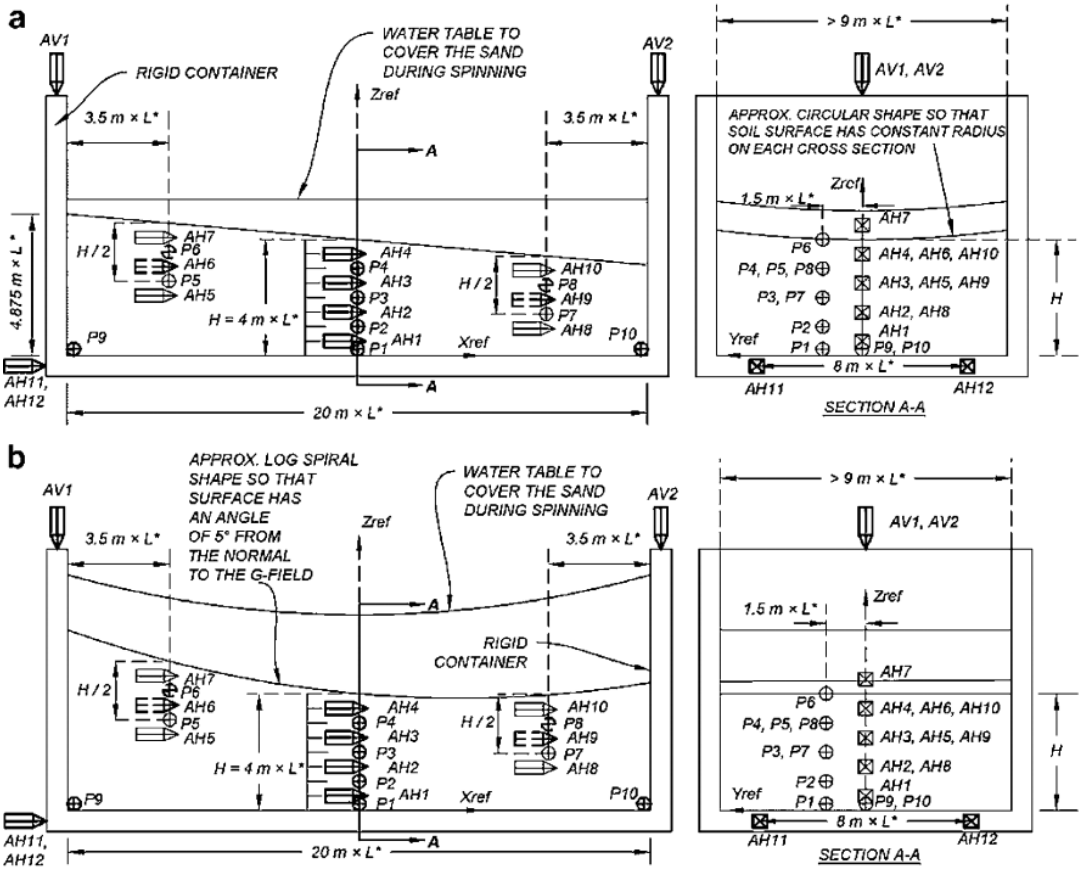

Figure 3-1 (a) Baseline schematic experiment for shaking parallel to the axis of the centrifuge. (b) Baseline schematic for LEAP-UCD-2017 experiment for shaking in the circumferential direction of the centrifuge [24]

3.1.1 Soil Material: Ottawa F-65 sand

The standard sand selected for the LEAP exercises was Ottawa F-65; which is a poorly graded, sub-rounded to sub-angular whole grain silica sand, with less than 0.5% fines by mass. To maintain consistency and reduce variability associated with potential variations, the sand was obtained from a single source, and shipped by UC Davis to all facilities prior to the models' development [97].

Due to the large quantity of sand supplied, and in order to properly verify the consistency, grain size analysis (according to the procedures specified in ASTM C136) was performed by UC Davis [97]. Figure 3-2 shows the envelope of the test results of 13 samples, and the referential curve indicated by the provider. Although some variability was observed, the entire batch was defined as a "uniform" material.

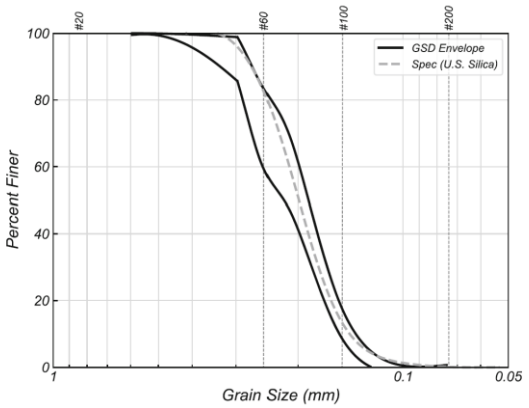

Figure 3-2 Grain size distribution envelope – Ottawa F-65 Sand [97]

Regarding the estimation of the Dr values, Carey et al. [97] performed a statistical analysis of the maximum and minimum dry densities of Ottawa F-65 sand (according to the procedures specified in ASTM D4253), by using samples that were used in the centrifuge models developed for LEAP; the recommended (ρ_{min}=1490.5 kg/m^3, ρ_{max}=1757.0 kg/m^3) were used in this manuscript.

In addition, El Ghoraiby et al. [98] conducted constant-head hydraulic conductivity tests to estimate the permeability of Ottawa F-65 sand for different void ratios. As shown in Figure 3-3, a linear relationship was found between the hydraulic conductivity (k), and the void ratio e_0.

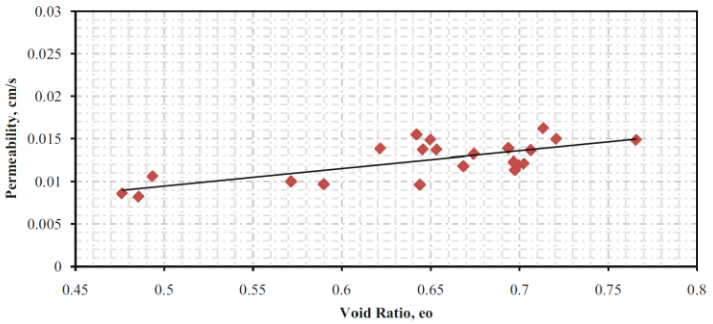

Figure 3-3 Hydraulic conductivity, k, vs. void ratio e_0

3.1.2 Scaling Laws

The "Conventional Scaling Law" and the "Generalized Scaling Law" for centrifuge modeling were used in the development of the tests. The "Generalized Scaling Law", proposed by Iai et. al [99], combines the the conventional scaling laws for centrifuge testing, and the ones used for 1-g tests. Figure 3-4 shows this two-stage scaling relationship, where the physical model parameters are initially scaled into a "Virtual 1G" field using the conventional scaling factor for centrifuge tests, η, and then scaled to the "Prototype" field with scaling factors for 1G tests, μ. Table 3-1 summarize the scaling relationships. [24]

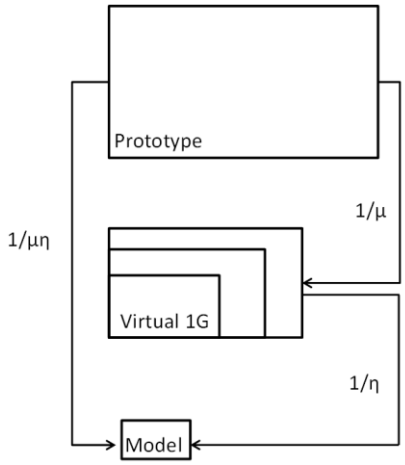

Figure 3-4 Relationship among a prototype, virtual 1G models and a centrifuge model for the "Generalized Scaling Law" [99]

Table 3-1 Generalized scaling relationships [99]

Variable	(1) Scaling factors for 1g test	(2) Scaling factors for centrifuge test	(3) Generalized scaling factors
Length	μ	η	$\mu\eta$
Density	1	1	1
Time	$\mu^{0.75}$	η	$\mu^{0.75}\eta$
Frequency	$\mu^{-0.75}$	$1/\eta$	$\mu^{-0.75}/\eta$
Acceleration	1	$1/\eta$	$1/\eta$
Velocity	$\mu^{0.75}$	1	$\mu^{0.75}$
Displacement	$\mu^{1.5}$	η	$\mu^{1.5}\eta$
Stress	μ	1	μ
Strain	$\mu^{0.5}$	1	$\mu^{0.5}$
Stiffness	$\mu^{0.5}$	1	$\mu^{0.5}$
Permeability	$\mu^{0.75}$	η	$\mu^{0.75}\eta$
Pore pressure	μ	1	μ

3.1.3 Model Preparation

Placement of the Sand by Pluviation

The specified technique for sand placement was air pluviation, which required the use of a mesh with an opening size of approximately 1.20 mm to deposit the sand (Figure 3-5). To maintain a uniform density, the elevation of the container during pluviation was required to be continually adjusted to ensure a constant vertical spacing between the sand surface and the mesh, with a maximum allowable change in drop height of 5%. Accurate measurements of the container dimensions and the volume of sand in the container were taken to determine the as-deposited sand density [24].

Figure 3-5 Referential equipment for air pluviation (a) Standard mesh. (b) Side view during air pluviation. (c) Slots arrange (d) Referential arrangement [24]

Model saturation

To facilitate the dissolution of gas bubbles that are trapped in the sand, the model container was required to be repeatedly evacuated and flooded with CO2 to replace approximately 98% of the air in the chamber by pure CO2 prior to saturation with de-aired viscous fluid [24]

Surface displacement measurement

To track the surface displacement, 3D printed surface markers were specified to be placed along the sand surface. As shown in Figure 3-6, the shape of the markers was designed to anchor to the soil and provide minimal restriction to pore pressure drainage, with a taper to facilitate insertion with reduced disturbance. Additionally, cameras (preferably high speed) were required to be mounted to measure the plan view lateral displacements of surface markers during spinning [24].

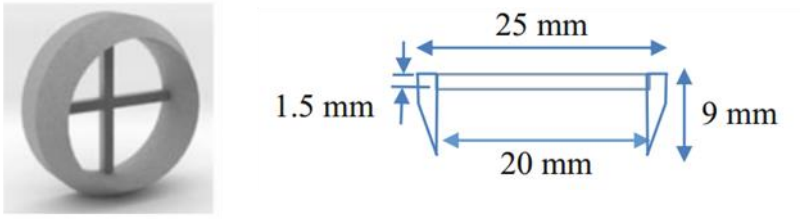

Figure 3-6 Specified unstained 3D printed surface markers [24]

3.1.4 Testing Procedures

Cone Penetration Testing

To obtain a better estimation of the density of the sand prior testing, an in-flight cone was designed with a top load cell and no custom strain gauges at the cone tip, as shown in Figure 3-7. Cone penetration tests were required to be performed before and after every destructive ground motion [24].

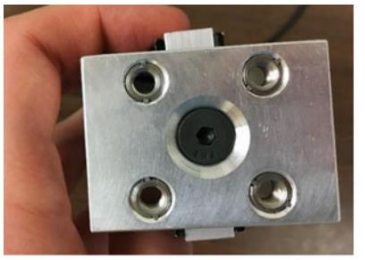

The spacing of the four M6x1mm bolts is 25.4 mm center to center in a square pattern.

Cone		Ref. Length (mm) (not counting conical tip)
1	Ehime	124
2	Kwater	202
3	Kaist	202
4	Kyoto	194
5	NCU	294
6	NCU	294
7	Zhejiang	694
8	Zhejiang	644

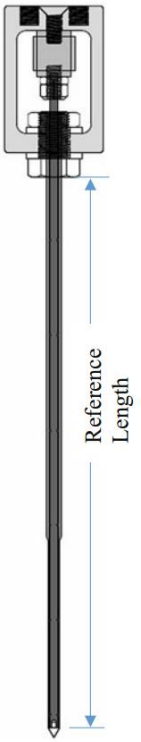

Figure 3-7 In-flight CPT device and rod lengths of the devices used at different facilities [24]

Ground Motions

The testing procedure included a shake sequence of 3 "destructive" input motions; each motion consisting of a ramped sinusoidal 1 Hz wave (Figure 3-8).

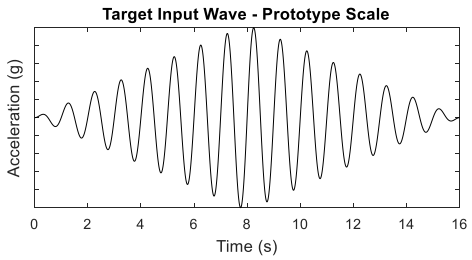

Figure 3-8 Specified Ramped Sine Wave

Kutter et. al [95], found that the recorded base acceleration was very sensitive to high-frequency components of the base motion, which varied significantly from facility to facility. The response of the model on the other hand is significantly more sensitive to lower frequency components, thus, the PGA (extracted directly from the experimental records) cannot be considered as a good parameter to describe the shaking intensity. Hence, LEAP (as a first approximation) proposed the use of an "effective PGA (PGA_{eff})" as a parameter to describe the shaking intensity and compare experiments, as follows [100]:

$$PGA_{eff} = PGA_{1Hz} + 0.5*PGA_{hf} \quad (3\text{-}1)$$

Where: "PGA_{1Hz}" represents the PGA of the 1 Hz component of the achieved motion (obtained from the isolated 1 Hz signal), and "PGA_{hf}" represents the higher frequency components of the ground motion (obtained from the isolated "noise"). An example of the filtering process is shown in Figure 3-9.

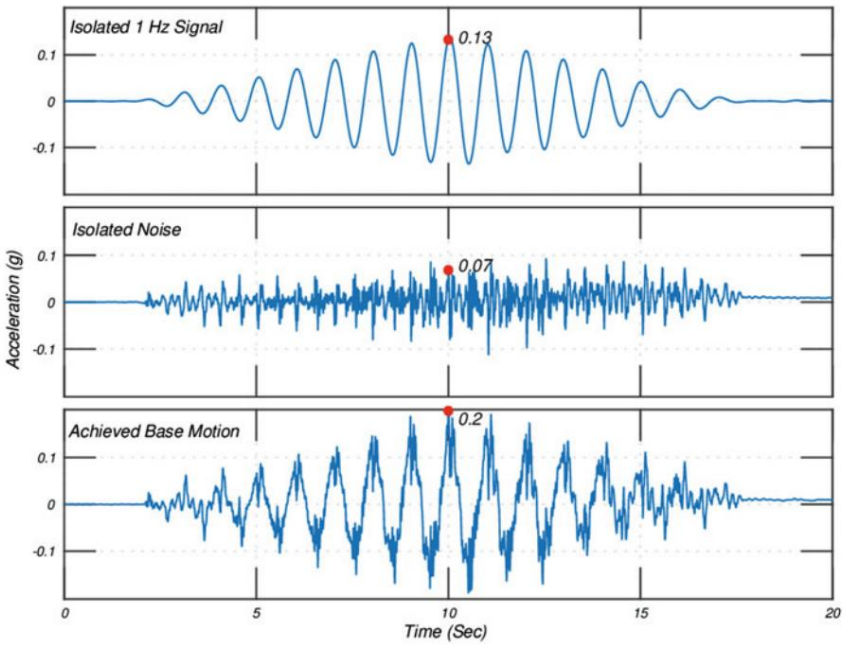

Figure 3-9 PGA_{eff} - Filtering Process - Achieved base acceleration time history (bottom), high-frequency noise isolated from achieved signal (middle), and 1 Hz signal (top)

3.2 Centrifuge Tests for LEAP Project at Kyoto University

3.2.1 Centrifuge Equipment at Kyoto University

Eight centrifuge tests under LEAP Framework (for LEAP-UCD-2017, and LEAP-ASIA-2019 exercises) were developed by the author of this manuscript in the geotechnical centrifuge at the Disaster Prevention Research Institute, Kyoto University, [101].

The geotechnical centrifuge has a capacity of 24 g-ton and can be described as a beam centrifuge with a swinging basket that allows testing models at an effective radius of 2.50 m (measured approximately at 2/3 of the model height). In order to compensate for the unbalance emerging from the weight of the model placed on the platform, an equivalent platform swings on the opposite arm which can be loaded with an equivalent weight. A scheme of the centrifuge facility is provided in Figure 3-10.

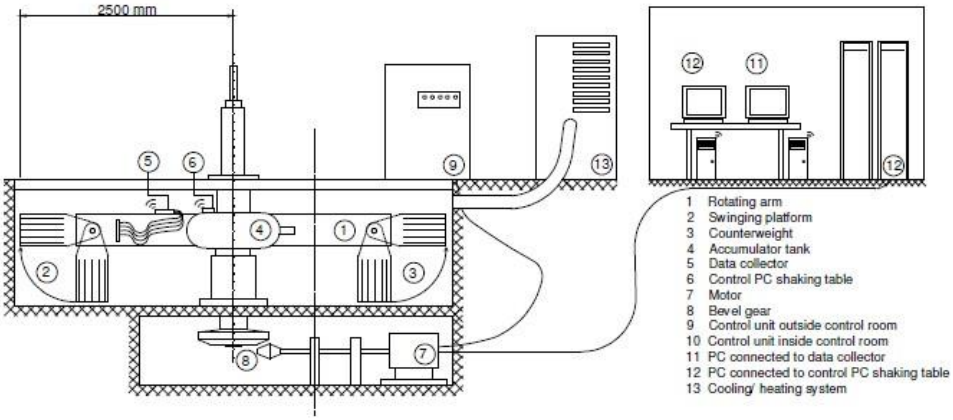

Figure 3-10 Schematic of the geotechnical centrifuge facility at DPRI

A displacement-controlled shaking table that allows the development of dynamic tests is mounted on the platform in the swinging basket; this shaking table has to be directly connected with a PC device and it needs to be placed on the centrifuge arm during flight. This PC is controlled remotely from the control room via a wireless connection.

3.2.2 Model Preparation

As mentioned in the previous section, eight models were developed as part of the LEAP framework (three for "LEAP-UCD-2017" and five for "LEAP-ASIA-2019") at Kyoto University; the models were designed in the sense that all of them would have the same dimensions in prototype scale (i.e. same "Generalized Scaling Factor"), despite that different scaling factors were used. Table 3-2 shows the scaling factors for each model.

Table 3-2 Scaling Factors for Centrifuge Test at Kyoto University

Exercise	Model	Scale factor for 1g test (μ)	Scaling factors for centrifuge test (η)	Generalized scaling factor
LEAP-UCD-2017	KyU_U_A1_1	1	44.4	44.4
	KyU_U_A2_1	1	44.4	44.4
	KyU_U_A3_1	1	44.4	44.4
LEAP-ASIA-2019	KyU_A_A1_1	1	44.4	44.4
	KyU_A_B1_1	2	22.2	44.4
	KyU_A_B1_2	4	11.1	44.4
	KyU_A_A2_1	1	44.4	44.4
	KyU_A_B2_1	2	22.2	44.4

As required by the LEAP Project specifications, Ottawa F-65 (shipped by UC Davis prior to the development of the models) was used in the development of the models. Figure 3-11 shows the geometry, dimensions, and instrumentation of the target models (in model scale), applicable to the tests developed at Kyoto University. As seen in this figure, all the required instrumentation was used in the tests.

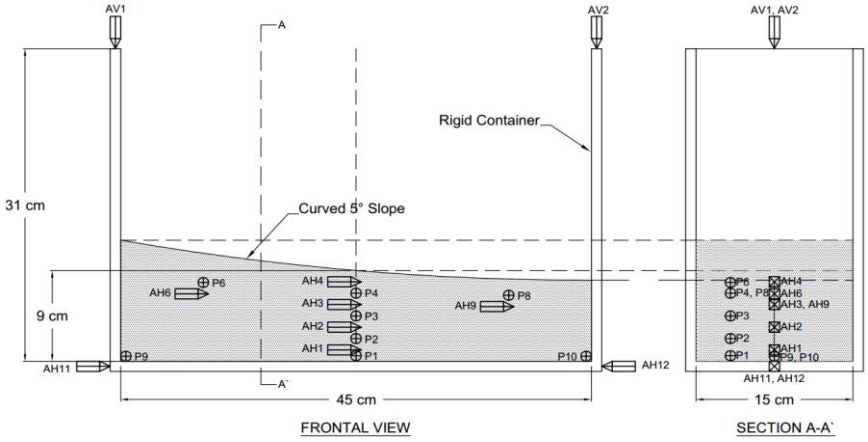

Figure 3-11 Model Dimensions for tests at Kyoto University– Model Scale

Model Preparation – Air Pluviation, and Placement of Instrumentation

As specified, the Air-Pluviation method was used for sand placement; the constant air pluviation height was defined following a calibration process (definition of a height-density relationship), prior each experiment. It was found that the height-density relationship was slightly different for each experiment; although it seems that the difference could be attributable to environmental conditions (such as humidity, temperature, etc.), further research would be required for confirmation.

In order to ensure a precise installation of the instrumentation (Accelerometers, and Excess Pore Water Pressure Transducers), without disturbing the surrounding ground, all the sensors were placed during the Air Pluviation process, at the heights required by the project specifications (see Figure 3-12). Additional details of the sensors are described by Tobita et al [93].

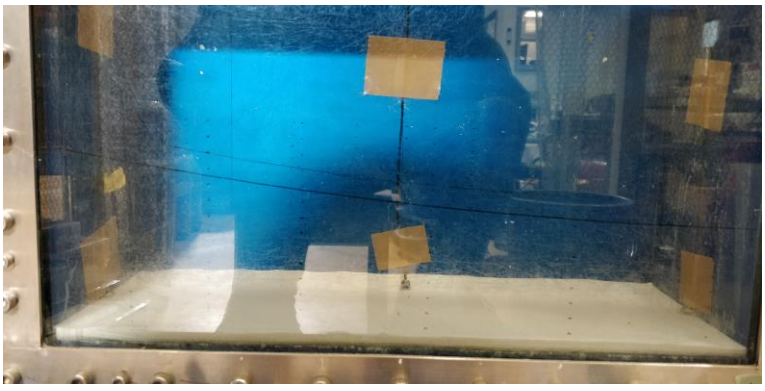

Figure 3-12 Placement of Sensors – Centrifuge Testing

During the sand placement, density was measured at 3 different stages in each model; in these measurements, less than 5% (in terms of relative density) of difference among layer's density was found. Table 3-3 shows the achieved dry densities (measured by means of mass and volume) for each model.

Table 3-3 Relative Density and Achieved Motion - PGAeff (1st Destructive Motion)

Exercise	Model	Achieved Density (kg/m3)	Achieved Dr	PGA	PGA 1Hz	PGAeff
LEAP-UCD-2017	KyU_U_A1_1	1683	75%	0.071	0.047	0.059
	KyU_U_A2_1	1659	67%	0.119	0.098	0.109
	KyU_U_A3_1	1637	59%	0.143	0.116	0.130
LEAP-ASIA-2019	KyU_A_A1_1	1677	73%	0.304	0.191	0.248
	KyU_A_B1_1	1673	72%	0.312	0.192	0.252
	KyU_A_B1_2	1669	71%	0.307	0.189	0.248
	KyU_A_A2_1	1628	56%	0.134	0.101	0.118
	KyU_A_B2_1	1633	58%	0.163	0.089	0.126

Since the centrifuge facility at Kyoto University is equipped with a shaking table in the circumferential direction, and, in order to avoid errors due to variations in the radial gravity field [93], the surface was curved according to the geometry of the facility (i.e. a circumference with 2.50 m radius), so, all points in the surface would have the same slope relative to the gravity field, and may represent ground with a constant, 5-degree slope angle in the prototype scale.

In order to achieve the curved surface without significant disturbance to the ground, the following steps were followed:

- A flat surface was obtained by air pluviation as shown in Figure 3-13.
- An aluminum guide was fabricated with the shape of the target curved surface
- A fixed-length aluminum pipe is conditioned to a vacuum apparatus
- Following the guide, vacuum is applied to reach the curved surface. A picture that shows the achieved curved surface is shown in Figure 3-14.

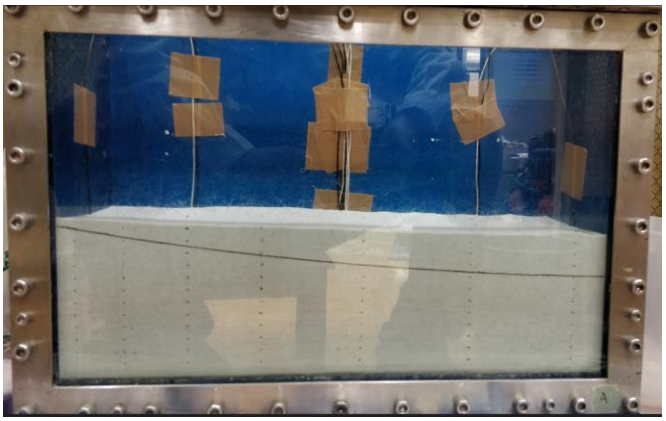

Figure 3-13 Model After Air Pluviation (Flat Surface prior curving)

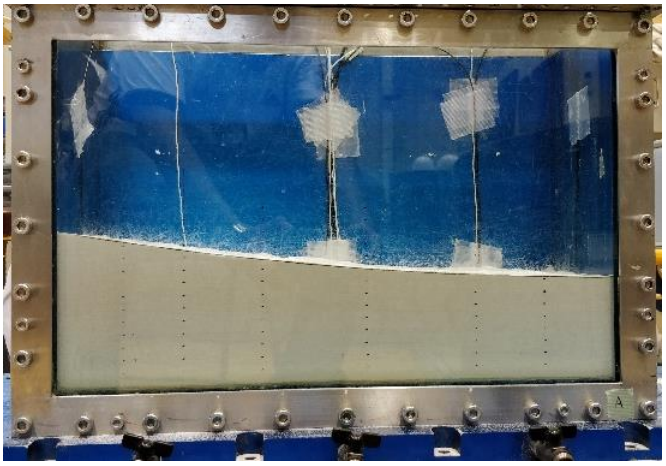

Figure 3-14 Achieved Curved Surface

Model Preparation – Model Saturation

To properly saturate the model, the rigid container containing the model was placed in a vacuum chamber. Initially, vacuum pressure of around ≈ - 0.1MPa was applied to facilitate the dissolution of gas bubbles, and CO2 was gradually flooded until reaching atmospheric pressure values. Vacuum pressure was then reapplied and maintained until the end of the saturation process.

Following the vacuum application, the sample was saturated from the top, using a de-aired solution of de-ionized water and Methylcellulose (SM-100, Shin'etsu Chemical Co.); the mixing rate was iteratively adjusted to achieve the target viscosity determined by the scaling laws (to scale the permeability).

Since the viscosity experience significant variations along with changes in temperature, the amount of Methylcellulose was properly adjusted to achieve the required viscosity at temperatures closer to the ones expected in the test. Figure 3-15 shows the viscosity-temperature curve for the model KyU_A_B2_1, measured using a "Tuning-Fork Vibration Viscometer" [102]. The effects of variations of viscosity during the testing are discussed in Section 6.4.

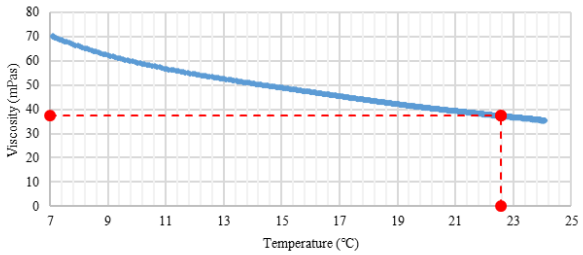

Figure 3-15 Viscosity – Temperature Curve- - Model KyU_A_B2_1

After depositing the viscous mixture, the applied vacuum was gradually removed until achieving the atmospheric pressure.

The degree of saturation of the model was estimated using the Okamura's method [103], which relates the degree of saturation with small variations of the water surface caused by pressure changes. In specific, a piece of polystyrene was placed floating over the model's "water" surface (Methylcellulose solution), and "small" amounts of vacuum (≈ - 0.02∼-0.03 MPa) were induced in the vacuum chamber. The vacuum-induced variations in the "water" surface height were measured using Laser Sensors, assuming that the variations of the floating polystyrene's height corresponds to variations of the "water" surface.

After confirming that the saturation of the model was higher than 99%, the model was transported by means of a crane from the vacuum chamber to a scale, to confirm the actual weight prior testing. Figure 3-16 shows the model after the saturation process.

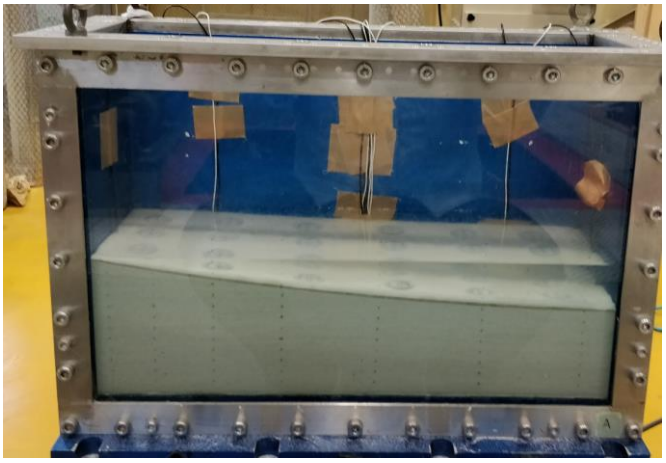

Figure 3-16 Model After Saturation

Model Testing

After confirming the actual weight of the model (required to estimate the required counterweight in the centrifuge equipment), the model was then transported and positioned on the swinging platform of the centrifuge, with careful attention paid to arranging the cables and accessories to account for the effects of

high gravity fields and platform movements. Figure 3-17 shows the setting of the model, including the mounting of the CPT device.

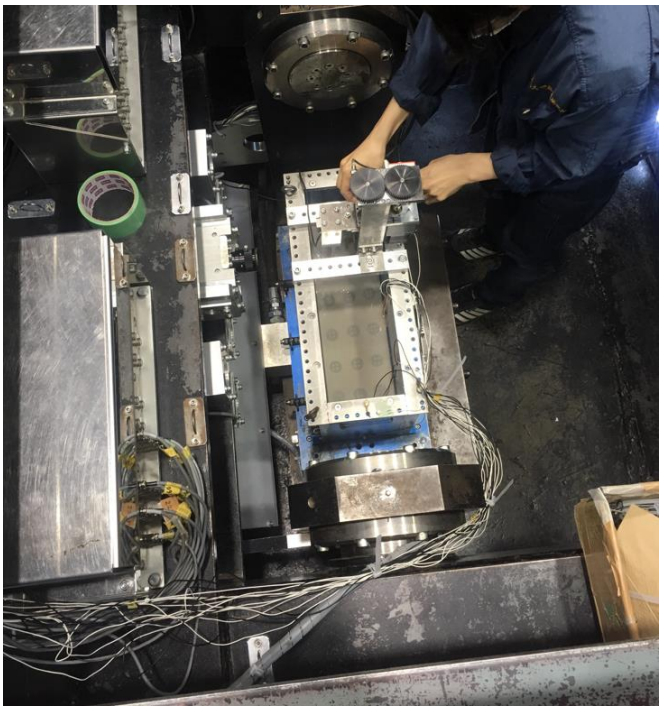

Figure 3-17 Installation of the model in the centrifuge's swinging platform

The testing procedure included a shake sequence of 3 “destructive” input motions; each motion consists of a ramped sinusoidal 1 Hz wave (refer to Figure 3-8); however, only the results of the first input motion (including the estimation of PGA_{eff}) are reported in the present thesis and used for the validation purposes; the achieved peak acceleration values are reported in Table 3-3.

As parameter to better estimate the density and ground uniformity, Cone Penetration Tests (CPT) were performed in each experiment (except for KyU_U_A1_1); for each experiment three CPT Tests were developed, one before each destructive motion, with a new 6 mm Mini-CPT [104]; this method, although providing an indirect measurement (i.e. tip resistance “qc”), has proven to be reliable in the estimation of the uniformity of the ground and its associated dry density [95] [97]. Due to the characteristics of the CPT apparatus, it was not possible to perform shaking while the apparatus was mounted; consequently, each time the CPT test was performed, the centrifuge had to: (1) be stopped to assemble the CPT, (2) increase the required g-level to perform the test, (3) stop again the facility to disassemble the CPT, and (4) increase the g-level for the shaking process.

Regarding the measurements of the dynamic displacements of the ground surface, the centrifuge was equipped with a High-Speed Camera (Nac Image Technology, Inc.; MEMRECAMfx RX-6G), which allowed the estimation (by means of image analysis) of the time-history values of the relative displacement

of the 3-D printed surface markers placed on the ground surface (see Figure 3-18).

The time-history displacement estimations at the center of the slope (Kutter et. al [95] [100] has defined this value as “Ux2”) were compared with the “Dynamic Displacement + Scaled IPRV” [95] to estimate its reliability. Kutter et. al [94] has defined the “Integrated Positive Relative Velocity” (IPRV) as a reasonable method to estimate the accumulation of lateral displacements, based on the integration of the positive terms of the velocity records; since this method doesn’t provide reliable information of the final value of the lateral displacement, the values are scaled to match the displacement determined from manual measurements developed before and after the shaking process. This function is added to the dynamic displacement (i.e. obtained by double integration of the acceleration records), to obtain the “Dynamic Displacement + Scaled IPRV” values.

As seen in Figure 3-19, a good agreement between the results of “Image Analysis” and “Dynamic Displacement + Scaled IPRV” were found, proving the reliability of this measurement method. Therefore, the time-history and residual deformation values estimated for all experiments (except KyU_U_A1_1) were estimated by means of image analysis.

It is important to mention that henceforth all results are reported in prototype scale.

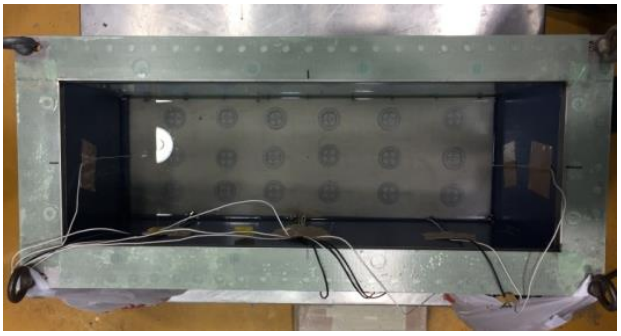

Figure 3-18 Placement of Surface Markers

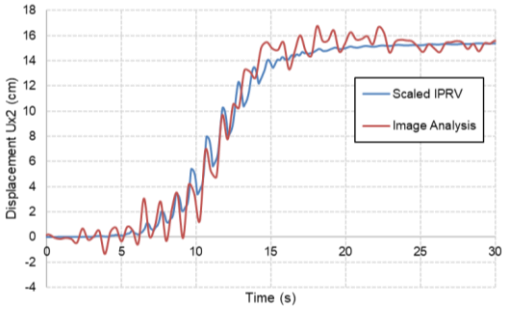

Figure 3-19 Dynamic Displacement of the center part of the slope (Ux2) of model KyU_A_B1_1 - Comparison of between Image Analysis and Scaled IPRV

3.3 Test Results – Centrifuge Tests at Kyoto University

This section describes the test results of the eight centrifuge tests performed at Kyoto University for this manuscript, including the results of the first destructive input motion. Additionally, since CPT testing was not carried out on Test KyU_U_A1_1, these test results are considered "for reference only", and not included in the analysis hereinafter. Complete datasets have been stored for public use, and can be found in [105] [106] [101] [25].

3.3.1 Excess Pore Water Pressure

As specified, nine Excess Pore Water Pressure Transducers (EPWPT) were placed inside the ground to measure the Excess Pore Water Pressure (Δu); Figure 3-20, and Figure 3-21 shows the values of Δu for all sensors during the First Destructive Motion, and Table 3-4 shows the maximum Excess Pore Water Pressure Ratio (ru) for the sensors located in the central array.

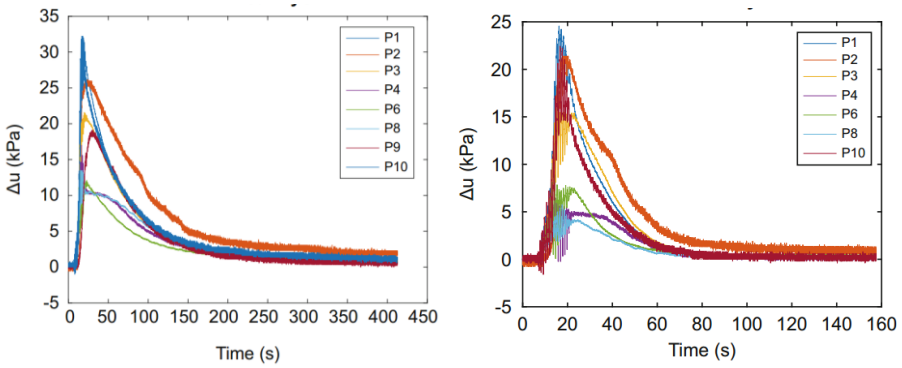

(a) (b)

Figure 3-20 Excess Pore Water Pressure Records (KyU Tests for LEAP-UCD-2017) –First Destructive Motion (a) Model KyU_U_A2_1, (b) Model KyU_U_A3_1

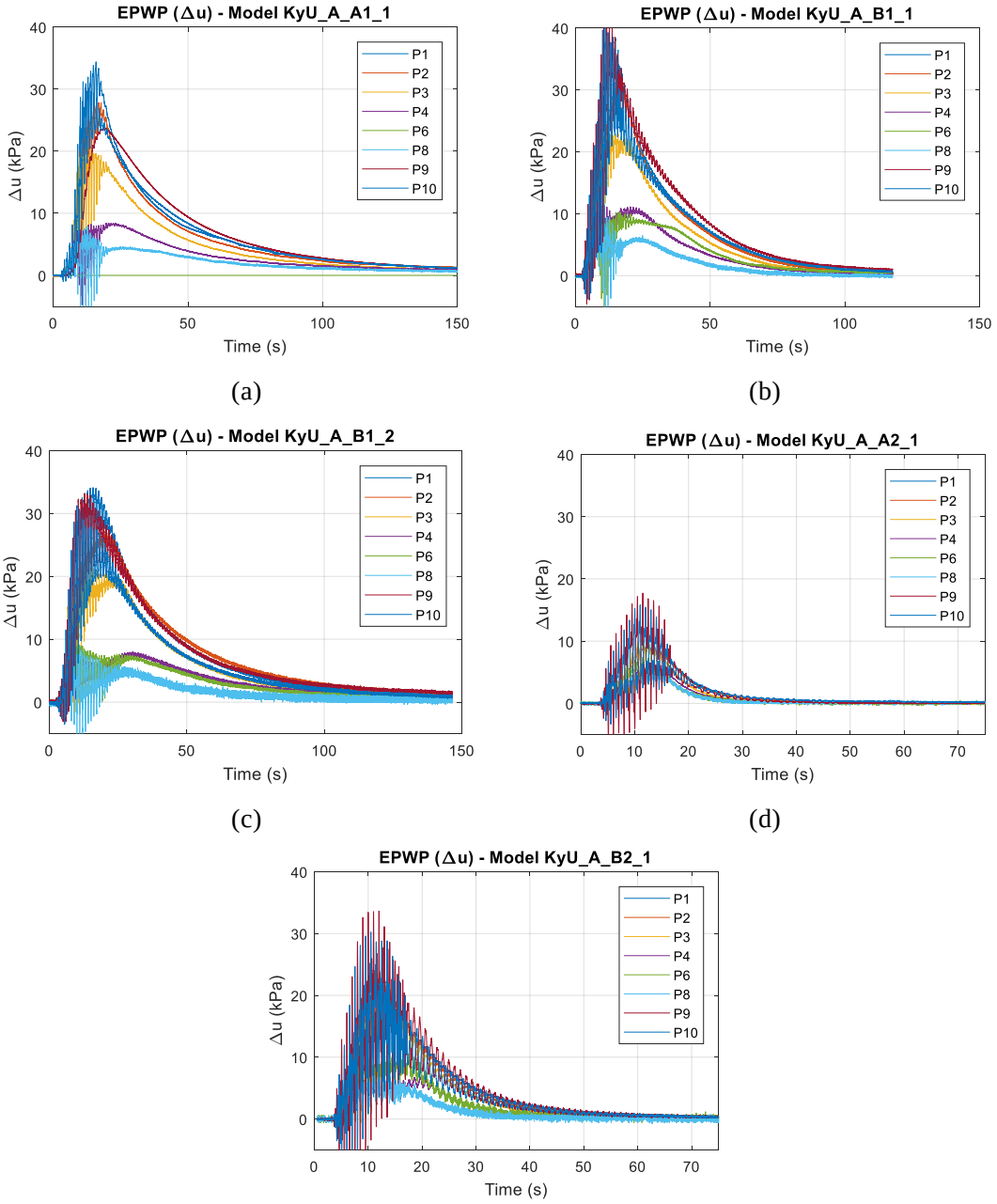

Figure 3-21 Excess Pore Water Pressure Records (KyU Tests for LEAP-ASIA-2019) –First Destructive Motion (a) Model KyU_A_A1_1, (b) Model KyU_A_B1_1, (c) Model KyU_A_B1_2, (d) Model KyU_A_A2_1, (e) Model KyU_A_B2_1

Table 3-4Maximum Excess Pore Water Pressure Ratio (ru) for the sensors located in the central array –First Destructive Motion

Exercise	Model	PGA	PGA_{eff}	ru_{max}			
				P1	P2	P3	P4
LEAP-UCD-2017	KyU_U_A2_1	0.119	0.109	0.80	0.76	0.85	1.00
	KyU_U_A3_1	0.143	0.130	0.68	0.76	0.86	0.77
LEAP-ASIA-2019	KyU_A_A1_1	0.304	0.248	0.89	0.90	0.99	0.97
	KyU_A_B1_1	0.312	0.252	0.95	0.91	1.00	1.00
	KyU_A_B1_2	0.307	0.248	0.85	0.82	1.00	1.00
	KyU_A_A2_1	0.134	0.118	0.26	0.31	0.47	0.50
	KyU_A_B2_1	0.163	0.126	0.63	0.77	0.90	0.90

3.3.2 Ground Motion Acceleration

Response time-histories for all accelerometers placed inside the deposit are reported in Figure 3-22, and Figure 3-23. It can be seen that neither significant amplification nor distortion has been recorded before the development of significant EPWP; after that, the motion significantly changed and developed sharp spikes. These spikes are characteristic of a dilative behavior of the liquefied ground, causing a decrease in the EPWP value (see Figure 3-20 and Figure 3-21); this behavior has been studied and reported in several cases previously [94] [107]. It is important to remark that the distortion in the acceleration starts (and also becomes larger) in the shallow zone of the deposit since the ru value increases faster in these zones [108].

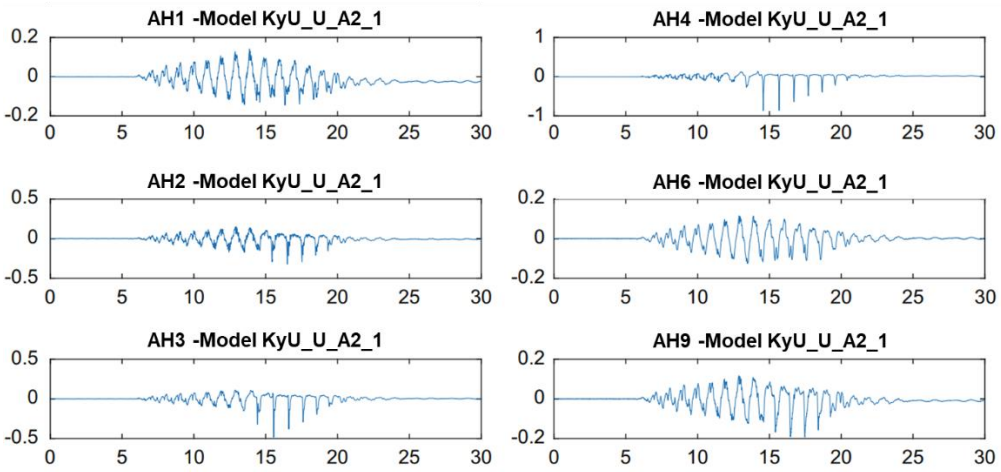

(a)

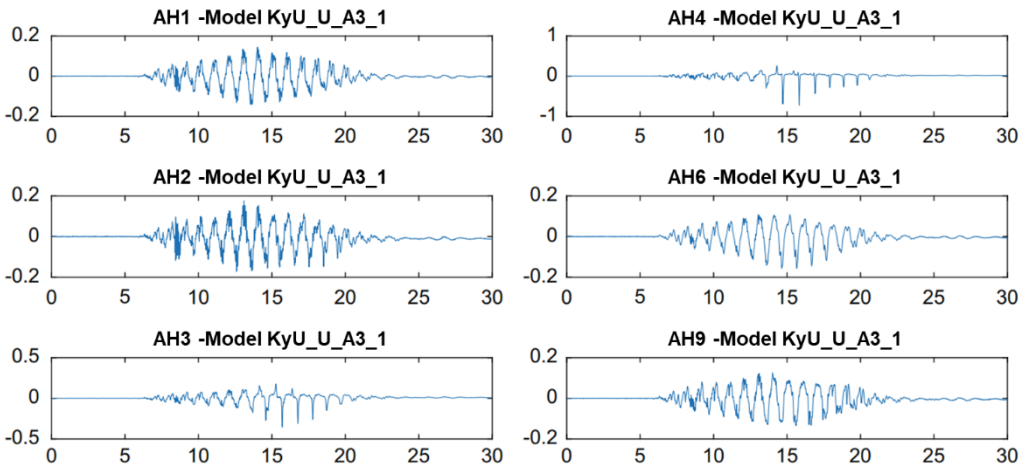

(b)

Figure 3-22 Ground Motion Acceleration Records – (KyU Tests for LEAP-UCD-2017) First Destructive Motion (Vert. Axis: Acc. (g); Hor, Axis: Time (s)) (a) Model KyU_U_A2_1, (b) Model KyU_U_A3_1

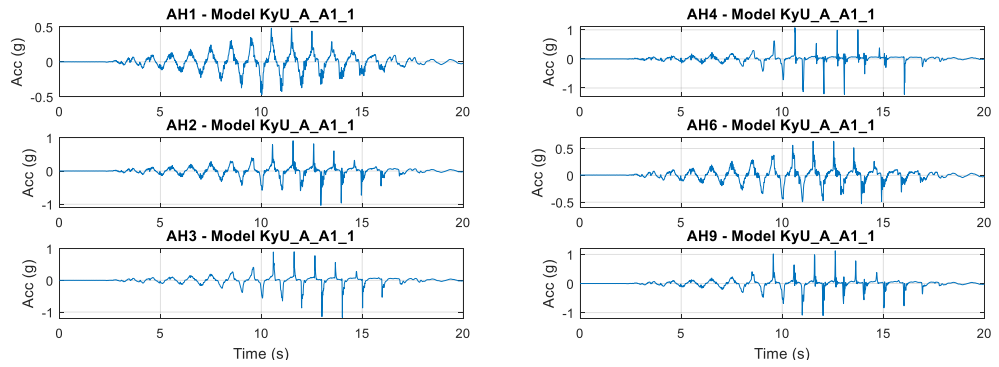

(a)

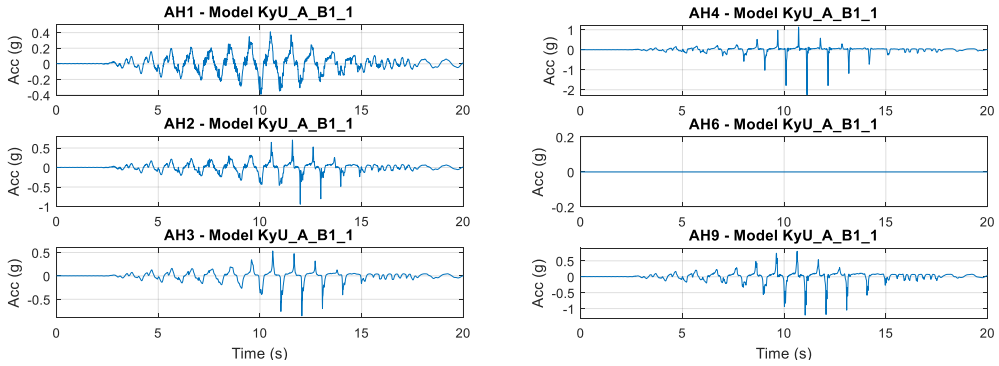

(b)

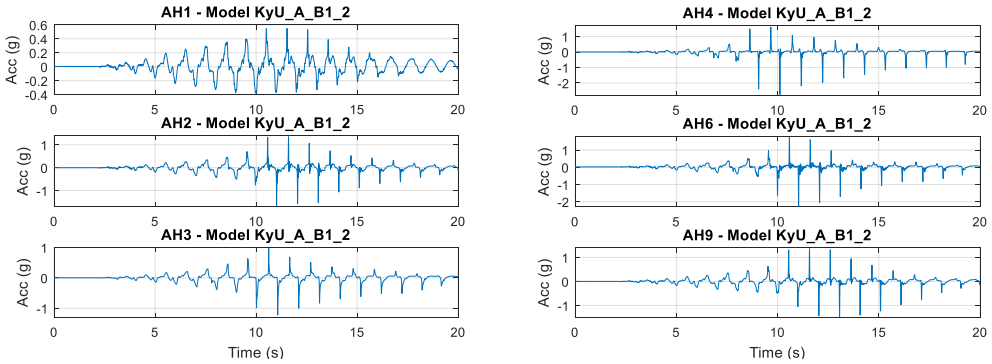

(c)

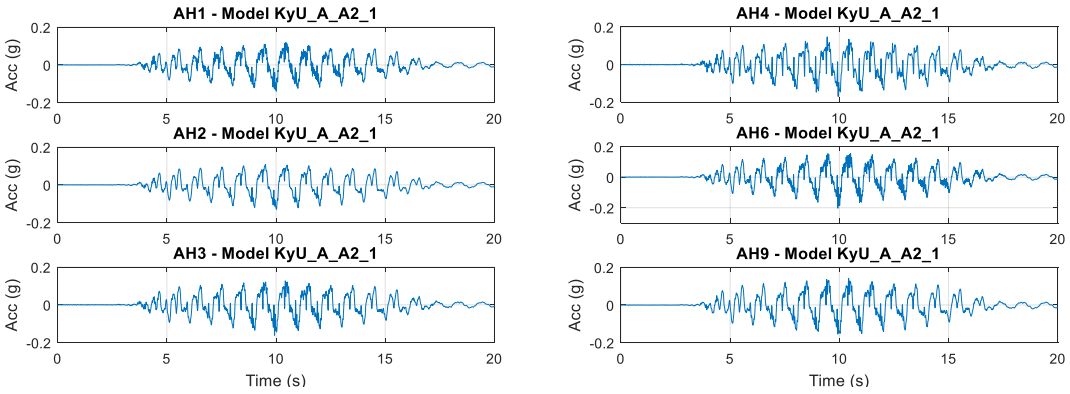

(d)

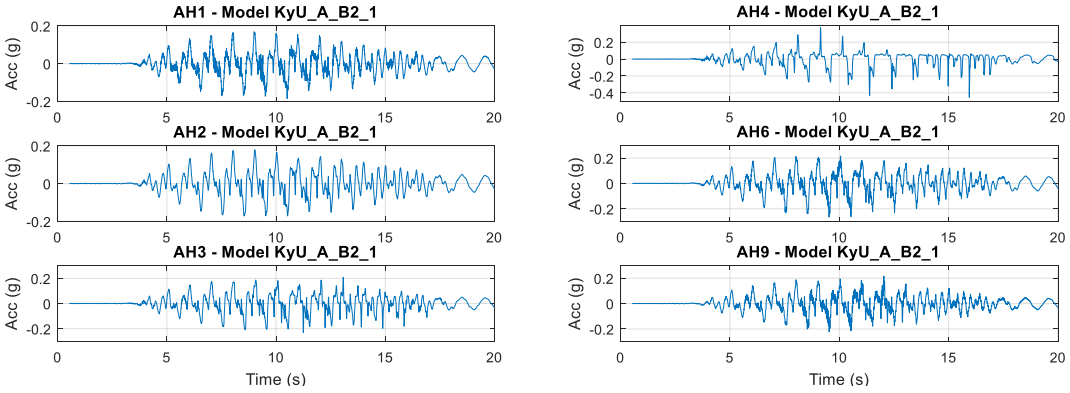

(e)

Figure 3-23 Ground Motion Acceleration Records –(KyU Tests for LEAP-ASIA-2019) First Destructive Motion (a) Model KyU_A_A1_1, (b) Model KyU_A_B1_1, (c) Model KyU_A_B1_2, (d) Model KyU_A_A2_1, (e) Model KyU_A_B2_1

3.3.3 Cone Penetration Test

As stated previously, in-flight Cone Penetration Tests (CPTs) were developed before each destructive motion; hence, CPT1, CPT2, and CPT3 were performed before Destructive Motions 1, 2 and 3 respectively. It is important to mention that Kutter et. al [100] [109], found that the tip resistance at the mid-depth (i.e. at 2.0 m) is well correlated with the initial relative density of the ground.

The CPT records are shown in Figure 3-24, and Figure 3-25.

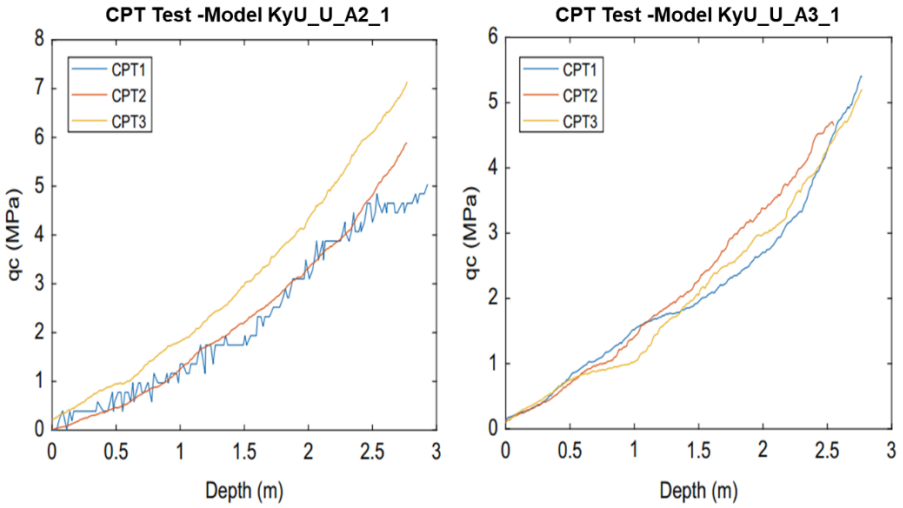

(a) (b)

Figure 3-24 CPT Test Records (KyU Tests for LEAP-UCD-2017) (a) Model KyU_U_A2_1, (b) Model KyU_U_A3_1

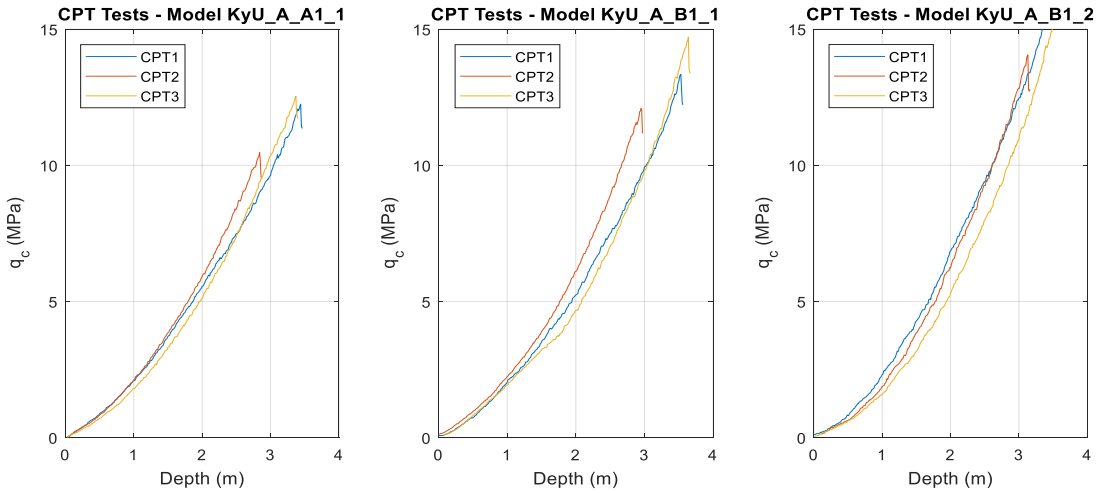

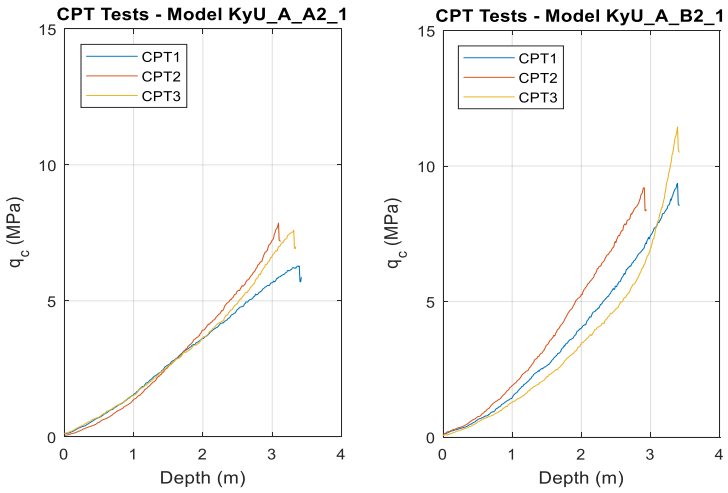

Figure 3-25 CPT Test Records (KyU Tests for LEAP-ASIA-2019) (a) Model KyU_A_A1_1, (b) Model KyU_A_B1_1, (c) Model KyU_A_B1_2, (d) Model KyU_A_A2_1, (e) Model KyU_A_B2_1

3.3.4 Surface Displacements

High-speed cameras were used to record the ground surface deformation during and after the motion; based on the recordings, the surface displacement was obtained by means of an image analysis procedure, implemented in the commercial software Dipp-Motion V. Figure 3-26, and Figure 3-27 shows the residual surface displacements.

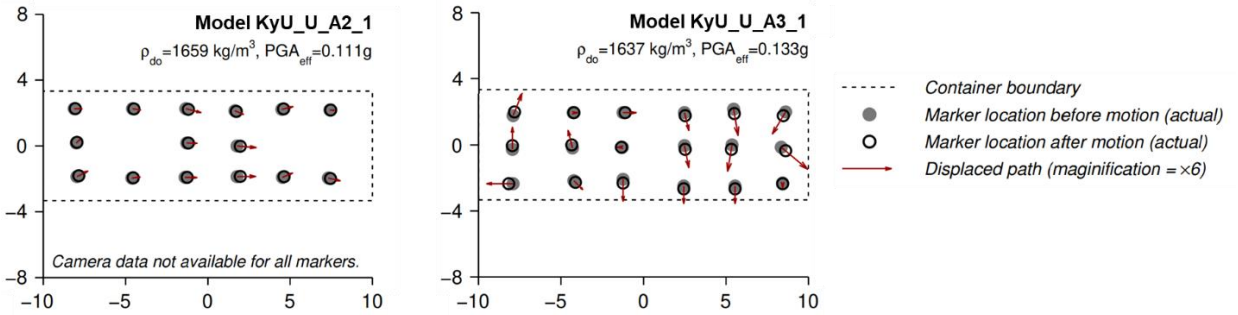

Figure 3-26 Surface Ground Displacements – (KyU Tests for LEAP-UCD-2017)First Destructive Motion - Models KyU_U_A2_1, and KyU_U_A3_1

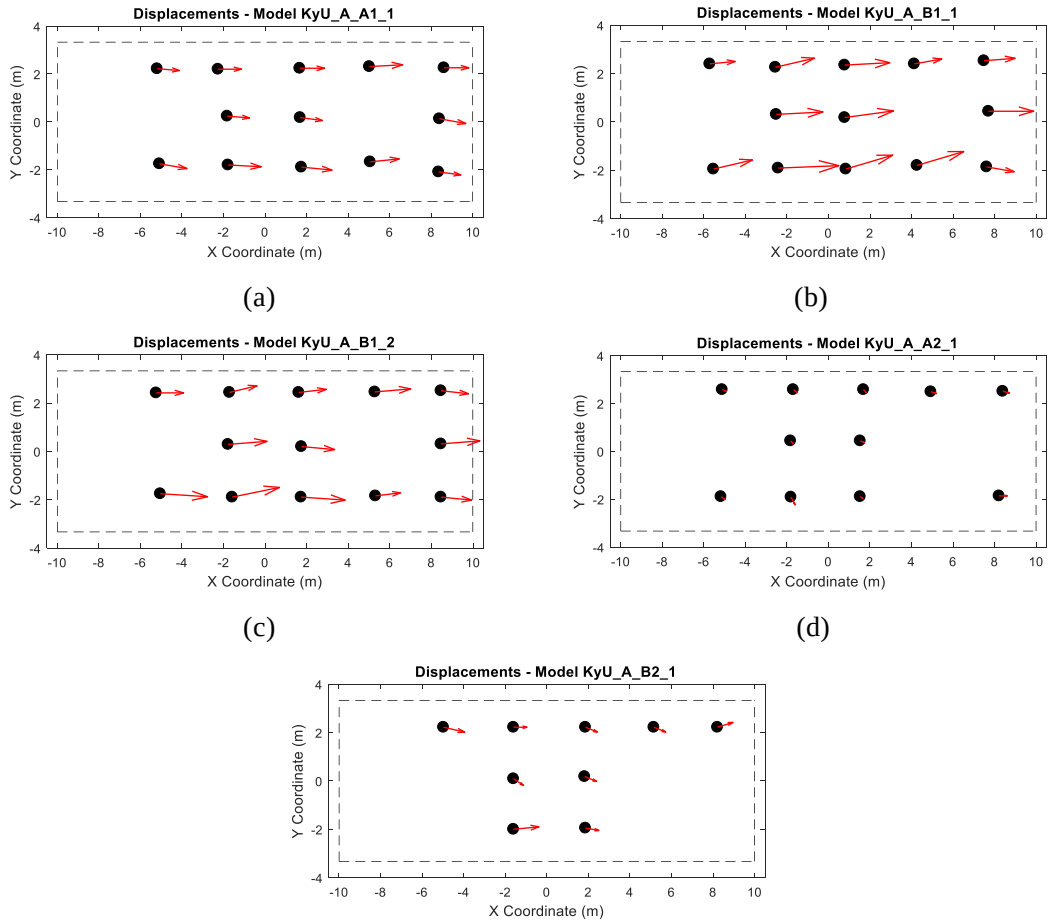

(a) (b) (c) (d) (e)

Figure 3-27 Surface Ground Displacements – (KyU Tests for LEAP-ASIA-2019)First Destructive Motion (a) Model KyU_A_A1_1, (b) Model KyU_A_B1_1, (c) Model KyU_A_B1_2, (d) Model KyU_A_A2_1, (e) Model KyU_A_B2_1

3.4 Data Processing – LEAP-UCD-2017, and LEAP-ASIA-2019

As mentioned in Section 2.5.5.2, forty-eight centrifuge tests that simulate the dynamic response of a saturated sloping ground were performed as part of LEAP-UCD-2017 (twenty-four experiments), and LEAP-ASIA-2019 (twenty-four experiments), following the specifications described in Section 3.1.

This section focusses on the data processing of the test results; and the establishment of a cross-checked, reliable, and large Centrifuge-Models database, used as a base for the validation exercise.

3.4.1 Centrifuge Tests

Ten centrifuges around the world (see Table 3-5) have participated in LEAP-UCD-2017, and LEAP-ASIA-2019 exercises. Table 3-6 shows the list of tests, including the scaling laws, and the reported density (estimated by means of mass and volume measurements).

Table 3-5 Tests Facilities and main characteristics of their Centrifuge Facilities

Centrifuge Facility Institution	Abbreviation	Shaking Direction	Radius (m)	Container Length/Width
Cambridge University, UK	CU	Tangential	3.56	0.45
Ehime University, Japan	Ehime	Parallel to axis	1.184	0.24
IFSTTAR, France	IFSTTAR	Parallel to axis	5.063	0.50
KAIST, Rep. of Korea	KAIST	Parallel to axis	5	0.45
Kyoto University, Japan	KyU	Tangential	2.5	0.33
National Central Univ., Taiwan	NCU	Parallel to axis	2.716	0.45
Rensselaer Poly. Inst., USA	RPI	Parallel to axis	2.7	0.42
Tokyo Institute of Technology, Japan	TIT	Parallel to axis	2.15	0.33
Univ. of California, Davis, USA	UCD	Tangential	1.094	0.63
Zhejiang University, China	ZJU	Parallel to axis	4.315	0.59

Table 3-6 List of Centrifuge Tests - LEAP-UCD-2017, and LEAP-ASIA-2019

Test	Exercise	Scale factor for 1g test (μ)	Scaling factors for centrifuge test (η)	Generalized scaling factor	Achieved Density from M&V (kg/m3)
IFSTTAR_A_A1_1	LEAP-ASIA-2019	1	50	50	1663
KAIST_A_A1_1	LEAP-ASIA-2019	1	40	40	1716.55
KyU_A_A1_1	LEAP-ASIA-2019	1	44.4	44.4	1677
KyU_A_A2_1	LEAP-ASIA-2019	1	44.4	44.4	1628
NCU_A_A1_1	LEAP-ASIA-2019	1	26	26	1643
RPI_A_A1_1	LEAP-ASIA-2019	1	23	23	1651

Test	Exercise	Scale factor for 1g test (μ)	Scaling factors for centrifuge test (η)	Generalized scaling factor	Achieved Density from M&V (kg/m3)
UCD_A_A1_1	LEAP-ASIA-2019	1	43.75	43.75	1713.3
UCD_A_A2_1	LEAP-ASIA-2019	1	43.75	43.75	1658.1
ZJU_A_A1_1	LEAP-ASIA-2019	1	30	30	1624.6
TIT_A_A1_1	LEAP-ASIA-2019	1	44.4	44.4	1645
TIT_A_A2_1	LEAP-ASIA-2019	1	44.4	44.4	1645
CU_A_B1_1	LEAP-ASIA-2019	0.5	80	40	1606
Ehime_A_B1_1	LEAP-ASIA-2019	2	20	40	1650.8
IFSTTAR_A_B1_1	LEAP-ASIA-2019	2	25	50	1645
KAIST_A_B1_1	LEAP-ASIA-2019	1.5	26.7	40.05	1720.6
KyU_A_B1_1	LEAP-ASIA-2019	2	22.2	44.4	1673
KyU_A_B1_2	LEAP-ASIA-2019	4	11.1	44.4	1669
KyU_A_B2_1	LEAP-ASIA-2019	2	22.2	44.4	1633
NCU_A_B1_1	LEAP-ASIA-2019	2	13	26	1626
RPI_A_B1_1	LEAP-ASIA-2019	0.5	46	23	1644
UCD_A_B1_1	LEAP-ASIA-2019	2	21.9	43.8	1711.7
ZJU_A_B1_1	LEAP-ASIA-2019	2	15	30	1632.7
TIT_A_B1_1	LEAP-ASIA-2019	2	22.2	44.4	1654
TIT_A_B2_1	LEAP-ASIA-2019	2	22.2	44.4	1648
RPI1	LEAP-UCD-2017	1	23	23	1650
RPI2	LEAP-UCD-2017	1	23	23	1659
RPI3	LEAP-UCD-2017	1	23	23	1623
KyU1	LEAP-UCD-2017	1	44.4	44.4	1683
KyU2	LEAP-UCD-2017	1	44.4	44.4	1659
KyU3	LEAP-UCD-2017	1	44.4	44.4	1637
KAIST1	LEAP-UCD-2017	1	40	40	1701.2
KAIST2	LEAP-UCD-2017	1	40	40	1592.5
ZJU1	LEAP-UCD-2017	1	30	30	1651
ZJU2	LEAP-UCD-2017	1	30	30	1599
ZJU3	LEAP-UCD-2017	1	30	30	1703
UCD1	LEAP-UCD-2017	1	43.75	43.75	1665
UCD2	LEAP-UCD-2017	1	43.75	43.75	1648
UCD3	LEAP-UCD-2017	1	43.75	43.75	1658
NCU1	LEAP-UCD-2017	1	26	26	1652
NCU2	LEAP-UCD-2017	1	26	26	1652
NCU3	LEAP-UCD-2017	1	26	26	1652
CU1	LEAP-UCD-2017	1	40	40	1656
CU2	LEAP-UCD-2017	1	40	40	1606
IFSTTAR1	LEAP-UCD-2017	1	50	50	1696
IFSTTAR2	LEAP-UCD-2017	1	50	50	1624
Ehime1	LEAP-UCD-2017	1	40	40	1649.05
Ehime2	LEAP-UCD-2017	1	40	40	1656.55
Ehime3	LEAP-UCD-2017	1	40	40	1692.83

3.4.2 CPT Tests and Density assessment

As a first attempt, the density of each model was estimated through mass and volume measurements; however, as described by Vargas et. al [106], small errors in the measurement of mass or volume lead to important deviations in the Dr estimation. In order to better estimate the actual density, it has been found that, although providing an indirect measurement, CPT test results allows a reliable estimation of the uniformity of the ground and its associated dry density [95] [109]. In that sense, most of the facilities developed CPT Tests for the models prepared for the LEAP-UCD-2017, and LEAP-ASIA-2019; Figure 3-28, and Figure 3-29 shows cone penetration tests for each exercise.

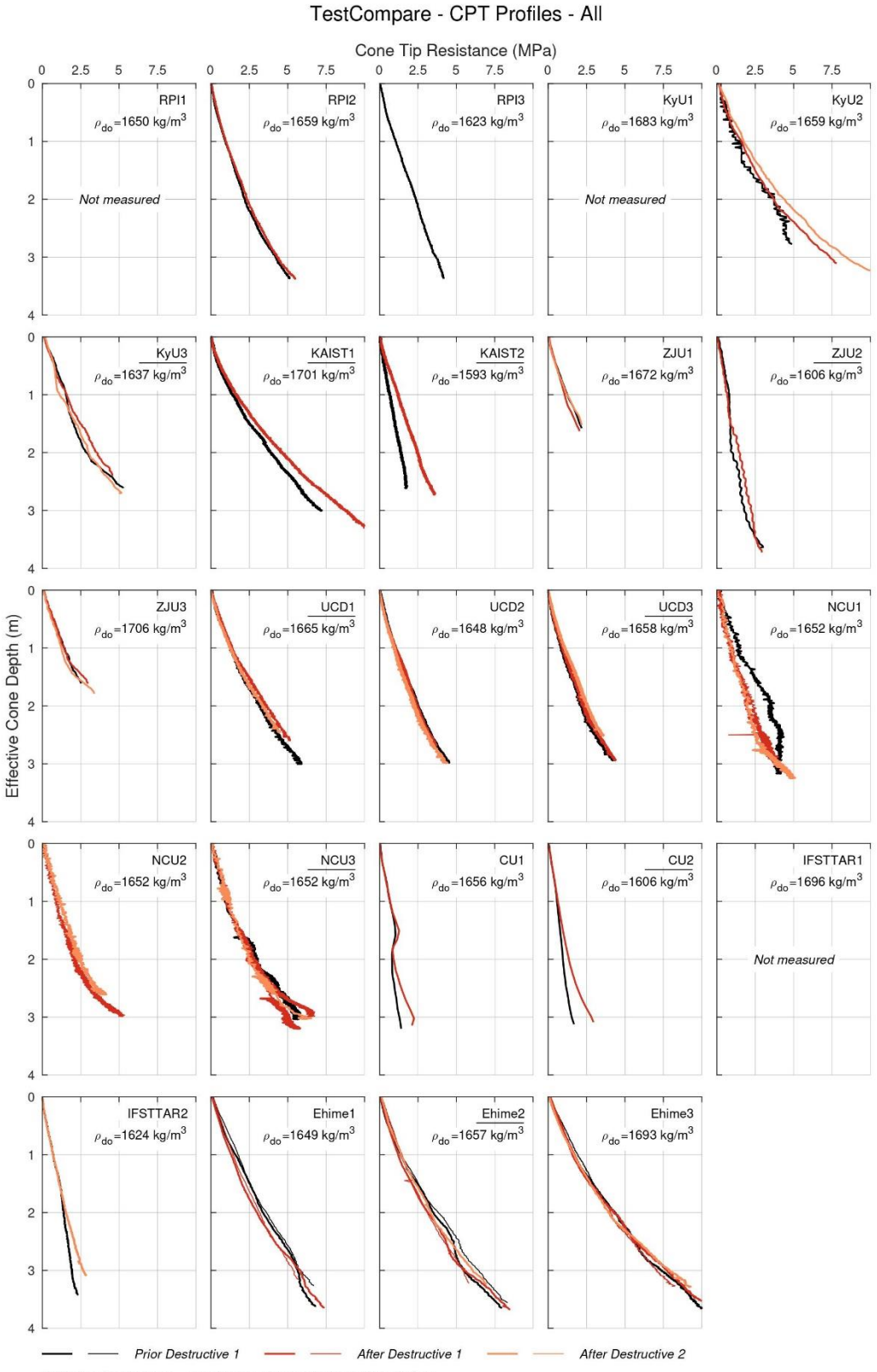

Figure 3-28 CPT Tests - LEAP-UCD-2017 [95] [105]

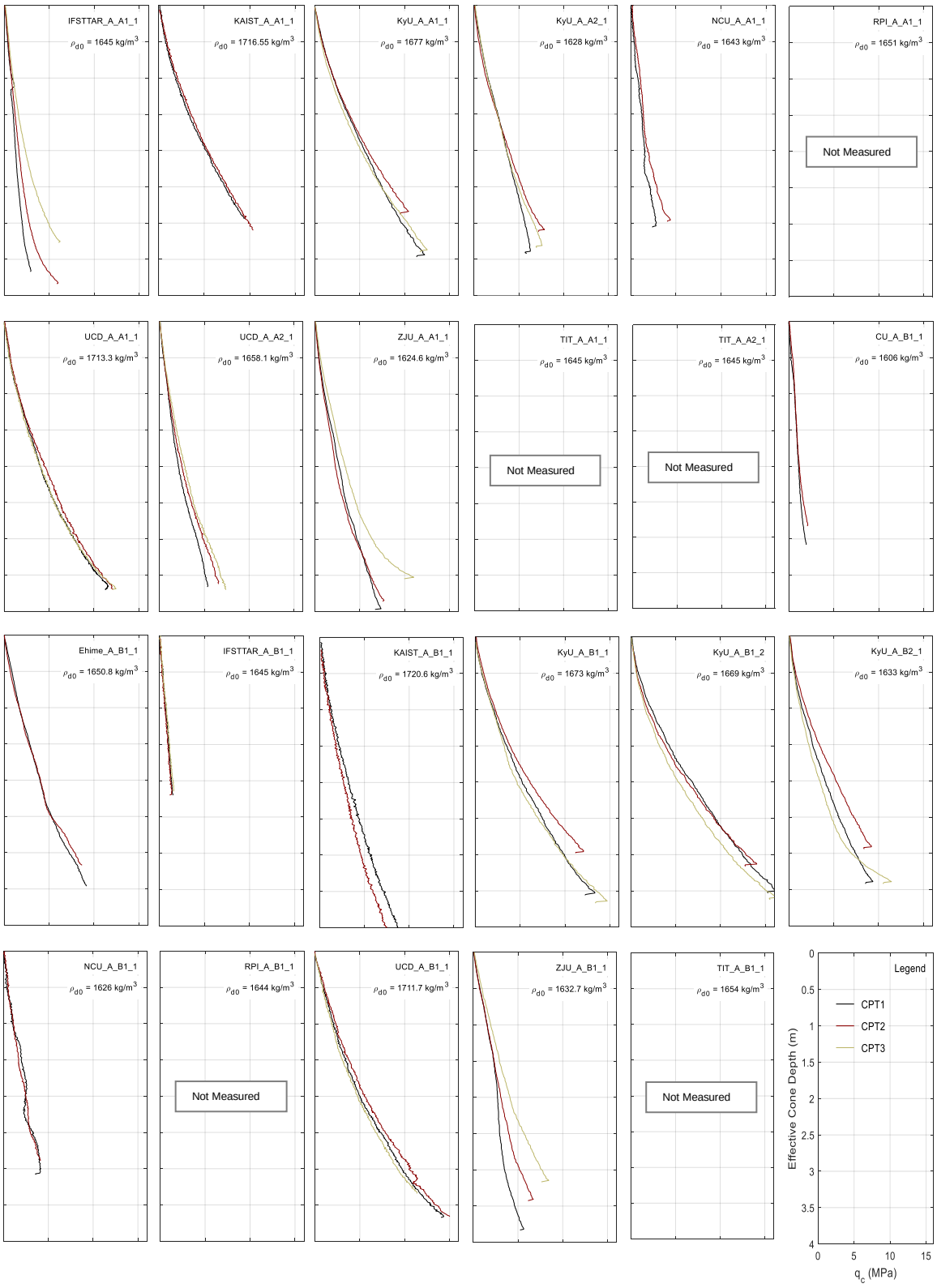

Figure 3-29 CPT Tests - LEAP-ASIA-2019

Carey et.al [109] pointed out that when comparing results from different centrifuge tests it is critical that the effective depth of cone be consistently defined; in this sense, all the CPT results were corrected

assuming that the "zero effective depth penetration" corresponds to the depth at which 2/3 of the cone tip has penetrated the ground.

Kutter et.al [95] found that the tip resistance at the mid-depth (i.e. at 2.0 m) is well correlated with the initial relative density of the ground; so, this parameter ($qc_{2.0}$ at CPT1) was used by Carey et. al [109], who found a correlation between the dry density and the tip resistance (see Figure 3-30), based on the results of LEAP-UCD-2017. In this correlation, it has been found that the achieved $qc_{2.0}$ value is highly influenced by the boundary conditions (especially the Container Width "w"), and the CPT size in prototype scale "Dc" (since all facilities used the same CPT size in model scale, different sizes in prototype scale were obtained based on the scaling relationships); so, different correlations were established depending on the test conditions.

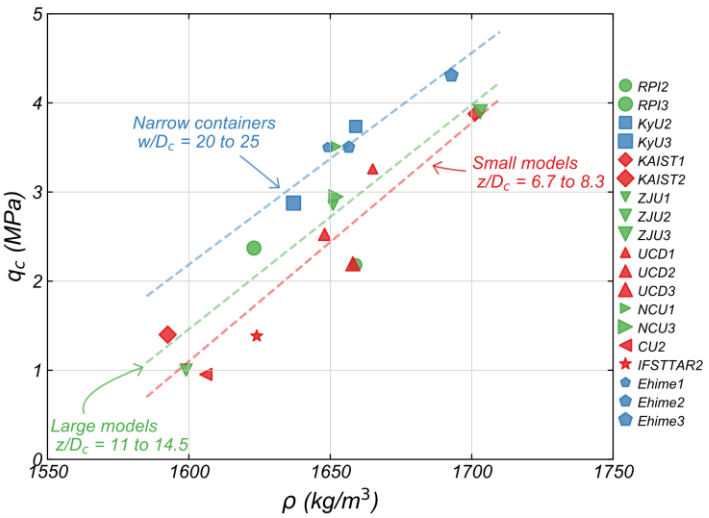

Figure 3-30 Correlation between the dry density ρ and the tip resistance qc2.0 - LEAP-UCD-2017 [109]

By combining the results obtained for LEAP-UCD-2017 and LEAP-ASIA-2019, the ρ- $qc_{2.0}$ correlation has been updated. As seen in Figure 3-31, similar trends (with respect to the previous correlation) were obtained. The correlations were developed in the same categories ("small models", "large models", and "narrow containers") based on the container dimensions and the "Dc" values; in this updated correlation it was found that a power-type correlation better fits the data than a linear-type correlation.

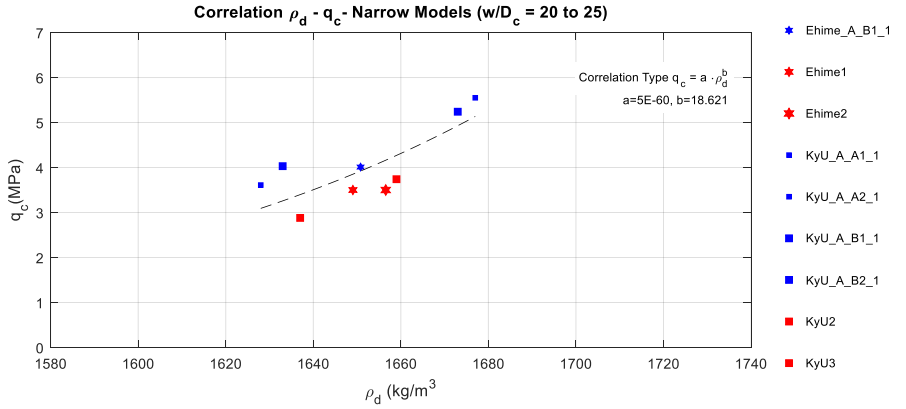

(a)

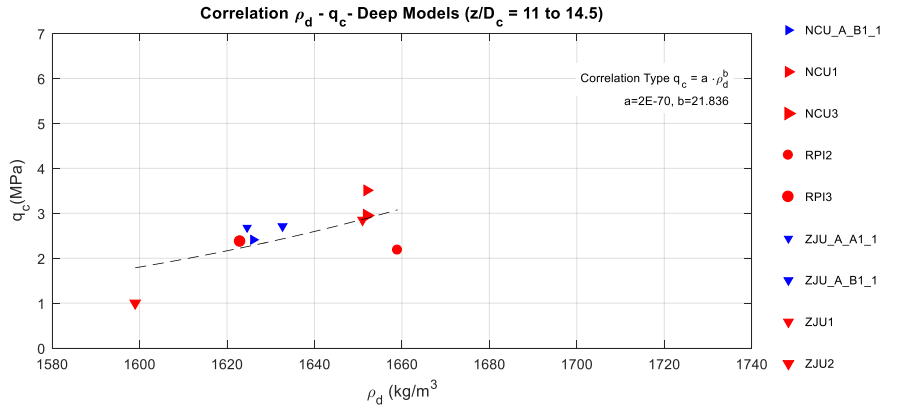

(b)

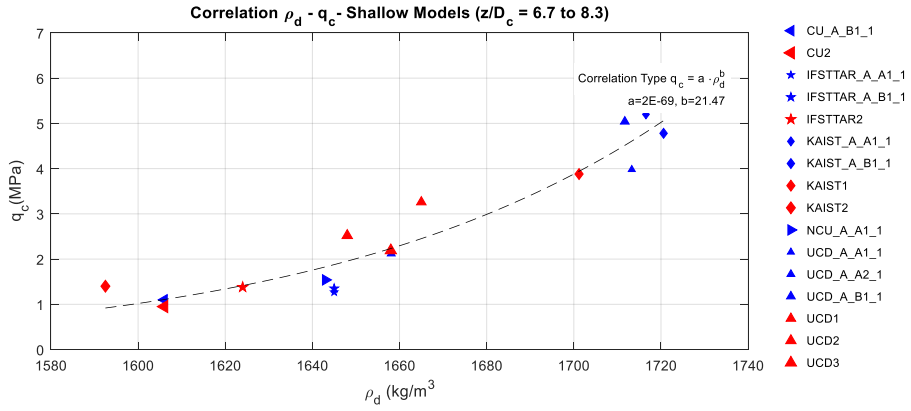

(c)

Figure 3-31 Updated correlations between the dry density ρ_d and the tip resistance $q_{c2.0}$ - LEAP-UCD-2017 and LEAP-ASIA-2019 (a) Narrow Models (w/Dc=20-25), (b) Deep Models (z/Dc=11-14.5), (c) Shallow Models (z/Dc = 6-8.3)

Based on the updated correlations, the dry densities and Dr-values were estimated based on the achieved $qc_{2.0}$ value. These values are shown in Table 3-7.

Table 3-7 Estimations of Density and Dr from $qc_{2.0}$ for tests developed at LEAP-UCD-2017 and LEAP-ASIA-2019

Test	Exercise	$qc_{2.0}$ (MPa)	Density from $qc_{2.0}$ (kg/m3)	Dr from qc 2.0
IFSTTAR_A_A1_1	LEAP-ASIA-2019	1.27	1621.52	53%
KAIST_A_A1_1	LEAP-ASIA-2019	5.20	1716.54	87%
KyU_A_A1_1	LEAP-ASIA-2019	5.55	1666.90	70%
KyU_A_A2_1	LEAP-ASIA-2019	3.61	1646.51	62%
NCU_A_A1_1	LEAP-ASIA-2019	1.54	1634.07	58%
RPI_A_A1_1	LEAP-ASIA-2019	-	-	-
UCD_A_A1_1	LEAP-ASIA-2019	3.98	1698.12	81%
UCD_A_A2_1	LEAP-ASIA-2019	2.12	1655.55	66%
ZJU_A_A1_1	LEAP-ASIA-2019	2.68	1639.62	60%
TIT_A_A1_1	LEAP-ASIA-2019	-	-	-
TIT_A_A2_1	LEAP-ASIA-2019	-	-	-
CU_A_B1_1	LEAP-ASIA-2019	1.10	1612.26	50%
Ehime_A_B1_1	LEAP-ASIA-2019	4.01	1651.47	64%
IFSTTAR_A_B1_1	LEAP-ASIA-2019	1.35	1625.44	55%
KAIST_A_B1_1	LEAP-ASIA-2019	3.26	1684.43	76%
KyU_A_B1_1	LEAP-ASIA-2019	5.24	1664.20	69%
KyU_A_B1_2	LEAP-ASIA-2019	6.86	1677.04	73%
KyU_A_B2_1	LEAP-ASIA-2019	4.03	1651.70	64%
NCU_A_B1_1	LEAP-ASIA-2019	2.41	1635.44	58%
RPI_A_B1_1	LEAP-ASIA-2019	-	-	-
UCD_A_B1_1	LEAP-ASIA-2019	5.04	1714.30	86%
ZJU_A_B1_1	LEAP-ASIA-2019	2.71	1640.16	60%
TIT_A_B1_1	LEAP-ASIA-2019	-	-	-
TIT_A_B2_1	LEAP-ASIA-2019	-	-	-
RPI1	LEAP-UCD-2017	-	-	-
RPI2	LEAP-UCD-2017	2.18	1631.43	57%
RPI3	LEAP-UCD-2017	2.37	1634.75	58%
KyU1	LEAP-UCD-2017	-	-	-
KyU2	LEAP-UCD-2017	3.74	1648.17	63%
KyU3	LEAP-UCD-2017	2.88	1635.89	59%
KAIST1	LEAP-UCD-2017	3.88	1696.26	80%
KAIST2	LEAP-UCD-2017	1.40	1627.88	56%
ZJU1	LEAP-UCD-2017	2.85	1642.17	61%
ZJU2	LEAP-UCD-2017	1.00	1600.51	45%
ZJU3	LEAP-UCD-2017	3.90	1654.89	65%
UCD1	LEAP-UCD-2017	3.26	1684.43	76%
UCD2	LEAP-UCD-2017	2.52	1667.13	70%
UCD3	LEAP-UCD-2017	2.19	1657.72	67%
NCU1	LEAP-UCD-2017	3.51	1689.46	78%
NCU2	LEAP-UCD-2017	-	-	-
NCU3	LEAP-UCD-2017	2.95	1677.60	74%
CU1	LEAP-UCD-2017	0.81	1592.39	42%

Test	Exercise	$qc_{2.0}$ (MPa)	Density from $qc_{2.0}$ (kg/m3)	Dr from qc 2.0
CU2	LEAP-UCD-2017	0.95	1602.79	46%
IFSTTAR1	LEAP-UCD-2017	-	-	-
IFSTTAR2	LEAP-UCD-2017	1.38	1627.14	55%
Ehime1	LEAP-UCD-2017	3.50	1645.10	62%
Ehime2	LEAP-UCD-2017	3.50	1645.14	62%
Ehime3	LEAP-UCD-2017	4.31	1654.92	66%

3.4.3 Input Motions and PGA_{eff}

As mentioned in Section 3.1 (refer to Figure 3-8), the specified input motion for the LEAP Exercises consists of a ramped sinusoidal wave. Although the wave should ideally contain only 1 Hz components when analyzed in the frequency domain, the centrifuge shakers produce motions that contain a broad range of additional high-frequency components. While these higher frequency components do have some effect on the model's behavior, their impact is relatively small. To address this issue, LEAP introduced the PGA_{eff} (see Eq. (3-1)) as a first attempt to represent the demand of the motion.

Based on Eq. (3-1) (an example of the filtering process is shown in Figure 3-9), the PGA_{eff}, the PGA, PGA_{1Hz}, and PGA_{eff}, values for all the tests were estimated, and the results are summarized in Table 3-8.

Table 3-8 Estimations of PGA_{eff} for tests developed at LEAP-UCD-2017 and LEAP-ASIA-2019

Test	Exercise	PGA (g)	PGA_{1Hz} (g)	PGA_{eff} (g)
IFSTTAR_A_A1_1	LEAP-ASIA-2019	0.43	0.26	0.35
KAIST_A_A1_1	LEAP-ASIA-2019	0.33	0.25	0.29
KyU_A_A1_1	LEAP-ASIA-2019	0.3	0.19	0.25
KyU_A_A2_1	LEAP-ASIA-2019	0.13	0.1	0.12
NCU_A_A1_1	LEAP-ASIA-2019	0.18	0.11	0.14
RPI_A_A1_1	LEAP-ASIA-2019	0.15	0.14	0.14
UCD_A_A1_1	LEAP-ASIA-2019	0.21	0.14	0.18
UCD_A_A2_1	LEAP-ASIA-2019	0.15	0.12	0.13
ZJU_A_A1_1	LEAP-ASIA-2019	0.35	0.19	0.27
TIT_A_A1_1	LEAP-ASIA-2019	0.16	0.11	0.13
TIT_A_A2_1	LEAP-ASIA-2019	0.15	0.11	0.13
CU_A_B1_1	LEAP-ASIA-2019	0.33	0.16	0.24
Ehime_A_B1_1	LEAP-ASIA-2019	0.2	0.12	0.16
IFSTTAR_A_B1_1	LEAP-ASIA-2019	0.53	0.28	0.41
KAIST_A_B1_1	LEAP-ASIA-2019	0.37	0.28	0.33
KyU_A_B1_1	LEAP-ASIA-2019	0.31	0.19	0.25
KyU_A_B1_2	LEAP-ASIA-2019	0.31	0.19	0.25
KyU_A_B2_1	LEAP-ASIA-2019	0.16	0.09	0.13
NCU_A_B1_1	LEAP-ASIA-2019	0.16	0.1	0.13
RPI_A_B1_1	LEAP-ASIA-2019	0.16	0.14	0.15

Test	Exercise	PGA (g)	PGA_{1Hz} (g)	PGA_{eff} (g)
UCD_A_B1_1	LEAP-ASIA-2019	0.15	0.13	0.14
ZJU_A_B1_1	LEAP-ASIA-2019	0.33	0.21	0.27
TIT_A_B1_1	LEAP-ASIA-2019	0.15	0.1	0.12
TIT_A_B2_1	LEAP-ASIA-2019	0.16	0.11	0.14
RPI1	LEAP-UCD-2017	0.15	0.14	0.15
RPI2	LEAP-UCD-2017	0.14	0.11	0.15
RPI3	LEAP-UCD-2017	0.17	0.14	0.16
KyU1	LEAP-UCD-2017	0.07	0.05	0.06
KyU2	LEAP-UCD-2017	0.12	0.10	0.11
KyU3	LEAP-UCD-2017	0.14	0.12	0.13
KAIST1	LEAP-UCD-2017	0.18	0.12	0.17
KAIST2	LEAP-UCD-2017	0.19	0.12	0.17
ZJU1	LEAP-UCD-2017	0.17	0.09	0.13
ZJU2	LEAP-UCD-2017	0.19	0.10	0.15
ZJU3	LEAP-UCD-2017	0.14	0.08	0.11
UCD1	LEAP-UCD-2017	0.17	0.12	0.15
UCD2	LEAP-UCD-2017	0.34	0.15	0.21
UCD3	LEAP-UCD-2017	0.19	0.13	0.18
NCU1	LEAP-UCD-2017	0.29	0.18	0.24
NCU2	LEAP-UCD-2017	0.22	0.15	0.20
NCU3	LEAP-UCD-2017	0.22	0.13	0.18
CU1	LEAP-UCD-2017	0.19	0.12	0.19
CU2	LEAP-UCD-2017	0.21	0.12	0.20
IFSTTAR1	LEAP-UCD-2017	0.21	0.12	0.17
IFSTTAR2	LEAP-UCD-2017	0.14	0.10	0.13
Ehime1	LEAP-UCD-2017	0.17	0.14	0.16
Ehime2	LEAP-UCD-2017	0.18	0.13	0.16
Ehime3	LEAP-UCD-2017	0.17	0.14	0.16

2.1.1 Excess Pore Water Pressure and Ground Response Acceleration

Figure 3-32, and Figure 3-33 show the records of the Excess Pore Water Pressure Transducers (EPWPT) of the central array (P1, P2, P3, and P4), and the bottom corner of the container (P10). It shall be noted that the initial effective overburden stresses for sensors P1, P2, P3, and P4 are approximately 10, 20, 30, and 40 kPa respectively.

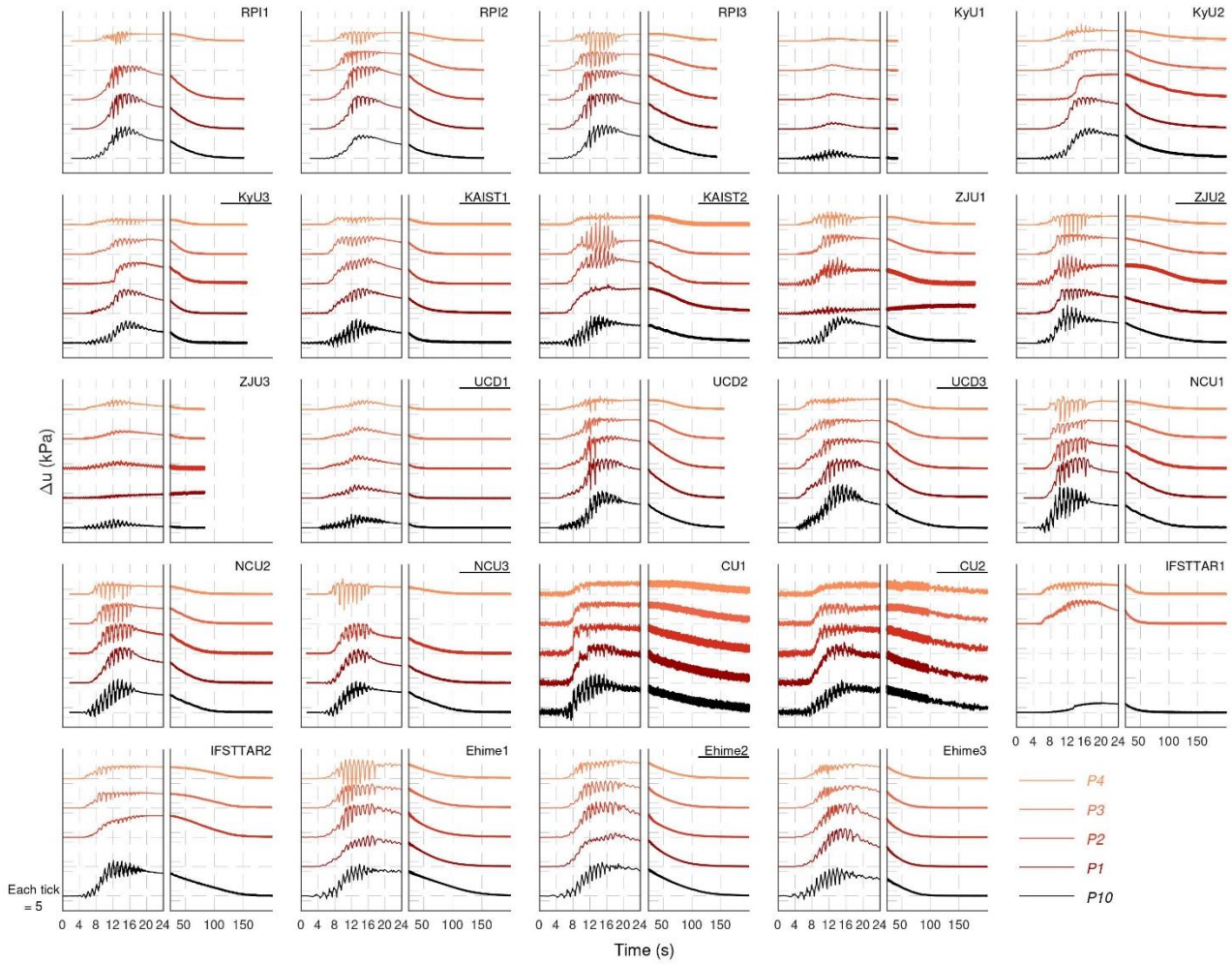

Figure 3-32 EPWP records for LEAP-UCD-2017 tests [95] [105]

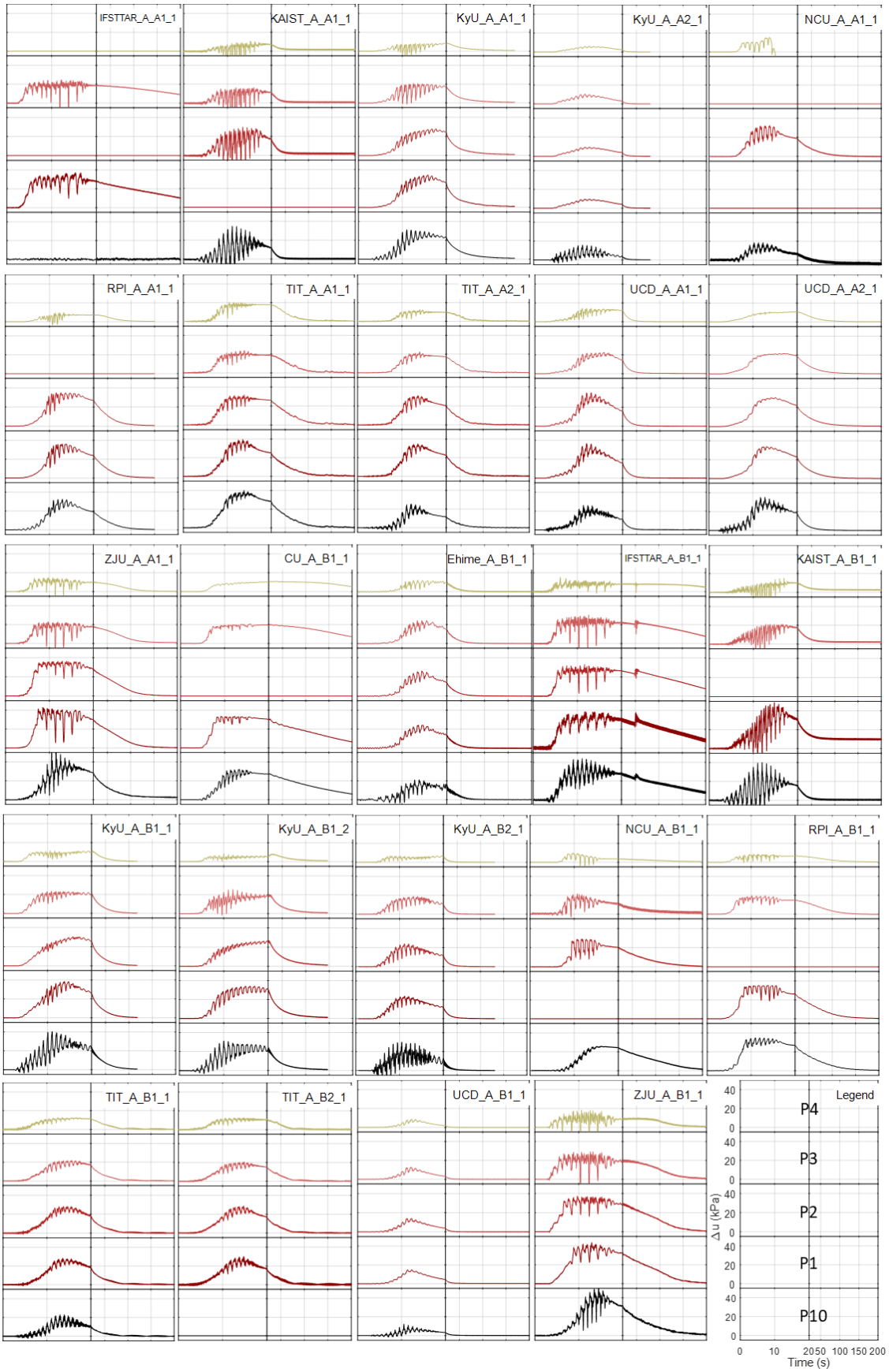

Figure 3-33 EPWP records for LEAP-ASIA-2019 tests

Similarly, Figure 3-34, and Figure 3-35 show the records of the Horizontal Ground Response Acceleration of the central array (AH1, AH2, AH3, and AH4), and the input acceleration (average record between AH11 and AH12). As it can be seen, all the records experienced significant distortions after experiencing a significant development of excess pore water pressure during the shaking; as mentioned in Section 3.3.2, the distortions are mostly composed by sharp spikes, which are characteristic of a dilative behavior of the liquefied ground, causing a decrease in the EPWP value (see Figure 3-32, and Figure 3-33).

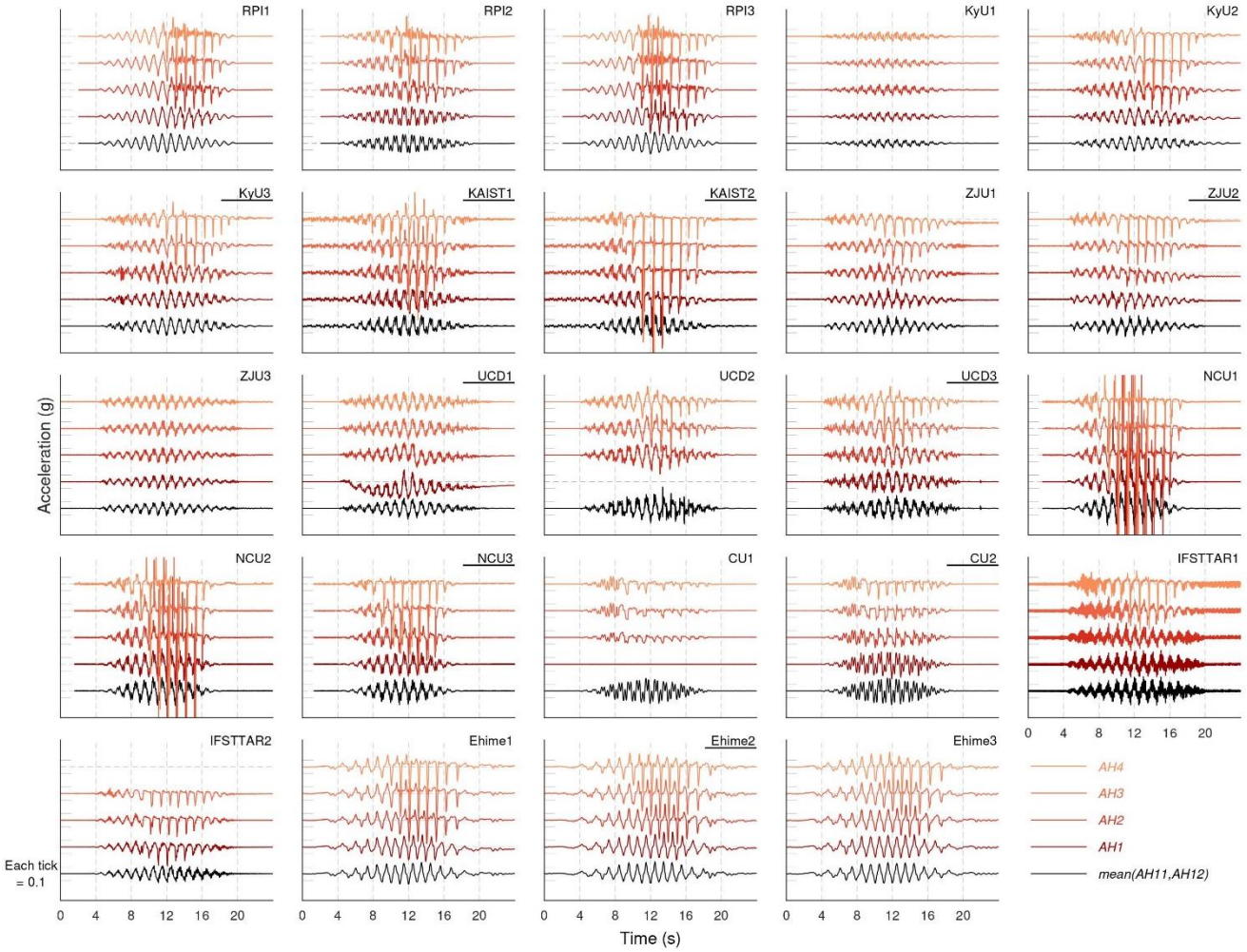

Figure 3-34 Ground Response Acceleration records for LEAP-UCD-2017 tests [95] [105]

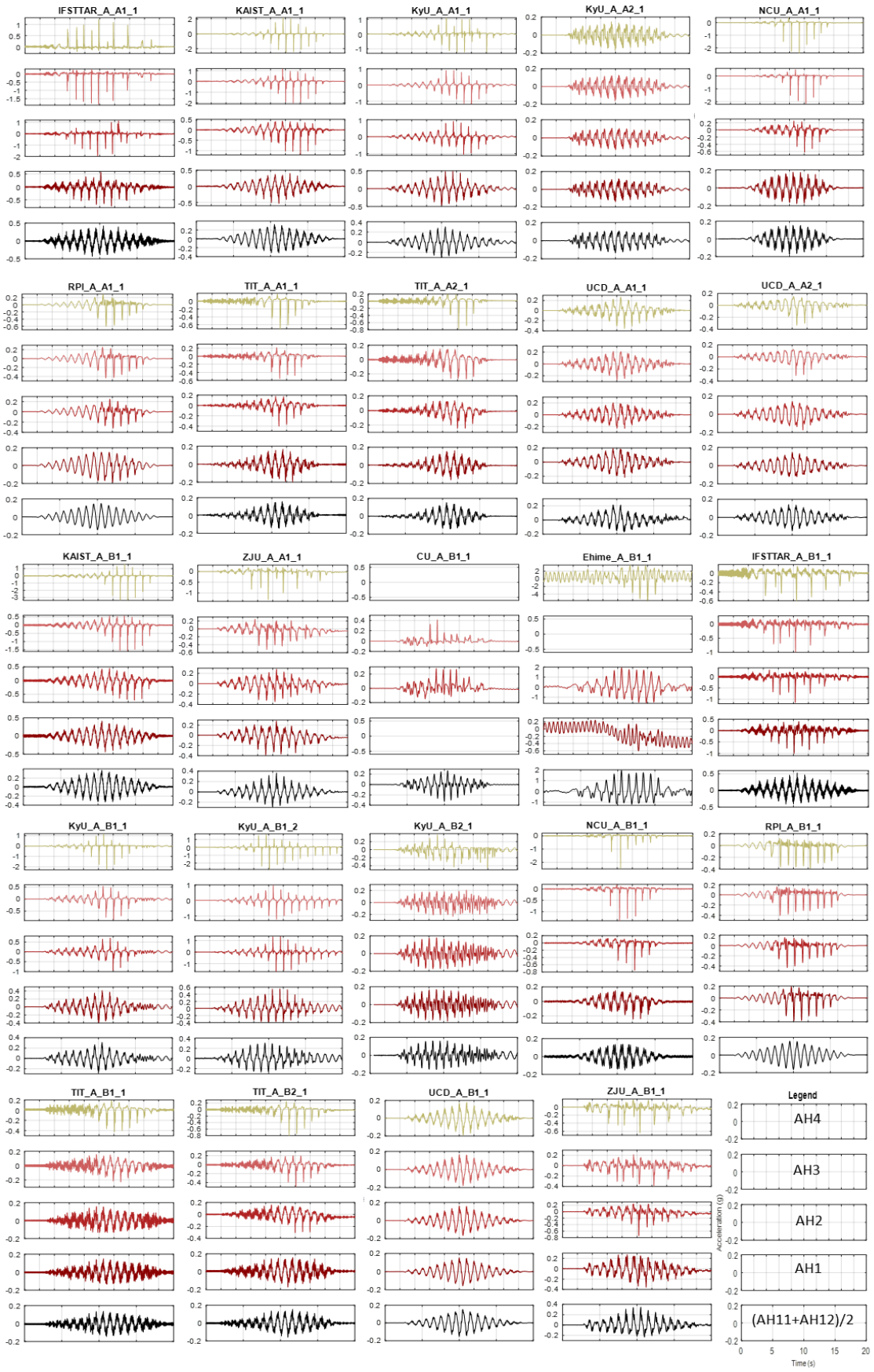

Figure 3-35 Ground Response Acceleration records for LEAP-ASIA-2019 tests

3.4.4 Surface Displacement

As specified in the exercise, the residual surface displacements of the surface markers were estimated by each facility by means of direct measurement (by rulers/calipers before and after the motion), or by using image analysis.

Vectors of the horizontal components of the displacements are shown in Figure 3-36, and Figure 3-37; in order to improve the visibility of the deformations, the vectors were magnified by a factor of 6.

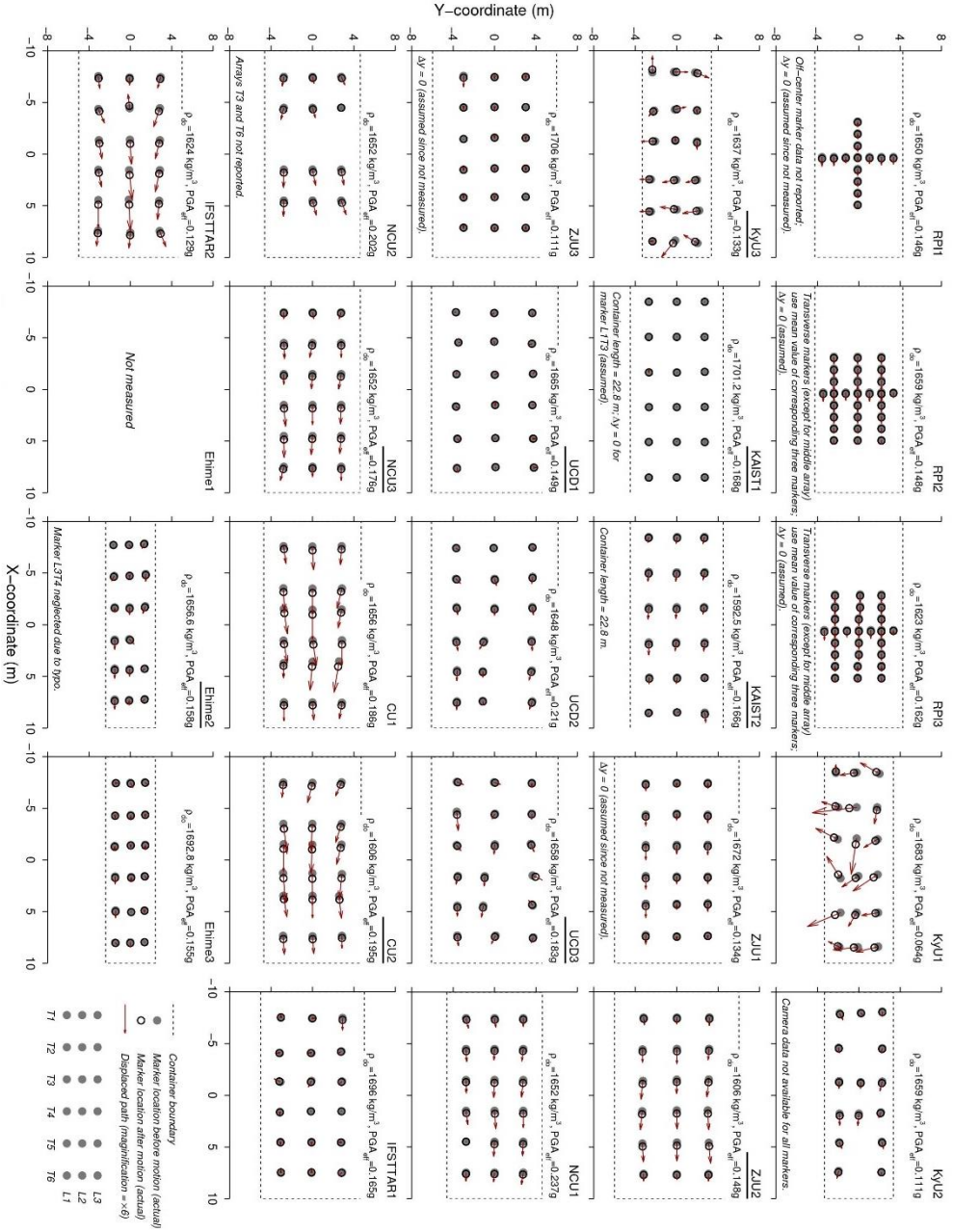

Figure 3-36 Residual Surface Displacement vectors for LEAP-UCD-2017 tests [95] [105]

Figure 3-37 Residual Surface Displacement vectors for LEAP-ASIA-2019 tests

Additionally, Table 3-9 shows a series of different metrics of the surface displacement values, special attention will be placed in the average value of the two central markers “Ux2”, because it was found that this value has a smaller variability (in comparison to the other displacement metrics), and it is less influenced by the boundary conditions.

Table 3-9 Displacement metrics (X-X direction) for tests developed at LEAP-UCD-2017 and LEAP-ASIA-2019

Test	Exercise	Avg. 2 Markers - Ux2 (mm)	Std. Dev 2 Markers (mm)	Avg. All Markers – UxA (mm)	Std. Dev All Markers (mm)	Avg. 8 Markers – Ux8 (mm)	Std. Dev 8 Markers (mm)
IFSTTAR_A_A1_1	LEAP-ASIA-2019	550.0	0.0	358.3	134.5	475.0	80.2
KAIST_A_A1_1	LEAP-ASIA-2019	33.9	0.0	30.5	13.1	34.7	9.3
KyU_A_A1_1	LEAP-ASIA-2019	71.0	0.0	84.4	13.2	83.6	15.0
KyU_A_A2_1	LEAP-ASIA-2019	11.1	3.1	14.5	5.7	11.1	2.4
NCU_A_A1_1	LEAP-ASIA-2019	181.5	27.0	150.7	31.5	162.7	21.1
RPI_A_A1_1	LEAP-ASIA-2019	99.6	13.6	87.7	22.2		
UCD_A_A1_1	LEAP-ASIA-2019	30.6	7.3	19.8	11.7	24.7	8.9
UCD_A_A2_1	LEAP-ASIA-2019	77.5	2.6	55.6	24.4	71.8	14.2
ZJU_A_A1_1	LEAP-ASIA-2019	390.0	42.4	321.7	100.7	393.8	32.8
TIT_A_A1_1	LEAP-ASIA-2019						
TIT_A_A2_1	LEAP-ASIA-2019	44.4	0.0	56.2	31.3	61.1	23.0
CU_A_B1_1	LEAP-ASIA-2019						
Ehime_A_B1_1	LEAP-ASIA-2019	56.6	0.0	36.6	39.7	56.6	42.8
IFSTTAR_A_B1_1	LEAP-ASIA-2019	777.8	100.0	555.9	178.2	685.0	108.5
KAIST_A_B1_1	LEAP-ASIA-2019	30.6	5.4	39.6	11.1	35.6	7.1
KyU_A_B1_1	LEAP-ASIA-2019	153.8	4.4	130.9	33.4	153.8	22.7
KyU_A_B1_2	LEAP-ASIA-2019	115.4	12.6	111.3	25.3	116.9	26.6
KyU_A_B2_1	LEAP-ASIA-2019	34.5	4.4	48.1	16.6	46.1	18.1
NCU_A_B1_1	LEAP-ASIA-2019	87.2	85.9	148.7	57.6	127.8	67.9
RPI_A_B1_1	LEAP-ASIA-2019	303.3	0.0	283.2	56.7		
UCD_A_B1_1	LEAP-ASIA-2019	-2.2	2.8	-0.7	1.7	-0.7	1.9
ZJU_A_B1_1	LEAP-ASIA-2019	678.8	60.0	486.7	176.5	594.0	122.7
TIT_A_B1_1	LEAP-ASIA-2019	125.6	0.0	102.0	68.3	109.9	44.4
TIT_A_B2_1	LEAP-ASIA-2019	62.8	0.0	62.8	32.4	70.6	22.2
RPI1	LEAP-UCD-2017	93.7	10.8			100.8	25.5
RPI2	LEAP-UCD-2017	134.0	12.5			128.0	22.4
RPI3	LEAP-UCD-2017	125.6	9.6			122.7	18.4
KyU1	LEAP-UCD-2017	377.4	282.6	64.1	216.0	116.6	282.7
KyU2	LEAP-UCD-2017	149.9	60.6	107.8	44.4	141.2	43.4
KyU3	LEAP-UCD-2017	0.0	62.8	12.3	109.6	11.1	61.7
KAIST1	LEAP-UCD-2017	2.3	2.0	0.9	3.3	-0.2	3.7
KAIST2	LEAP-UCD-2017	162.7	28.3	118.4	56.7	154.2	37.4
ZJU1	LEAP-UCD-2017	135.0	21.2	133.3	55.9	150.0	52.6
ZJU2	LEAP-UCD-2017	262.5	53.0	220.8	86.4	283.1	32.5
ZJU3	LEAP-UCD-2017	30.0	21.2	29.2	42.3	26.3	15.5
UCD1	LEAP-UCD-2017	0.0	27.8	12.2	29.5	0.0	27.7
UCD2	LEAP-UCD-2017	124.7	9.3	108.6	48.0	130.7	25.2
UCD3	LEAP-UCD-2017	159.7	3.1	116.4	79.6	134.0	35.3
NCU1	LEAP-UCD-2017	287.3	1.4	197.3	70.3	248.0	40.1
NCU2	LEAP-UCD-2017	256.1	0.0	187.9	82.9	238.7	48.5
NCU3	LEAP-UCD-2017	279.4	56.5	233.5	78.9	270.2	58.7

Test	Exercise	Avg. 2 Markers - Ux2 (mm)	Std. Dev 2 Markers (mm)	Avg. All Markers – UxA (mm)	Std. Dev All Markers (mm)	Avg. 8 Markers – Ux8 (mm)	Std. Dev 8 Markers (mm)
CU1	LEAP-UCD-2017	440.0	56.6	358.7	77.4	402.5	56.0
CU2	LEAP-UCD-2017	490.0	42.4	358.9	95.7	427.5	65.0
IFSTTAR1	LEAP-UCD-2017	50.0	71.0	21.0	62.0	25.0	46.0
IFSTTAR2	LEAP-UCD-2017	437.5	53.0	272.2	160.4	296.9	226.6
Ehime1	LEAP-UCD-2017						
Ehime2	LEAP-UCD-2017	100.0	28.3	89.4	48.0	102.9	39.0
Ehime3	LEAP-UCD-2017	60.0	28.3	55.6	36.7	65.0	36.6

3.5 Mean Response and Variability of Physical Models

This section presents the estimation of the main trends and associated variability of the experimental results (i.e. estimation of the experimental outputs), focusing on the estimation of the final surface displacements (Ux), and the identification of the key parameters that mainly define its behavior and variability.

3.5.1 LEAP Correlations

Kutter et al. [100] found that, for the lateral spreading phenomenon, the residual surface displacements are primarily a function of the intensity of shaking and the relative density of the sand.

Based on the LEAP-UCD-2017 test results, Kutter et al. [95] developed a nonlinear correlation to estimate the median trend value of the final surface displacements (Ux) as a function of the peak ground acceleration (PGA_{eff}) and the relative density (Dr).

The shape of the surface proposed by Kutter et al. [95] was based on the γ_{max} (maximum shear strain) vs FS_{liq} (Factor of Safety of Liquefaction) curves proposed by Yoshimine et al. [110], and the FS_{liq} correlations proposed by Iddriss and Boulanger [27], as follows.

$$U_x = b_2 \left(b_1 - \frac{(D_r - 0.125)^{n_3} + 0.05}{1.3 PGA_{\text{eff}}} \right)^{n_1} \quad (3\text{-}2)$$

Where n_1, n_3, b_1, and b_2 were estimated by a nonlinear regression.

Figure 3-38 shows the correlation estimated by Kutter et al. [95]; it shall be noticed that the correlation includes only the estimation of the median trend.

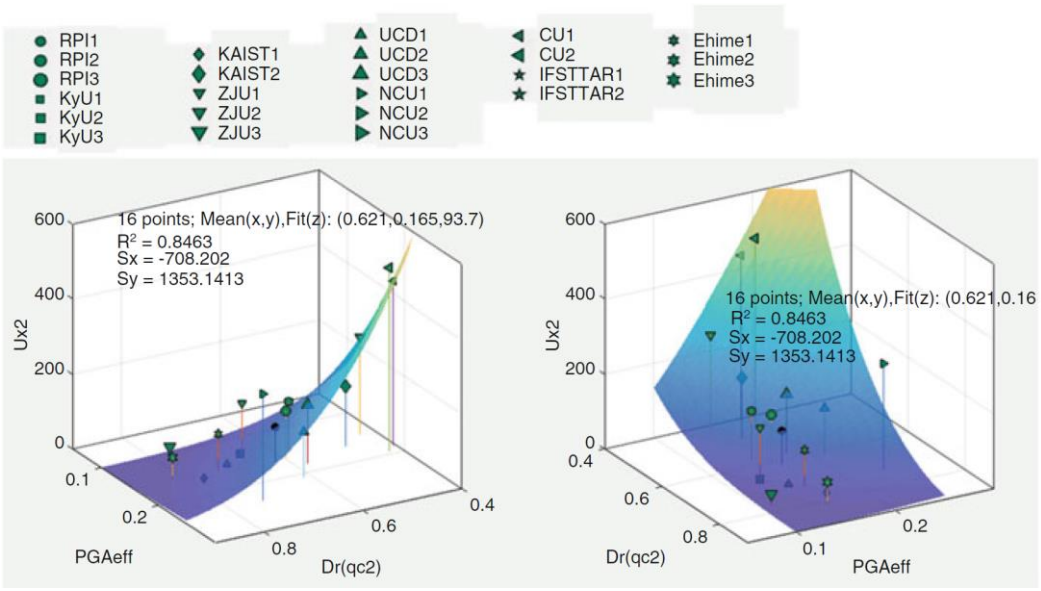

Figure 3-38 Correlation between the final surface displacements (Ux), the peak ground acceleration (PGAeff), and the relative density (Dr), estimated using the results of LEAP-UCD-2017 [95]

Later, by including the results of LEAP-ASIA-2019, Vargas [111] and Tobita et. al [25] updated the above-mentioned correlation, as shown in Figure 3-39.

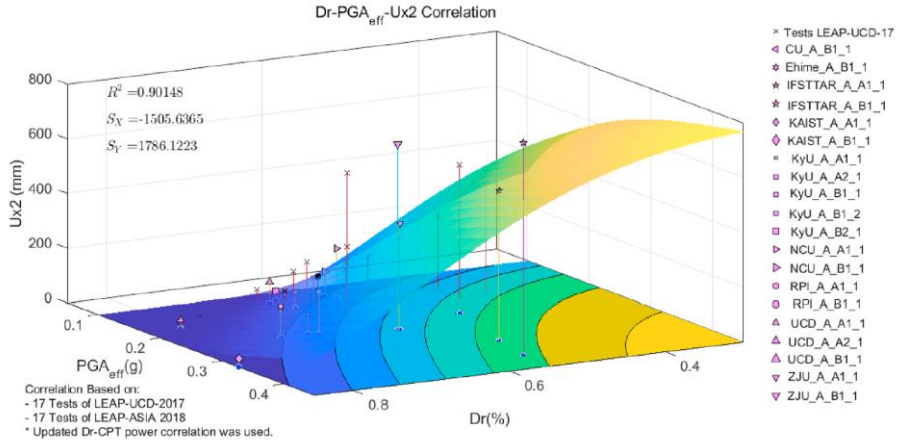

Figure 3-39 Correlation for Dr-PGAeff-Ux, based on the LEAP-UCD-2017 & LEAP-ASIA 2019 test results [111] [25]

Also, as an initial attempt to quantify the associated variability, Vargas [111] and Tobita et. al [25] estimated the variability of the correlation shown in Figure 3-39, by assuming that that the displacement values can be represented as a random variable that follows a Gaussian distribution, as shown in Figure 3-40.

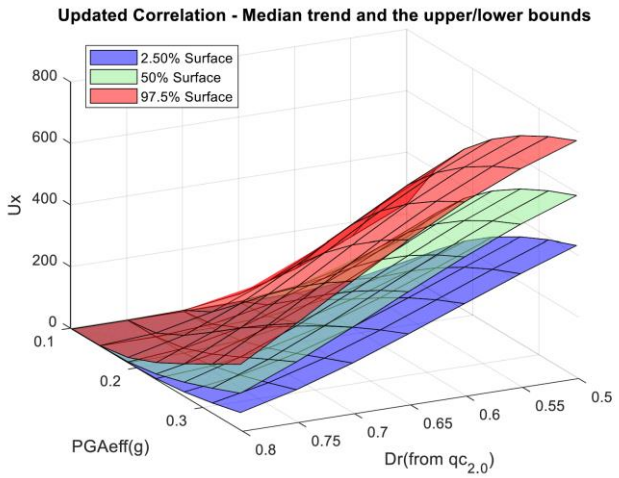

Figure 3-40 Correlation for Dr-PGAeff-Ux based on the LEAP-UCD-2017 & LEAP-ASIA 2019 test results – Initial attempt to estimate the associated variability

3.5.2 Correlation and Variability Estimation of Experimental Results

Following the requirements of the proposed validation methodology (refer to Section 1.4), and as recommended by Ching and Phoon [112], a proper assessment of the results of observations and experiments requires the evaluation not only of the median trend, but also of its associated variability.

In order to properly estimate the associated variability of Ux, the concept of Bayesian statistics [113] is used in this study [114]. The advantage of using Bayesian statistics is that the (posterior) distribution of the model input parameters, as well as that of the model uncertainty variables, are provided.

In this study, the probability distribution function (PDF) of the experimental results, x_i (i.e., the final surface displacements, Ux), was assumed to follow a log-Cauchy distribution, as follows:

$$f\left(\boldsymbol{x}|\mu_{U_x},\sigma_{U_x}\right)=\prod_{i=1}^{n}\frac{1}{\pi x_i}\frac{\sigma_{U_x}}{\left(ln\,x_i-\mu_{U_x}\right)^2+\sigma_{U_x}^2} \tag{3-3}$$

where $\mathbf{x}=\left\{x_1,\,x_1,\,\cdots,\,x_n\right\}$ is a vector representing the experimental data, and *n* is the number of data. $\mu_{U_x}\in\mathbb{R}$, and $\sigma_{U_x}>0$ are the location and scale parameters, respectively, of the log-Cauchy distribution.

Figure 3-41 shows comparisons between the log-Cauchy (LC) and the lognormal (LN) distributions with the same values for parameters μ_{U_x} and σ_{U_x} (subscript U_x is omitted in the figure). It can be seen that the former distributions have heavier tails than the latter ones.

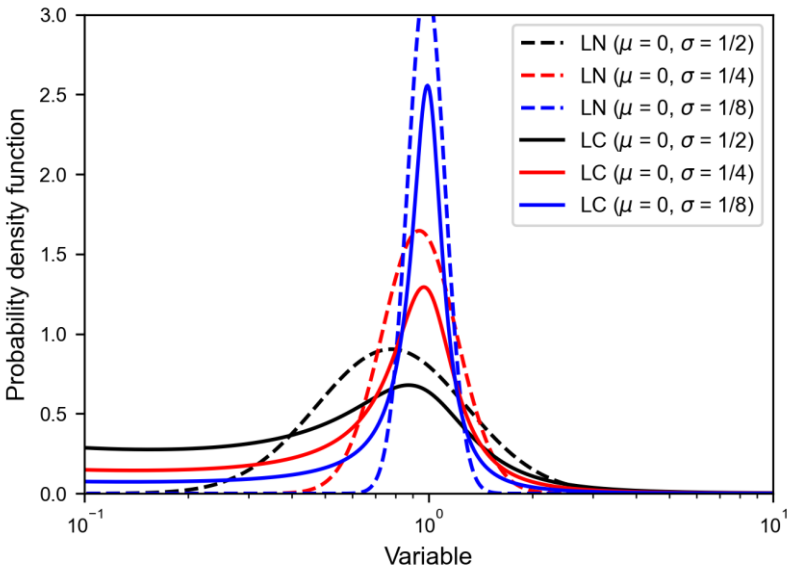

Figure 3-41 Comparisons between log-Cauchy (LC) and lognormal (LN) distributions

Referring to the relationship between the mean and the standard deviations in a lognormal distribution [115], location parameter μ_{U_x} was assumed as follows:

$$\mu_{U_x} = ln\, E_{U_x} - \frac{1}{2}\sigma_{U_x}^2 \tag{3-4}$$

As for the median E_{U_x} of the log-Cauchy distribution, it was modeled following the shape of the correlation introduced in Section 3.5.1, with n_1, and b_2 defined as constant values (as suggested by Vargas [111] and Tobita et. al [25]).

$$E_{U_x} = 100\left[b_1 - \frac{(D_r - 0.125)^{n_3} + 0.05}{1.3PGA_{\text{eff}}}\right]^4 \tag{3-5}$$

with input parameters b_1 and n_3 .

Regarding the definition of the E_{U_x} of the log-Cauchy distribution (likelihood), it is important to mention that the definition of this shape influences the shape of the posterior distribution (especially on areas with limited amount of data). While the definition of the shape would not be required when a significant amount of data is available, since the Physical Modeling consists on forty-eight tests "only" (with few amounts of data specifically for PGA_{eff} values larger than 0.25g), the definition of the shape results beneficial because allows to provide a "reference" for the correlations based on prior experimental and empirical data (the shape of the correlation γ_{max} vs FS_{liq} curves proposed by Yoshimine et al. [110], and the FS_{liq} correlations proposed by Iddriss and Boulanger [27]). It is, however, pertinent to acknowledge that alternative

correlation shapes are also viable for consideration.

The reason for using the log-Cauchy distribution instead of the lognormal distribution in Eq. (3-3) was to prevent the Bayesian estimation results from being dragged too much by the outliers [116] [117] [118]. This is because, as previously mentioned, the log-Cauchy distributions have heavier tails (see Figure 3-41).

Given that there is no prior knowledge of model input parameters b_1 and n_3, the following uniform distributions were adopted as the non-informative prior distributions [113]:

$$f(b_1) \propto 1, \quad -\infty < b_1 < +\infty \tag{3-6}$$

$$f(n_3) \propto 1, \quad -\infty < n_3 < +\infty \tag{3-7}$$

Meanwhile, the prior distribution of positive scale parameter σ_{U_x} was assumed to be the half-Cauchy distribution, as follows:

$$f(\sigma_{U_x}|0,1) = \frac{2}{\pi}\frac{1}{1+\sigma_{U_x}^2}, \quad 0 < \sigma_{U_x} < +\infty \tag{3-8}$$

The half-Cauchy distribution is a Cauchy distribution truncated to have a probability density only for values greater than the location parameter, which may take on any real value. However, it is set to 0 for most applications, as shown in Eq. (3-8).

As Gelman [119] and Polson-and-Scott [120] stated, the reason for using the half-Cauchy distribution is that the half-Cauchy can be a convenient weakly informative family for variance parameters that are estimated from a small number of groups.

Substituting these prior distributions and the centrifuge experimental data (Dr_i, PGA_{eff_i}, and Ux_i values are reported in Table 3-7, Table 3-8, and Table 3-9, respectively) into Eq. (3-3), along with Eq. (3-4), the posterior PDF of all the uncertain parameters results in the expression shown in Eq. (3-9).

$$f(\mu_{U_x}, \sigma_{U_x}|\boldsymbol{x}) = f(b_1, n_3, \sigma_{U_x}|\boldsymbol{x}) = kf(b_1)f(n_3)f(\sigma_{U_x})\prod_{i=1}^{n} f(x_i|b_1, n_3, \sigma_{U_x}) \tag{3-9}$$

where *k* is a normalization constant employed to make the integration of the posterior PDF equal to unity.

The posterior samples were collected using a hybrid Markov Chain Monte Carlo (MCMC) simulation (e.g., Gelman et al [113]). Figure 3-42 illustrates the correlation among Ux, PGA, and Dr obtained from the hybrid

MCMC-based Bayesian estimation.

In future efforts concerning the definition of the necessary amount of data (i.e., the number of experiments) for the accurate estimation of mean trends and variability, it is recognized that while more data generally yields benefits, a reasonable balance must be kept between the advantages of obtaining additional data and the associated time and costs. Various criteria may be proposed to determine the "optimum" amount of data for validation purposes; however, a pragmatic approach would be to continue data collection until the inclusion of additional data does not significantly alter the estimation of the mean trend and its associated variability. In this context, the definition of "significant alterations" should be closely aligned with the validation objectives and the corresponding validation metrics.

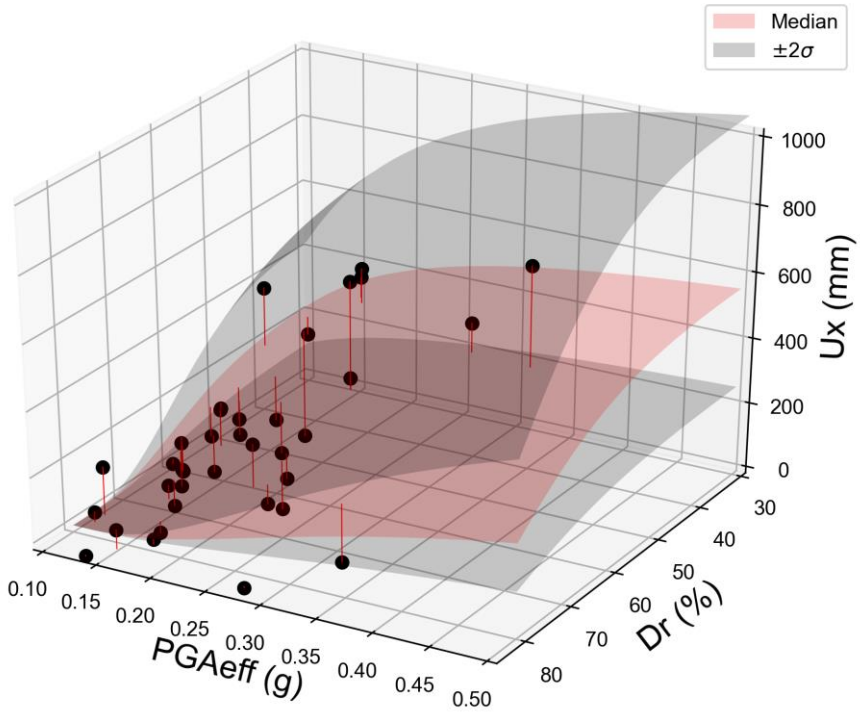

Figure 3-42 Correlation among final surface displacements (Ux), peak ground acceleration (PGA_{eff}), and relative density (Dr) estimated through MCMC-based Bayesian modeling

3.6 Section Conclusions

This section presents in detail the physical-model tests used in the validation process (i.e. centrifuge model tests developed for LEAP-UCD-2017, and LEAP-ASIA-2019), including: (1) an overview of the testing specifications (scaling laws, model preparation, and testing procedures), (2) a detailed information of the tests performed at Kyoto University, (3) the data processing of the tests (forty-eight centrifuge experiments), (4) the correlation and variability estimation of the final surface displacement (Ux), as a function of the peak ground acceleration (PGAeff) and the relative density (Dr).

- To build a high- quality database of cross-checked physical models for validation purposes, the development of comparable high-quality tests is required. However, due to its complexity, the results of centrifuge experiments significantly vary if they are not performed under the same conditions. Therefore, a clear definition of the Model Specifications is critical.
- As part of the LEAP Framework, an unprecedented quantity of centrifuge model tests (48 tests) was produced to simulate the lateral spreading phenomena under a wide range of input motions and soil density. The results of the physical models were found to be consistent and were cross-checked among ten centrifuge facilities worldwide, including eight tests produced at the facilities of Kyoto University.
- The achieved Dr is a key parameter in the model response, and, since small errors in the measurement of mass/volume lead to important deviations in the Dr estimation (when performed through mass and volume measurements), special attention shall be put to perform a proper estimation. It has been found that, although providing an indirect measurement, CPT test results allows a reliable estimation of the uniformity of the ground and its associated dry density.
- The achieved PGA is a key parameter in the model response. The achieved PGA was found to be highly sensitive to high-frequency components, which greatly vary from facility to facility. Since the response of the model is more sensitive to lower frequency components, PGA may not be the most suitable parameter to describe the shaking intensity; therefore, as a first attempt to better quantify the shaking intensity, PGA_{eff} was proposed.
- Hybrid MCMC-based Bayesian correlations were used to estimate the mean trends and associated variability of the response of the sloping sand deposit under a wide range of densities (Dr50% - Dr 85%) and peak accelerations (0.1g – 0.35g). These estimations characterize the outputs obtained in the Physical Models and are ready to be used in the development of current and future V&V processes of liquefaction models.

4 Element Tests

Aiming to further understand the dynamic behavior of Ottawa F-65 sand, efforts have been made to increase the database of laboratory tests in order to characterize the physical and mechanical properties of this sand [97] [121] [98] [122] [123].

In specific, Vasko [123] conducted a series of monotonic and cyclic triaxial tests for a certain relative density, Parra Bastidas [122] performed monotonic and cyclic simple shear tests for a diverse range of relative densities, El Ghoraiby et. al [98] have conducted cyclic triaxial shear tests for three different relative densities, and El Ghoraiby et. al [121] have conducted cyclic direct simple shear tests under two different overburden stresses (σ'v=40 kPa, and σ'v=100 kPa) for a certain relative density.

Although the mechanical characterization through triaxial testing, and simple shear testing has greatly contributed to the understanding of the dynamic behavior of Ottawa F-65 sand, the following issues prevent a comprehensive understanding of the dynamic properties:

- Triaxial tests, as pointed out by Ishihara et al. [124] [125], and shown in Figure 4-1, produces greater pore pressures on the side of extension than on the side of compression, producing asymmetric stress-strain curves (i.e. larger strains in the extension side than in the compression side) in dynamic testing.
- Simple shear tests allow the development of symmetric stress-strain responses, however, the initial stress conditions (i.e. initial K0 value), nor the stress conditions during loading, cannot be measured.

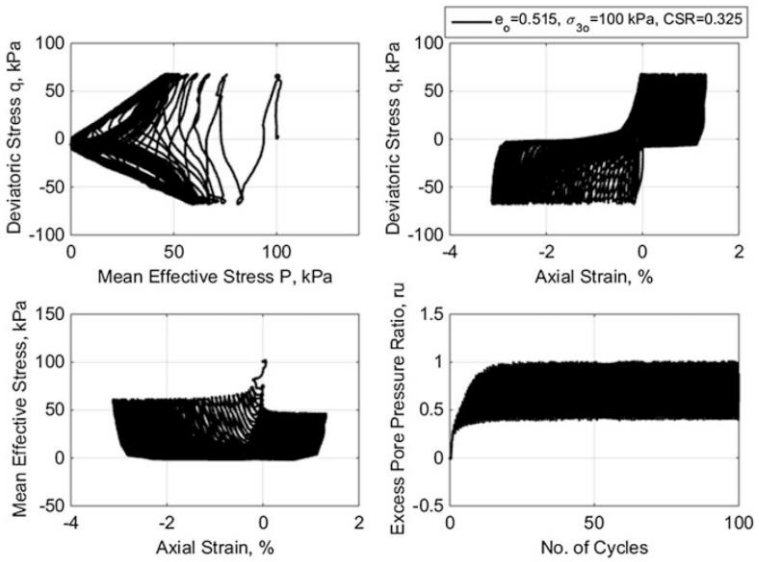

Figure 4-1 Triaxial cyclic testing results of Ottawa F-65 sand [98]

In order to provide a more complete understanding of the mechanical properties of Ottawa F-65 Sand, several challenges needed to be addressed, including the asymmetric stress-strain curves produced by the triaxial test apparatus and the inability to measure stress conditions during loading in simple shear tests. To overcome these challenges, a series of high-quality Hollow Cylinder Cyclic Torsional Shear Tests were conducted, which allows for the measurement of stress conditions at every step and produces a symmetric stress-strain response. The tests were conducted for four different relative densities (Dr=50%, 60%, 70%, and 85%) and under a wide range of Cyclic Stress Ratio (CSR) values.

4.1 Torsional Shear Apparatus

The torsional shear apparatus used during the testing is schematically shown in Figure 4-2. As shown in this figure, the apparatus allows the static and dynamic testing of a hollow cylindrical sample (inner diameter of 6 cm, an outer diameter of 10 cm, and a height of 10 cm) under a diverse range of stress paths.

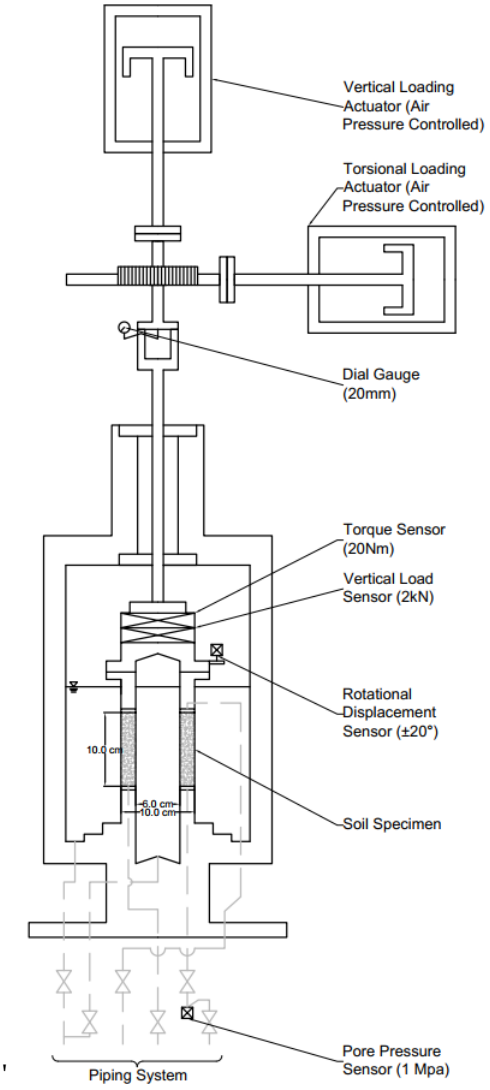

Figure 4-2 Torsional Shear Apparatus used in the tests

This apparatus (Figure 4-2) is capable of independently applying the vertical load and torque using pneumatic cylinders. To eliminate the effects of friction between the loading shaft and the bearing house, as suggested by Koseki et. al [126], the load cell used to measure the vertical load and torque was placed inside the pressure cell.

To ensure uniform normal stresses across the sample and to prevent different axial strains due to Poisson's effects, the same inner and outer pressures were applied at all steps during the tests (i.e. $\sigma'_r = \sigma'_\theta$). Also, volumetric strains were measured using a low-capacity differential pressure transducer that measures the water changes in a burette connected to the backpressure (which is kept constant at around 200 kPa) and the specimen. In addition, the rotational and axial deformations were measured by a potentiometer and a dial gauge respectively, allowing for comprehensive data collection during the tests.

Table 4-1 shows the measured variables and the characteristics of the sensors used for its measurement.

Table 4-1 Sensor List for Hollow-Cylinder Torsional Shear Tests

Variable	Type	Capacity	Manufacturer	Model
Torque Load (M_T)	Load Cell	20 N.m	Seishikou	KTU-20Ti
Vertical Load (W)	Load Cell	2 kN	Seishikou	KTU-20Ti
Angular Deformation (θ)	Potentiometer	±20°	Midori	CP-2UTX
Volumetric Deformation (ε_v)	Pressure Sensor	±3200 psi	Validyne	DP15-28
Pore Pressure (Δu)	Pressure Sensor	1 Mpa	TEAC	TP-BR
Vertical Strain(ε_a)	Dial Gauge	20 mm	Showa Sokki	TCL-20FA

As stated by Ishihara et al. [124], and Iddriss and Boulanger [27], for tests under anisotropic consolidation, the Cyclic Stress Ratio (CSR) can be defined as (1) the applied shear stress normalized by the mean effective stress ($\tau_{Z\theta}=\sigma'_{m0}$), or (2) the applied shear stress normalized by the vertical effective stress ($\tau_{Z\theta}=\sigma'_{Z0}$). In order to establish a comparison between the isotropically and anisotropically consolidated tests, in this manuscript, the $\tau_{Z\theta}=\sigma'_{m0}$ expression will be used as the definition of the CSR. It is important to mention that, for Cyclic Torsional Shear Tests, the mean effective stress (σ'_{m0}) is defined Eq. (4-1):

$$\sigma'_{m0} = \frac{\sigma'_{Z0} + \sigma'_{r0} + \sigma'_{\theta 0}}{3} \tag{4-1}$$

Where σ'_{Z0} is the initial vertical stress, σ'_{r0} is the initial radial stress, and $\sigma'_{\theta 0}$ is the initial tangential stress.

4.2 Cyclic Torsional Shear Tests and Model Preparation

Twenty-three Hollow Cylinder Cyclic Torsional Shear Tests were conducted to study the stress-strain behavior of Ottawa F-65 Sand under cyclic loadings [26], using the Torsional Shear Apparatus described in Section 4.1.

Sixteen tests were carried out under isotropic conditions under a wide range of relative densities (Dr = 50%, 60%, 70%, and 85%); additionally, seven tests were developed under initial anisotropic conditions (for densities Dr = 60%, and 70%), aiming to study the K0 effects. Table 4-2, and Table 4-3 show the nomenclature and characteristics of each test.

Table 4-2 Hollow Cylinder Cyclic Torsional Shear Tests under isotropic conditions

Specimen No.	Initial Dr (%)	Dr after consolidation (%)	Effective confining stress σ'_{m0} (kPa)	Shear stress $\tau_{z\theta}$ (kPa)	Shear stress ratio ($\tau_{z\theta}/\sigma'_{m0}$)
Dr50-1-1	48.2	50.4	103.0	10.2	0.099
Dr50-1-2	48.5	50.5	104.5	13.3	0.127
Dr50-1-3	48.6	50.6	103.0	15.3	0.149
Dr50-1-4	50.9	53.1	106.1	20.3	0.191
Dr60-1-1	58.7	60.7	103.0	12.1	0.117
Dr60-1-2	58.4	60.4	103.0	12.8	0.125
Dr60-1-3	59.1	61.0	105.0	15.1	0.144
Dr60-1-4	59.0	60.6	104.0	18.1	0.174
Dr60-1-5	61.6	63.6	104.0	20.6	0.199
Dr70-1-1	68.7	70.2	102.9	20.5	0.199
Dr70-1-2	70.8	71.9	106.0	26.2	0.247
Dr70-1-3	73.3	73.9	106.2	26.4	0.248
Dr70-1-4	69.2	70.7	104.1	28.3	0.272
Dr85-1-1	82.3	84.0	103.1	28.3	0.274
Dr85-1-2	81.4	82.9	103.2	30.6	0.296
Dr85-1-3	83.3	84.9	106.6	41.6	0.390

Table 4-3 Hollow Cylinder Cyclic Torsional Shear Tests under anisotropic conditions

Specimen No.	Initial Dr (%)	Dr after consolidation (%)	Ko	Initial vertical effective stress σ'_{z0} (kPa)	Initial radial effective stress σ'_{r0} (kPa)	Initial mean effective stress σ'_{m0} (kPa)	Shear stress $\tau_{z\theta}$ (kPa)	Shear stress ratio ($\tau_{z\theta}/\sigma'_{m0}$)
Dr50-2-1	48.3	50.3	0.5	152.7	75.7	101.4	16.4	0.162
Dr50-2-2	50	50.7	0.5	153.4	76.3	102.0	19.3	0.189
Dr50-2-3	49.1	51.2	0.51	155	78.4	103.9	23.3	0.224
Dr70-2-1	69.5	70.9	0.52	155.4	80.5	105.5	26	0.247
Dr70-2-2	69.5	71.1	0.51	152.1	78	102.7	28.5	0.278
Dr70-2-3	70.2	71.7	0.51	152.4	77.7	102.6	32.8	0.320
Dr70-2-4	71.5	73.6	0.5	151.5	76.2	101.3	36	0.355

Details of the sand properties are provided in Section 3.1.1.

Model Preparation – Mold Setting, and Air Pluviation

The specimens were prepared taking as a reference the Japanese Standards JGS-0550-2009 (“Practice for preparing hollow cylindrical specimens of soils for torsional shear tests”) [127], and JGS-0551-2009 (“Method for torsional shear test on hollow cylindrical specimens of soils”) [128].

Two concentric rubber membranes with diameters of 6 cm and 10 cm respectively were used to produce hollow cylinder specimens. Due to the characteristics of the sand in a dry state, a dedicated metallic mold was used during the fabrication of the specimen; also, to ensure the final shape of the model is defect-free (defects are frequently caused by air intrusions between the membrane and the mold), a small vacuum was applied between the mold and the outer membrane, ensuring that the membrane adopts the shape of the mold at all times during the preparation. Figure 4-3 shows the installed membranes and mold before the model preparation.

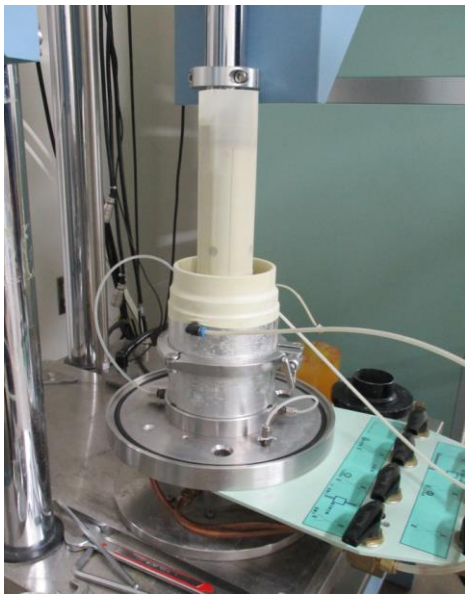

Figure 4-3 Setting of rubber membranes and mold prior model preparation

To obtain a fabric similar to the physical models, the samples were prepared through the "Air Pluviation" technique (see Figure 4-4). To guarantee the homogeneity of the sample and reduce the variability, the height of the pluviation tool was increased during the sample preparation, aiming to keep the dropping-height constant along with the sample.

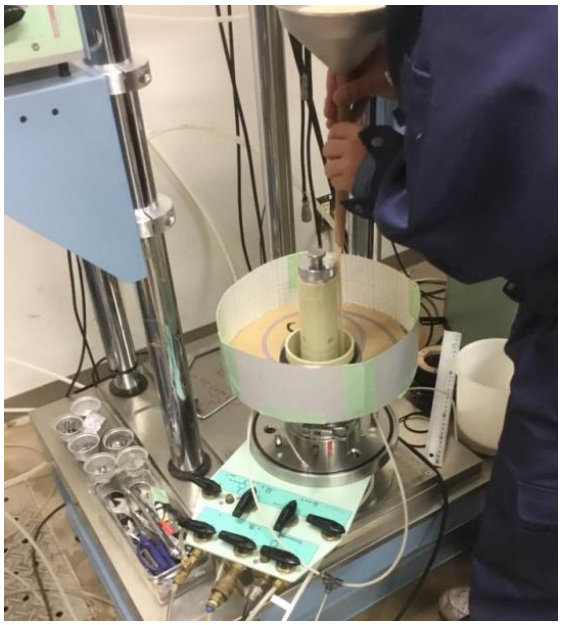

Figure 4-4 Air Pluviation – Hollow Cylinder model preparation

After the air pluviation process was complete, the top-cap was placed, and negative pressure (approximately -15kPa) was applied to the model (between the membranes) to maintain the shape of the sample while removing the molds and place the cell chamber. Figure 4-5 shows the sample after the placement of the top-

cap and the removal of molds. To reduce variability and ensure consistency among the experiments, precise measurements of the specimen dimensions and sand weight were taken after mold removal, as even small variations in weight or dimensions can significantly affect the estimated relative density.

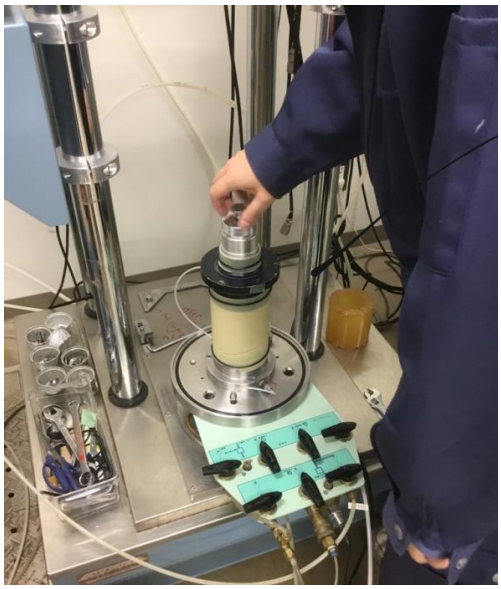

Figure 4-5 Hollow Cylinder model preparation – Removal of molds

Model Preparation – Saturation

After confirming the model's density, the outer chamber was carefully placed, and fixed to prevent any leakage, as shown in Figure 4-6.

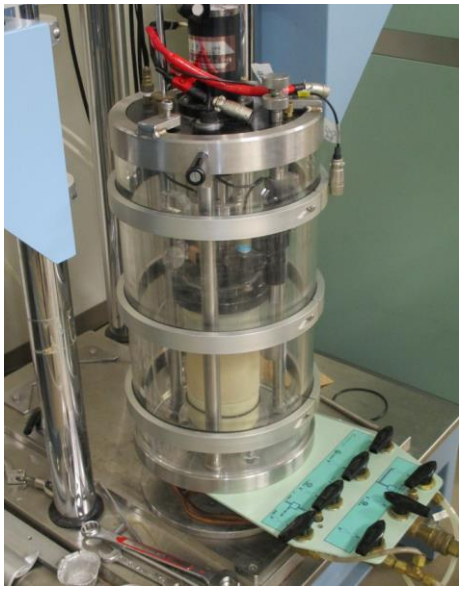

Figure 4-6 Outer chamber setting

After filling the outer and inner cells with water, an isotropic 20 kPa pre-consolidation was applied to both the inner and outer cell (to avoid deformations in the following steps), and the vacuum previously applied to the sample (to maintain its shape prior to molds removal) was released.

Following the pre-consolidation application, the saturation process began by flowing CO_2 through the sample for approximately 15 minutes to facilitate dissolution of gas bubbles trapped in the sand. Subsequently, degassed water was flowed through the sample until at least 1 liter of degassed water (approximately twice the volume of the sample) had passed through the sample. It is relevant to mention that the pressure and rate of CO_2, and degassed water flow shall be properly controlled (i.e. kept as minimum as possible) to avoid disturbing the sample.

After confirming that the required amount flowed through the sample, a back pressure of 200 kPa was applied (pressure applied to the sample, the outer chamber, and the inner chamber). The saturation level was then checked by measuring the Skempton's B value. It was verified that in every test, the B value was higher than 0.95 for an increment of 20 kPa under isotropic and undrained conditions.

Model Preparation – Consolidation, and Testing

Following the saturation process, the loading actuator (for vertical, and torsional loading) was carefully coupled to the upper cap, allowing the consolidation under a wide range of initial-stress conditions. Figure 4-7 shows the coupling process.

Figure 4-7 Loading actuator's coupling

Regarding the consolidation process, for the isotropically consolidated tests, the specimen was isotropically consolidated to a total pressure of approximately 300 kPa (i.e. 100 kPa of effective stress) under drained conditions. After the consolidation process, a stress-controlled cycling sinusoidal torque was applied to the sample in undrained conditions (Figure 4-8 shows the applied target wave). As specified in the Japanese

Standard JGS-0541-2009 [129], the load was applied until achieving at least 7.5% of double amplitude shear strain. Additionally, since the loads were applied using a stress-controlled mechanism, reliable information could not be obtained at very large strains.

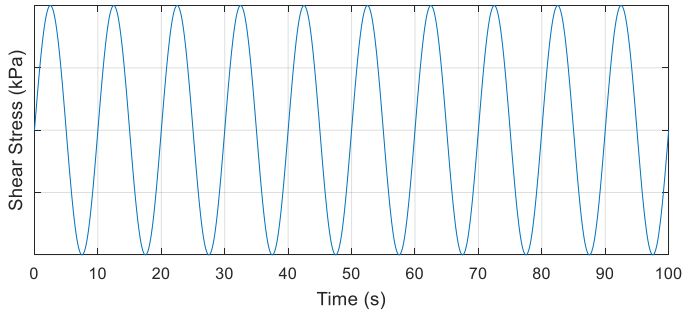

Figure 4-8 Cycling sinusoidal Shear Stress applied to the sample

As for the anisotropically consolidated tests, after measuring the B value, the specimen was consolidated under drained conditions, by applying small increments of the vertical, radial and tangential stresses, in order to keep anisotropic conditions during the consolidation process (i.e. $\Delta\sigma'_r = \Delta\sigma'_\theta = K_0\Delta\sigma'_Z$). The small increments were applied until achieving approximately $\sigma_{z0=}$350 kPa, and $\sigma_{r0}=\sigma_{\theta0}$=275 kPa (i.e. σ'_{Z0}=150 kPa, $\sigma'_{r0}=\sigma'_{\theta0}$=75 kPa, and σ'_{m0}=100 kPa). The loading process was similar as the one described for the isotropically consolidated tests; however, as pointed out by Ishihara et al. [124], and Sawada et al. [130], in order to reproduce a correct mode of deformation taking place in the field under seismic loading, the lateral deformations during the test should be restrained; this was achieved by restraining the vertical displacements by using a mechanical locking device, and monitoring that no volumetric strains were generated.

Additionally, as shown in Table 4-2 Table 4-3, densification between 1 and 2% was observed at the end of the consolidation process for both isotropically and anisotropically consolidated tests.

Also, to measure the induced volumetric strains triggered by liquefaction, a re-consolidation process (after the undrained cyclic testing) was developed until no changes in the pore water pressure nor volumetric changes were recorded.

4.3 Test Results

As mentioned in Section 4.1, twenty-three Hollow Cylinder Cyclic Torsional Shear Tests were conducted, and the stress-strain characteristics of each model were estimated based on the measured variables (see Table 4-1), and following the Japanese Standard JGS-0551-2009 (“Method for torsional shear test on hollow cylindrical specimens of soils”).

This section provides a summary of the experimental procedure and data processing methods used in the

tests. Detailed test results are provided in Appendix 2.

4.3.1 Isotropically consolidated tests

Figure 4-9a shows the Liquefaction Resistance Curve (LRC) of Ottawa F-65 sand for γ_{DA}=7.5%, estimated based on the isotropically consolidated tests. This LRC shows the number of cycles required to reach a 7.5% double amplitude shear strain.

Figure 4-9b shows the relation between the R_{L10}, R_{L20}, and R_{L30} values (i.e. the shear stress ratio that would induce γ_{DA}=7.5% in 10, 20, and 30 cycles) and the relative density (Dr), it can be noticed that they can be correlated by means of a second-order polynomial relationship.

Additionally, Ishihara [28] and Towhata [131] suggest that the CSR required to cause γ_{DA} = 7.5% under 20 load cycles (i.e. R_{L20}) is a useful factor to quantify the liquefaction resistance of a sand.

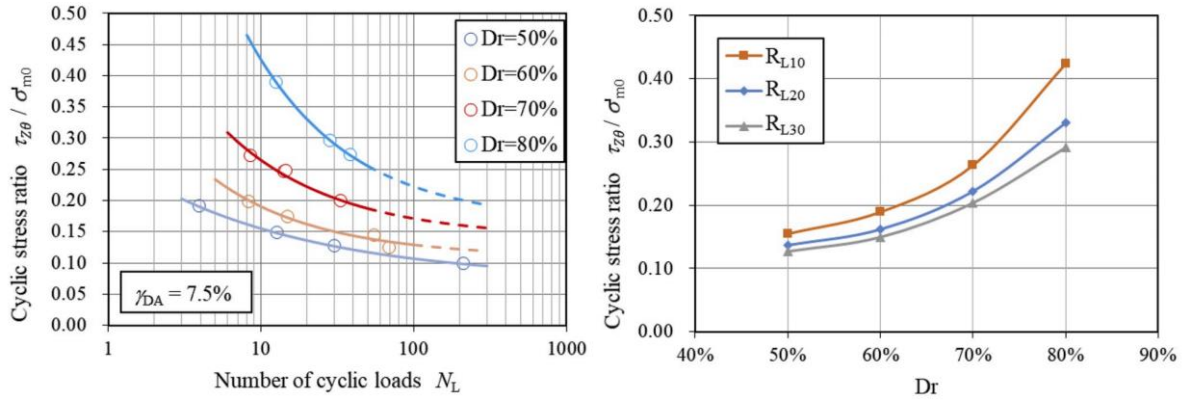

(a) (b)

Figure 4-9 (a) Liquefaction Resistance curve for Isotropically Consolidated Samples of Ottawa F-65 Sand for γ_{DA}=7.5% (b) Relationship between R_{L10}, R_{L20}, and R_{L30}; and Dr, for γ_{DA}=7.5%

The liquefaction resistance curves for γ_{DA}=3.0%, γ_{DA}=1.5%, and ru =0.95 are shown in Figure 4-10, Figure 4-11, and Figure 4-12, respectively. It has been found that, regardless of CSR and density, the development of ru =0.95 coincide with the γ_{DA}=3.0% condition (see Figure 4-10, and Figure 4-12).

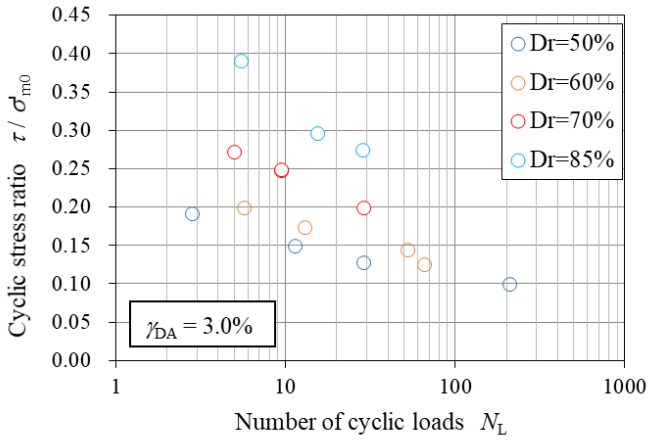

Figure 4-10 Liquefaction Resistance curve for Isotropically Consolidated Samples of Ottawa F-65 Sand for γ_{DA}=3.0%

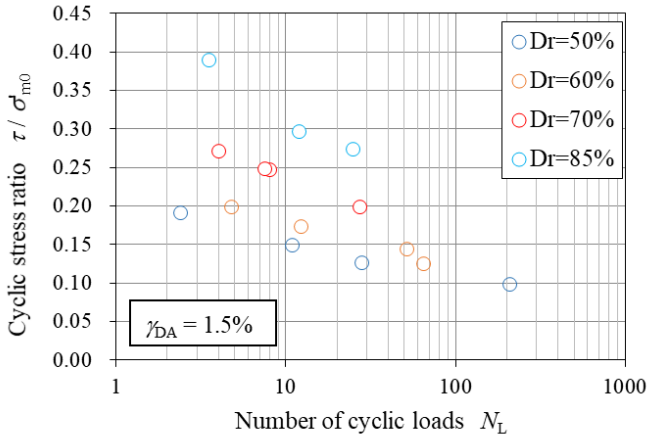

Figure 4-11 Liquefaction Resistance curve for Isotropically Consolidated Samples of Ottawa F-65 Sand for γ_{DA}=1.5%

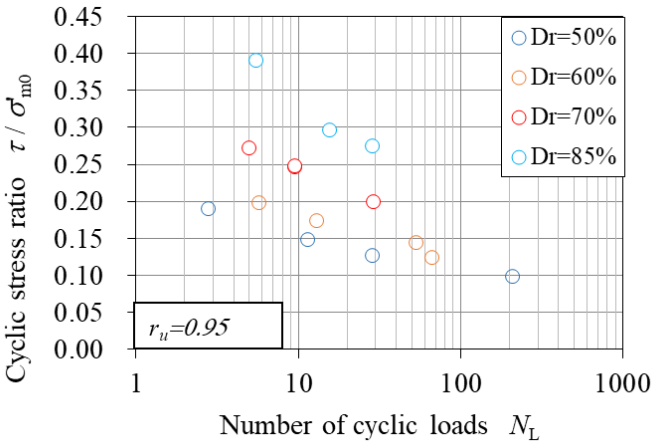

Figure 4-12 Liquefaction Resistance curve for Isotropically Consolidated Samples of Ottawa F-65 Sand for r_u=0.95

Figure 4-13 shows that the friction angle ϕ_f remained constant for all relative densities ($\phi_f \approx 35$ °). On the other hand, the phase transformation angle ϕ_p increased with the relative density, ranging from 20.2° to 25.0° for relative densities between 50% and 85%.

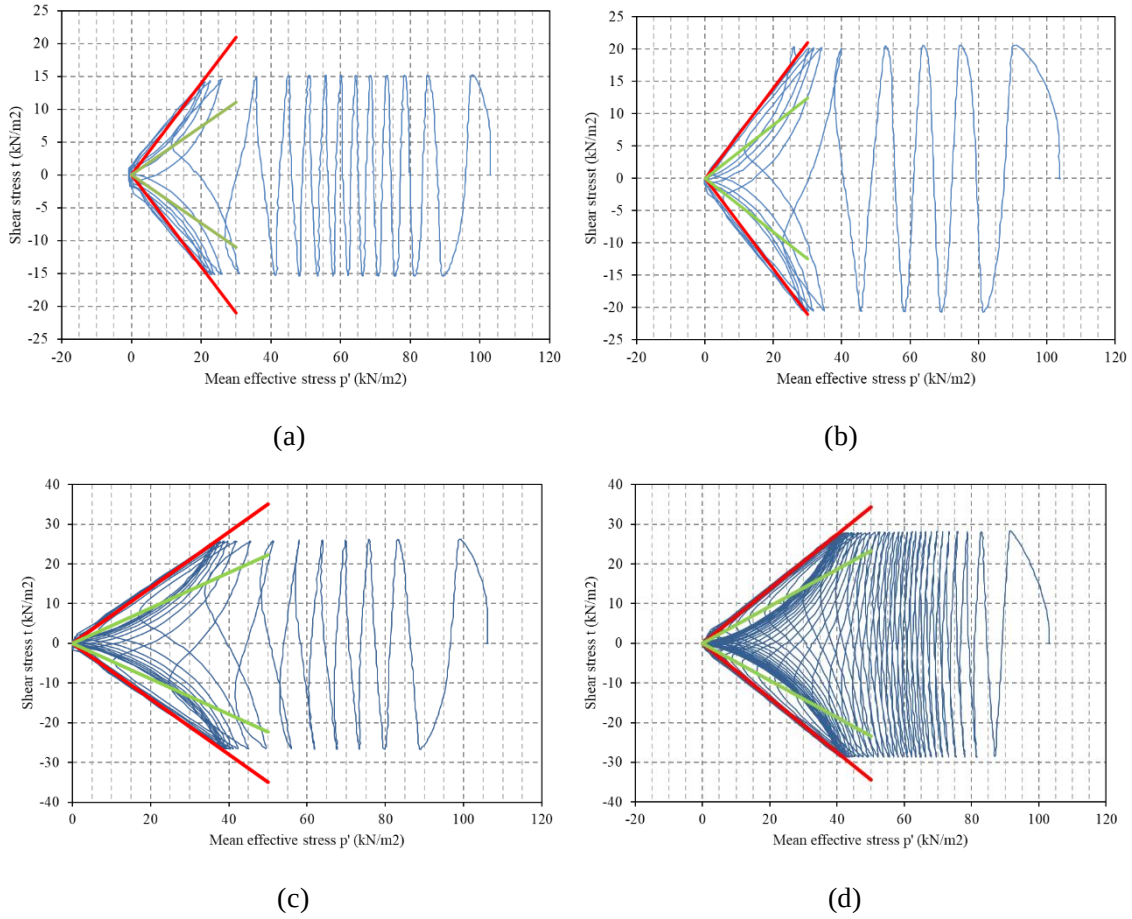

Figure 4-13 (a) Stress path for Model Dr50-1-3 (b) Stress path for Model Dr60-1-5 (c) Stress path for Model Dr70-1-3 (d) Stress path for Model Dr85-1-2

To examine the effect of the relative density on the behavior of Ottawa F-65 Sand, samples Dr50-1-3 (τ/σ'_{m0} = 0.15) and Dr85-1-2 (τ/σ'_{m0} = 0.30) were selected. As shown in Figure 4-12, although significant different CSR values are achieved, both samples require a similar number of cycles (around 15 cycles) to develop ru=0.95.

Figure 4-14(a,b) and Figure 4-15(a,b) show the time history of ru development and the stress path respectively. In Sample Dr50-1-3, the ru value reached unity only after half cycle after reaching a 0.95, while in Sample Dr85-1-2, the ru value required more than 6 cycles to increase from 0.95 to 1. This observation, along with the rate of strain generation (Figure 4-14(c) and Figure 4-15(c)), is consistent with the fact that the state parameter (ξ) increases with higher Dr values [132].

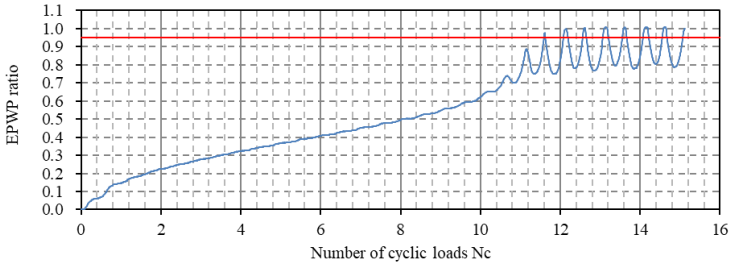

(a)

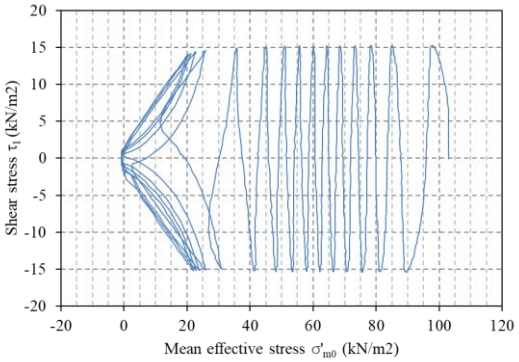

(b)

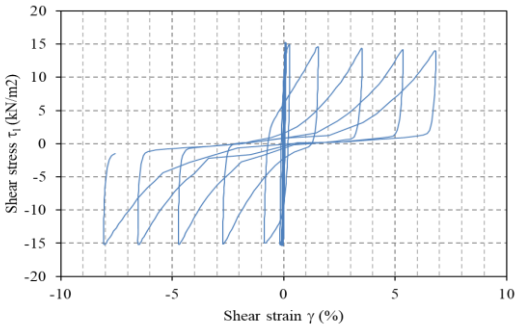

(c)

Figure 4-14 (a) Time History of EPWP ratio development - Model Dr50-1-3 (b) Stress path - Model Dr50-1-3 (c) Stress-Strain response - Model Dr50-1-3

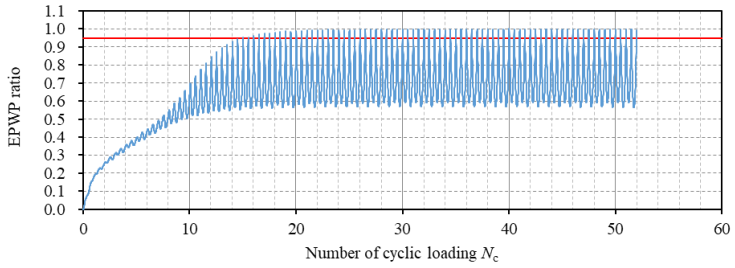

(a)

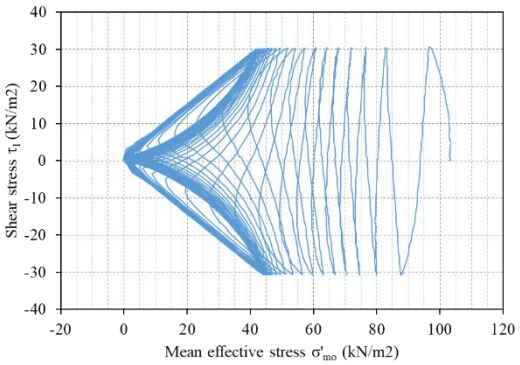

(b)

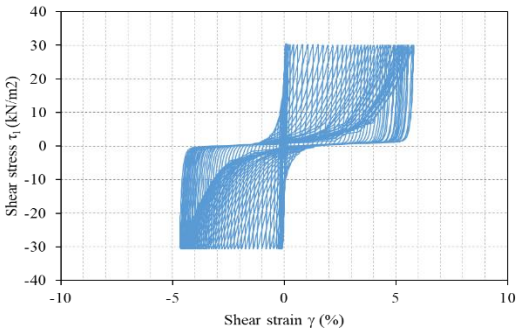

(c)

Figure 4-15 (a) Time History of EPWP ratio development - Model Dr85-1-2 (b) Stress path - Model Dr85-1-2 (c) Stress-Strain response - Model Dr85-1-2

4.3.2 Anisotropically consolidated tests

Figure 4-16, Figure 4-17, Figure 4-18, and Figure 4-19 shows the liquefaction resistance curve for Anisotropically Consolidated Samples of Ottawa F-65 sand (K0=0.50) for γ_{DA}=7.5%, γ_{DA}=3.0%, γ_{DA}=1.5%, and ru=0.95 respectively. In a similar way, as found in the isotropically consolidated tests, a clear trend and consistency among the tests were found.

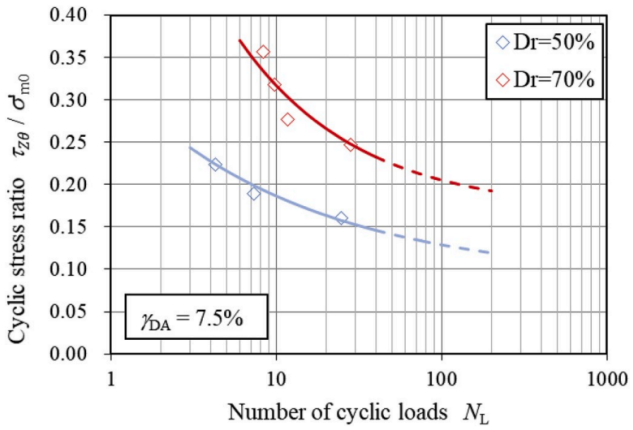

Figure 4-16 Liquefaction Resistance curve for Anisotropically Consolidated Samples (K0 =0.50) of Ottawa F-65 Sand for γ_{DA} = 7.5%

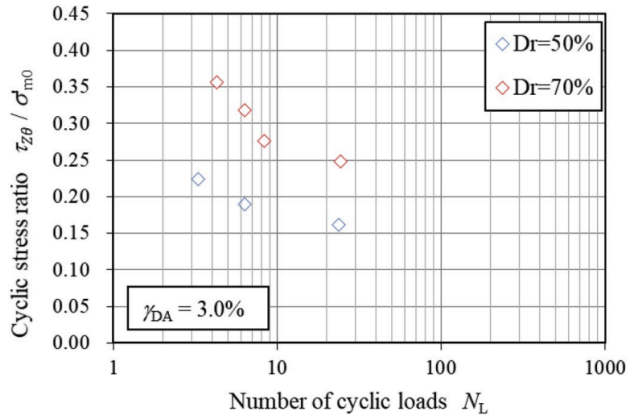

Figure 4-17 Liquefaction Resistance curve for Anisotropically Consolidated Samples (K0 =0.50) of Ottawa F-65 Sand for γ_{DA} = 3.0%

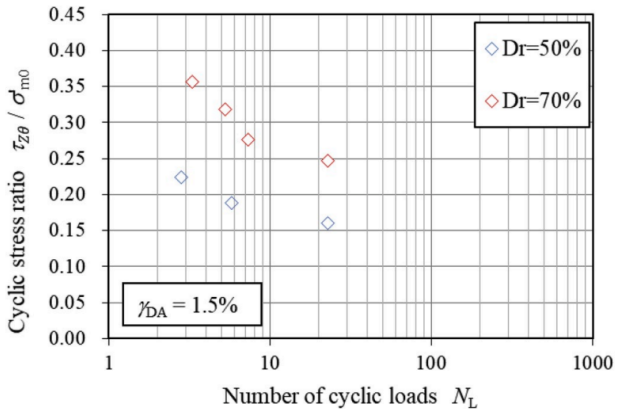

Figure 4-18 Liquefaction Resistance curve for Anisotropically Consolidated Samples (K0 =0.50) of Ottawa F-65 Sand for γ_{DA} = 1.5%

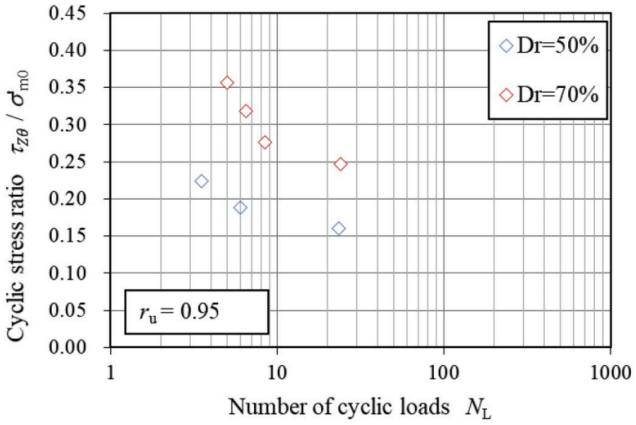

Figure 4-19 Liquefaction Resistance curve for Anisotropically Consolidated Samples (K0 =0.50) of Ottawa F-65 Sand for ru = 0.95

As in the case of the isotropically consolidated tests, it was found that, in all of the anisotropically consolidated cases (K0=0.50), the development of ru=0.95 coincide with the γ_{DA}=3.0% condition irrespective of the CSR and the density (see Figure 4-17, and Figure 4-19).

Figure 4-20 and Figure 4-21 show the time history of ru development, the stress path, and the stress-strain history of samples Dr50-2-2 ($\tau_{Z\theta}/ \sigma'_{m0}$ = 0.19) and Dr70-2-3 ($\tau_{Z\theta}/\sigma'_{m0}$ = 0.32) respectively. Similar to the isotropically consolidated samples, these two elements were selected because, despite the difference in the CSR, both samples require a similar number of cycles (around six cycles) to develop ru = 0.95. Similar behavior was found (regarding further generation of EPWP and strain rates), as described for the isotropically consolidated tests.

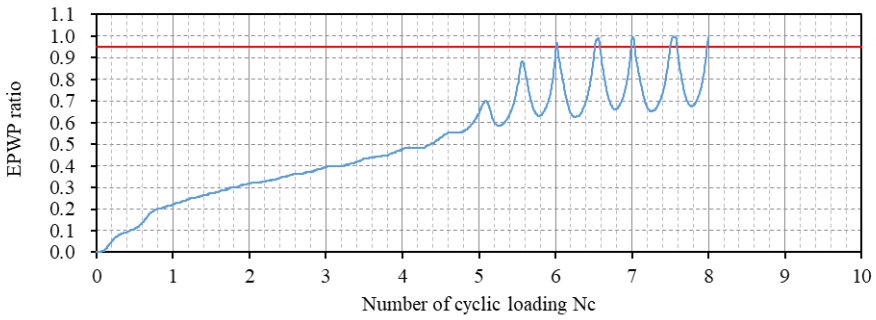

(a)

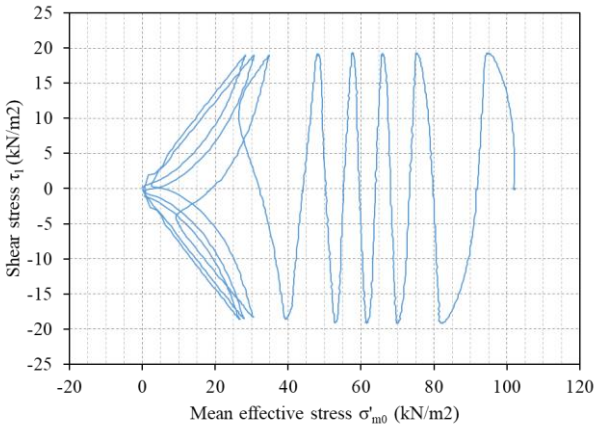

(b)

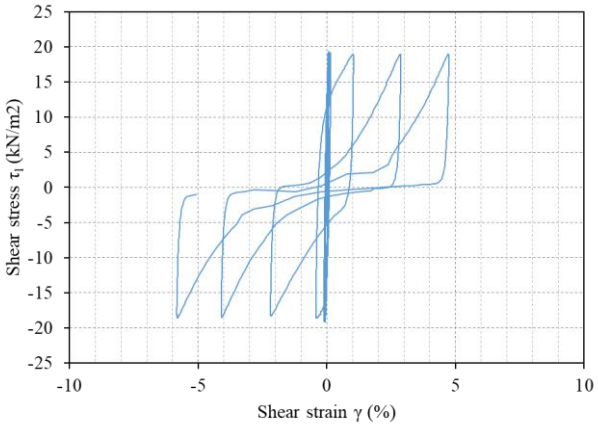

(c)

Figure 4-20 (a) Time History of EPWP ratio development - Model Dr50-2-2 (b) Stress path - Model Dr50-2-2 (c) Stress-Strain response - Model Dr50-2-2

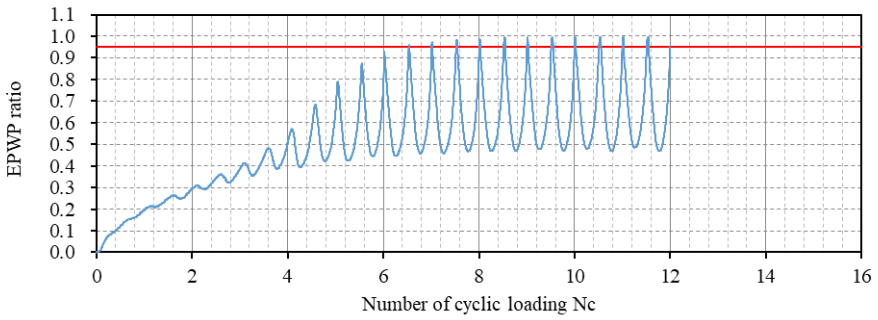

(a)

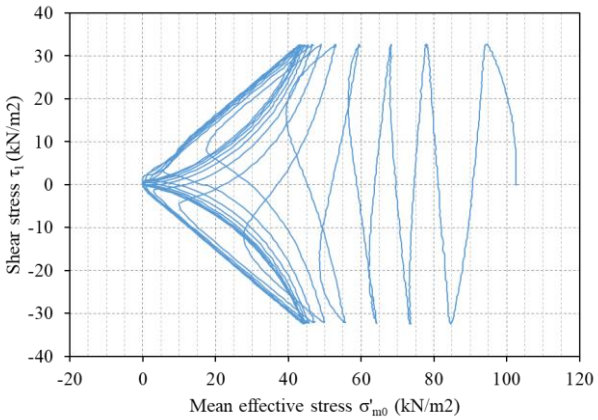

(b)

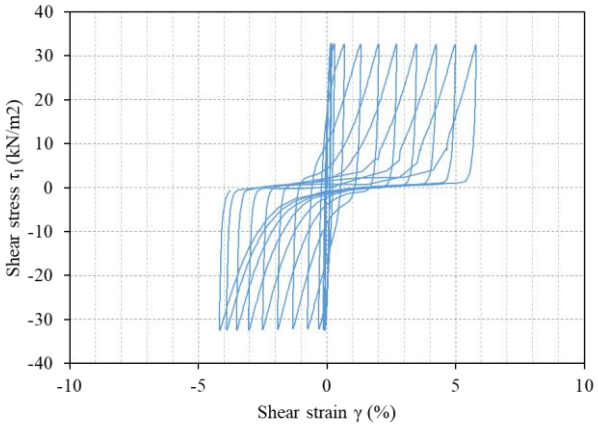

(c)

Figure 4-21 (a) Time History of EPWP ratio development - Model Dr70-2-3 (b) Stress path - Model Dr70-2-3 (c) Stress-Strain response - Model Dr70-2-3

As pointed out in Section 4.1, to reproduce a correct mode of deformation taking place in the field under seismic loading, the generation of vertical strains were not allowed on the tested samples during the cyclic process; this caused a successive reduction of the applied axial load (see Figure 4-22a). Since the radial effective stress (and hence the tangential effective stress) decreased at a slower rate than the vertical effective stress (see Figure 4-22b), a progressive increment of the anisotropic ratio (σ'_Z/σ'_r), from K0 = 0.50 in the initial state until achieving a nearly isotropic state after reaching liquefaction, was observed.

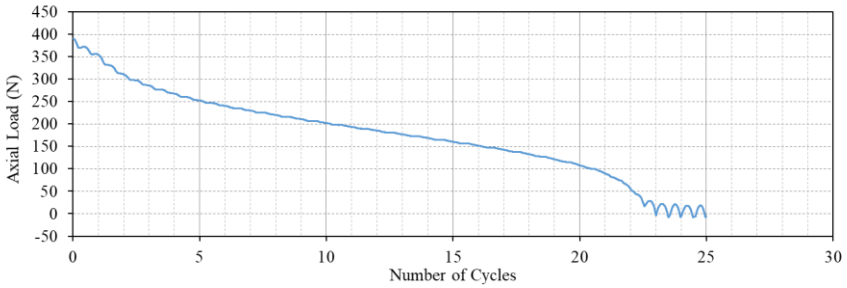

(a)

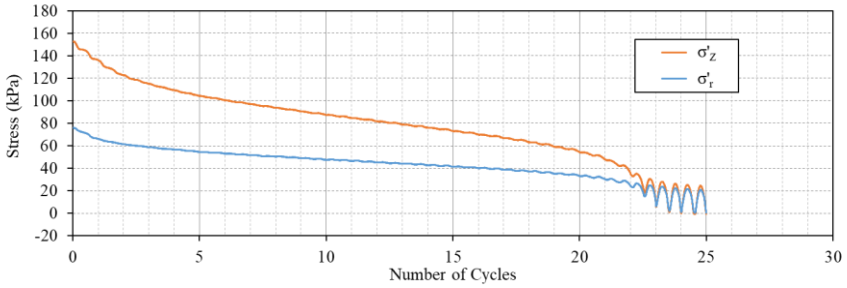

(b)

Figure 4-22 (a) Time History of the applied Axial Load - Model Dr50-2-1 (b) Time History of the Effective Vertical and Radial stresses (σ'_z and σ'_r respectively) - Model Dr50-2-1

As reported by Ishihara et al. [133], the transition from the K0 value (prior shaking) to isotropic states (after reaching liquefaction) can be encountered during earthquakes in level-ground saturated soil deposits.

4.3.3 Comparison between isotropically consolidated tests and anisotropically consolidated tests

Figure 4-23a shows a comparison between the liquefaction resistance curves (γ_{DA}=7.5%) of the isotropically consolidated tests (Dr = 50% and Dr = 70%), and the corresponding anisotropically consolidated tests. The results show that the liquefaction resistance of the anisotropically consolidated tests is approximately 20% higher than the tests developed under isotropic consolidation, regardless of the density and the strain level (it was also confirmed for γ_{DA}=1.5 - 7:5%).

Figure 4-23b shows that the liquefaction resistance curve of the anisotropically consolidated tests can be brought in line with the isotropically consolidated tests by multiplying the CSR values of the former by a factor of 1/1.2. It is worth noting that, as seen in Figure 4-24, a similar behavior was found in the experiments performed by the Public Works Research Institute of Japan [134], which were performed using Dr=60% samples of Toyoura Sand under σ'_{m0} = 100kPa.

Although valuable experimental information was obtained, further efforts are needed to understand these observations, and explore the effect of other key factors (such as different K0 values, initial fabric, different σ'_{m0} values, etc.) that may allow to comprehensively understand the mechanism behind the increase in the liquefaction resistance exhibited by the anisotropically consolidated clean sands.

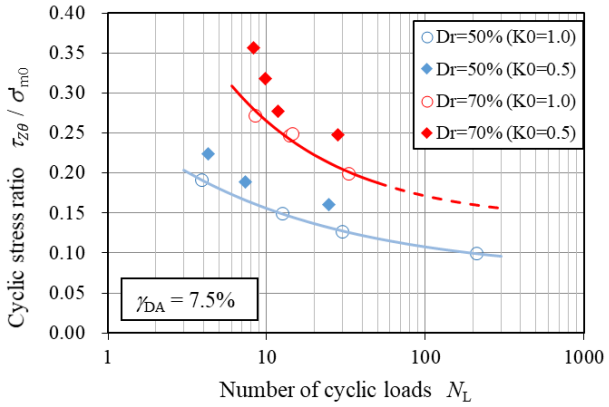

(a)

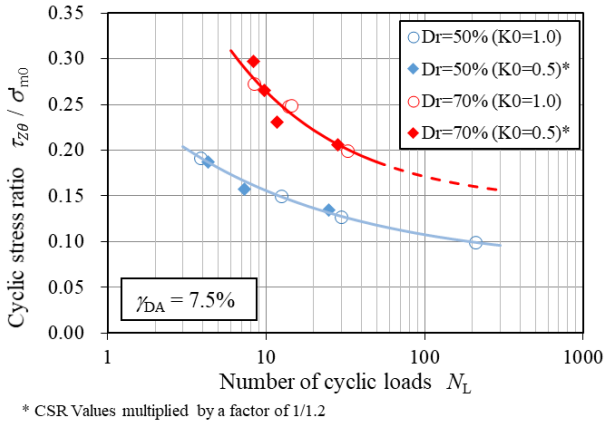

(b)

Figure 4-23 (a) Comparison of the Liquefaction Resistance curves for Isotropically and Anisotropically Consolidated Samples of Ottawa F-65 Sand for γ_{DA}=7.5% (b) Comparison of the Liquefaction Resistance curves for Isotropically and Anisotropically Consolidated Samples (CSR values multiplied by 1/1.2) of Ottawa F-65 Sand for γ_{DA}=7.5%

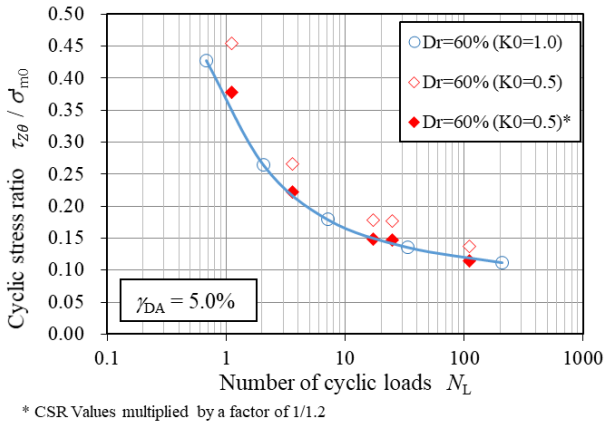

Figure 4-24 Comparison of the Liquefaction Resistance curves for Isotropically and Anisotropically Consolidated Samples of Toyoura Sand for γDA=5.0% [134]

4.3.4 Volumetric strain due to post-cyclic reconsolidation

To measure the induced volumetric strains triggered by liquefaction, after applying the cyclic loading, a re-consolidation process was developed by opening the drainage line of the test sample in order to dissipate the developed residual pore water pressure, and the volumetric changes were recorded until no changes in the pore water pressure were recorded. The same procedure was used by Ishihara et al. [135], and Sento et al. [136] to develop simplified procedures to estimate liquefaction-induced settlements. Figure 4-25a shows the correlation between the volumetric strain due to post-cyclic reconsolidation (ε_v) and the maximum single-amplitude shear strain during undrained loading (γ_{max}), proposed by Ishihara et al. [135]; despite the scatter observed in the data, a good agreement was obtained for Dr > 60%. On the other hand, Sento et al. [136] proposed a correlation between ε_v and the cumulative shear strain during undrained loading ($\gamma_{acm} = \int_0^t |\dot{\gamma}(t)| dt$); as seen in Figure 4-25, a good agreement was found as well between the experimental data and the proposed correlation for Dr >60% (by considering a=0.32Dr + 30.5; and b = 0:50. “a” and “b” correspond to internal variables in the correlation [136]).

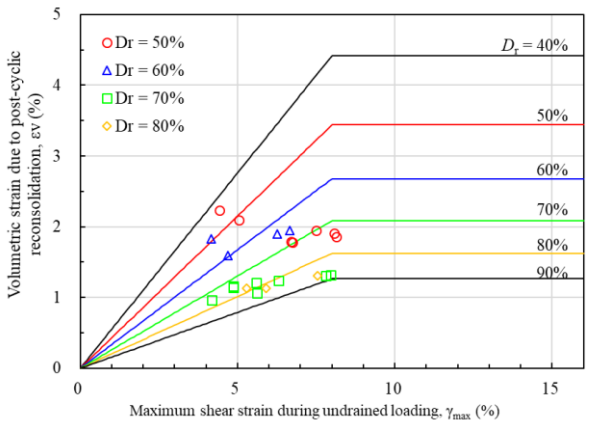

(a)

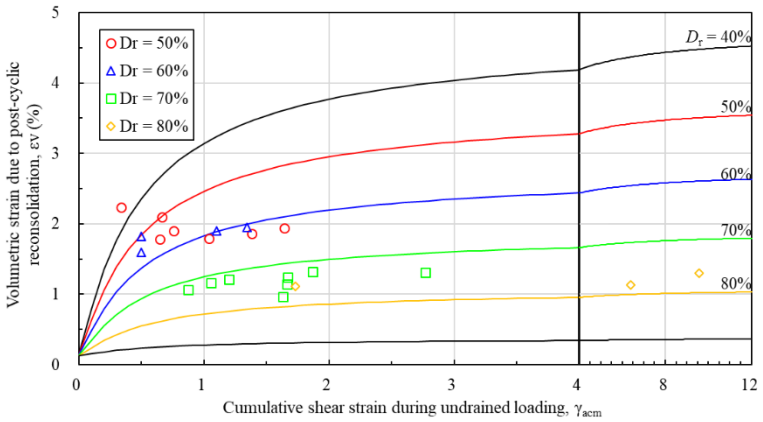

(b)

Figure 4-25 (a) Comparison of the volumetric strain due to post-cyclic reconsolidation with the correlations proposed by Ishihara et. al [135](b) Comparison of the volumetric strain due to post-cyclic reconsolidation with the correlations proposed by Sento et. al [136]

4.4 Repeatability of test results

To ensure the consistency and reliability of the test results, a repeatability test was performed using the same testing conditions as the specimen Dr70-1-2. The specimen Dr70-1-3 was prepared and tested as the repeatability test specimen.

Figure 4-26 shows a comparison between the repeatability test and the original test in terms of the development of Excess Pore Water Pressure ratio (EPWP ratio), the development of Shear Strain, and the corresponding Stress Path. The results demonstrate good agreement between the two tests, indicating that the tests are repeatable and consistent with each other.

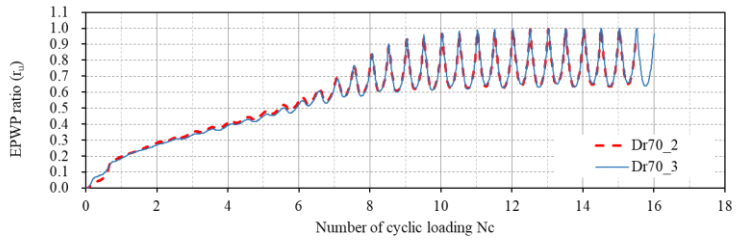

(a)

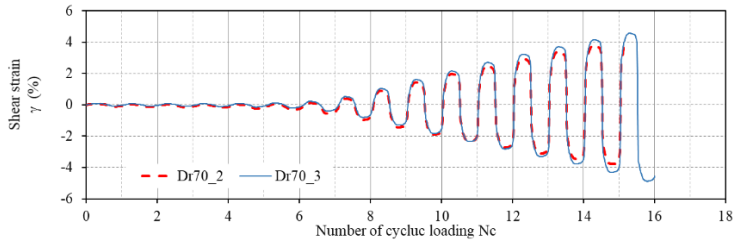

(b)

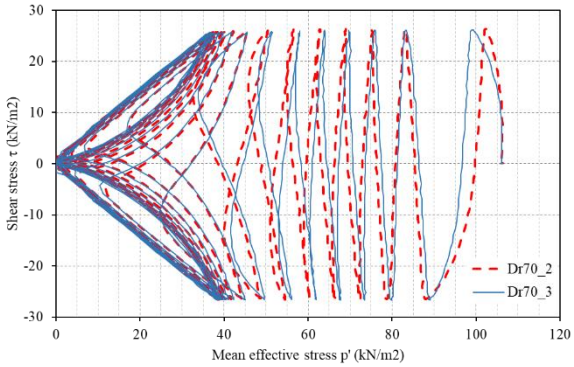

(c)

Figure 4-26 (a) Development of EPWP – Models Dr70-1-2 and Dr70-1-3 (b) Development of Shear Strain – Models Dr70-1-2 and Dr70-1-3 (c) Stress path – Models Dr70-1-2 and Dr70-1-3

4.5 Mean Response and Variability of Element Tests

This section presents the estimation of the main trends and associated variability of the element test results (i.e., estimation of the element test`s outputs), focusing on the estimation of the Liquefaction Resistance Curve (LRC), and the identification of the key parameters that mainly define its behavior and variability.

As mentioned in Section 1.4, an evaluation of the experimental variation is essential, particularly when a high level of skill and experience is required to conduct the experiments, such as the cyclic undrained torsional shear tests. Hence, in order to estimate the median trend and the associated variability of the torsional test results (i.e., liquefaction strength curves), a Bayesian estimation with a hybrid MCMC was developed, using a similar approach as in Section 3.5 (uncertainty quantification of the physical models).

In this study, the PDF of the liquefaction strength ratio was assumed to adhere to a normal distribution, as follows:

$$f\left(\mathbf{x}\,|\,\mu_{R_L},\sigma_{R_L}\right)=\prod_{i=1}^{n}\frac{1}{\sqrt{2\pi}\sigma_{R_L}}\exp\left[-\frac{\left(x_i-\mu_{R_L}\right)^2}{2\sigma_{R_L}^2}\right] \tag{4-2}$$

where μ_{R_L} and σ_{R_L} are the mean and standard deviations of the normal distribution, respectively. As for the shape of the mean value, μ_{R_L}, it was modeled according to Tatsuoka et al [137].

$$\mu_{R_L}=R_{L20}\left(\frac{N_c}{20}\right)^{b_1\frac{D_r}{100}+b_0} \tag{4-3}$$

where R_{L20} and N_c represent the liquefaction strength at 20 cycles and the number of cyclic loads, respectively.

As shown in Figure 4-9b, since it was found that R_{L20} and Dr are correlated by means of a second-order polynomial relationship, R_{L20} is given by Eq. (4-4).

$$R_{L20}=a_2\left(\frac{D_r}{100}\right)^2+a_1\frac{D_r}{100}+a_0 \tag{4-4}$$

Parameters a_i (i = 0, 1, and 2) and b_i (i = 0 and 1) are the parameters to be estimated.

Given that there was no prior knowledge of either the model input parameters or the model uncertainty

variable, σ_{R_L} the following uniform distributions were adopted as the non-informative prior distributions [113]:

$$f\left(a_i\right) \propto 1, \quad -\infty < a_i < +\infty \quad \left(i = 0,1,2\right) \tag{4-5}$$

$$f\left(b_i\right) \propto 1, \quad -\infty < b_i < +\infty \quad \left(i = 0,1\right) \tag{4-6}$$

$$f\left(\sigma_{R_L}\right) \propto 1, \quad 0 < \sigma_{R_L} < +\infty \tag{4-7}$$

Substituting these prior distributions and the laboratory test data into Eq. (4-2), the posterior PDF of all the uncertain parameters can be given as:

$$\begin{aligned} & f\left(\mu_{R_L}, \sigma_{R_L} \mid \mathbf{x}\right) = f\left(a_0, a_1, a_2, b_0, b_1, \sigma_{R_L} \mid \mathbf{x}\right) \\ & = kf\left(a_0\right) f\left(a_1\right) f\left(a_2\right) f\left(b_0\right) f\left(b_1\right) f\left(\sigma_{R_L}\right) \prod_{i=1}^{n} f\left(x_i \mid a_0, a_1, a_2, b_0, b_1, \sigma_{R_L}\right) \end{aligned} \tag{4-8}$$

where k is a normalization constant that makes the integration of the posterior PDF equal to unity.

As in Section 3.5, the posterior samples were collected by a hybrid MCMC simulation. Figure 4-27, and Figure 4-28 illustrate the medium trend and the associated variability of the liquefaction resistance curve (LRC), as a function of the relative density (Dr), obtained from the hybrid MCMC-based Bayesian estimation.

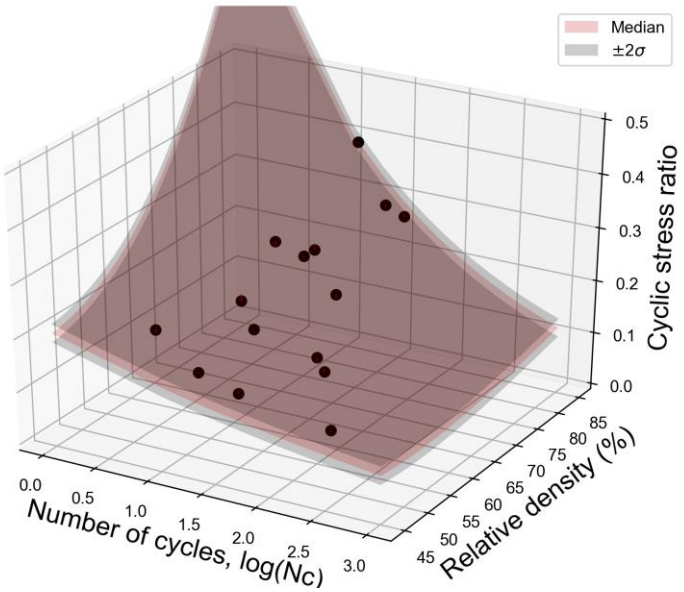

Figure 4-27 Correlation among liquefaction strength, number of cycles (Nc), and relative density (Dr) based on MCMC-based Bayesian modeling

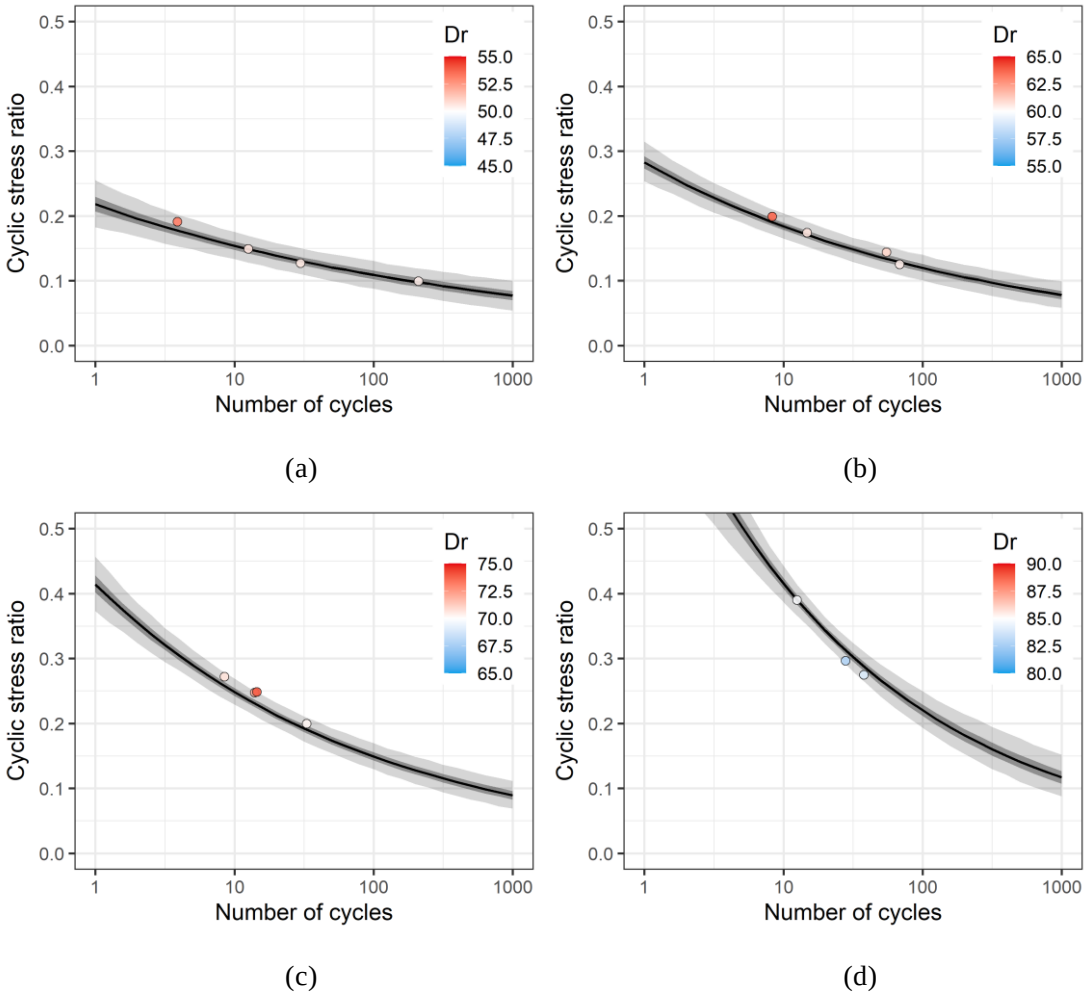

Figure 4-28 Mean trend and associated variability of LRCs estimated by MCMC-based Bayesian modeling (dark and light gray colors represent 50% and 95% intervals, respectively)

4.6 Section Conclusions

This section describes the element tests conducted to study the mechanical properties of Ottawa F-65 Sand, required to calibrate the numerical model in the validation process. The tests included a series of high-quality Hollow Cylinder Cyclic Torsional Shear Tests, focusing on the influence of the relative density and the K0 effects. The characteristics of preparation, test development, and the experimental findings have been presented. It was found that the results can be used as a reliable database to calibrate the numerical model in this, and future validation processes.

- Sixteen isotropically consolidated tests were conducted to investigate the stress-strain characteristics of Ottawa F-65 Sand under four different densities and a wide range of shear stress ratios. These tests were complemented by seven anisotropically consolidated tests (K_0= 0.50) to study the K0 effect.
- It was found that the RL_{20} values and the relative density (Dr), can be correlated by means of a second-order polynomial relationship.

- To replicate a correct mode of deformation taking place in the field under seismic loading, the lateral deformations, during an anisotropically consolidated test, were restrained; this process caused a successive reduction of the vertical stress and an increase of the anisotropic ratio ($\sigma'_Z=\sigma'_r$) value from $K_0=0.50$ in the initial state, until achieving a nearly isotropic state after reaching liquefaction.
- It was found that the liquefaction resistance of the anisotropically consolidated tests ($K_0=0.5$) is approximately 20% higher than the tests developed under isotropic consolidation, irrespective of the initial density and the strain level (for γ_{DA} = 1:5 - 7:5 %).
- The experimental results for the volumetric strain due to post-cyclic reconsolidation (ε_v), were in good agreement with the correlations proposed by Ishihara et al. [135] and Sento et al. [136], for Dr>60%.
- The good agreement in the repeatability tests demonstrated that the tests are consistent and repeatable.
- Hybrid MCMC-based Bayesian correlations were used to estimate the mean trends and associated variability of the dynamic behavior of Ottawa F-65 sand. These estimations characterize the outcomes obtained in the Element Tests and are ready to be used in the development of current and future V&V processes of liquefaction models.

5 Numerical Modeling

As stated in Section 1.3, the primary objective of this manuscript is to introduce a comprehensive probabilistic validation methodology for numerical models used in the prediction of the liquefaction phenomena, through its implementation on an actual validation exercise that explores the capabilities of the "Strain Space Multiple Mechanism Model" [16] to simulate the lateral spreading phenomenon. A detailed description of the governing equations, finite element formulation, and the model formulation has been included in Appendix 3.

This section provides a description of the numerical simulations for element tests and the physical models, including the mean trend and associated variability.

5.1 Simulations of Element Tests

The simulations of the element tests were conducting using the "Strain Space Multiple Mechanism Model", which was implemented in the commercial finite element program "FLIP ROSE". It is important to mention that the original version of the model was proposed by Iai et.al [138] in 1992 as a strain-space model for cyclic mobility, and later updated in 2011 [16] to incorporate a new stress-dilatancy relationship. A complete description of the model has been included in Appendix 3.

5.1.1 Model Parameters

For a plane-strain application of the model, and by assuming an isotropic texture of the material, the strain space multiple mechanism model has 17 primary parameters for the analysis of liquefaction; among them, five specify the volumetric mechanism, three specify the shear mechanism, and nine controls the dilatancy.

Table 5-1 shows a summary and a brief description of the model parameters.

Table 5-1 Model Parameters [16]

Symbol	Mechanism	Parameter Designation
ρ_t	Volumetric	Mass density
p_a	Volumetric	Reference confining pressure
$K_{L/Ua}$	Volumetric	Bulk modulus
r_K	Volumetric	Reduction factor of bulk modulus for liquefaction analysis
l_K	Volumetric	Power index of bulk modulus for liquefaction analysis
G_{ma}	Shear	Shear modulus
ϕ_f^{PS}	Shear	Internal friction angle for plane strain

Symbol	Mechanism	Parameter Designation
h_{max}	Shear	Upper bound for hysteretic damping factor
ϕ_p	Dilatancy	Phase transformation angle
ε_d^{cm}	Dilatancy	Limit of contractive component
$r_{\varepsilon_d^c}$	Dilatancy	Parameter controlling contractive component
r_{ε_d}	Dilatancy	Parameter controlling dilative and contractive components
q_1	Dilatancy	Parameter controlling initial phase of contractive component
q_2	Dilatancy	Parameter controlling final phase of contractive component
S_1	Dilatancy	Small positive number to avoid zero confining pressure
c_1	Dilatancy	Parameter controlling elastic range for contractive component
q_{us}	Dilatancy	Undrained shear strength (for steady state analysis)

5.1.2 Estimation of Model Parameters for Mean Trend

Although a comprehensive simulation of the element tests constitutes a complex 3-D problem, if the analysis is focused on the "average" behavior of a small central portion of the element, the test can be simulated as an element under cyclic simple shear stress and 2-D plane-strain conditions.

The numerical implementation of the element tests was performed under the following conditions.

- A single element with four nodes, modeled under 2D plane-strain conditions.
- The vertical displacements of all nodes are restricted. The horizontal displacements of 2 nodes are restricted, while the horizontal displacements of 2 nodes are left unrestricted (aiming to simulate a cyclic simple shear stress).
- The following analysis are implemented.
    - A consolidation analysis is initially carried out to replicate the consolidation process of the sample (refer to Section 4.2). This analysis is conducted in static-conditions, and solved using Eq. (A3-76) and (A3-77).
    - A dynamic analysis, aiming to replicate the cyclic-simple shear process. Following the testing conditions, this analysis was conducted in undrained conditions, and the simulation results are obtained by using the Wilson's θ method (solving Eq. (A3-110)).

To estimate the model parameters for the mean trend of the four densities under study, an iterative procedure

was employed, based on a parametric study. The goal was to replicate the stress-strain behavior of the tests and the mean trend of the LRCs obtained through the hybrid MCMC Bayesian simulation (refer to Figure 4-27 and Figure 4-28). The analysis focused on the interval defined by N=10~100 cycles, in which most of the element tests were conducted. The estimated parameters for each density are presented in Table 5-2.

Figure 5-1 shows a comparison between the mean LRCs estimated by the hybrid MCMC analysis, and the LRCs computed by means of the numerical model of the element tests. Additionally, Figure 5-2, Figure 5-3, and Figure 5-4 provide detailed comparisons of the element test simulations and the hollow cylinder torsional shear tests for Dr=70%, including the records of the time-history of the shear strain development, the time history of the EPWP ratio development, the stress-strain response, and the stress path.

Table 5-2 Estimated Model Parameters

Parameter	Units	Case			
		Dr 50%	**Dr 60%**	**Dr 70%**	**Dr 85%**
ρ_t	t/m3	2.01	2.025	2.04	2.06
p_a	kPa	100	100	100	100
$K_{L/Ua}$	kPa	209270	241912	328000	440700
r_K	-	0.75	0.65	0.5	0.4
l_K	-	2	2	2	2
G_{ma}	kPa	75976	90717	123000	165263
ϕ_f^{PS}	°	38	40.3	41.5	42.8
h_{max}	-	0.24	0.24	0.24	0.24
ϕ_p	°	20.2	22.6	24	25
ε_d^{cm}	-	0.85	0.85	0.85	0.85
$r_{\varepsilon_d^c}$	-	7.5	4.1	2.5	1.33
r_{ε_d}	-	0.15	0.3	0.18	0.1
q_1	-	4.6	5.5	7	9
q_2	-	1.2	1.2	1.25	1.55
S_1	-	0.005	0.005	0.005	0.005
c_1	-	1.49	1.59	2	2.47
q_{us}	-	Large value	Large value	Large value	Large value

It is worth noting that Ottawa F-65 sand is a clean sand, and therefore, the undrained shear strength q_{us} for the steady state was set to a very large value. Moreover, the permeability of the ground was estimated based on the tests developed by El Ghoraiby et al. [121] (refer to Section 3.1.1) on Ottawa F-65 sand. In that study the permeability values obtained were: $k_x=k_y=0.0207e_0^{-0.0009}$ cm/s, where e_0 is the initial void ratio.

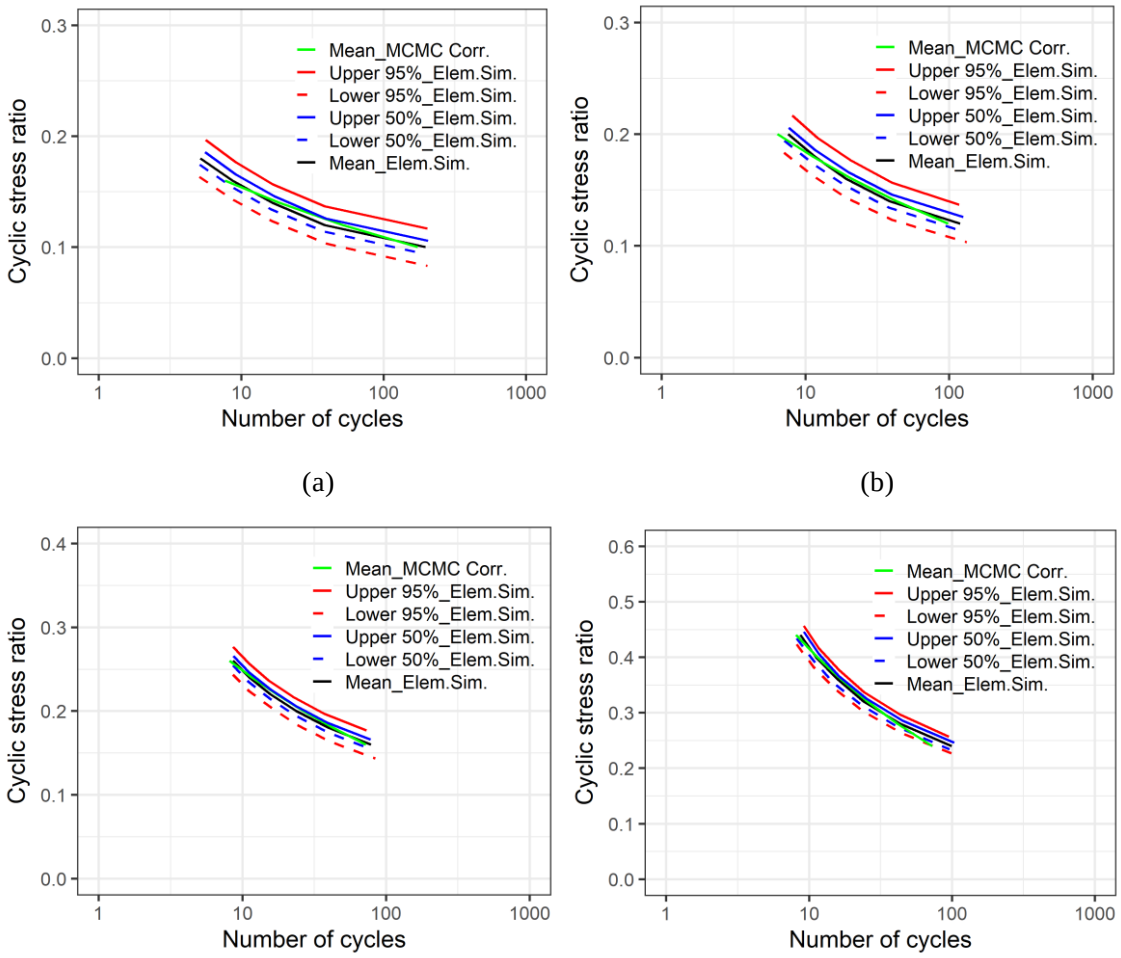

Figure 5-1 Simulated LRCs - Comparison between median trend of hybrid MCMC analysis (i.e., target value) and upper/lower (2.5%) boundaries for 95% and 50% probability: (a) Dr=50%, (b) Dr=60%, (c) Dr=70%, and (d) Dr=85%

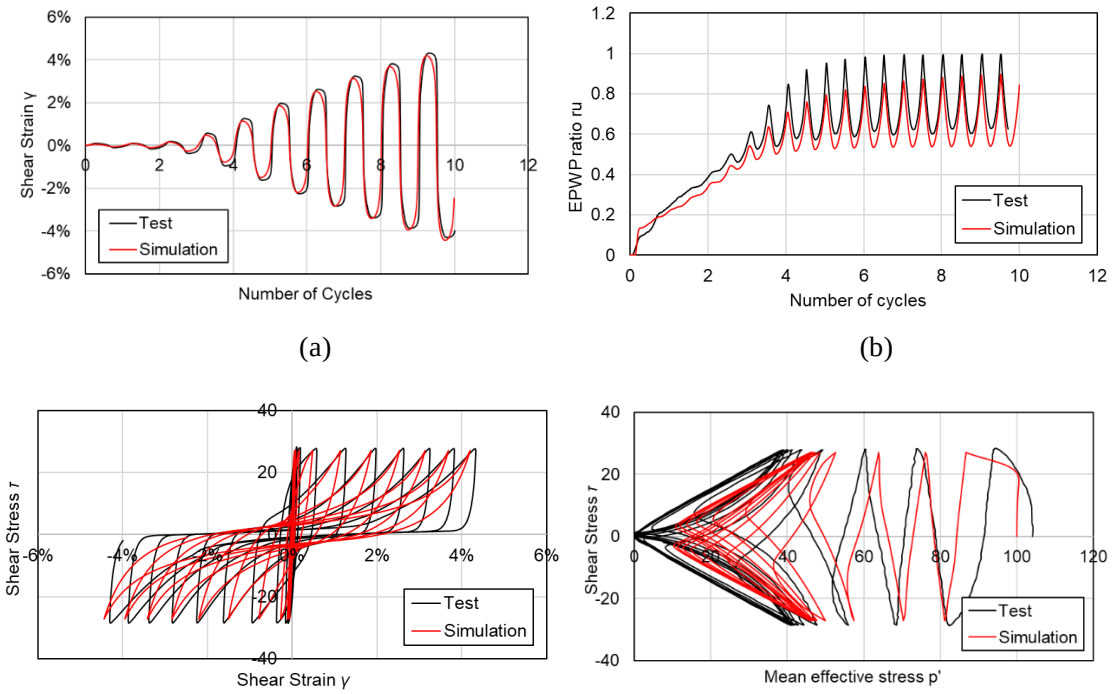

Figure 5-2 Numerical simulation of element tests with Dr=70% and CSR=0.272: (a) Time history of shear strain development, (b) Time history of EPWP ratio development, (c) Stress-strain response, and (d) Stress path

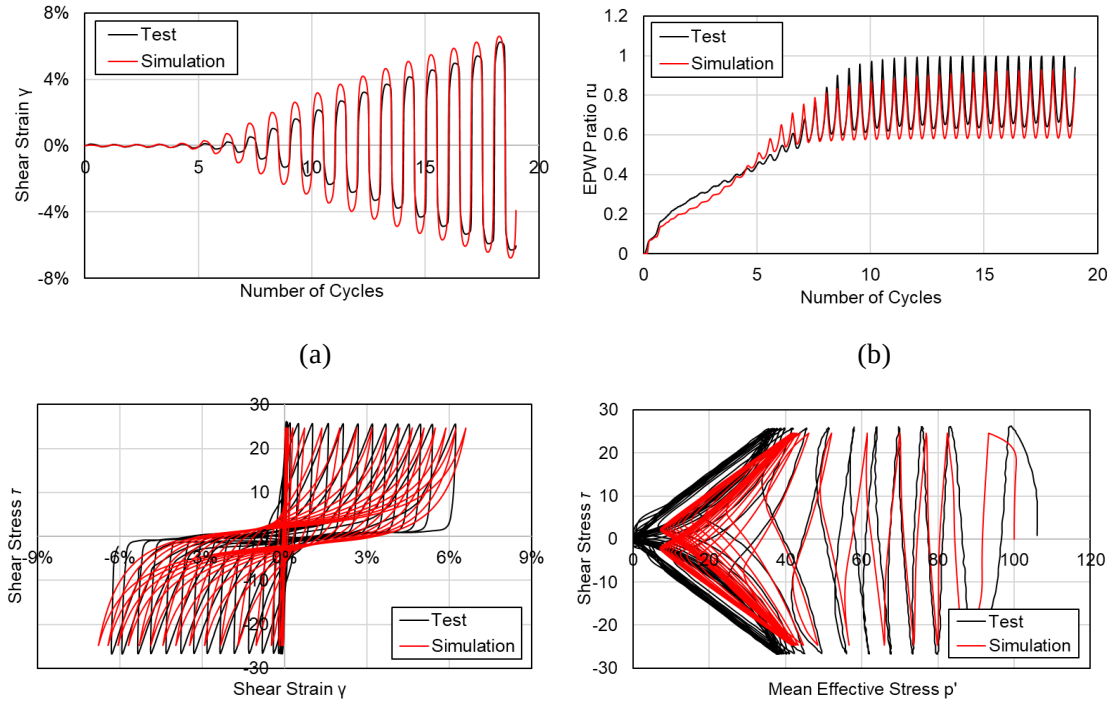

Figure 5-3 Numerical simulation of element tests with Dr=70% and CSR=0.247: (a) Time history of shear strain development, (b) Time history of EPWP ratio development, (c) Stress-strain response, and (d) Stress path

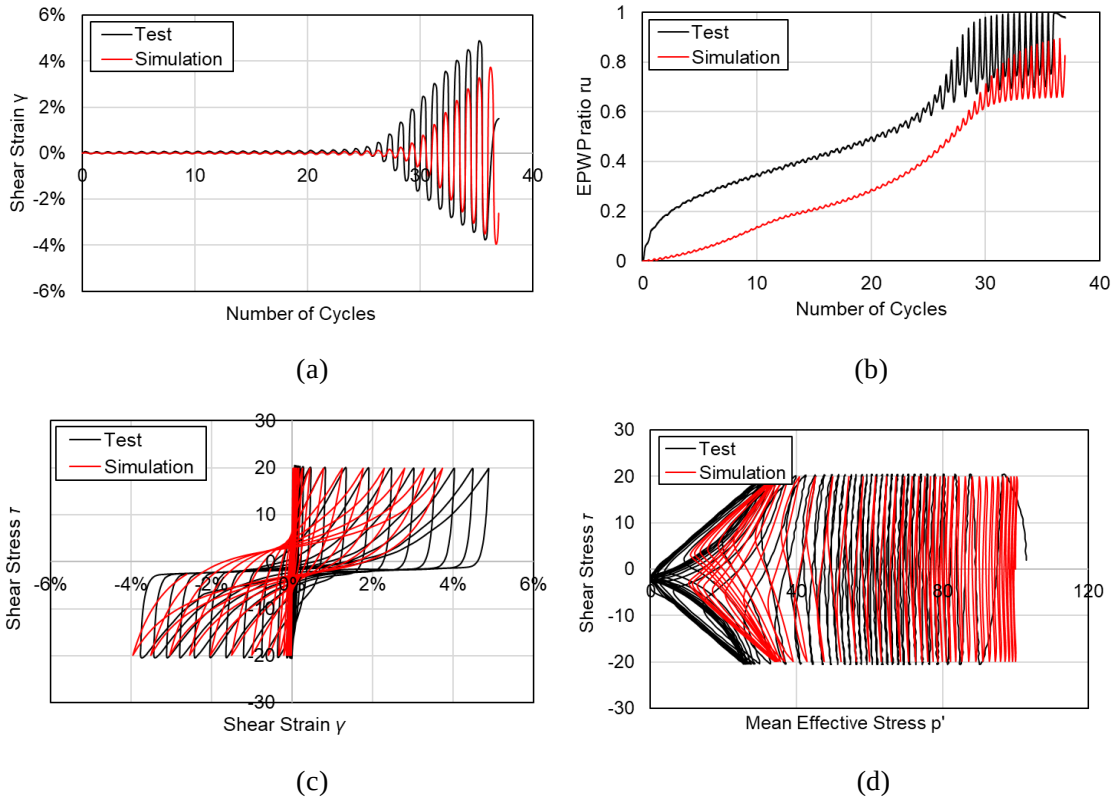

Figure 5-4 Numerical simulation of element tests with Dr=70% and CSR=0.199: (a) Time history of shear strain development, (b) Time history of EPWP ratio development, (c) Stress-strain response, and (d) Stress path

5.1.3 Input uncertainty in numerical modeling

According to the ASME's standard [2], [17], uncertainties enter into computational simulations from a variety of sources, such as variability in the input parameters, lack of or insufficient information pertaining to model inputs, and modeling assumptions and approaches. By recognizing the existence of the variability, and taking into account that parts of the variability are inherent or irreducible, the approach is to assess the effects of this variability on the results of the simulation and the performance of the system.

A well-known approach (and also suggested ASME's standard) for quantifying the model uncertainty involves treating model parameters as random variables, estimating their uncertainty, and propagating it through the model. This approach is reasonable and effective for cases in which the model parameters can be independently estimated and the correlation between them can be established. However, in the case of effective-stress liquefaction models (such as the “Strain Space Multiple Mechanism Model”) , the current state of the art in liquefaction modeling and soil element testing does not allow for independent estimations of all parameters due to the large number of required parameters, regardless of whether or not each model parameter has a physical interpretation.

As mentioned previously in Section 5.1.2, the actual estimation of the parameters is usually performed in an iterative fashion, aiming to simulate the LRCs and the stress-strain behavior (based on the element tests).

This methodology of parameter estimation implies that more than one combination of parameters can be obtained for a specific LRC (i.e., more than one set of parameters can simulate similar LRCs).

During the numerical simulation process, it has been observed that similar stress/strain responses are achieved with different sets of parameters, leading to almost identical simulated LRCs. This suggests that the results of the numerical modeling for lateral spreading mainly depend on the simulated LRCs rather than on a specific set of parameters (this is valid for the specific conditions of the exercise only, and it is strongly recommended that its validity shall be analyzed in a case-by-case basis). Moreover, several well-established constitutive models capable of simulating liquefaction (Iai et al. [16], Elgamal et al. [53], Ling and Yang [54], Manzari and Dafalias [55], Cubrinovski and Ishihara [56], Taiebat [57], Oka et al. [58]), define different sets of parameters, but share a common practical methodology for estimating the model parameters, based on a comparison of the measured and simulated LRCs.

Therefore, this study expresses the model input variability as variations in the simulated LRCs, rather than individual parameter variations. Following this, the upper and lower boundaries of the 50% and 95% probability (as shown in Figure 4-27, and Figure 4-28) are used to define the range of variability in the LRCs.

Since it is challenging to exactly reproduce specific LRCs in the element simulation, this study focuses on reproducing the range between the upper and lower boundaries (ΔCSR, obtained in the hybrid MCMC analysis) in the target interval (i.e., N=10～100 cycles). In other words, the ΔCSR that defines the upper and lower boundaries for 95% and 50% in the target interval is used to define the upper and lower boundaries for 95% and 50% in the simulated LRCs.

Figure 5-1 shows the median trend and the associated variability (95% and 50% probability boundaries) of the simulated LRCs by means of element tests, compared with the mean trend of the hybrid MCMC analysis. As shown in this figure, a good agreement was found between the simulated LRCs and the results of the hybrid MCMC analysis.

It is important to mention that, since the centrifuge experiments were developed under laboratory conditions with precise/calibrated instruments, sources of uncertainty such as variability in the boundary conditions (rigid boundaries were used in all experiments), uncertainty in the input wave (the same shape of the input wave was used in all experiments), etc., were not considered in this study.

Furthermore, Appendix 1 and ElGhoraiby et al. [139] suggest that only slight differences in the soil response are expected when studying a fairly “homogeneous” ground. Therefore, given that both the element tests and the centrifuge tests were prepared using the air-pluviation technique (keeping the height constant), it is assumed that the effects of spatial variability are negligible.

5.2 Simulations of the Physical Models

As previously mentiones, the simulations of the physical models were conducted using the commercial finite element software, "FLIP ROSE" (in which the "Strain Space Multiple Mechanism Model" is implemented). Based on the characteristics of the models, the analysis was carried out under 2-D plane-strain conditions, aiming to simulate the models in prototype scale.

The mesh and boundary conditions used in the analysis are shown in Figure 5-5 . The mesh consisted of 384 4-node quadrilateral elements, including the pore water elements. The size of the mesh was defined following the recommendations of Alford et al. [140].

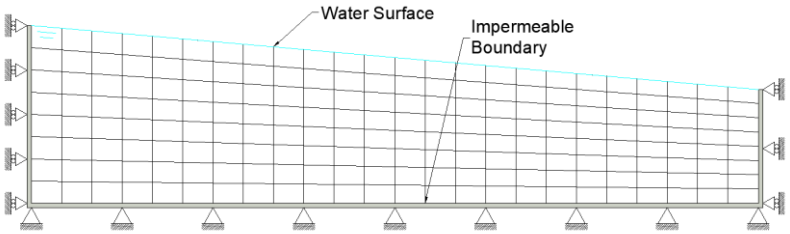

Figure 5-5 FEM Mesh and Boundary Conditions for Numerical Analysis

To replicate the boundary condition of the experiments (rigid boxes were used in all the experiments), horizontal and vertical displacements were fixed at the base boundary, meanwhile only vertical displacements were allowed at the lateral boundaries. In addition, the lateral and base boundaries were set to be impermeable, and the pore water pressure at the ground surface was specified to represent a hydrostatic condition.

The following analysis are implemented.

- Initially, a self-weight analysis was performed to obtain the initial stress distribution before shaking. This analysis is conducted in static-conditions, and solved using Eq. (A3-76) and (A3-77).
- Subsequently, a dynamic response analysis was conducted for 130 s, considering pore water flow migration (during and after the shaking). Therefore, as indicated in Appendix 3, the SSpj method was used for numerical time integration (i.e., solving Eq. (A3-135) and (A3-136)), with a time step of Δt=0.002 s. To ensure the stability of the calculation process, Rayleigh damping (α=0.0, β=0.00032) was used as suggested by Ueda et. al [19].

The results of the simulations are presented in Section 6.1, along with the comparisons with the Physical Model results.

5.3 Section Conclusions

This section presents in detail the numerical modeling process used in the validation process, including: (1) a description of the target Numerical Model and its numerical implementation, (2) a detailed description of the element test simulations, and the methodology for model parameter estimation, (3) a proposal of a novel alternative to define the input uncertainty, and (4) details of the numerical modeling and the propagation of the model uncertainty.

- For numerical models that simulate liquefaction phenomena, it has been found that expressing the input variability of in terms of the Liquefaction Resistance Curve's variability is a more effective and efficient method than expressing it in terms of individual parameter changes.
- A numerical model was built to reproduce the centrifuge tests developed for LEAP-UCD-2017 and LEAP-ASIA-2019. The validity of the numerical model is ready to be assessed by comparing the simulation outcomes against the centrifuge testing outcomes (both in terms of mean value and associated variability).

6 Numerical Model Assessment

As described in Section 1.4.6, the validation exercise concludes with a quantitative comparison of the outcomes obtained by the Physical Modeling (see Section 3) and the Numerical Modeling (Section 5), and a verification of whether the requirements (validation metrics) have been satisfied or not.

In this section, a comparison between the Physical Models outcomes (refer to Section 3.5), and the corresponding Numerical Model outcomes is presented in Section 6.1, and the verification of the validation requirements (including a discussion of the Validation Metrics) is included in Section 6.2. Additionally, the importance of repeatability in physical modeling and type B simulations are presented in Section 6.3; finally, a brief discussion on the influence of the fluid's viscosity on the centrifuge modeling and its numerical simulations are presented in section 6.4 [114].

6.1 Quantitative Comparison between Physical Model Outputs, and Numerical Model Outputs

In Section 3.5, it has been shown that for the lateral spreading phenomenon (studied in the framework of LEAP), the residual surface displacements are primarily a function of the PGA_{eff} and the Dr (obtained from the CPT Tests at the mid-depth of the model). Based on this, Physical Model Outputs（ground response), including the median trend and its associated variability, was estimated by means of a Hybrid MCMC-based Bayesian correlation, as shown in Figure 3-42. This correlation was developed using a Large Centrifuge-Models Database that included forty-eight models from LEAP, covering a wide range of Dr and PGA_{eff} values.

By using the model introduced in Section 5.2, and based on the parameters estimated on Section 5.1 (mean values, and 95% and 50% probability boundaries), the Numerical Models Outputs were calculated/estimated aiming to replicate the combinations of Dr-PGA_{eff} for which the correlation was developed (i.e. 50% <Dr< 85%, and 0.1g < PGA_{eff} < 0.35g).

Figure 6-1, Figure 6-2, Figure 6-3, and Figure 6-4 show comparisons between the between Physical Model Outputs, and Numerical Model Outputs for Dr= 50%, 60%, 70%, and 85%, respectively. It is important to mention that the figures include comparisons between the mean values and the upper/lower boundaries for a 95% probability.

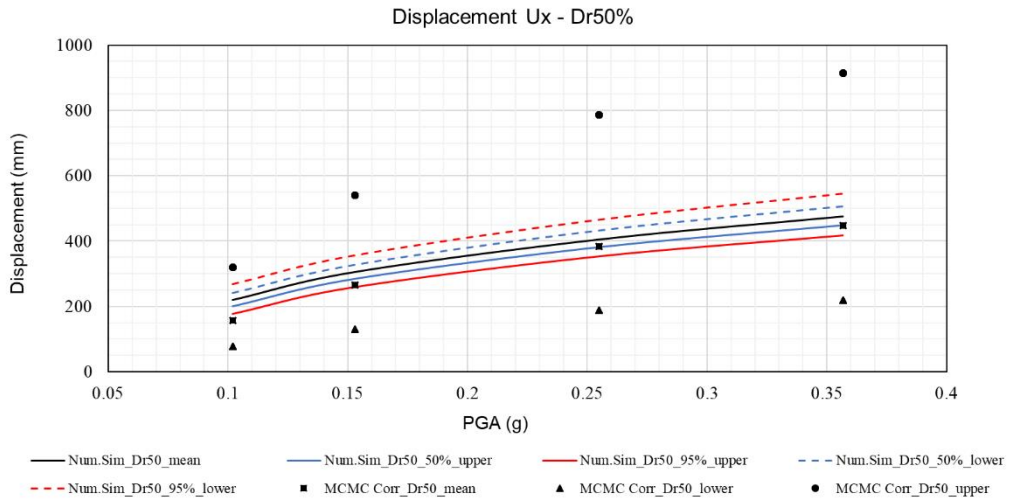

Figure 6-1 Comparison between displacements obtained in physical and numerical models for Dr = 50%

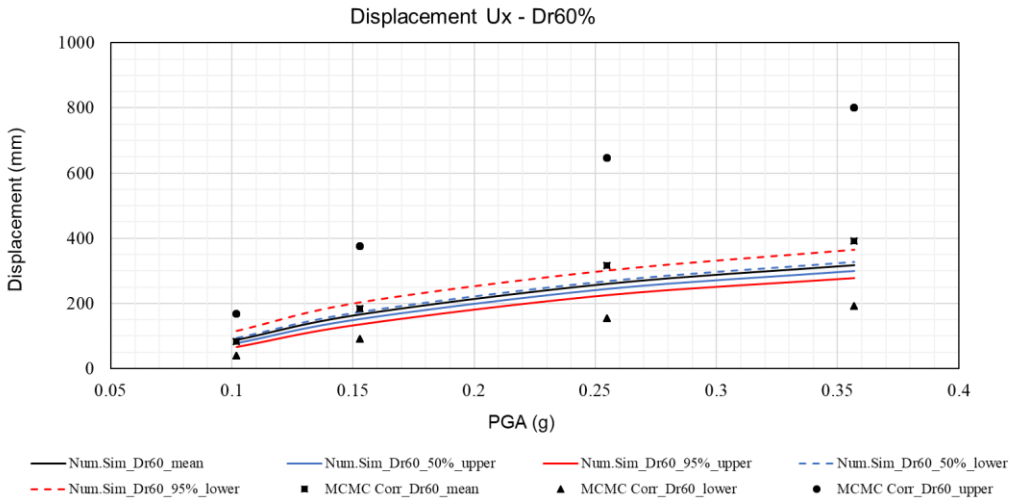

Figure 6-2 Comparison between displacements obtained in physical and numerical models for Dr = 60%

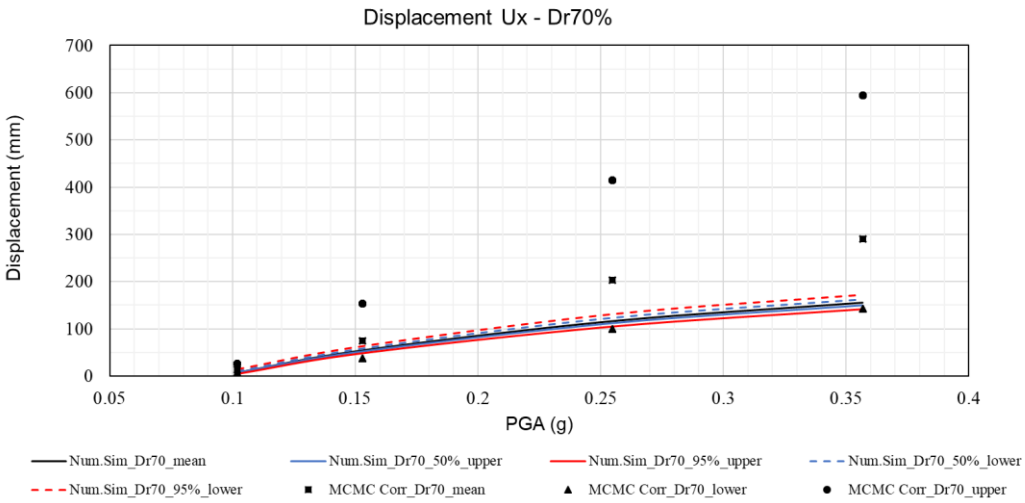

Figure 6-3 Comparison between displacements obtained in physical and numerical models for Dr = 70%

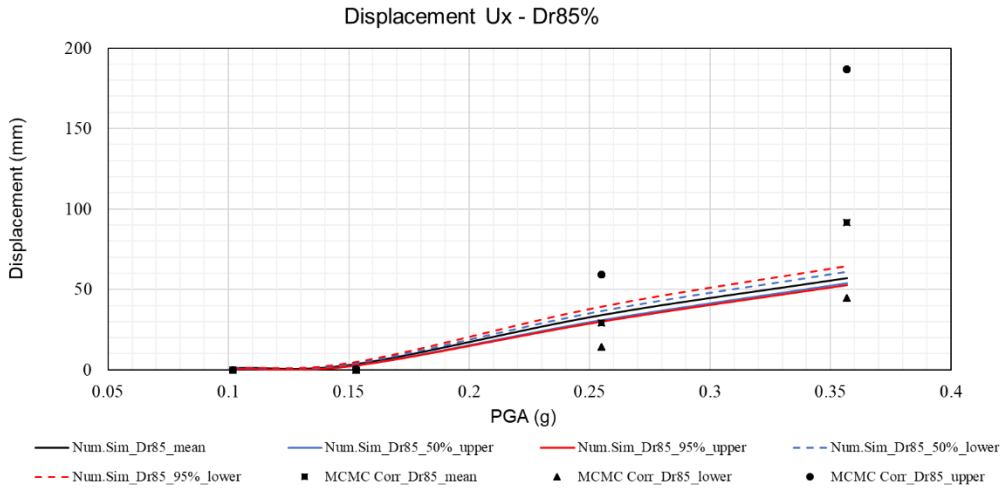

Figure 6-4 Comparison between displacements obtained in physical and numerical models for Dr = 85%

6.2 Validation Requirements and Validation Metrics

According to the validation methodology proposed in this manuscript (see Section 1.4.1), the validation exercise concludes through the assessment of the suitability of the model by means of validation metrics. The ASME Standard [2] [17] requires a validation metric that incorporates uncertainties, and provides a single measure of the relative difference between the simulation outcomes and the validation experiments Additionally, in order to assess the model suitability, a validation requirement (i.e. maximum or minimum values of the metric) are required to be specified.

Setting validation requirements requires careful consideration of several factors, including:

- Predictive accuracy of the computational model based on the intended use.
- Limitations based on obtaining experimental measurements based on sensor capabilities, project schedule, experimental facilities, financial resources, etc.
- The current point in the engineering development cycle.
- Consequences of the engineering system not meeting performance, reliability, and safety requirements.

Depending on the characteristics of the quantity under validation, different metrics can be used. In this study, the validation of a scalar quantity (i.e., surface displacements at the center of the slope Ux) is studied, and the ASME's illustrative guide [17] suggests using the "area metric."

The "area metric" is based on the computation of the area between the cumulative distribution functions (CDFs) of the measured and the computed quantities (see Figure 6-5). The area metric M is defined as the area between the experimental CDF ($F^{exp}(y)$) and the model CDF ($F^{mod}(y)$), normalized by the absolute mean of the experimental results ($\bar{\mu}^{exp}$). Thus, the area metric can be estimated by Eq. (6-1).

$$M = \frac{1}{|\bar{\mu}^{exp}|}\int_{-\infty}^{+\infty}\left|F^{mod}(y) - F^{exp}(y)\right|dy \qquad (6\text{-}1)$$

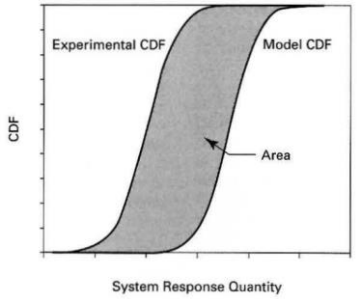

Figure 6-5 Illustration of the basis of the Area Metric

However, it has been proven that, for cases where two CDFs do not cross, the integral $\int_{-\infty}^{+\infty}\left|F^{mod}(y) - F^{exp}(y)\right|dy$ is equal to the absolute difference between the mean values [17], leading to the fact that the variability is not taken into account. As an illustration of this aspect, the area between the CDF of two normal distributions with the same mean values (μ_1=260, μ_2=305) and different standard deviations (σ_1=5 - 50, σ_2=20) has been calculated, and the influence of the standard deviation in the area between CDFs has been estimated; as shown in Figure 6-6, the area for cases where two CDFs do not cross is equal to the absolute difference between the mean values.

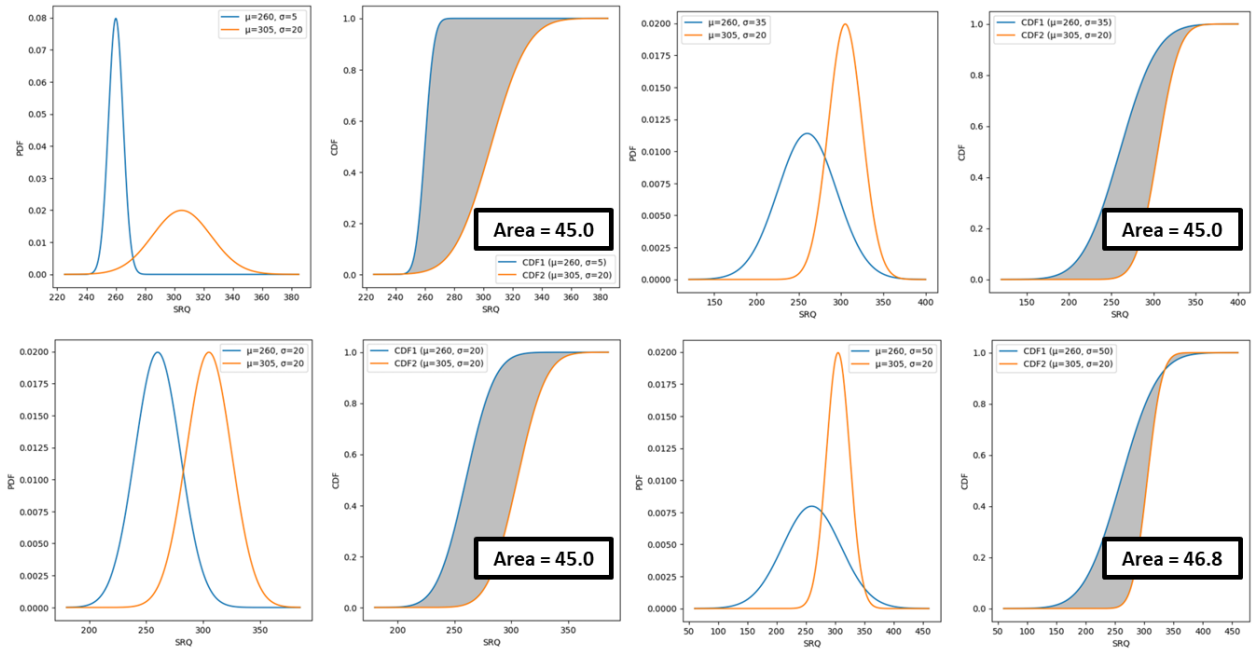

(a)

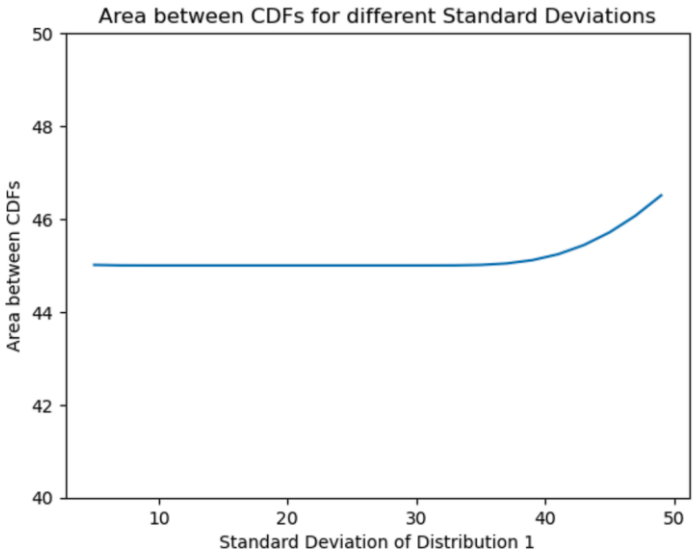

(b)

Figure 6-6 Area Metric Illustration (a) Cases under analysis, (b) Influence of the standard deviation in the area between CDFs

Since the area metric may not effectively take the variability into account, it is suggested that other metrics should be used in combination with or instead of the area metric for validation purposes. For this study, a comparison of the percentiles for a 95% probability (i.e., 2.5% and 97.5% percentiles) is suggested as an effective metric for validation because it directly accounts for variability.

Therefore, the following two conditions are required for validation:

Condition 1: $Ux2^{sim}_{2.5\%} - Ux2^{exp}_{2.5\%} \geq 0$

Condition 2: $Ux2^{exp}_{97.5\%} - Ux2^{sim}_{97.5\%} \geq 0$

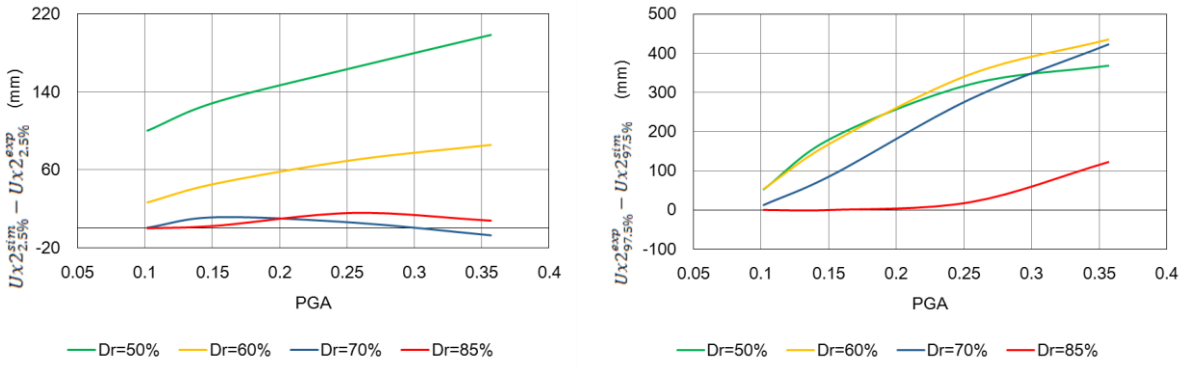

(a) (b)

Figure 6-7 Validation Metric/Conditions (a) Condition 1 ($Ux2^{sim}_{2.5\%} - Ux2^{exp}_{2.5\%}$), (b) Condition 2 ($Ux2^{exp}_{97.5\%} > Ux2^{sim}_{97.5\%}$)

By using the above conditions as a validation metric, the outcomes of this validation exercise can be summarized as follows:

- The area metric may not effectively take variability into account. Therefore, a new validation metric is proposed that requires numerical simulation outcomes (mean values and associated variability) to be within the range of variability found in physical experiments. It is important to indicate that the validation metric has a significant impact in the final results and conclusions of the validation exercise, therefore its selection shall be based on the objectives of the validation.
- As for the median response, a good agreement between the computed displacements and the estimated correlation was found for PGA<0.25g. This suggest that, if the model parameters are calibrated based on high-quality laboratory tests, a good agreement can be obtained.
- The validation metric is established on the basis that a numerical model is considered validated if the confidence intervals of the computed displacements fall within the confidence intervals of the experimental results. As illustrated in Figure 6-7, which displays plots of the $Ux2^{sim}_{2.5\%} - Ux2^{exp}_{2.5\%}$ (Condition 1) and $Ux2^{exp}_{97.5\%} > Ux2^{sim}_{97.5\%}$ (Condition 2) values, the model achieves validation when positive values are observed. Conversely, the model fails to meet validation criteria if negative values are recorded in any of the conditions. Specifically, for PGA values less than 0.25g, it has been verified that the 95% confidence intervals of the computed displacements are consistently within the confidence intervals of the experimental data (indicating positive values in Figure 6-7), thereby validating the model for PGA values below 0.25g.

- It was found that the variability of the experimental results is significantly higher than the variability of the numerical simulations. This might be explained by the fact that the experimental results were developed by different teams and with different equipment, leading to different uncertainty levels for each experiment (such as achieved densities, calibration of accelerometers, methods of displacement measurement, etc.). In contrast, the element tests were developed in a unique facility, using the same equipment.
- For PGA values greater than 0.25g, it was found that the model does not meet the validation criteria (in specific Condition 1 for DR=70%), and also important variations in the trend of the mean values were found between the experimental and the numerical results. This may be explained by the fact that the induced CSR values could not be replicated in the element tests (due to the instability of the sample), hence the estimated parameters may not be suitable in this range. Moreover, few physical models were developed in this range of accelerations (which also partially explains the increment in variability in comparison to the PGA<0.25 range). Thus, additional research efforts would be required to explore the validity of the "Strain Space Multiple Mechanism Model" in this range of accelerations.

6.3 Type B Simulations and the Importance of Repeatability in Physical Models

Up to the previous section, a validation exercise that explore the suitability of a numerical model to simulate the displacements in the central part of a sloping ground due to lateral spreading was developed. However, other quantities (such as the ground response acceleration and the EPWP) are also of interest in the study of the lateral spreading phenomenon.

Since these quantities are represented by a time-history record, a common approach to assess the model corresponds to the development of Type B Numerical Simulations. As described by Ueda et. al. [19], the type B simulations require that the modeler does not change the model parameters to match the results obtained in the physical model; in fact, the parameters should be estimated based only on the knowledge of the element tests.

To obtain proper feedback from the development of Type-B simulations, the selection of reliable tests is required. Regarding the tests developed for LEAP, although the results of the physical models were found to be consistent among each other, significant variability was found. As an illustrative example, test UCD_A_A1_1 (Dr =81%, PGA_{eff}=0.18) reported a displacement Ux2=30.6 mm, meanwhile test KAIST1 (Dr =85%, PGA_{eff}=0.17) reported a displacement Ux2=2.3 mm. It shall be noted that despite the fact that both tests reported similar Dr and PGA_{eff} values, significantly different displacement values were obtained.

Although, as mentioned in section 2.5.4, in the absence of noticeable errors/deviations in the experiments, it may not be possible to judge whether the differences between the experiments are due to one of them being correct or incorrect. In fact, in most cases, none of the experiments will show the "correct values", hence, the differences shall be considered as part of the variability involved in modeling the phenomena.

Nevertheless, given that the mean trend and the associated variability have been quantified (refer to Figure

4-27, and Figure 4-28), repeatable tests with values close to the mean trend are more likely to be reliable and considered closer to the "correct value".

While the centrifuge tests were performed under laboratory conditions and using the same specifications (developed for LEAP), the repeatability of these tests has not been assessed. Therefore, in order to assess the repeatability capabilities of the physical models, an additional test, named KyU_A_A1_2, was developed after approximately 6 months, aiming to replicate the characteristics of the KyU_A_A1_1 test.

As shown later in this section, the KyU_A_A1_2 test was found to be repeatable and reliable, and a Type B numerical simulation was carried out to explore the capabilities of the “Strain Space Multiple Mechanism Model” to simulate the ground response acceleration and the EPWP.

Time-history records for the input and center-line accelerometers (AH1, AH2, AH3, and AH4) are reported in Figure 6-8. It can be seen that the input acceleration was properly replicated in the repeatability test. Regarding the ground response acceleration, a good agreement between the physical models was obtained, both prior and after the occurrence of liquefaction. Even in the occurrence and magnitude of the spikes caused by the dilative behavior of the sand, good repeatability was obtained.

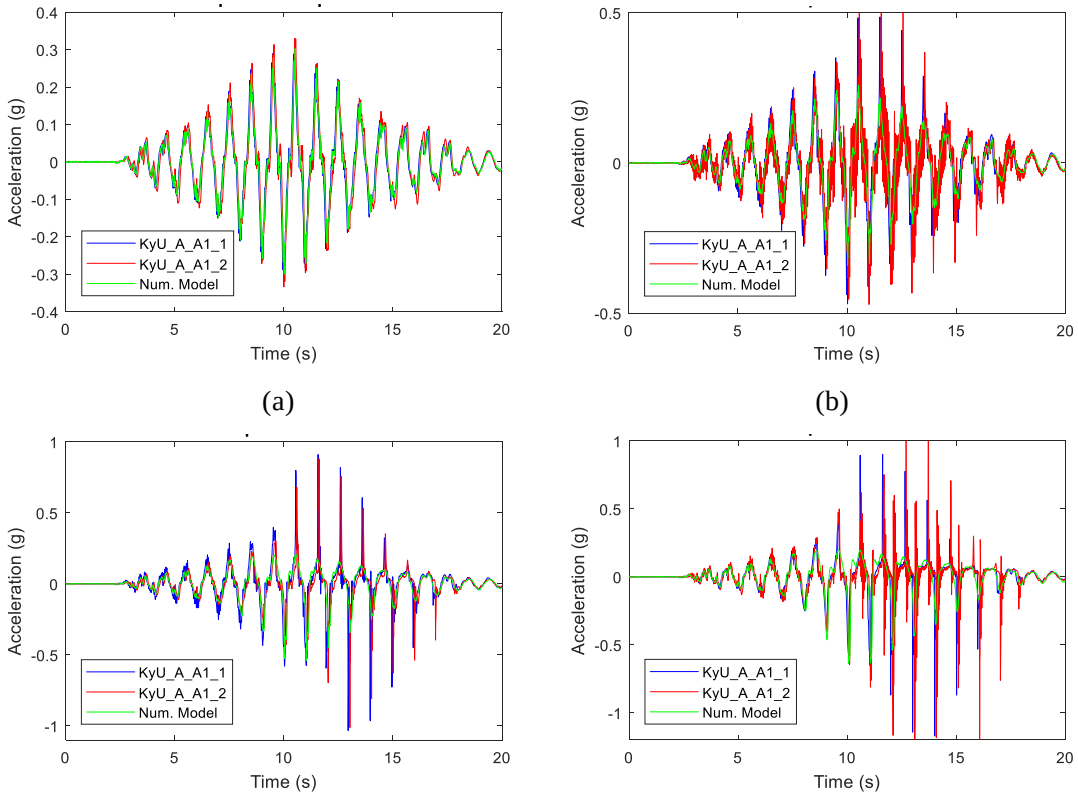

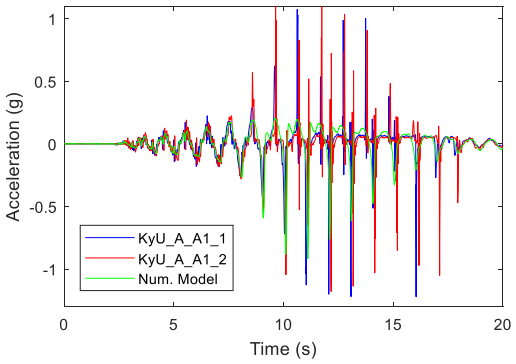

(e)

Figure 6-8 Ground Acceleration Records - Tests KyU_A_A1_1, KyU_A_A1_2, and Type B Numerical Simulation (a) Input Acceleration, (b) Accelerometer AH1, (c) Accelerometer AH2, (d) Accelerometer AH3, (e) Accelerometer AH4

Regarding the numerical model, a good agreement with the physical models was obtained, particularly prior to liquefaction occurrence. The acceleration spikes were well captured in the negative direction (i.e. in the up-slope direction), however, the model is unable to predict the positive spikes.

Figure 6-9 shows the EPWP records for the centerline sensors (P1, P2, P3, and P4); a good agreement with the physical models was found during the shaking process, which keeps consistency with the agreement found in the accelerometer records. However, some discrepancies can be observed in the dissipation process, despite the good similarity between the numerical model and the test KyU_A_A1_1. Since the dissipation process is closely related to the viscosity of the fluid in the physical models (and hence the permeability of the ground), the discrepancies in the dissipation process can be attributed to the uncertainty in the fluid's viscosity due to the small temperature changes (refer to Figure 3-15).

Figure 6-10 shows the dynamic displacement of the center part of the slope of model KyU_A_A1_1 and the Numerical Model, in which a relatively good agreement was found.

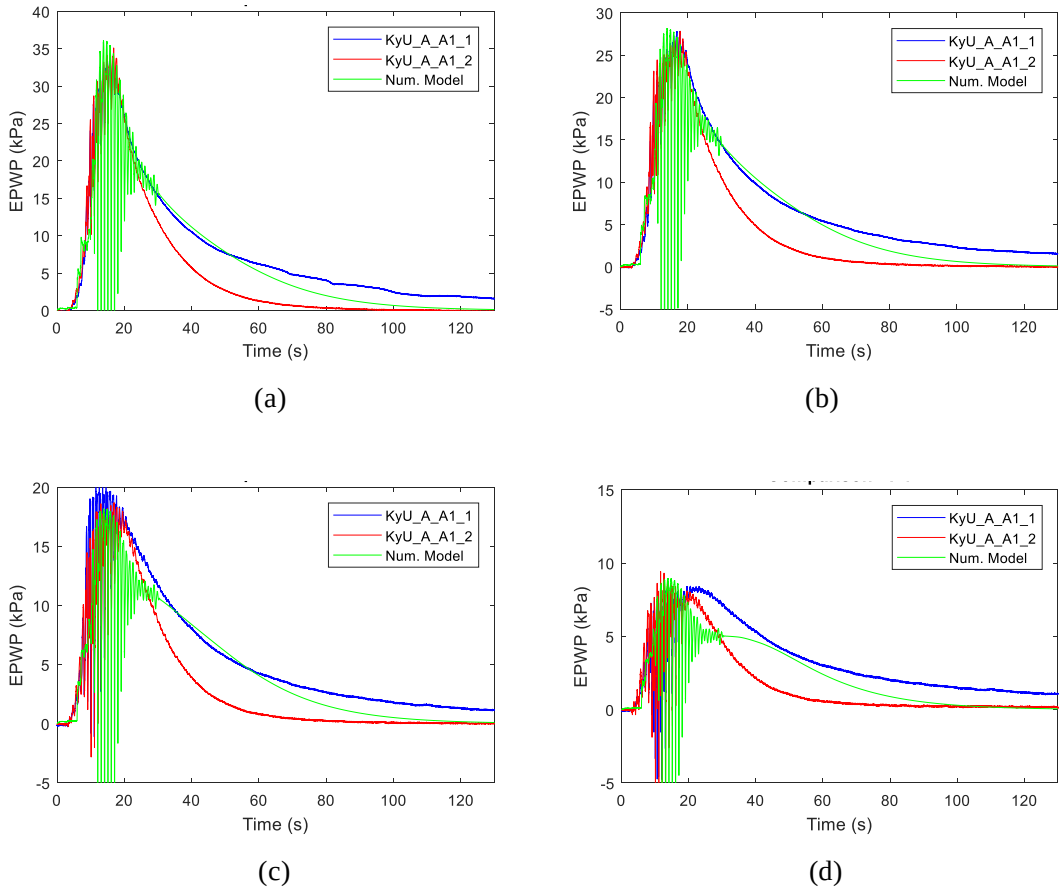

Figure 6-9 Excess Pore Water Pressure Records - Tests KyU_A_A1_1, KyU_A_A1_2, and Numerical Model (a) EPWPT P1, (b) EPWPT P2, (c) EPWPT P3, (d) EPWPT P4

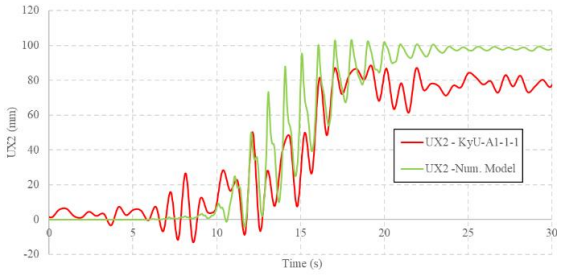

Figure 6-10 Dynamic Displacement of the center part of the slope (Ux2) of model KyU_A_A1_1 and Numerical Model

6.4 *Type B Simulations, and a Brief Discussion on the Influence of the Fluid's Viscosity in Centrifuge Models*

As discussed in the previous section, changes in the fluid's viscosity were attributed to be the main cause of the discrepancies in the dissipation process among the tests. To further investigate this phenomenon, an additional test "KyU_A_A1_3" was developed to replicate the characteristics of the KyU_A_A1_1 (in terms of Dr and PGAeff), although, using water to saturate the ground instead of the viscous fluid.

According to Okamura et. al [141], in practical terms, this (test with water instead of viscous fluid) corresponds to testing a ground with significantly higher permeability (44.4 times in this case).

To evaluate the consistency of the test, and explore the capabilities of the numerical model under the drastic change of a parameter, another Type B numerical simulation was conducted. This simulation was carried out using the same parameters and following exactly the same characteristics as the one described in the previous section, except for the permeability value, which was increased 44.4 times.

Ground Acceleration Response and Excess Pore Water Pressure records are shown in Figure 6-11, and Figure 6-12. Compared to KyU_A_A1_1 and KyU_A_A1_2, a completely different behavior was observed, despite that only the permeability value has been modified. EPWPT records show no accumulation of excess pore water pressure, indicating that the pore pressure dissipation process occurred not only after the shaking process but also during it. This keeps consistency with the acceleration response records, in which no significant distortion was found.

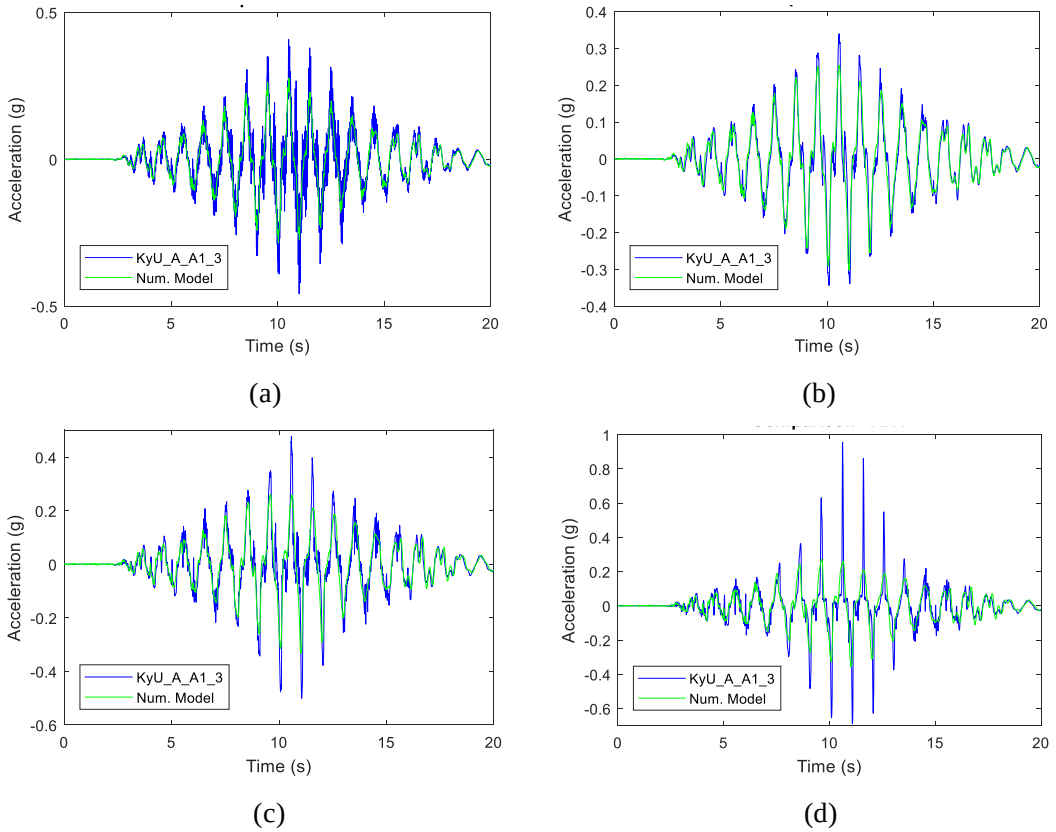

Figure 6-11 Ground Acceleration Records - Tests KyU_A_A1_3 and its Type B Simulation (a) AH1, (b) AH2, (c) AH3, (d) AH4

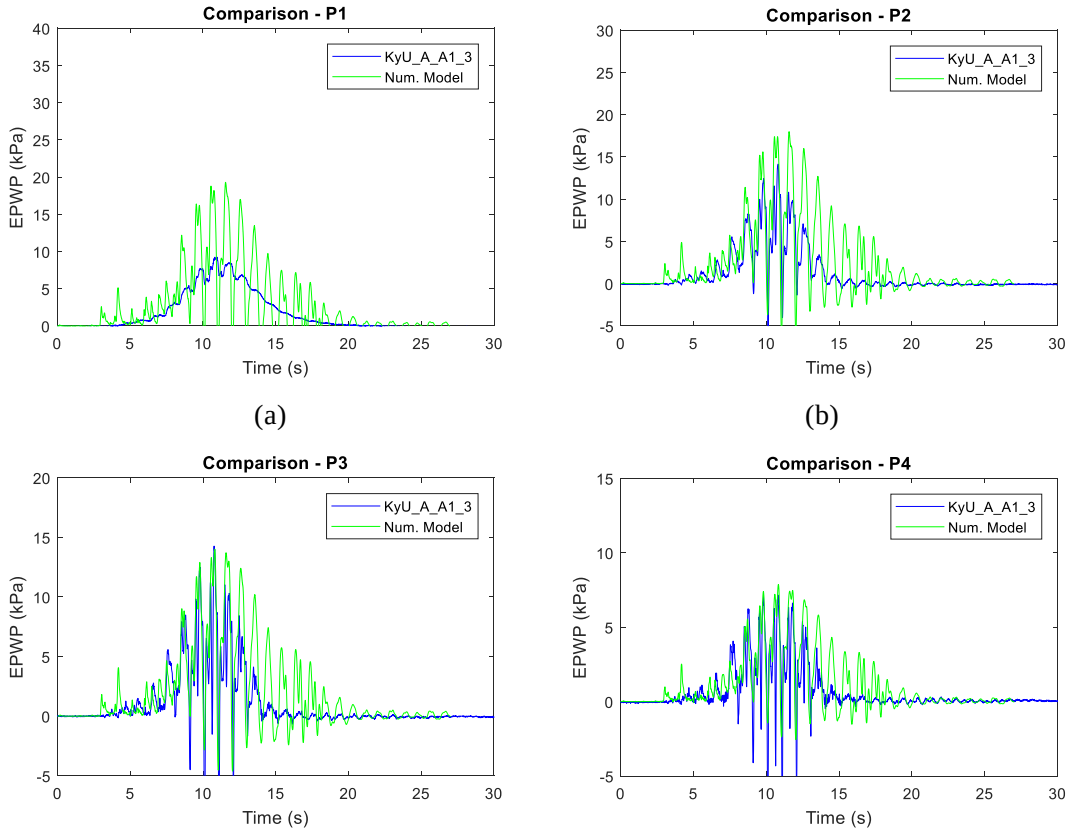

Figure 6-12 Excess Pore Water Pressure Records - Tests KyU_A_A1_3 and its Type B Simulation (a) EPWPT P1, (b) EPWPT P2, (c) EPWPT P3, (d) EPWPT P4

The findings in test KyU_A_A1_3 confirm that the main cause of the discrepancies in the dissipation process among the repeatability tests presented in the previous section can be attributed to the changes in the viscosity of the fluid, which was caused mainly due to the changes in temperatures. Therefore, in order to increase the accuracy in future experiments, special attention should be placed in an accurate control of the fluid's viscosity during the testing process.

It worth noting also that a good agreement was found between the Type B Simulation and the experimental results, suggesting that changes in the fluid's viscosity are directly correlated with changes in the soil permeability; these results also confirm the capabilities of the "Strain Space Multiple Mechanism Model" to simulate the lateral spreading phenomenon, even under the drastic change of a parameter.

6.5 Section Conclusions

This section describes the final step of the validation process, which involves a quantitative comparison of the outcomes obtained from the Physical Modeling (see Section 3) and the Numerical Modeling (Section 5). The comparison outcomes are evaluated using the proposed validation metrics. The main findings of

this analysis are as follows:

- While the area metric is commonly used as a validation metric, it has been found that it may not effectively take variability into account. Therefore, a comparison of percentiles for a 95% probability is suggested as an effective metric for validation, as it directly accounts for variability
- Regarding the mean trend response, a good agreement between the computed displacements and the estimated correlation was found for PGA values less than 0.25g.
- For a 95% of probability, the confidence bounds of the computed displacements are located between the confidence bounds of the experimental outcomes (with few exceptions between 0.1-0.15g at Dr 70% and 85%); validating the model for PGA values lesser than 0.25g, and Relative Density values between 50% to 85%.
- For PGA values greater than 0.25g, important variations were found between the experimental and the numerical results. This may be explained by the fact that the induced CSR values could not be replicated in the element tests (due to the instability of the sample), hence the estimated parameters may not be suitable in this range. Moreover, few physical models were developed in this range of accelerations (which also partially explains the increment in variability in comparison to the PGA<0.25 range). Thus, additional research efforts would be required to explore the validity of the "Strain Space Multiple Mechanism Model" in this range of accelerations.
- In addition to the validation exercise, Type B Simulations demonstrated that the model can replicate the most important characteristics of the soil behavior (acceleration, EPWP, and displacement) for reliable and repeatable tests, even if the conditions change (such as drastic changes in the permeability).
- The applicability of the proposed fully-probabilistic validation methodology has been demonstrated in its successful application to complex numerical models for liquefaction prediction.

7 Conclusions and Future Works

This thesis manuscript proposes a novel and comprehensive probabilistic validation methodology for numerical models used in predicting liquefaction phenomena, and demonstrates its practical application.

Although previous studies proposed validation methodologies for such models, they have relied on a comparison between the mean values obtained from a limited amount of non-cross-checked experimental results and their corresponding numerical simulations. However, when modeling complex phenomena such as liquefaction, comparing results from similar tests performed in different laboratories reveals significant variability/differences, these differences are attributed to the characteristics of the facilities/machines, the skill/experience of the experimenter, etc. In the absence of noticeable errors/deviations in the experiments, it may not be possible to determine whether the differences between the experiments are due to one of them being correct or incorrect; in fact, in most cases, none of the experiments shows the "correct values". Therefore, these differences should be considered as part of the variability involved in modeling the phenomena.

While validation exercises using non-cross-checked experimental results are important, especially in the early stages of a model development, a model validated under these conditions would carry the biases of the selected set of experiments and provide no estimate of the associated variability of the phenomena. Thus, these validation results may not provide sufficient evidence to fully validate a numerical model, as neither the main trends nor the variability can be accurately assessed.

The proposed methodology overcomes the limitations of previous validation efforts, and provides a more robust and comprehensive approach to numerical model validation by:

- Building upon state-of-the-art validation standards (ASME Standards and JSCE Guidelines), a large and internationally cross-checked database of physical models, and high-quality element tests.
- Proposing the validation based on a quantitative comparison between the Physical Model outcomes, and Numerical Model outcomes.
- Expressing Physical Model outcomes, and Numerical Model outcomes as probability distributions to account for the mean trends and the associated variability.
- Using a validation metric quantitatively define the suitability/validity of the model, taking into account both the mean trends and the involved variability.

The proposed validation methodology is presented through the implementation of an actual validation exercise that explores the capabilities of the "Strain Space Multiple Mechanism Model" for liquefaction predictions.

The body of this manuscript is presented in the following 5 Sections:

- Section 1 – Introduction
  - This section provides an introduction to the manuscript, outlining the background issues that are addressed, and highlights the need for a new methodology that incorporates uncertainty quantification including cross-checked experimental data, following state-of-the art methodologies for Numerical Models in Solid/Fluid Mechanics and Civil Engineering. This section also covers: (1) the definition of the objectives of the study, and (2) the description of the methodology of the study.
- Section 2 – Literature Review
  - This section provides a detailed overview of the key elements covered in the study, including soil liquefaction, lateral spreading, centrifuge modeling, effective stress models, and validation and verification (V&V). The chapter establishes the context for the research, and establish the state-of-the-art in related studies; emphasizing the importance of the development of quantitative validation implementations including uncertainty quantification, based on cross-checked experimental data.
- Section 3 – Physical Modeling
  - This section presents the physical-model tests used as the comparison base for the validation process (forty-eight centrifuge models developed in 10 institutions around the world), including: (1) a description of the testing specifications, (2) a detailed information of the tests performed at Kyoto University, (3) the data processing of the tests (forty-eight centrifuge experiments), (4) the estimation of the main trends and variability estimation of the Physical Model's quantities of interest (displacement at the center of the slope Ux).
- Section 4 – Element Tests
  - This section presents the element tests conducted to study the mechanical properties of the ground under study (Ottawa F-65 Sand), which were required to calibrate the Numerical Models and define its input uncertainty. This section includes: (1) a description of the testing specifications, (2) a detailed information of the Hollow Cylinder Cyclic Torsional Shear Tests, performed at Kyoto University, (3) the data processing of the element tests, (4) the estimation of the main trends and variability estimation of the Element Test's quantities of interest (Liquefaction Resistance Curve LRC)
- Section 5 – Numerical Modeling
  - This section the numerical modeling process used in the validation process, including: (1) a description of the target Numerical Model and its numerical implementation, (2) a detailed description of the element test simulations, and the methodology for model parameter estimation, (3) the proposal of a novel alternative to define the input uncertainty for liquefaction modeling, and (4) the details of the numerical modeling and the propagation of the model uncertainty.

- Section 6 – Numerical Modeling Assessment
  - This section describes the final step of the validation process, which involves a quantitative comparison of the outcomes obtained from the Physical Modeling and the Numerical Modeling.

In the following sections, the main findings, and suggestions for future works are summarized.

7.1 Study Conclusions

A comprehensive probabilistic validation methodology for numerical models used in the prediction of the liquefaction phenomena has been proposed. The key background points in which the study has been built up are summarized as follows:

- Soil liquefaction is a complex geotechnical phenomenon that can occur under cyclic loading, causing the soil to experience a sudden loss of strength and stiffness, resulting in significant damage to buildings, infrastructure, and other critical structures. In order to understand the phenomena and prevent future losses/damages, the development of physical and numerical models has become necessary to enable more accurate predictions.
- Despite the advancements in the numerical model for liquefaction predictions, significant discrepancies between numerical models and physical models still exist; therefore, to ensure its reliability and accuracy, rigorous verification and validation (V&V) exercises against high-quality physical models or field observations are necessary.
- As stated in state-of-the-art V&V standards/guidelines, the development of quantitative validation implementations including uncertainty quantification, is indispensable for establishing valid and credible models in practical applications. It has been shown that although some examples of quantitative validation incorporating uncertainty quantification have been performed in the recent years, they are still based on a few amounts of non-crosschecked experimental data.
- When modeling complex phenomena (such as liquefaction), although the physical models are conducted under laboratory conditions, significant variability/differences exist in the results of similar tests performed in different laboratories due to facilities/machines' characteristics, experimenter's skills/experience, etc. Hence, in the absence of noticeable errors/deviations, these differences shall be considered as part of the variability involved in modeling the phenomena.

The key findings of the study are summarized as follows:

- Cross-checked experiments are necessary to provide sufficient evidence to properly validate a numerical model. While validation exercises using non-cross-checked experimental results are important in early model development stages, their results may not provide sufficient evidence to fully

validate a numerical model as they fail to assess the mean trends and variability involved. Although it is highly recommended to obtain a set of cross-checked experiments performed under the same specifications, a dataset may also be obtained based on a collection of data existing in the literature; in this case, special attention shall be placed in selecting datasets that are comparable, placing special attention on the specification's details (including sample preparation, testing process, data processing, etc.). The inclusion (or exclusion) of the tests on a validation database shall be carefully considered, primarily focusing on the differences among the datasets and the validation requirements.

- The proposed probabilistic validation methodology is based on a comprehensive comparison between the mean trends and associated variability observed in cross-checked experimental results and those in numerical simulations derived from high-quality element tests, in accordance with the recommendations of state-of-the art validation standards The methodology is detailed and presented through implementation of a validation exercise that explores the capabilities of the "Strain Space Multiple Mechanism Model" for liquefaction predictions (specifically, displacements caused by lateral spreading in sloping grounds). It is important to note that the applicability of the proposed methodology and techniques described in this manuscript shall be evaluated on a case-by-case basis; this evaluation is particularly crucial in scenarios involving tests performed under varying specifications, a limited number of tests, more complex deformation / failure patterns, the introduction of additional sources of variability, etc. In such cases, the limitations of the proposed methodology should be thoroughly analyzed and carefully revised.
- The main findings related to the physical modeling process are summarized as follows:
  - To build a high-quality database of cross-checked physical models for validation purposes, high-quality tests conducted under the same specifications are required.
  - As part of the LEAP Framework, an unprecedented quantity of centrifuge model tests (48 tests) was produced to simulate the lateral spreading phenomena under a wide range of input motions and soil density. The results of the physical models were found to be consistent and were cross-checked among ten centrifuge facilities worldwide, including eight tests produced at the facilities of Kyoto University.
  - The achieved Dr is a key parameter in the model response. It has been found that, although providing an indirect measurement, CPT test results allows a reliable estimation of the uniformity of the ground and its associated dry density.
  - The achieved PGA is a key parameter in the model response. It has been found that PGA may not be the most suitable parameter to describe the shaking intensity, mainly due to its sensitivity to high-frequency components. Therefore, as a first attempt to better quantify the shaking intensity, PGAeff was proposed.
  - Hybrid MCMC-based Bayesian correlations were used to estimate the mean trends and associated variability of the response of the sloping sand deposit under a wide range of densities (Dr50% - Dr 85%) and peak accelerations (0.1g – 0.35g). These estimations characterize the outcomes

obtained in the Physical Models and are ready to be used in the development of current and future V&V processes of liquefaction models.

- The main findings related to the element testing process are summarized as follows:
  - Sixteen isotropically consolidated tests were conducted to investigate the stress-strain characteristics of Ottawa F-65 Sand under four different densities and a wide range of shear stress ratios. These tests were complemented by seven anisotropically consolidated tests (K_0= 0.50) to study the K0 effect.
  - It was found that the RL_{20} values and the relative density (Dr), can be correlated by means of a second-order polynomial relationship.
  - It was found that the liquefaction resistance of the anisotropically consolidated tests (K_0=0.5) is approximately 20% higher than the tests developed under isotropic consolidation, irrespective of the initial density and the strain level (for γ_{DA} = 1:5 - 7:5 %).
  - The experimental results for the volumetric strain due to post-cyclic reconsolidation (ε_v), were in good agreement with the correlations proposed by Ishihara et al. [135] and Sento et al. [136], for Dr>60%.
  - The good agreement in the repeatability tests demonstrated that the tests are consistent and repeatable.
  - Hybrid MCMC-based Bayesian correlations were used to estimate the mean trends and associated variability of the dynamic behavior of Ottawa F-65 sand. These estimations characterize the outcomes obtained in the Element Tests and are ready to be used in the development of current and future V&V processes of liquefaction models.
- The main findings related to the numerical modeling process are summarized as follows:
  - For numerical models that simulate liquefaction phenomena, it has been found that expressing the input variability in terms of the Liquefaction Resistance Curve's variability is an effective and practical method (rather than expressing it in terms of individual parameter changes). It shall be pointed out that this finding is valid for the conditions of the exercise only; it is strongly recommended that the validity shall be analyzed in a case-by-case basis.
  - A numerical model was built to reproduce the physical models. The validity of the numerical model is then assessed by comparing the numerical simulation and physical models' outcomes (both in terms of mean value and associated variability).
- The main findings related to the numerical model assessment are summarized as follows:
  - While the area metric has been commonly used as a validation metric, it has been found that it may not effectively take variability into account. Therefore, a comparison of percentiles for a 95% probability is suggested as an effective metric for validation, as it directly accounts for variability.
  - For a 95% of probability, the confidence bounds of the computed displacements are located between the confidence bounds of the experimental outcomes (with few exceptions between 0.1-0.15g at Dr 70% and 85%); validating the model for PGA values lesser than 0.25g, and Relative

Density values between 50% to 85%. For PGA values greater than 0.25g, important variations were found between the experimental and the numerical results.

- In addition to the validation exercise, Type B Simulations demonstrated that the model can replicate the most important characteristics of the soil behavior (such as acceleration, EPWP, and displacement) for reliable and repeatable tests, even if the conditions change (such as drastic changes in the permeability).

- This manuscript makes a significant contribution to the field of geotechnical engineering by demonstrating the applicability of the proposed fully-probabilistic validation methodology through a successful application to complex numerical models for liquefaction prediction. Furthermore, the study has also meticulously characterized the mean trends and variability of internationally cross-checked physical models and high-quality element tests; such characterization not only forms the base of the validation process presented herein but also establishes a robust foundation for future validation exercises. Moreover, the identification of several challenges throughout this research lays a solid groundwork for guiding subsequent investigations in this field.

7.2 Proposed Future Works

During the course of the validation study, it was identified that additional works would be required in the following areas to further develop and validate numerical models for liquefaction prediction.

- Although the centrifuge tests developed for LEAP have been found to be consistent among each other, and were therefore used in the validation exercise, there are still significant differences in the test results; this is partially evidenced by the fact that the Physical Model's variability was found to be significantly larger than the Numerical Model's variability. Therefore, to further enhance the reliability of liquefaction predictions, efforts are needed to reduce the physical model's variability by developing standard testing procedures, promoting international collaboration, providing comprehensive training to experimenters, and further developing model preparation techniques (including equipment, sensors, in-flight measurement devices, etc.).
- The liquefaction resistance of the anisotropically consolidated tests (K_0=0.5) was found to be approximately 20% higher than the tests developed under isotropic consolidation, irrespective of the initial density and the strain level. Although there is experimental evidence, further studies are needed to fully understand this phenomenon.
- The study has identified significant variations between experimental and numerical results for PGA values greater than 0.25g. To reduce the differences, effort in the following areas would be required:

    - The upper bound of the CSR values induced in Physical Models could not be replicated in element tests due to equipment limitations, therefore, the estimated parameters may not be suitable for large

accelerations. To reduce the differences, and further explore the validity of numerical models (including the "Strain Space Multiple Mechanism Model") in this range of accelerations, additional research efforts are needed to develop experimental equipment that allows conducting element tests at high CSR values.

- The variability in Physical Models significantly increased for PGA>0.25, this may be explained by the fact that few physical models were developed in this range of accelerations. Therefore, the development of additional testing following the LEAP Specifications for PGA>0.25 may contribute to reduce the variability of the Physical Models.

- Consistent and repeatable element tests (Hollow Cylinder Torsional Shear Tests) were performed; however, no cross-checking has been performed; therefore, additional efforts are needed to better understand the variability of the dynamic stress/strain behavior of the ground under consideration through cross-check exercises (with different experimenters and facilities).
- The proposed validation methodology was found to be effective to validate the “Strain Space Multiple Mechanism Model”. To further establish the proposed methodology, efforts are needed to assess the reliability of other numerical models, not limited to FEM models.
- Through the validation exercise, it was found that the “Strain Space Multiple Mechanism Model” simulates reasonably well the lateral spreading phenomena, however, it may fail to capture some the aspects found in the physical model (such as cases with PGA>0.25, the response-acceleration spikes, etc.); therefore, the comparison results provide a good opportunity for model developers to further develop/enhance the model.
- The validation exercise was focused on the lateral spreading phenomena in clean sands. The applicability of the proposed methodology and techniques to other geotechnical problems (such as consolidation, soils other than clean sands, non-saturated ground, soil-structure interaction, etc.) shall be properly thoroughly in future studies based on its specific characteristics and validation requirements. Modifications would be required based on a deep analysis of the limitations and the applicability of the hypotheses and simplifications.
- The sources of the variability explored in the exercise are somewhat limited, primarily due to the characteristics of the target experiment (uniform 5 degrees sloping sand deposit on a rigid box, subjected to sinusoidal waves); therefore, additional efforts (including element tests, physical models, site investigation) would be required to comprehensively understand the effects of other sources of variability (such as spatial variability, initial conditions, different boundary conditions, different wave shape and frequency contents, etc.).

A1. Effects of Spatial Variability on liquefaction behavior of horizontally layered ground [108]

As indicated in Section 5.1.3, the spatial variability of the ground was not taken into account given that the centrifuge experiments were performed in laboratory-conditions, aiming to obtain a homogeneous ground (using the air-pluviation method). This appendix summarizes a study of the effects of Spatial Variability on liquefaction behavior; although the study was performed on horizontally layered ground, it could be used as a reference to assume that only a small difference in the soil response is expected when studying a fairly "homogeneous" ground (Figure A1-11).

A1-1 Introduction

In order to predict the liquefaction potential and liquefaction-induced damage to soil-structure systems during earthquakes, effective stress analyses based on the finite element method are often used as a reliable tool in seismic design. The analyses require accurate modeling of liquefiable ground properties (e.g. cyclic shear strength), which greatly affect the numerical results. Although the soil properties are typically specified by using deterministic (uniform) models in the standard design, they intrinsically have spatial variability even in the case of horizontally layered ground. In addition, the heterogeneity of soil properties has been proven to affect the dynamic behavior of ground and to induce significant variability in the predicted response for some cases [142] [143] [144]. However, the effect has not yet been fully studied in a quantitative way.

In this study, two-dimensional nonlinear finite element analyses are carried out to investigate the effects of soil heterogeneity on the liquefaction potential and dynamic response of stochastically heterogeneous soil deposits subjected to seismic loading. The analyses build on a Monte Carlo simulation approach, following the methodology proposed by Popescu [142]. The material nonlinearity of soils is expressed by using a strain space multiple mechanism model [138]. Numerical simulation procedures using the model in the finite element program FLIP [138] [145] are described. In the simulation, the spatial distribution of the SPT N1 value, the shear wave velocity (i.e. shear modulus) and the internal friction angles in the liquefiable deposits are separately taken into account by using sample functions of discretized triangular and exponential stochastic fields [146] in addition to Gaussian one. Simulation results for stochastic models are compared to those for deterministic models by focusing on ground lateral displacement and excess pore water pressure (EPWP) build-up.

A1-2 Modeling Of Spatial Variability of Soil Properties

The SPT N1 value, shear wave velocity (Vs), and internal friction angle (ϕ_f) are separately considered as probabilistic variables in this study. That is to say, only one property among them expresses the variability with the other two properties kept constant (in order to estimate the effects of the variability of each property in the ground response). However, when the SPT N1 value is considered to be a stochastic field, the other two properties automatically vary following a simplified method for parameter identification of FLIP program [147] as described later.

For each soil property, a one-variate, two-dimensional (1V-2D) stochastic field [148], which produces the probability and cumulative distribution functions (PDF, CDF), is required in order to perform stochastic analyses. In this study, twenty seven sample functions of the 1V-2D field are generated for the Monte Carlo simulation by using sample functions of discretized Gaussian, triangular, and exponential stochastic fields. In other words, each type of stochastic fields creates three possible realizations for each soil property over the analysis domain. It is important to mention that, as a first trial for this study, only eighteen simulations were performed (i.e. two different realizations per each case); in order to confirm the results, nine additional simulations were developed (i.e. one additional realization per each case), and (as it will be stated later) no significant difference among stochastic fields nor realizations was found; so, twenty seven simulations were considered enough for the purpose of this study.

Spectral density functions of the two-dimensional stochastic fields are given as shown in Table A1-1 by applying the following Wiener-Khinchin theorem [146].

$$S = \frac{1}{(2\pi)^2} \int_{-\infty}^{\infty} \int_{-\infty}^{\infty} R \exp\left\{-i\left(\kappa_x \xi_x + \kappa_y \xi_y\right)\right\} d\xi_x d\xi_y \qquad \text{(A1-1)}$$

where $R(\xi_x, \xi_y)$ is the correlation function (CF) of the stochastic fields, ξ_x ($=x_1-x_2$) and ξ_y ($=y_1-y_2$) are the distance between two points in x and y direction, respectively, and $\boldsymbol{\kappa}=(\kappa_x, \kappa_y)^T$ is a wave number vector. In Table A1-1, σ denotes the standard deviation of variational parameters, and dx, dy are the correlation distance in x and y direction, respectively. By following Nadim et al. [149], dx=10.0 m and dy=1.0 m were used in this study.

Table A1-1 *Spectral density functions of two-dimensional stochastic fields.*

Type	Spectral density function $S(\kappa_x, \kappa_y)$
Gaussian	$\sigma^2 \cdot \frac{d_x d_y}{4\pi} \cdot \exp\left\{-\left(\frac{d_x^2}{4}\kappa_x^2 + \frac{d_y^2}{4}\kappa_y^2\right)\right\}$
Triangular	$\sigma^2 \cdot \frac{4\sin^2(d_x\kappa_x/2)\sin^2(d_y\kappa_y/2)}{\pi^2 d_x d_y \kappa_x^2 \kappa_y^2}$
Exponential	$\sigma^2 \cdot \frac{1}{(2\pi)^2} \cdot \left(\frac{2d_x}{d_x^2\kappa_x^2+1}\right)\left(\frac{2d_y}{d_y^2\kappa_y^2+1}\right)$

According to Shinozuka and Deodatis [150], a random process following the spectral density functions are derived, by assuming the mean value is zero, as follows:

$$f(x,y) = \sqrt{2}\sum_{k=1}^{K_x}\sum_{l=1}^{K_y} A_{kl} \times\left[\cos\left(\kappa_{xk}x + \kappa_{yl}y + \Phi_{kl}^{(1)}\right) + \cos\left(\kappa_{xk}x - \kappa_{yl}y + \Phi_{kl}^{(2)}\right)\right] \tag{A1-2}$$

$$A_{kl} = \sqrt{2S\left(\kappa_{xk}, \kappa_{yl}\right)\Delta\kappa_x\Delta\kappa_y} \tag{A1-3}$$

where Φ_{kl} is an independent random phase angle distributed with uniformity between 0 and 2π. K_x and K_y are the division number for calculating wave number in x and y direction, respectively, and may be different from the division number of finite element mesh, and $\Delta\boldsymbol{\kappa}=(\Delta\kappa_x, \Delta\kappa_y)^T$ is an incremental vector of wave number. In this study, $K_x=K_y=1000$ and $\Delta\kappa_x=\Delta\kappa_y=0.01$ were used.

Spatial variability of the stochastic field could be determined by the sum of the mean value (f_m) and the previously estimated random process ($f(x,y)$), as follows:

$$F(x,y) = f_m + f(x,y) \tag{A1-4}$$

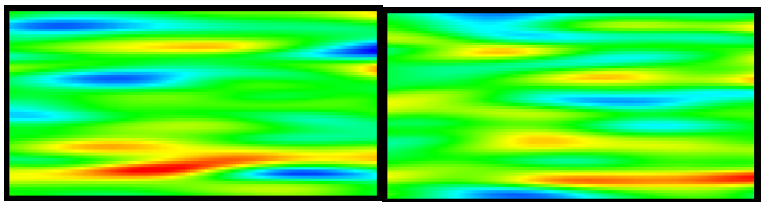

(a) Gauss

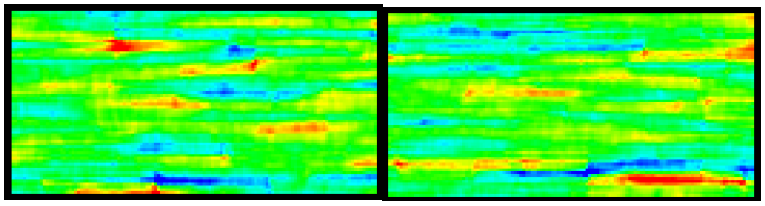

(b) Triangular

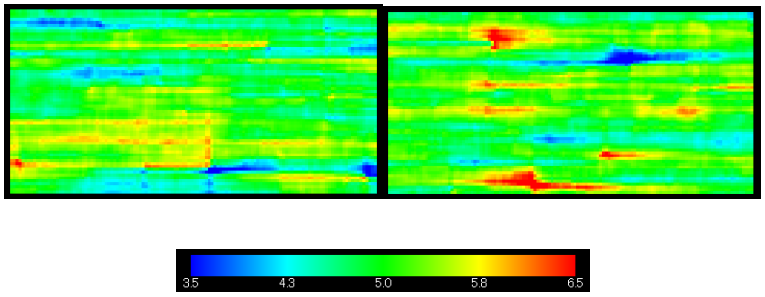

(c) Exponential

Figure A1-1 *Spatial distribution of two realizations for SPT N1 value, for Gaussian, Triangular and Exponential Stochastic Fields.*

Finally, the spatial distribution F of stochastic variables representing the heterogeneity of soil properties is given as shown in Figs. A1-1 through A1-3.

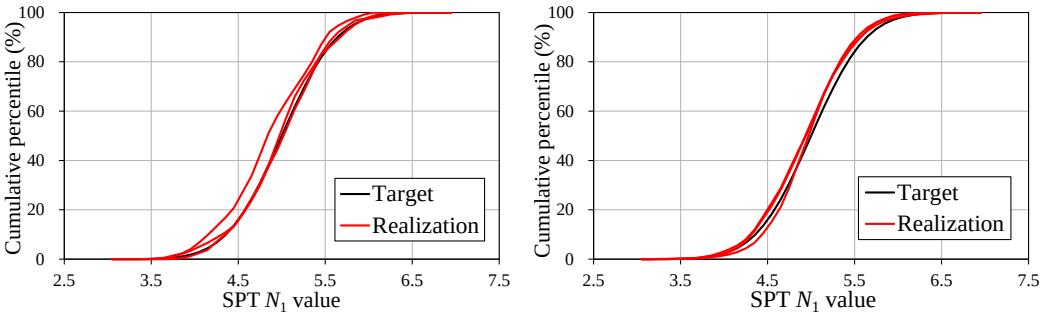

(a) Gaussian

(b) Triangular

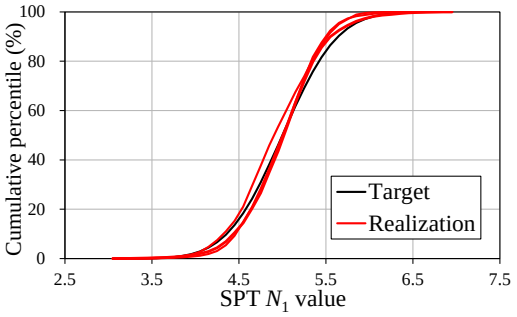

(c) Exponential

Figure A1-2 *Cumulative distribution function for N1.*

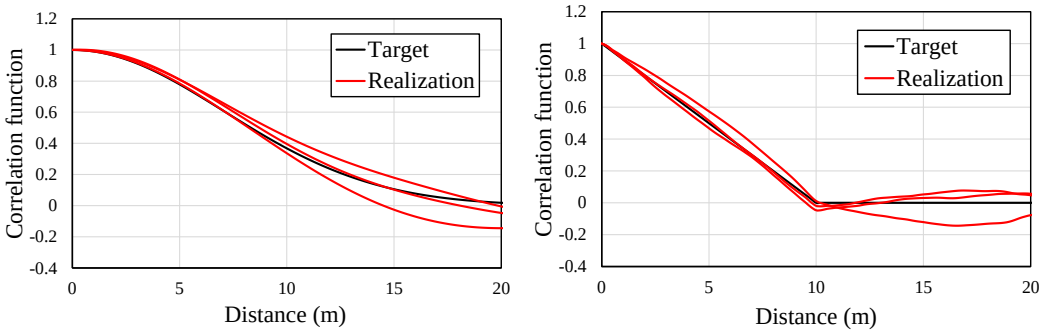

(a) Gaussian

(b) Triangular

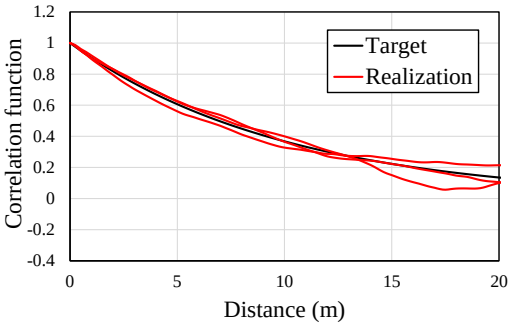

(c) Exponential

Figure A1-3 *Correlation function for N1.*

A1-3 Numerical Simulation Procedure

Two dimensional nonlinear seismic response analyses were performed on a liquefiable sand deposit shown in Fig. A1-4 using a finite element program for soil-structure systems (FLIP). The finite element mesh has 64 rows with 128 columns, for a total of 16,384 elements (including 8,192 pore water elements). The liquefiable de-posit, consisting of clean sand, was modeled using a strain space multiple mechanism model [138]. Model parameters (e.g. initial shear modulus ($G_{ma}=\rho V_s^2$), internal friction angle (ϕ_f), including dilatancy parameters, were determined by a simplified method for parameter identification of FLIP program [147] [151] based on the SPT N value with effective overburden pressure (=98 kPa) and fines content (=0%). Simulated liquefaction resistance curve is shown in Fig. A1-5 with the cases of N=5, 10 and 15.

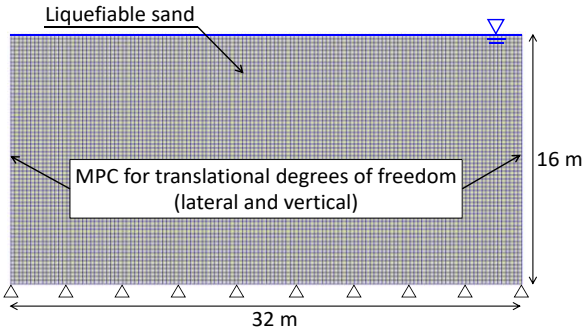

Figure A1-4 *Finite element mesh of horizontally layered liquefiable ground.*

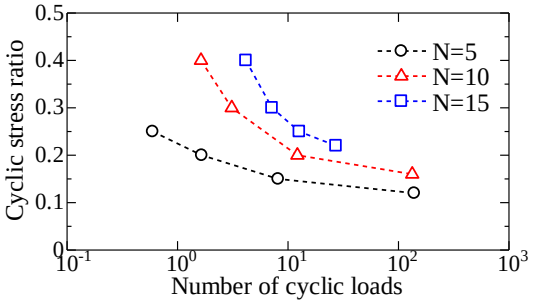

Figure A1-5 *Liquefaction resistance curve.*

The boundary conditions for displacement were selected to replicate horizontally layered ground. The displacement degrees of freedom on the left side boundary were slaved to move together with their counterparts on the right boundary. Rigid base boundaries were used at the bottom of the model. The ground water table was set at the ground surface. In the simulation, stochastic variability for the SPT N1 value, the shear wave velocity (Vs), and the internal friction angle (ϕ_f) described in the previous section was separately taken into account to investigate the effects of soil heterogeneity on the dynamic response of stochastically heterogeneous liquefiable deposits subjected to seismic loading. The simulation was carried out under undrained condition, and thus the results of this study are valid just after the shaking process (i.e. before the EPWP dissipation), so the ground settlement after shaking is out of scope in this study.

The input motion applied to the base, consisted in a ramped sine wave of 20 cycles with a PGA of 1 m/s^2, and a frequency of 1 Hz (the fundamental frequency of the soil structure for small vibrations has an approximate value of 2 Hz [152]), as shown in Fig. A1-6

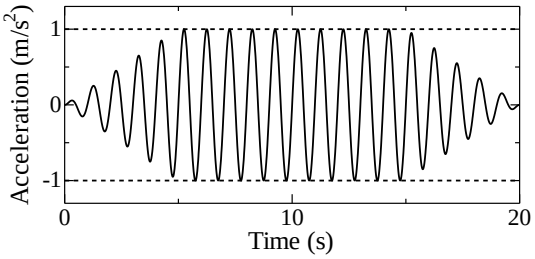

Figure A1-6 *Input ground motion.*

A1-4 Analysis Results

(1) Maximum Lateral Displacement

The variations of maximum lateral displacement at the right (or left) boundary with depth are shown in Fig. A1-7 with the results of three uniform (i.e. deterministic) models. For each stochastic model, an averaged profile over three realizations is depicted. When the SPT N1 value is treated as a stochastic variable (see Figs. A1-1 through A1-3), a similar profile is obtained regardless of the type of stochastic fields in Fig. A1-7(a). From the surface until a depth of around 12.5 m, the lateral dis-placements for these stochastic realizations are less than those for uniform models with N1 value between the 20th and 80th percentiles; however, in the deepest zones, the displacements values are close to the 20th percentile deterministic model. This may be because a domain-averaged EPWP ratio in the stochastic models is less than that in the deterministic models as shown in Fig. A1-9(a) later and the difference affects the shear strain development.

When the shear wave velocity and friction angle are treated as stochastic variables, the difference in the type of stochastic fields has no significant effect on the displacement profiles (Fig. A1-7), as is the case with the SPT N1 value. When the shear wave velocity is variable, the 50th percentile is closest to the stochastic models in Fig. A1-7(b). Thus, the heterogeneity of shear wave velocity (or initial shear modulus) is considered to have no significant effect on lateral displacement profiles.

Figure A1-7(c) indicates that the distributions of displacements for the stochastic realizations are less than those models with an deterministic value of ϕ_f (except for the deepest zones), however, the surface displacement is close to the deterministic value of 20th percentile ϕ_f =31.2); so, the precise representative ϕ_f value is currently hard to be specified because whether less percentile values give a closer profile to the stochastic cases were not tested. The less surface displacements in the stochastic models may be due to the difference in the averaged EPWP ratio between the deterministic and stochastic models as shown in Fig. A1-9(c).

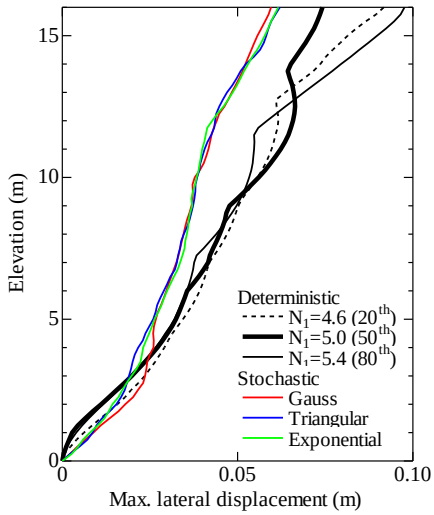

(a) The case of variable SPT N1 value

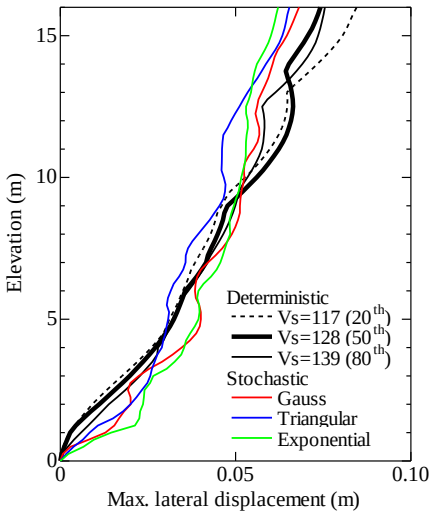

(b) The case of variable shear wave velocity

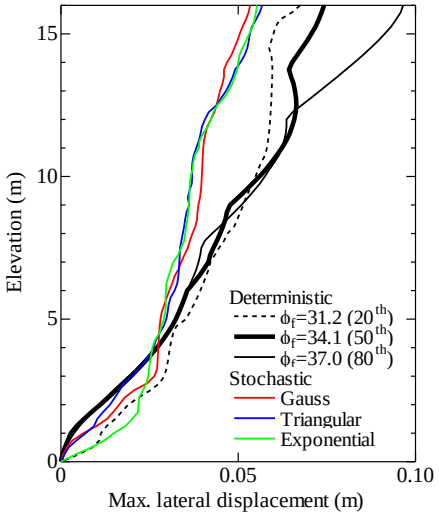

(c) The case of variable internal friction angle

Figure A1-7 *Maximum lateral displacement profiles*

(2) Excess Pore Water Pressure Ratio

Time history of simulated EPWP ratio is shown in Figs. A1-8 and A19.

Figure A1-8 shows the largest value (Pmax) among 8,192 soil elements, while Fig. A1-9 shows the domain-averaged value (Pave) over the elements. The difference between Pmax and Pave is considered to indicate the magnitude in the simulated EPWP variation in location. When the SPT N1 value is treated as a stochastic variable, a similar response is observed regardless of the type of stochastic fields in Figs. A1-8(a) and A1-9(a) as is the case with the lateral displacement profiles. Pmax eventually results in the same value (=0.97)

after shaking between the uniform and stochastic models, although the build-up process is different during shaking (Fig. A1-8(a)). In contrast, a final value of Pave in the stochastic models is about 10% smaller than that in the uniform models between the 20th and 80th percentiles (Fig. A1-9(a)).

The comparison of the time history of EPWP ratio for stochastic and deterministic models in Figs. A1-8(a) and A1-9(a) with the lateral displacement profiles in Fig. A1-7 illustrate how the representative N1 value depends on the specific response measure and the timing of concern. Different from the value for the lateral displacement profiles, the representative N1 value is almost the same as the mean N1 value (i.e. the 50th percentile) during and after shaking if Pmax is the response measure of concern. In contrast, the representative N1 value varies depending on the timing if Pave is the response measure of concern. After 3 s, we can-not find the representative value between the 20th and 80th percentiles.

When the shear wave velocity is treated as a stochastic variable, no significant difference is recognized among the uniform and stochastic models for both Pmax and Pave shown in Figs. A1-8(b) and A1-9(b), respectively, as is the case with the lateral displacement profiles (Fig. A1-7(b)). This is because the variation of shear wave velocity (or initial shear modulus) may only affect linear elastic behavior within a small strain range, whereas a strength parameter (e.g. internal friction angle, undrained shear strength at steady state) is thought to exercise a dominant influence on nonlinear behavior such as liquefaction.

Figures A1-8(c) and A1-9(c) show the time history of EPWP ratio obtained from stochastic simulations in which the variability of internal friction angle is taken into account. The overall trend is similar to the case of SPT N1 value being a stochastic variable (Figs. A1-8(a) and A1-9(a)). As described in a former paragraph, the representative ϕ_f value de-pends on the specific response measure and the timing of concern.

The ϕ_f value is between the 20th and 50th percentiles during shaking and almost the same as the mean N1 value after shaking if Pmax is the response measure of concern. In contrast, no difference is observed before 3s among the three uniform and three stochastic models when Pave is the response measure of concern. The difference of the uniform and stochastic models becomes larger and larger between 3 and 5 s, and is kept constant after 5s up to the end of shaking. The final difference of Pave is between 15% and 20%, which are larger than that in the case of SPT N1 value being a stochastic variable (Fig. A1-9(a)).

Figure A1-10 shows some examples of the distribution of EPWP ratio after shaking when the SPT N1 value is treated as a deterministic and stochastic variable, respectively. Each figure corresponds to the counterpart in Fig. A1-1 (e.g. the left figure in Fig. A1-10(a) was obtained using the spatial distribution located on the left side of Fig. A1-1(a)). Whereas uniform distribution of EPWP ratio (=0.97) is obtained except for the bottom layer of the analytical do-main in the deterministic model, the contrast between looser (i.e. higher EPWP ratio) and denser zones (i.e. lower EPWP ratio) is clearly recognized in the stochastic models. The difference among the three types of stochastic fields in Fig. A1-10 has a superficial similarity to that of the

spatial distribution of SPT N1 value shown in Fig. A1-1. Therefore, the distribution of EPWP ratio after shaking is considered to be affected by the spatial variability of input soil parameters. The reason EPWP is locally hard to build up in the case of stochastic models may be that liquefaction of locally looser zones (see Fig. A1-1) decreases the amount of shear stress (or acceleration) on surrounding denser zones essentially having higher resistance to liquefaction. This interpretation may hold only in the given condition (e.g. soil properties such as SPT N1 value, model geometry, input motions), and further studies are required in order to clarify whether deterministic models are more prone to liquefaction than stochastic ones under other conditions.

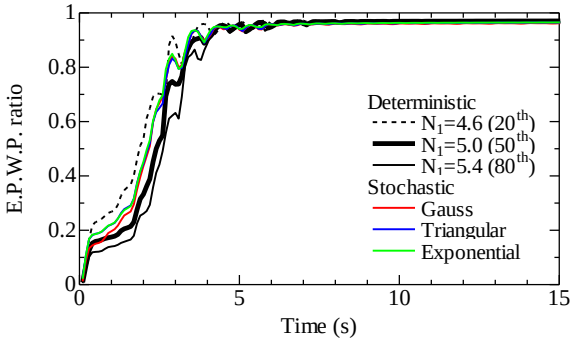

(a) The case of variable SPT N1 value

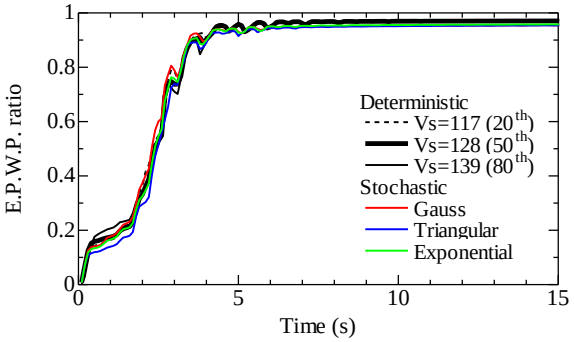

(b) The case of variable shear wave velocity

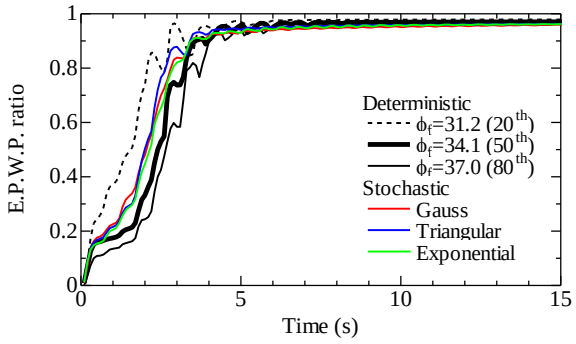

(c) The case of variable internal friction angle

Figure A1-8 *Time history of maximum EPWP ratio*

(3) Effect of Mean N1 Value and Degree of Variability

The effect of varying the mean SPT N1 value was investigated by performing simulations with a mean value N1=15 and twice the acceleration amplitude of the input motion shown in Figure A1-6. The amplitude was determined to obtain almost the same liquefaction condition (i.e. maximum EPWP ratio after shaking) as the case of N1=5 for deterministic models. In the simulations, the N1 value was treated as a stochastic variable following the Gaussian model. The variations of maximum lateral displacement with depth are

shown in Figure A1-11(a) with the results of nine stochastic realizations, and three uniform models. The trend could be considered similar to the stochastic realizations shown in Figure A1-7(a) with a mean N1=5, the surface displacement for the Gaussian stochastic are less than those for uniform models with N1 value between the 20th and 80th percentiles, as is the case with a mean N1=5.

The time history of maximum EPWP ratio (Pmax) is depicted in Figure A1-11(b), no significant difference in the behavior among stochastic fields was founded in comparison with the case with a mean value of N1=5 (Figure A1-7(b)).

Relating to the average EPWP ratio (Pave), Figure A1-11(c) shows that there not exist significant differences between the realizations with stochastic fields, and the realizations with deterministic models; this figure shows a different behavior in comparison to the obtained in Figure A1-9(a) (with a mean value N1=5). The reason has not been yet confirmed, but may be related to the fact that increasing the mean value reduce the contrast between looser and denser sands (i.e. for N1=5, the value of the 20th percentile in the Gaussian distribution corresponds around 66% of the mean value, however for N1=5, the same percentage is increased to 91.3%), however further studies are required to reach a definitive conclusion.

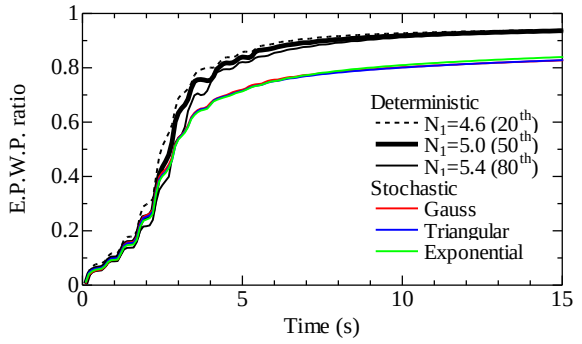

(a) The case of variable SPT N1 value

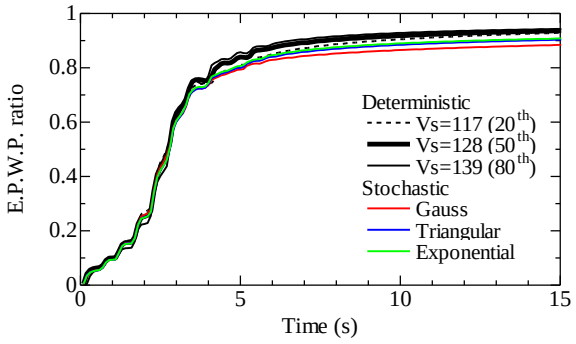

(b) The case of variable shear wave velocity

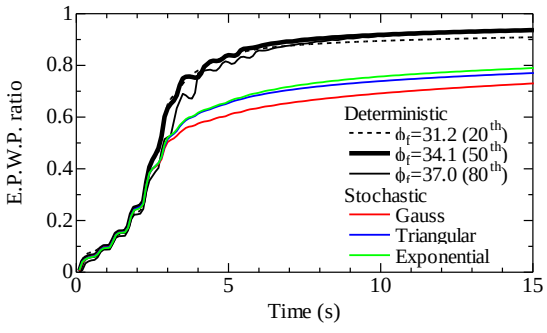

(c) The case of variable internal friction angle

Figure A1-9 *Time history of averaged EPWP ratio.*

For comparative purposes, all previous stochastic fields were generated with the same degree of variability (i.e. coefficient of variability cv=0.1); so, in order to investigate the effect of the change in the variability, nine Gaussians stochastic models, and three uniform models, considering a cv=0.4 and mean value of N1=15 were performed (Figure A1-12).

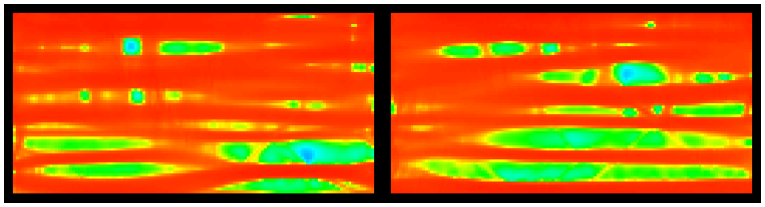

(a) Stochastic model: Gaussian

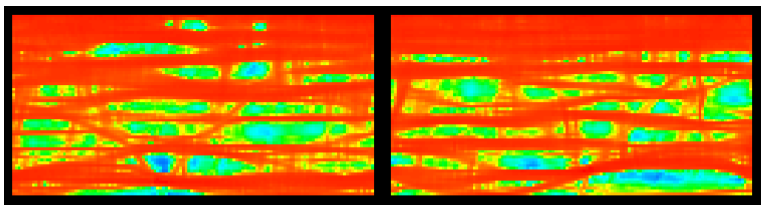

(b) Stochastic model: Triangular

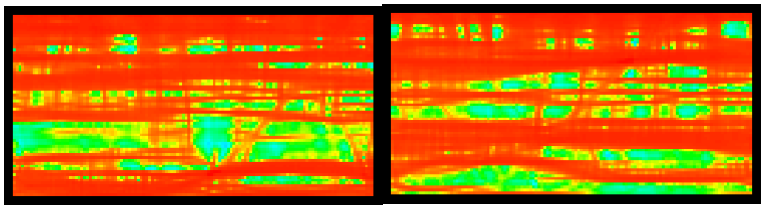

(c) Stochastic model: Exponential

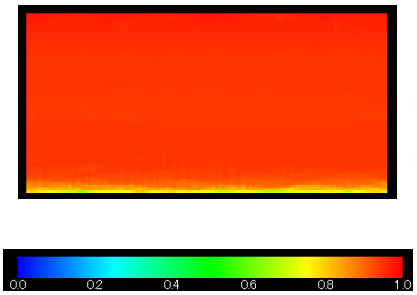

(d) Deterministic model (N1=5)

Figure A1-10 *Distribution of EPWP ratio after shaking (the case of variable SPT N1 value).*

As expected, in general, the results show that along with the increase of the input variability, an increase in the variability among each stochastic realizations is obtained (Figures A1-11 and A1-12). In the case of the horizontal displacements, it was founded that the stochastic realizations cover a wider range of displacements within the depth than the deterministic models, however, it should be noticed that the surface displacements always results less than the obtained with the deterministic mean value (i.e. 50th percentile).

Relating to the maximum EPWP values (Figure A1-12(b)), a higher rate during the generation of excess pore water pressure was obtained (in comparison to Figure A1-11(b)), this effect may be related to that increasing the input variability increase the contrast between looser and denser zones (i.e. for cv=0.1, the value of the 20th per-centile in the Gaussian distribution corresponds around 91.3% of the mean value, however for cv=0.4, the same percentage is decreased to 66.7% approximately), so, the looser zones would experiment a considerable smaller liquefaction resistance, and build up the EPWP faster than the deterministic models.

Regarding to the average value of EPWP, a similar response to Figure A1-9(a) were founded (in contrast to Figure A1-11(c)), because a reduction in the average value is founded, however, as in this case the variability is increased, a decreasing between 8% to 20% was founded (in Figure A1-9(a) the reduction corresponds to 10% approximately). This effect may also be related to the fact that the increase in the input variability would increase the contrast between looser and denser sands, which will produce a faster increase of EPWP in locally looser zones, and would decrease the amount of shear stress on surrounding denser zones (increasing its liquefaction resistance).

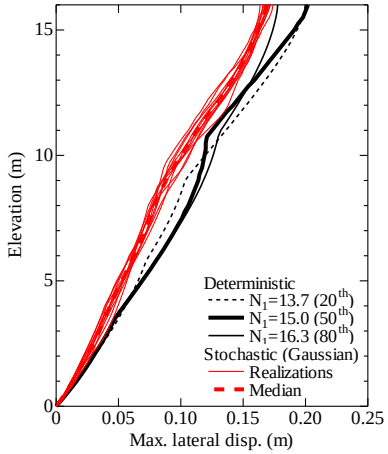

(a) The case of variable SPT N1 value (mean N1=15, cv=0.1)

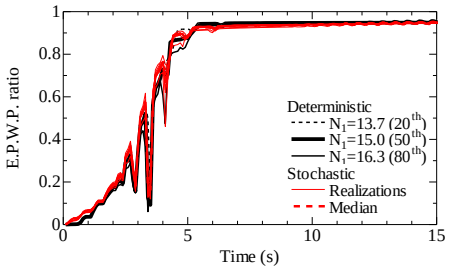

(b) Time history of maximum EPWP ratio (mean N1=15, cv=0.1)

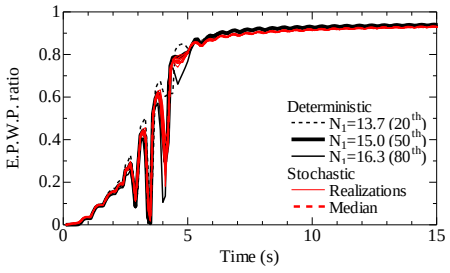

(c) Time history of Average EPWP ratio (mean N1=15, cv=0.1)

Figure A1-11 *Maximum lateral displacement profile, Maximum EPWP Ratio, and Average EPWP ratio for Gaussian Realizations (mean N1=15, cv=0.1).*

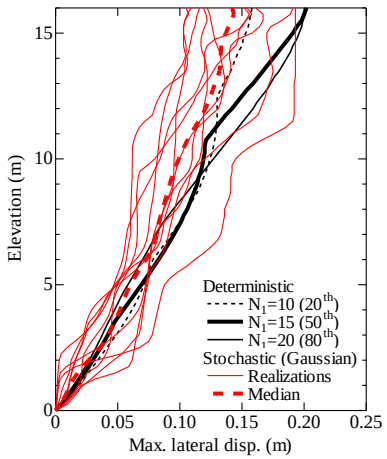

(a) The case of variable SPT N1 value (mean N1=15, cv=0.4)

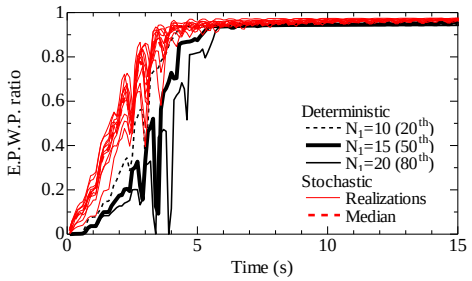

(b) Time history of maximum EPWP ratio (mean N1=15, cv=0.4)

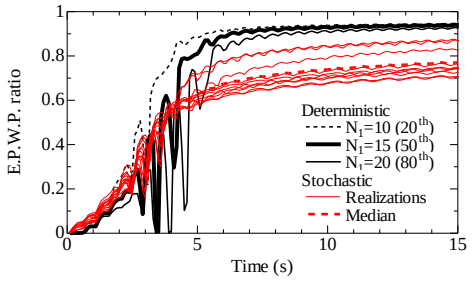

(c) Time history of Average EPWP ratio (mean N1=15, cv=0.4)

Figure A1-12 *Maximum lateral displacement profile, Maximum EPWP Ratio, and Average EPWP ratio for Gaussian Realizations (mean N1=15, cv=0.4).*

A1-5 Conclusions

The effects of soil heterogeneity on the liquefaction potential and dynamic response of stochastically heterogeneous soil deposits was examined using two-dimensional nonlinear seismic response analyses under undrained conditions, so it is important to remark that the results of this study are valid for the conditions only after the shaking process (i.e. the study of the behavior during and after EPWP dissipation would be analyzed in further steps). In order to consider the spatial variability of soil properties, three types of sample functions (i.e. Gaussian, triangular, and exponential) of discretized stochastic fields were used for the spatial distribution of the SPT N1 value, shear wave velocity, and internal friction angle in the liquefiable deposits.

A series of the analyses has revealed that the heterogeneity of shear modulus has no significant effect on the maximum lateral displacement profiles and the distribution of excess pore water pressure ratio if other parameters remain constant. In contrast, the results were influenced by the spatial variability in SPT N value and internal friction angle. The average value of excess pore water pressure ratio for the stochastic models became less than that for the deterministic models. In particular, the heterogeneity of internal friction angle has been recognized to reduce the average value to about 80% of that in the case of homogeneity. This is because the variation of shear wave velocity (or initial shear modulus) may only affect linear elastic behavior, whereas a strength parameter (e.g. internal friction angle) is considered to exercise a dominant influence on nonlinear behavior such as liquefaction.

Comparison between the stochastic and deterministic models has illustrated how the representative value depends on the specific response measure and the timing of concern. When the SPT N1 value and the internal friction angle were treated as a stochastic variable for loose sandy ground, the lateral displacements for the stochastic realizations were out of the range between the 20th and 80th percentiles. With regard to the time history of excess pore water pressure ratio, the representative N1 value was almost the same as a mean N1 value (i.e. the 50th percentile) if the maximum value of excess pore water pressure ratio during and after shaking was the response measure of concern. In contrast, the representative value has been confirmed to vary depending on the timing if the average value of excess pore water pressure ratio is the response measure of concern.

Analysis of the influence of “Increase the degree of variability” and “Increase of the mean value” showed that with the increase of variability in the input parameters, as expected, the variability among stochastic realizations would be increased; also, it was pointed out that the behavior of “maximum” and “average” EPWP, may be influenced by the contrast (in percentage) between looser and denser zones in the stochastic fields.

A2. Stress Strain Characteristics of the Hollow Cylinder Cyclic Torsional Shear Tests [26]

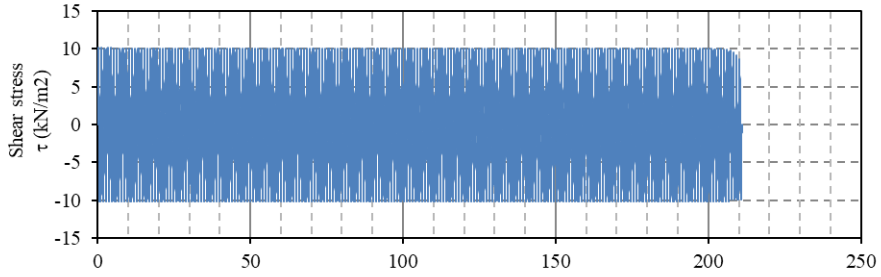

(a)

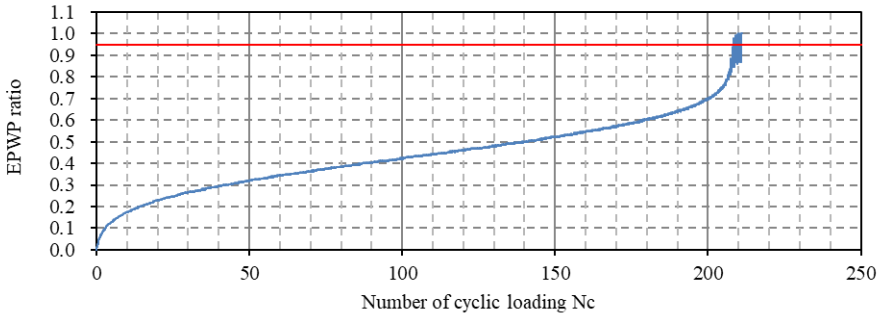

(b)

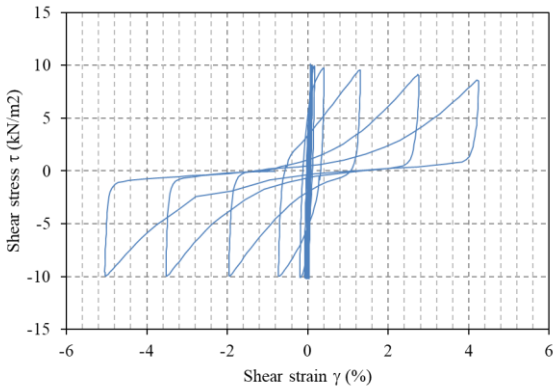

(c)

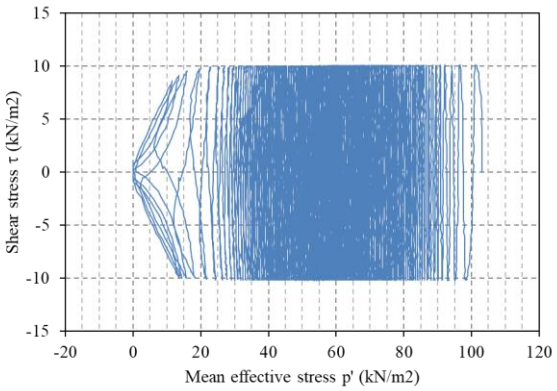

(d)

Figure A1 (a) Time History of Shear Stress - Model Dr50-1-1 (b) Time History of EPWP ratio development - Model Dr50-1-1 (c) Stress-Strain curve - Model Dr50-1-1 (d) Stress path - Model Dr50-1-1

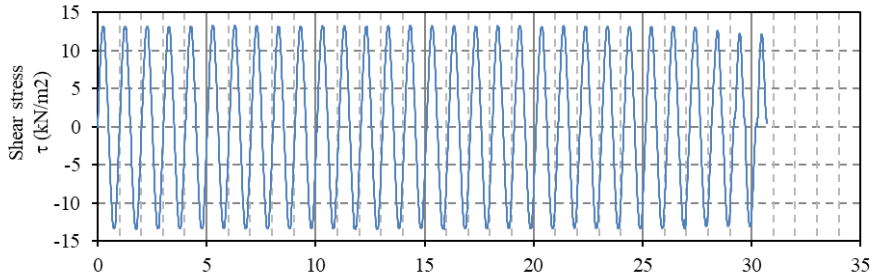

(a)

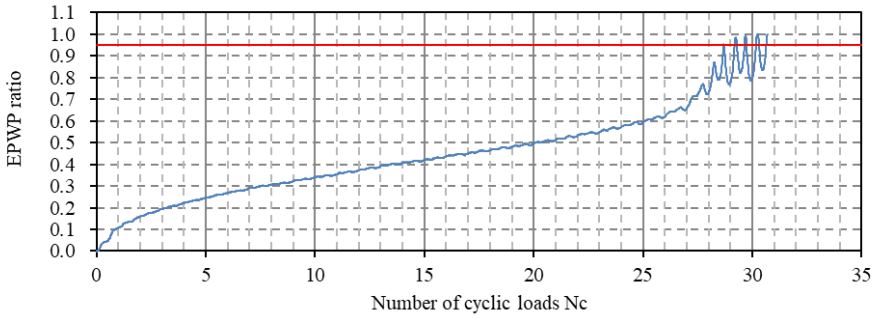

(b)

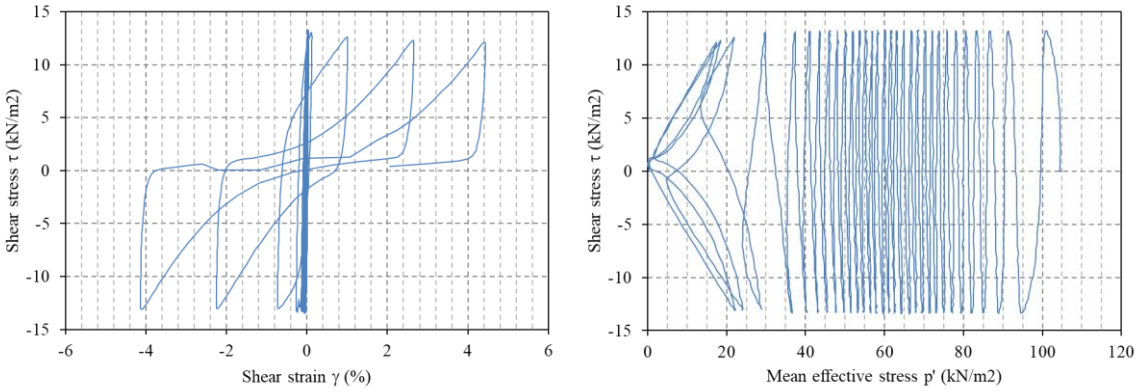

(c) (d)

Figure A2 (a) Time History of Shear Stress - Model Dr50-1-2 (b) Time History of EPWP ratio development - Model Dr50-1-2 (c) Stress-Strain curve - Model Dr50-1-2 (d) Stress path - Model Dr50-1-2

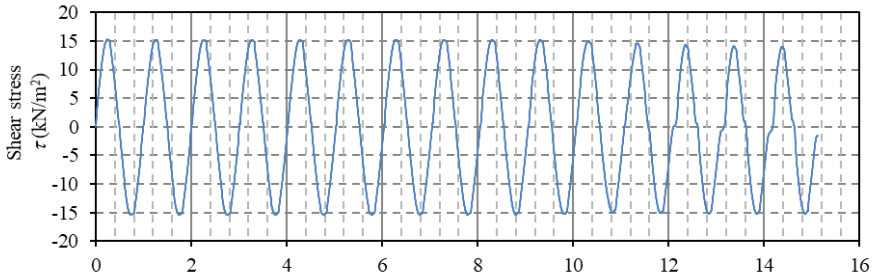

(a)

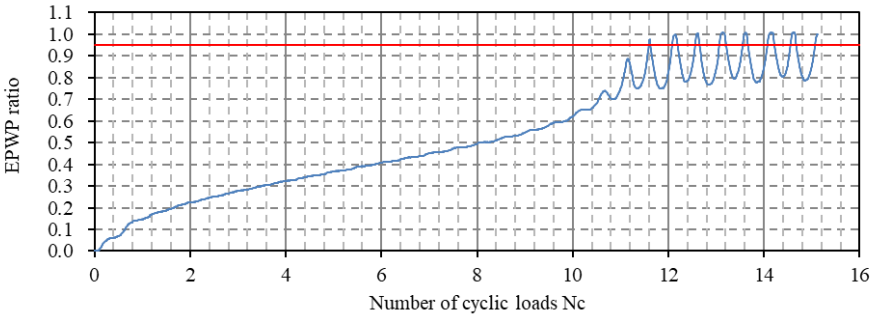

(b)

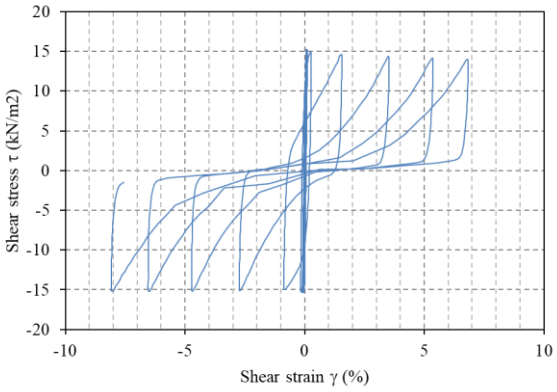

(c)

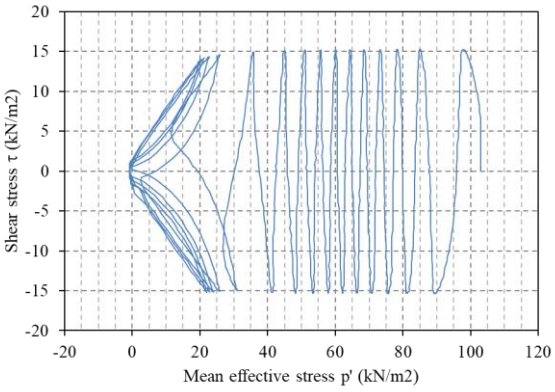

(d)

Figure A3 (a) Time History of Shear Stress - Model Dr50-1-3 (b) Time History of EPWP ratio development - Model Dr50-1-3 (c) Stress-Strain curve - Model Dr50-1-3 (d) Stress path - Model Dr50-1-3

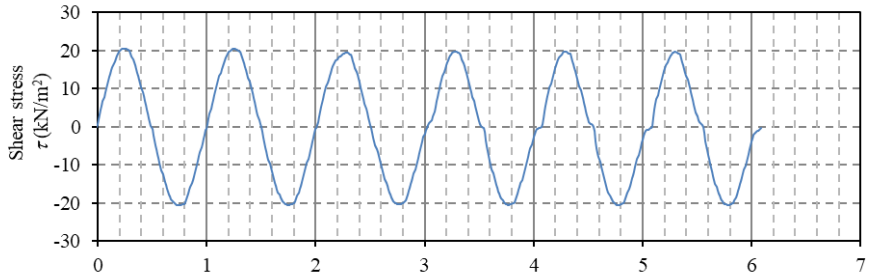

(a)

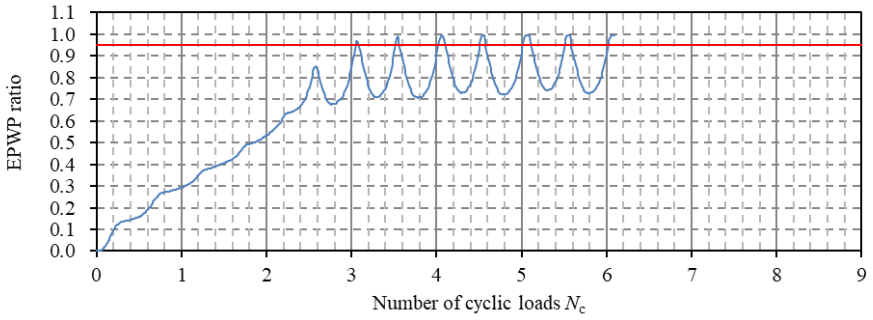

(b)

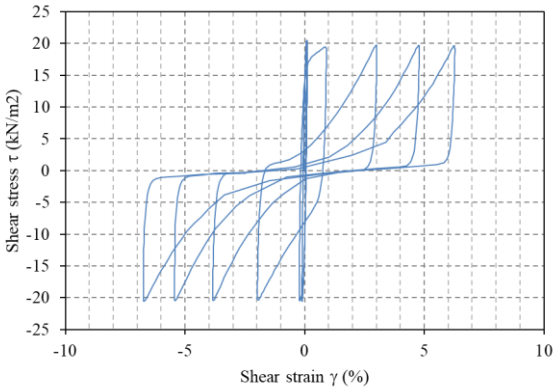

(c)

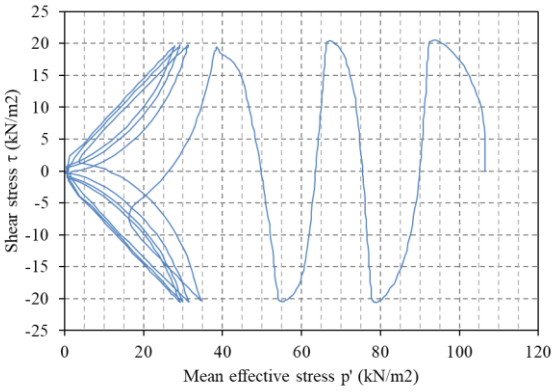

(d)

Figure A4 (a) Time History of Shear Stress - Model Dr50-1-4 (b) Time History of EPWP ratio development - Model Dr50-1-4 (c) Stress-Strain curve - Model Dr50-1-4 (d) Stress path - Model Dr50-1-4

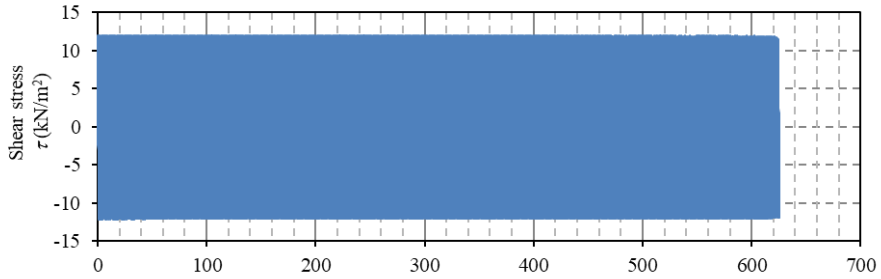

(a)

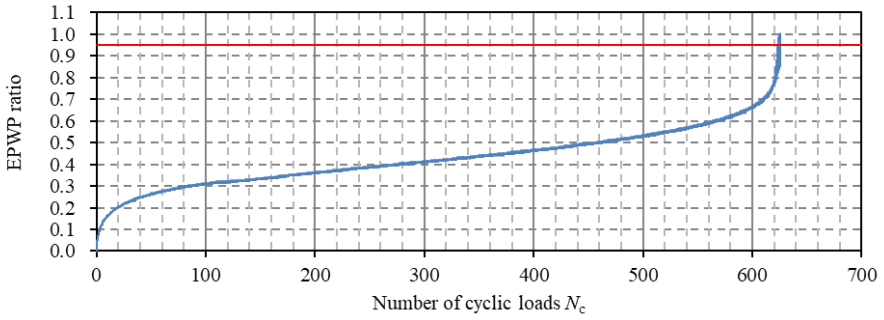

(b)

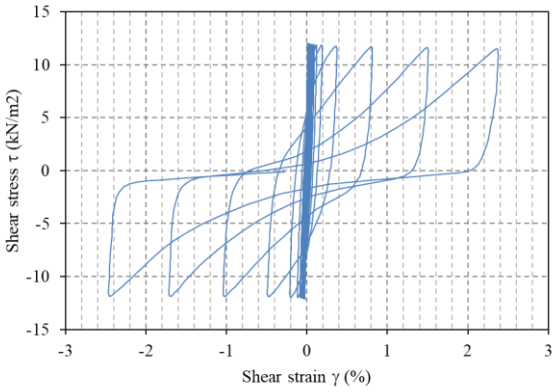

(c)

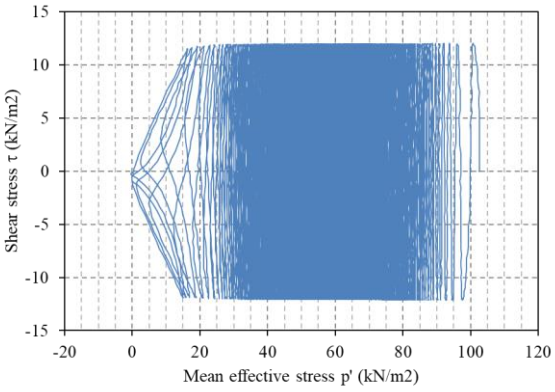

(d)

Figure A5 (a) Time History of Shear Stress - Model Dr60-1-1 (b) Time History of EPWP ratio development - Model Dr60-1-1 (c) Stress-Strain curve - Model Dr60-1-1 (d) Stress path - Model Dr60-1-1

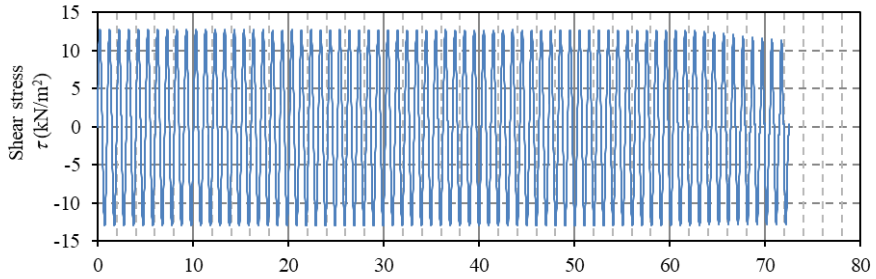

(a)

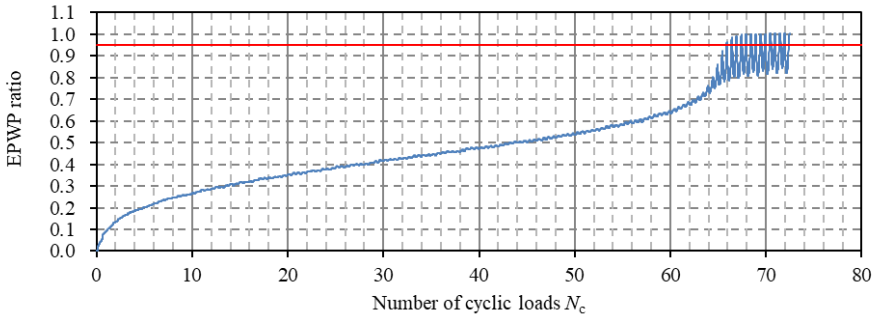

(b)

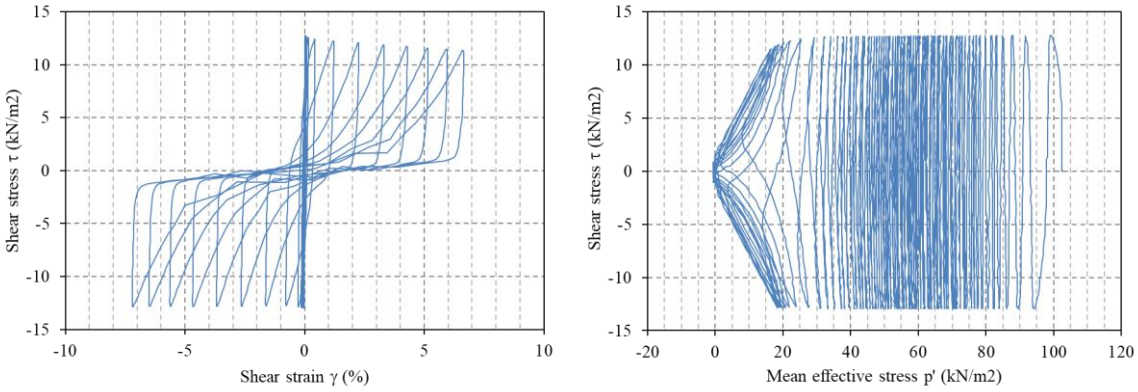

(c) (d)

Figure A6 (a) Time History of Shear Stress - Model Dr60-1-2 (b) Time History of EPWP ratio development - Model Dr60-1-2 (c) Stress-Strain curve - Model Dr60-1-2 (d) Stress path - Model Dr60-1-2

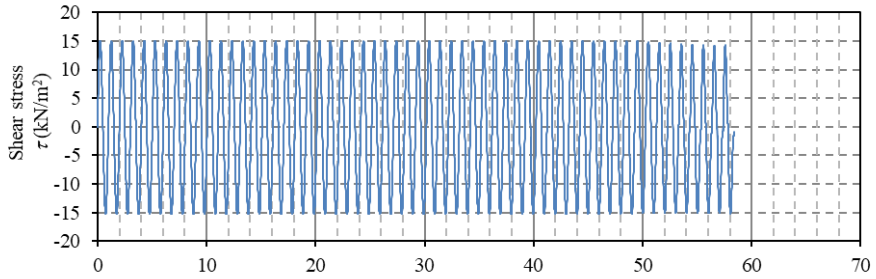

(a)

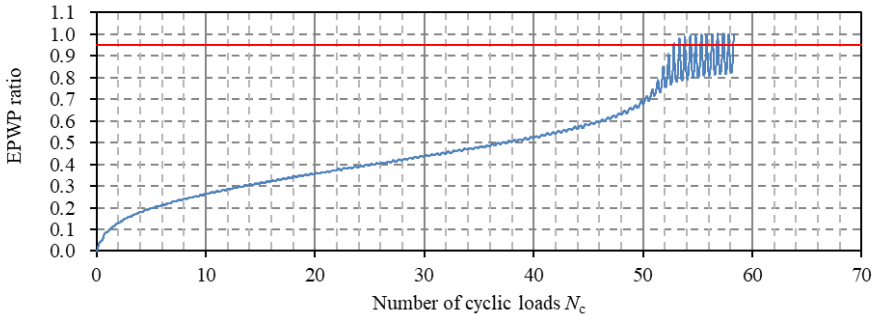

(b)

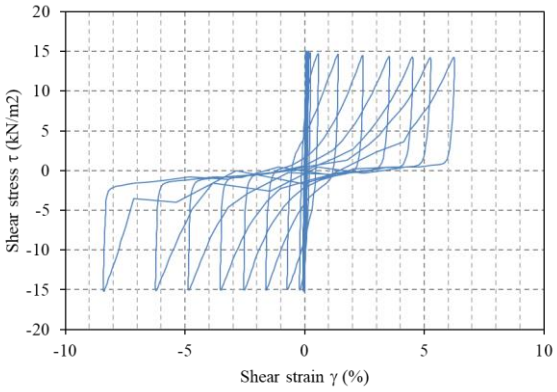

(c)

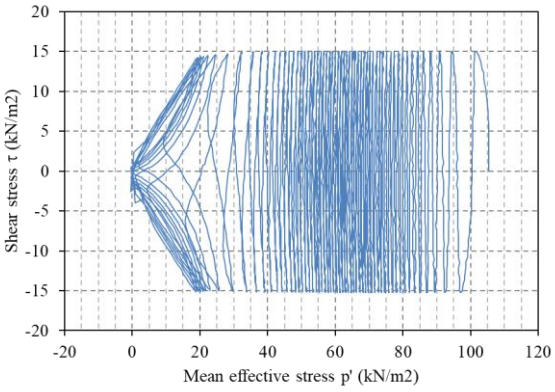

(d)

Figure A7 (a) Time History of Shear Stress - Model Dr60-1-3 (b) Time History of EPWP ratio development - Model Dr60-1-3 (c) Stress-Strain curve - Model Dr60-1-3 (d) Stress path - Model Dr60-1-3

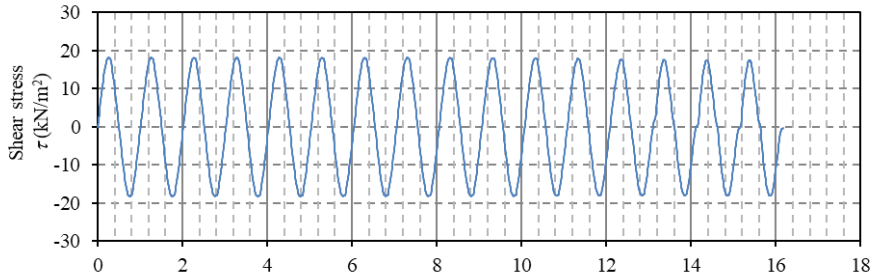

(a)

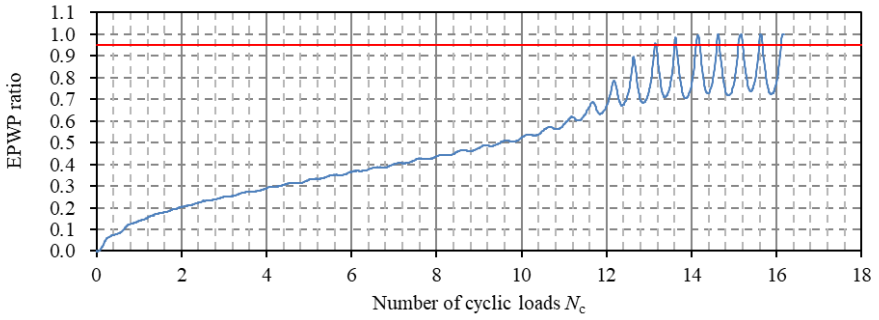

(b)

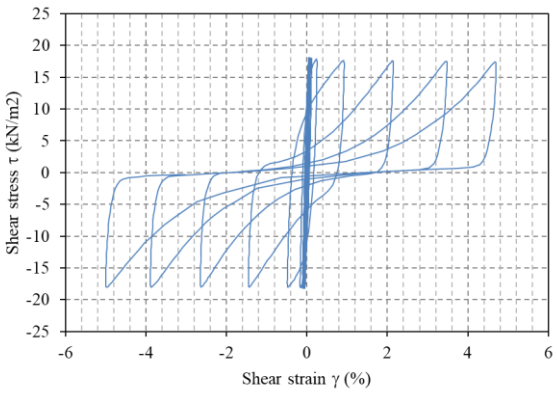

(c)

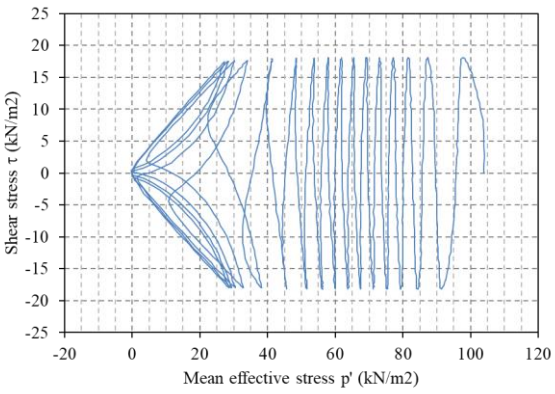

(d)

Figure A8 (a) Time History of Shear Stress - Model Dr60-1-4 (b) Time History of EPWP ratio development - Model Dr60-1-4 (c) Stress-Strain curve - Model Dr60-1-4 (d) Stress path - Model Dr60-1-4

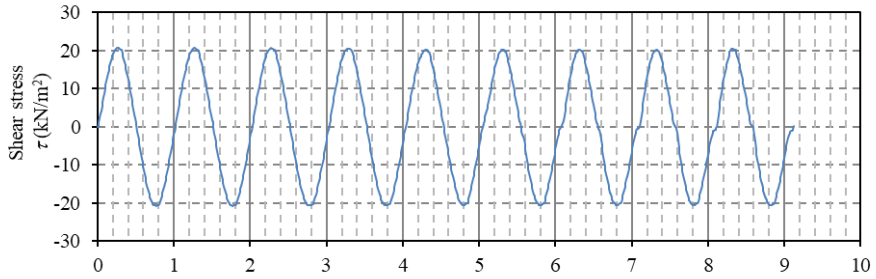

(a)

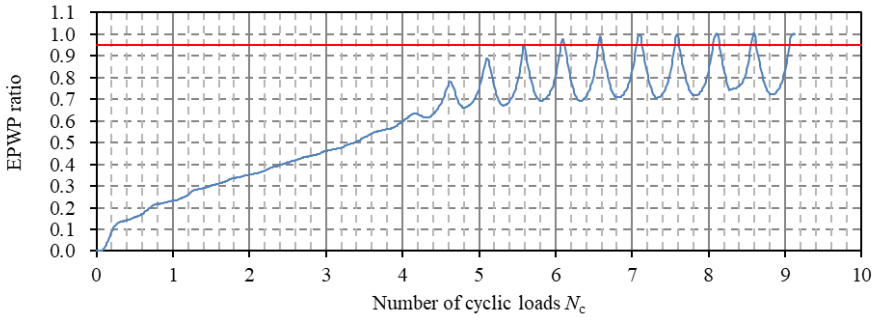

(b)

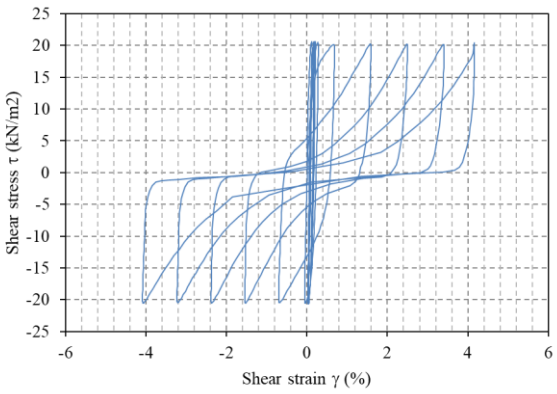

(c)

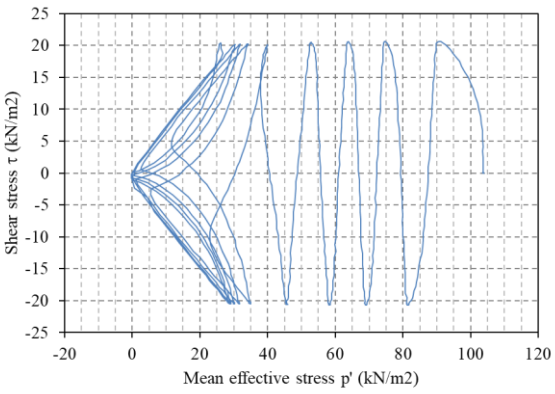

(d)

Figure A9 (a) Time History of Shear Stress - Model Dr60-1-5 (b) Time History of EPWP ratio development - Model Dr60-1-5 (c) Stress-Strain curve - Model Dr60-1-5 (d) Stress path - Model Dr60-1-5

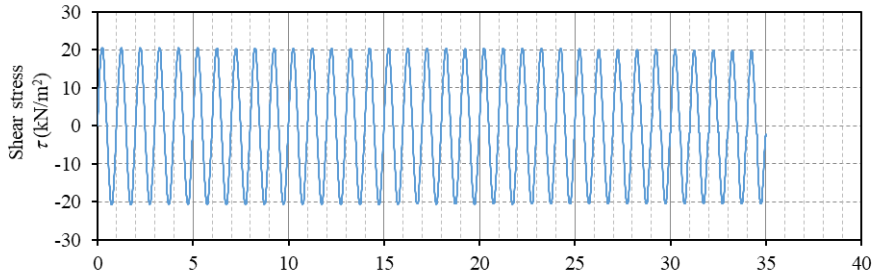

(a)

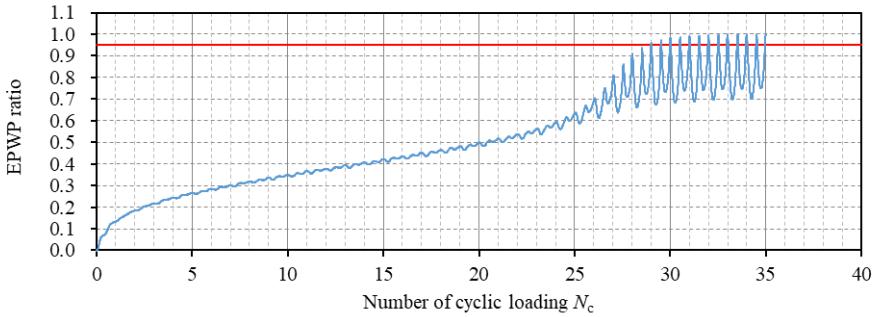

(b)

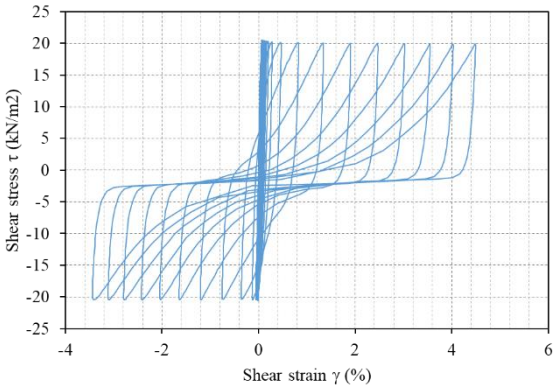

(c)

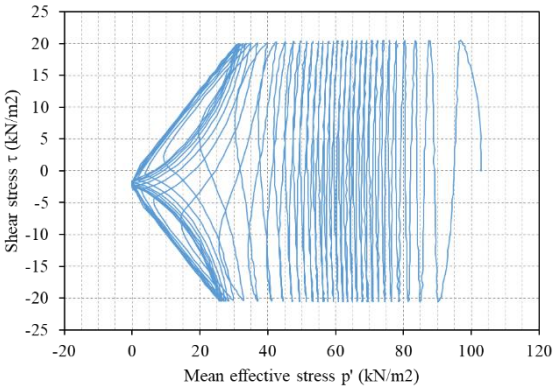

(d)

Figure A10 (a) Time History of Shear Stress - Model Dr70-1-1 (b) Time History of EPWP ratio development - Model Dr70-1-1 (c) Stress-Strain curve - Model Dr70-1-1 (d) Stress path - Model Dr70-1-1

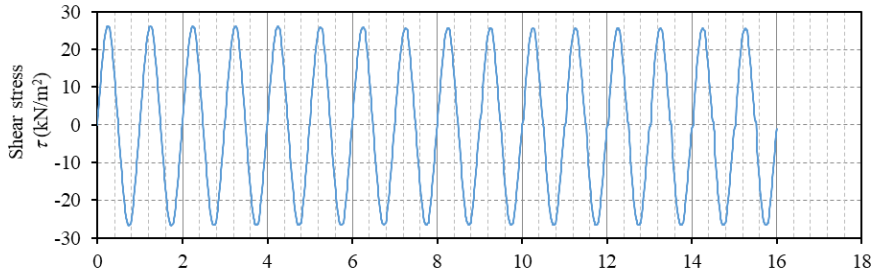

(a)

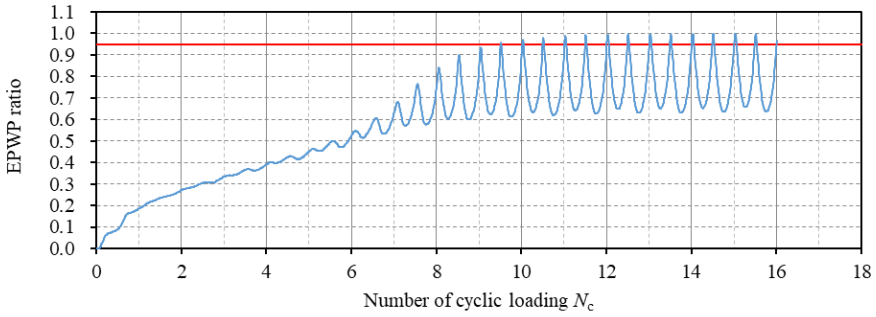

(b)

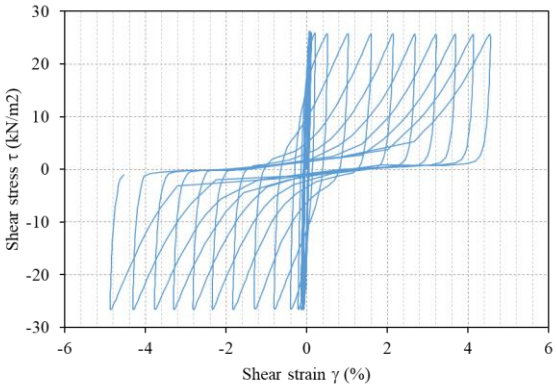

(c)

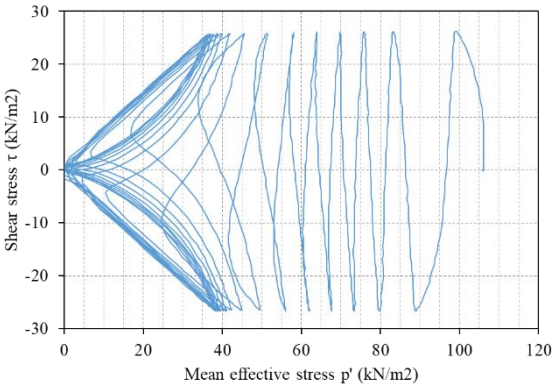

(d)

Figure A11 (a) Time History of Shear Stress - Model Dr70-1-2 (b) Time History of EPWP ratio development - Model Dr70-1-2 (c) Stress-Strain curve - Model Dr70-1-2 (d) Stress path - Model Dr70-1-2

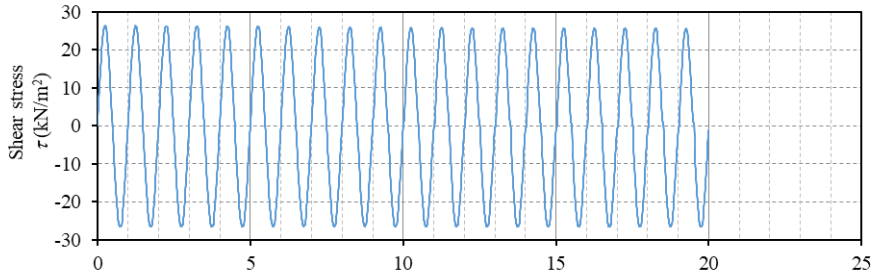

(a)

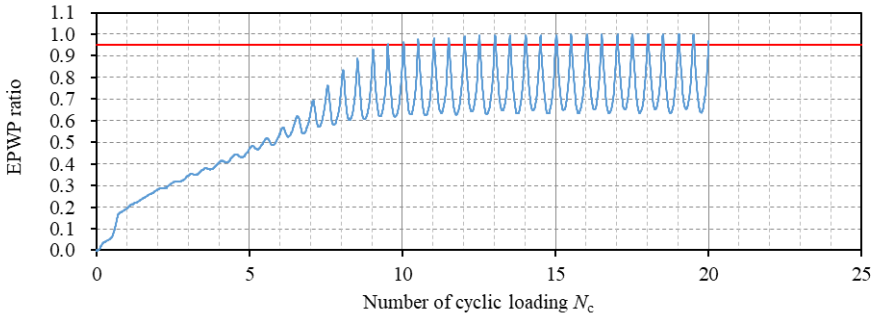

(b)

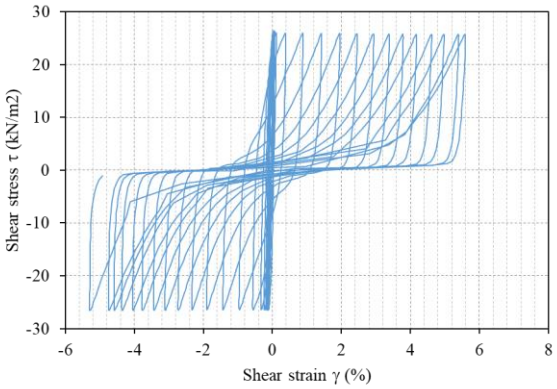

(c)

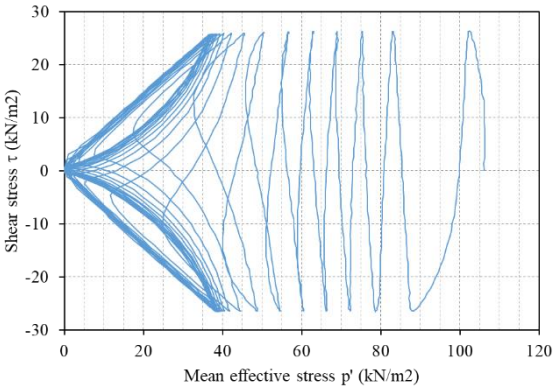

(d)

Figure A12 (a) Time History of Shear Stress - Model Dr70-1-3 (b) Time History of EPWP ratio development - Model Dr70-1-3 (c) Stress-Strain curve - Model Dr70-1-3 (d) Stress path - Model Dr70-1-3

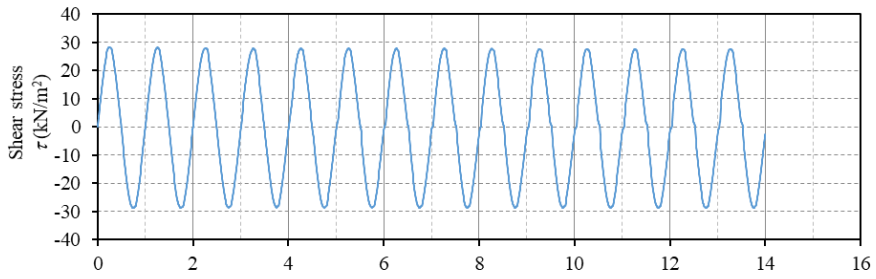

(a)

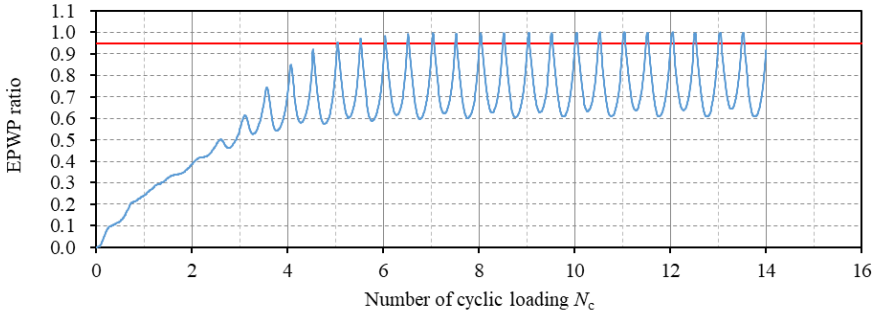

(b)

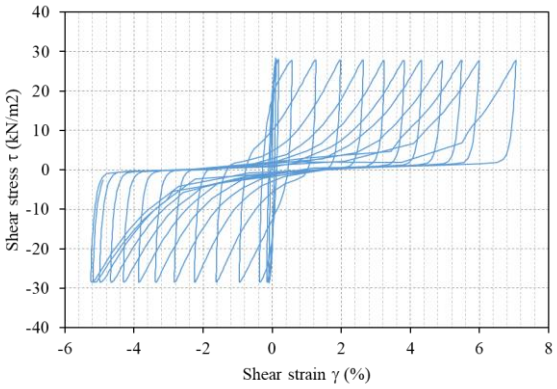

(c)

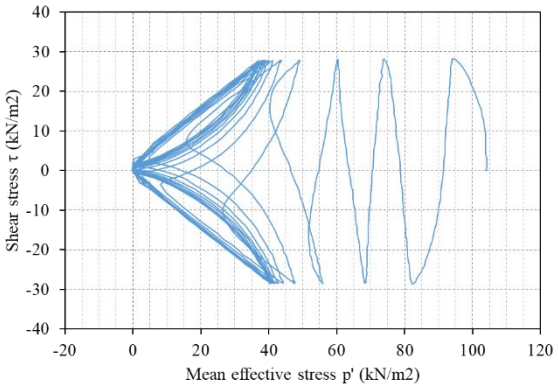

(d)

Figure A13 (a) Time History of Shear Stress - Model Dr70-1-4 (b) Time History of EPWP ratio development - Model Dr70-1-4 (c) Stress-Strain curve - Model Dr70-1-4 (d) Stress path - Model Dr70-1-4

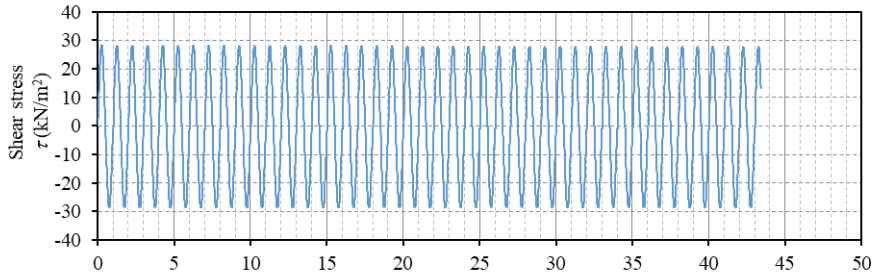

(a)

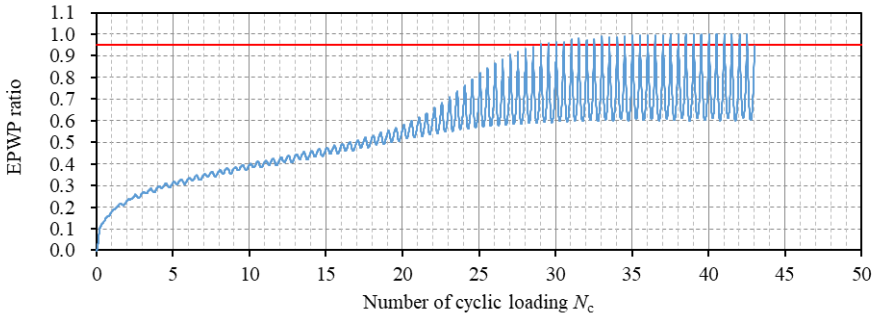

(b)

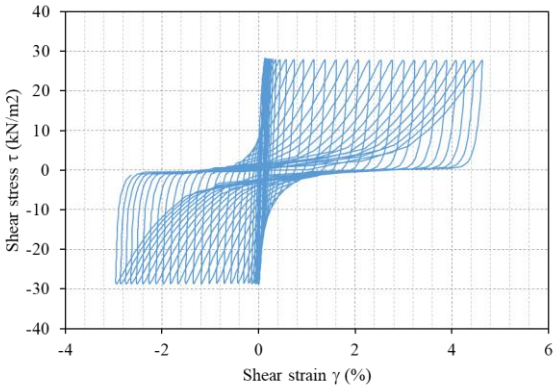

(c)

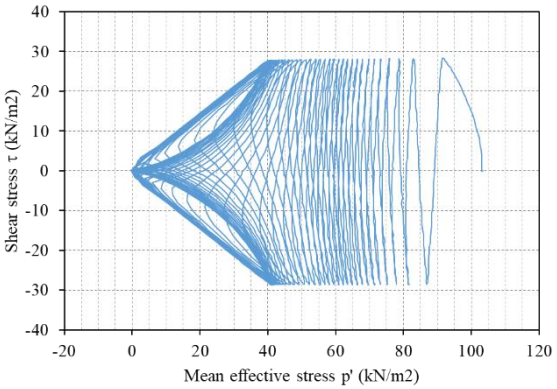

(d)

Figure A14 (a) Time History of Shear Stress - Model Dr85-1-1 (b) Time History of EPWP ratio development - Model Dr85-1-1 (c) Stress-Strain curve - Model Dr85-1-1 (d) Stress path - Model Dr85-1-1

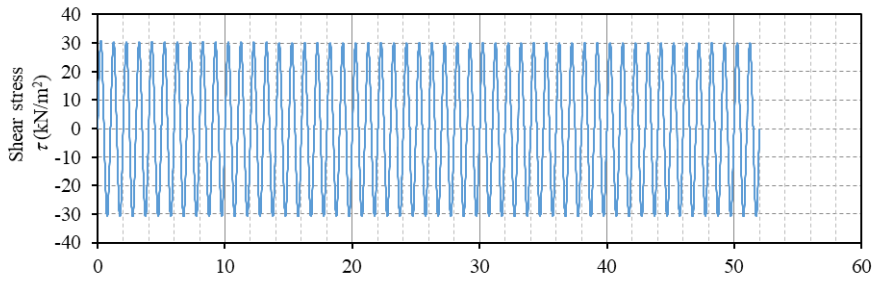

(a)

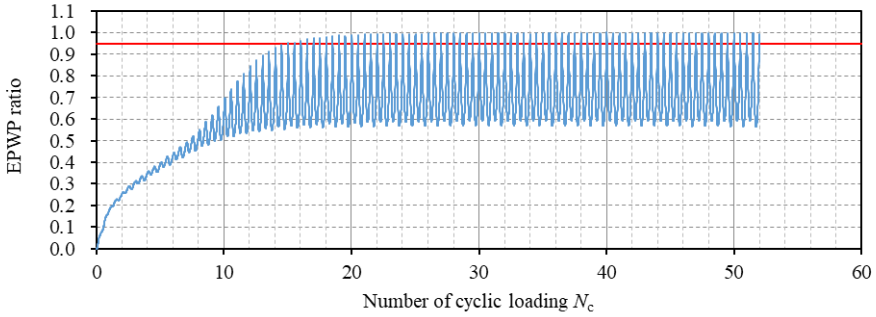

(b)

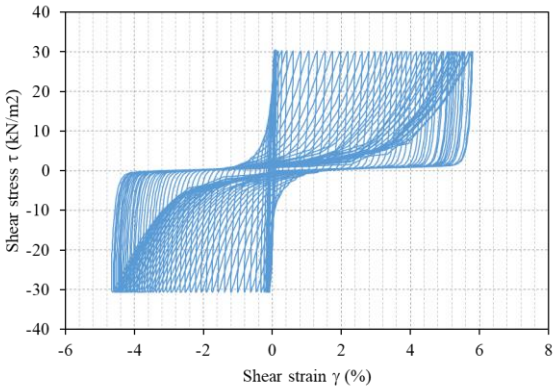

(c)

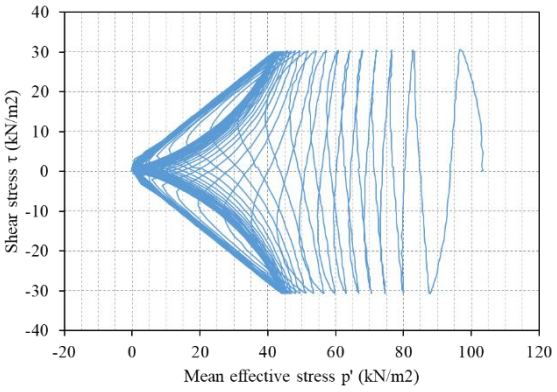

(d)

Figure A15 (a) Time History of Shear Stress - Model Dr85-1-2 (b) Time History of EPWP ratio development - Model Dr85-1-2 (c) Stress-Strain curve - Model Dr85-1-2 (d) Stress path - Model Dr85-1-2

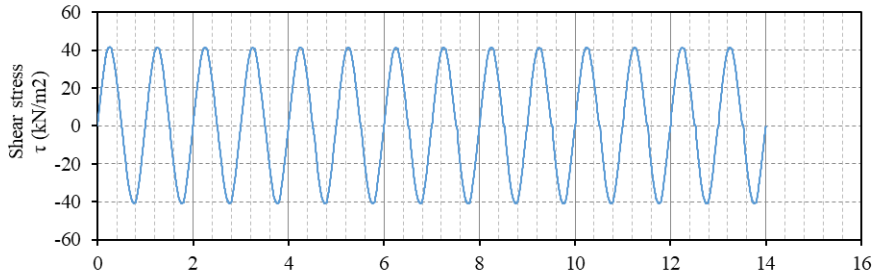

(a)

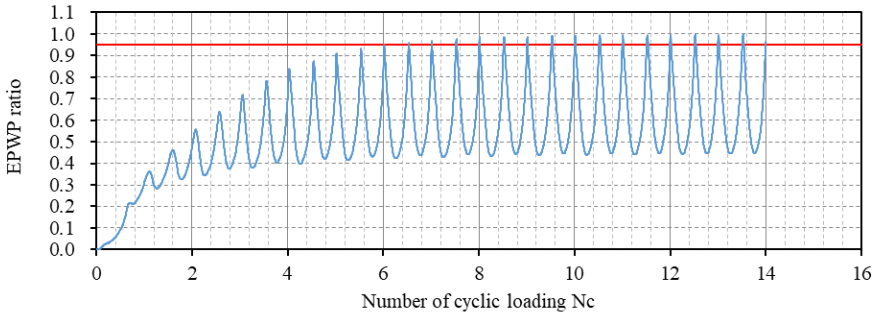

(b)

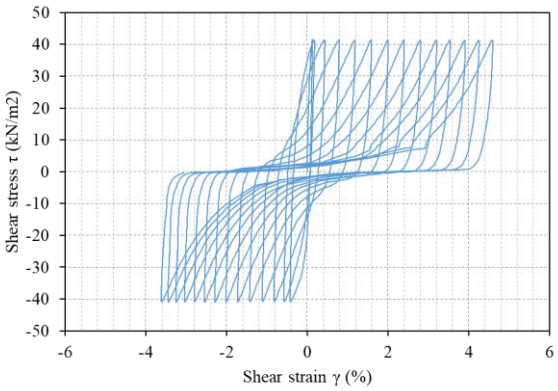

(c)

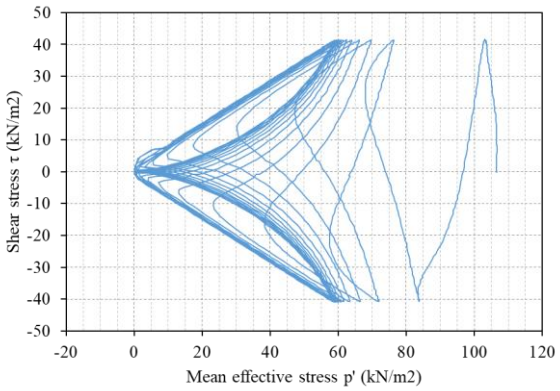

(d)

Figure A16 (a) Time History of Shear Stress - Model Dr85-1-3 (b) Time History of EPWP ratio development - Model Dr85-1-3 (c) Stress-Strain curve - Model Dr85-1-3 (d) Stress path - Model Dr85-1-3

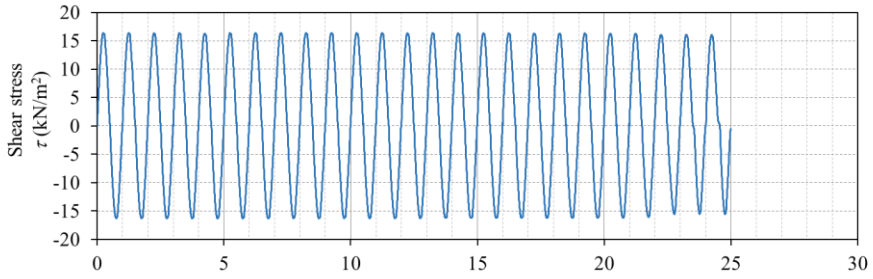

(a)

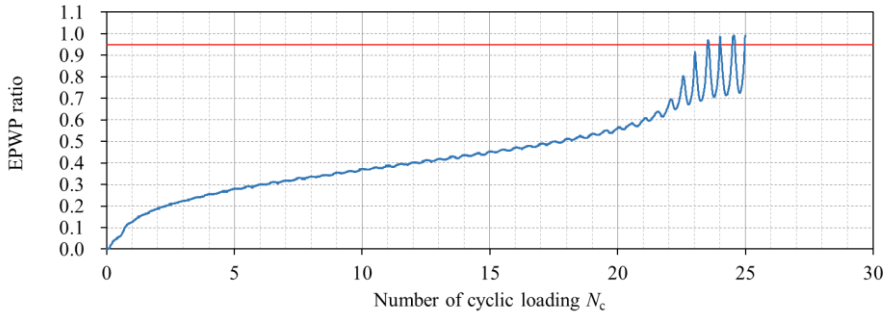

(b)

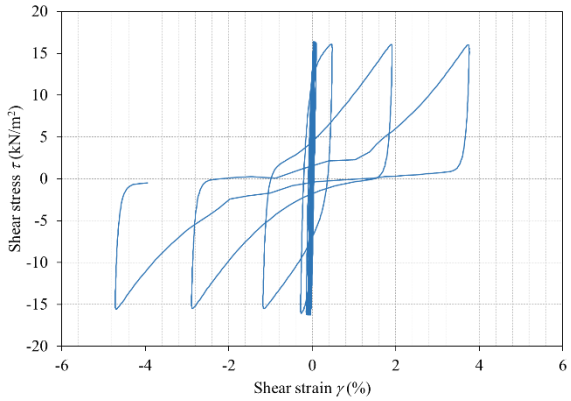

(c)

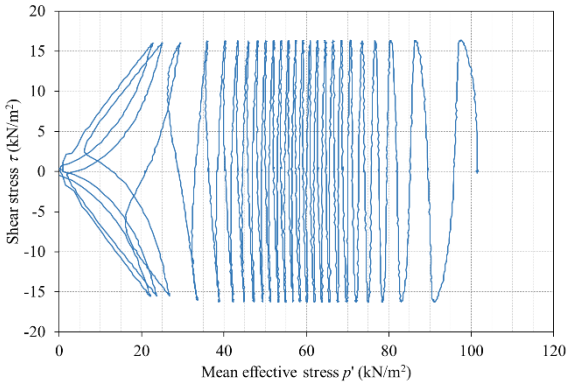

(d)

Figure A17 (a) Time History of Shear Stress - Model Dr50-2-1 (b) Time History of EPWP ratio development - Model Dr50-2-1 (c) Stress-Strain curve - Model Dr50-2-1 (d) Stress path - Model Dr50-2-1

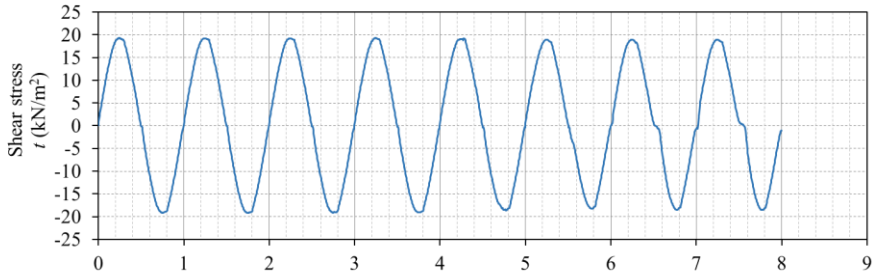

(a)

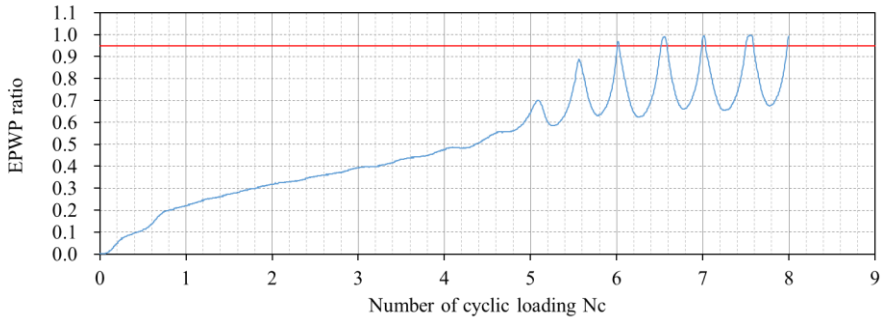

(b)

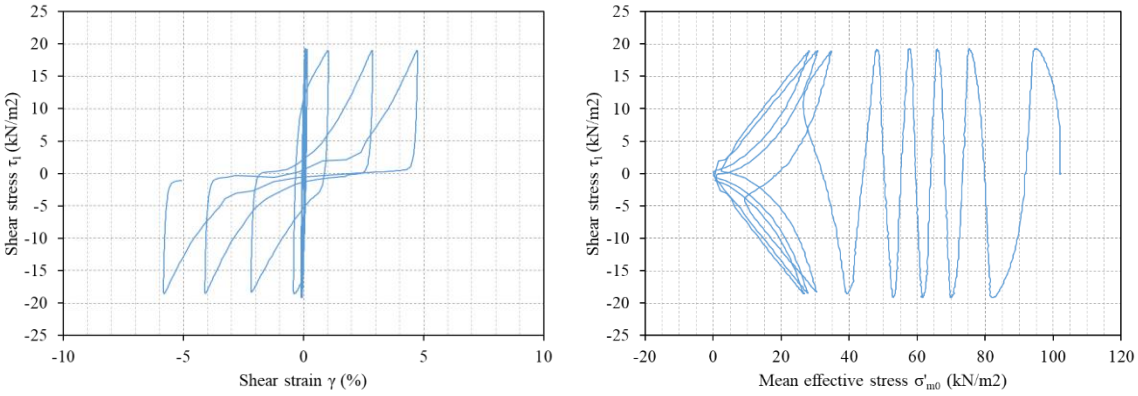

(c) (d)

Figure A18 (a) Time History of Shear Stress - Model Dr50-2-2 (b) Time History of EPWP ratio development - Model Dr50-2-2 (c) Stress-Strain curve - Model Dr50-2-2 (d) Stress path - Model Dr50-2-2

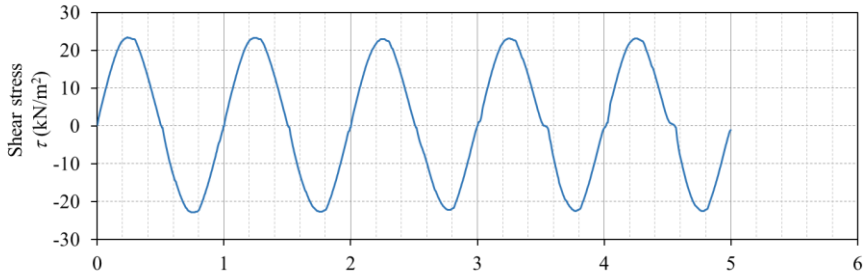

(a)

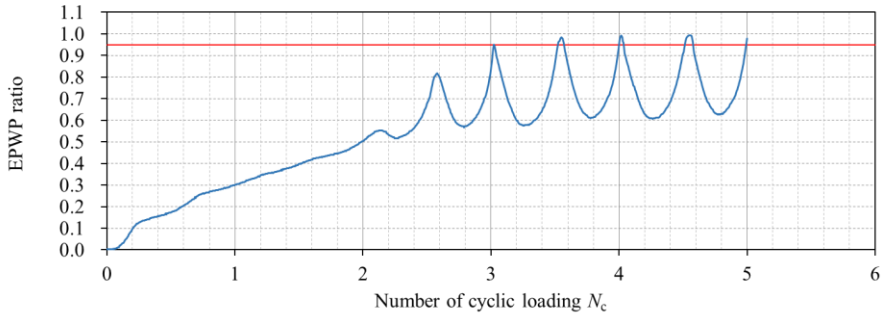

(b)

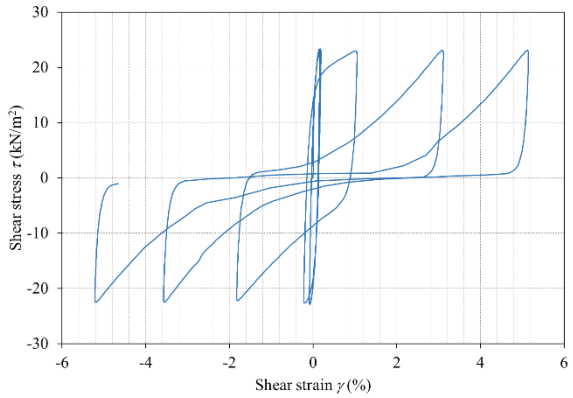

(c)

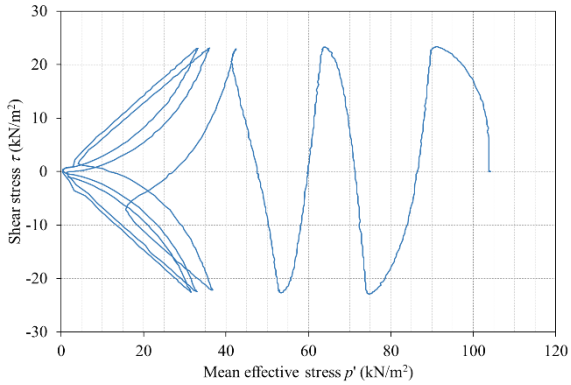

(d)

Figure A19 (a) Time History of Shear Stress - Model Dr50-2-3 (b) Time History of EPWP ratio development - Model Dr50-2-3 (c) Stress-Strain curve - Model Dr50-2-3 (d) Stress path - Model Dr50-2-3

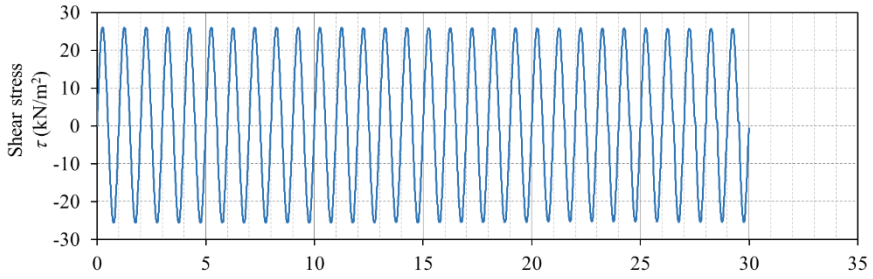

(a)

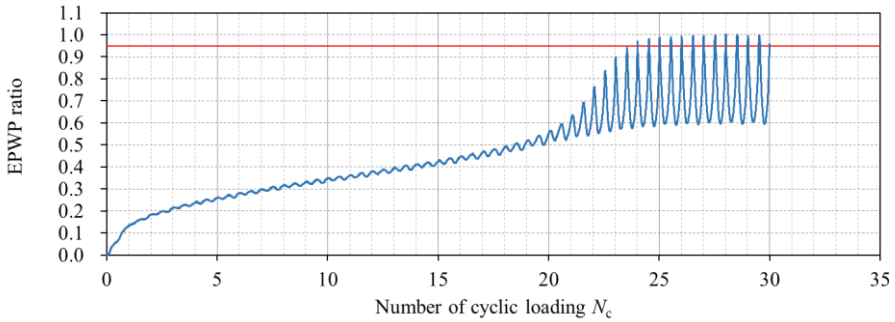

(b)

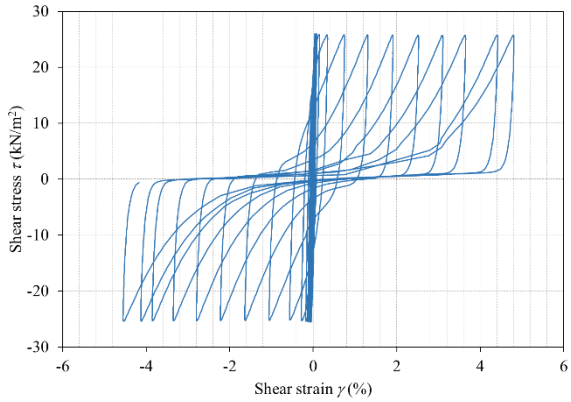

(c)

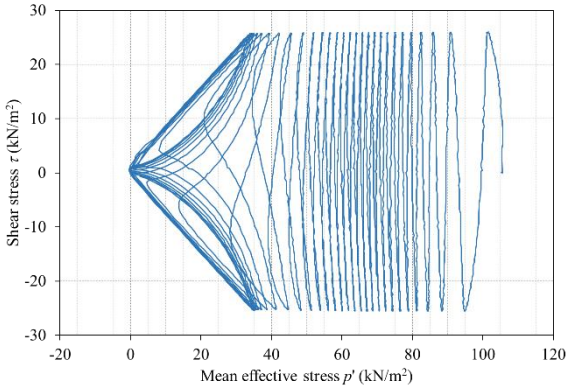

(d)

Figure A20 (a) Time History of Shear Stress - Model Dr70-2-1 (b) Time History of EPWP ratio development - Model Dr70-2-1 (c) Stress-Strain curve - Model Dr70-2-1 (d) Stress path - Model Dr70-2-1

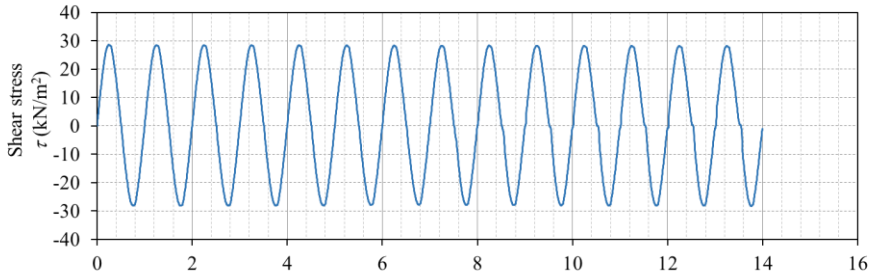

(a)

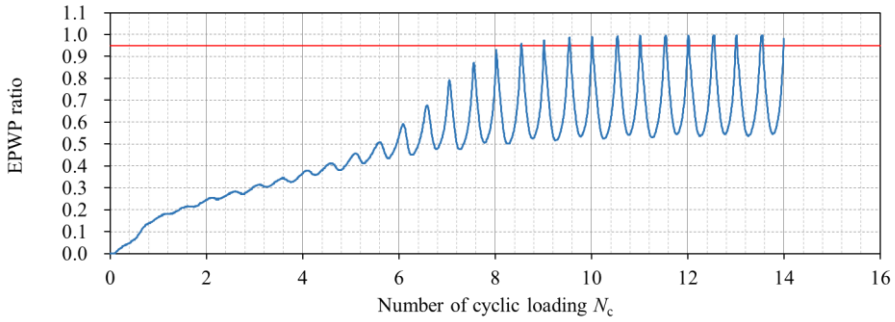

(b)

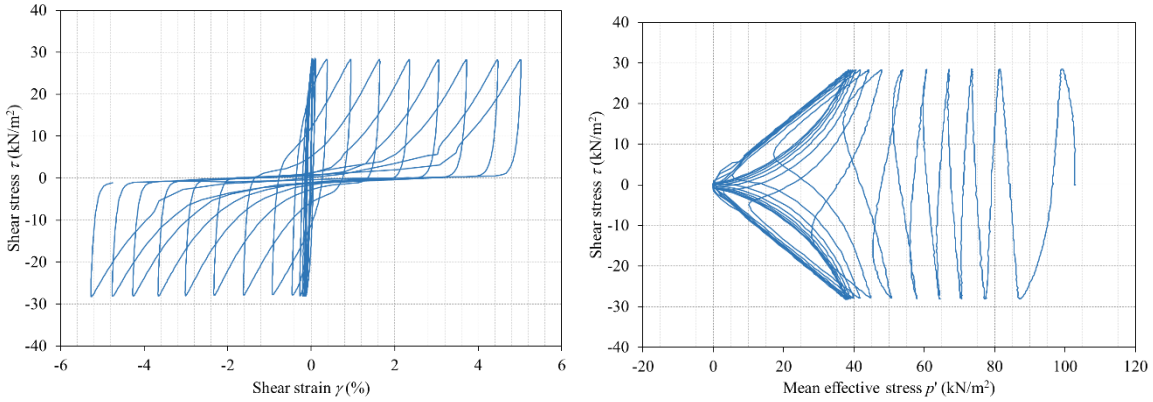

(c) (d)

Figure A21 (a) Time History of Shear Stress - Model Dr70-2-2 (b) Time History of EPWP ratio development - Model Dr70-2-2 (c) Stress-Strain curve - Model Dr70-2-2 (d) Stress path - Model Dr70-2-2

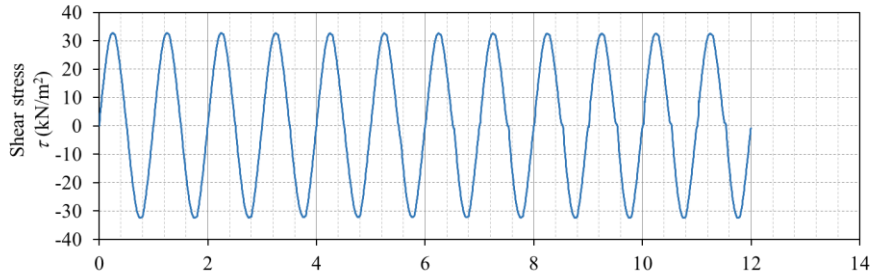

(a)

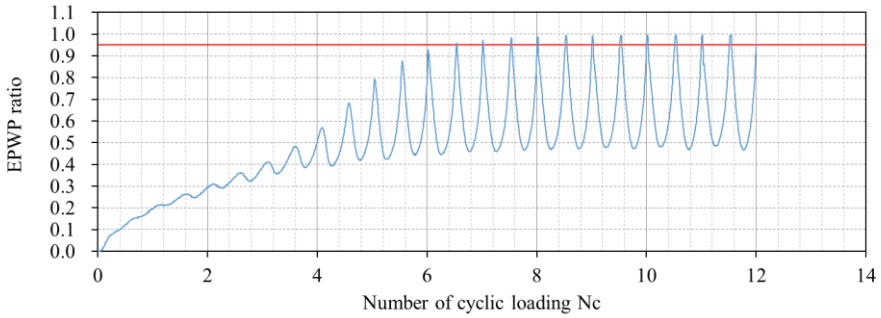

(b)

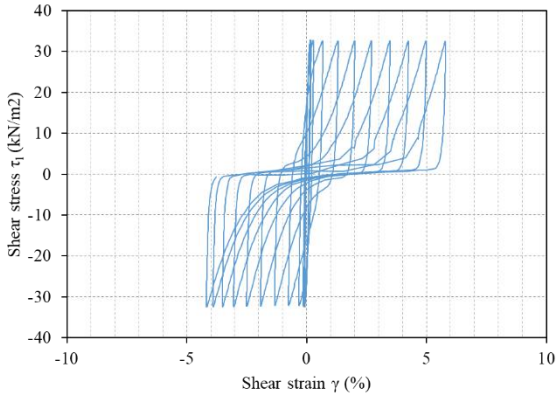

(c)

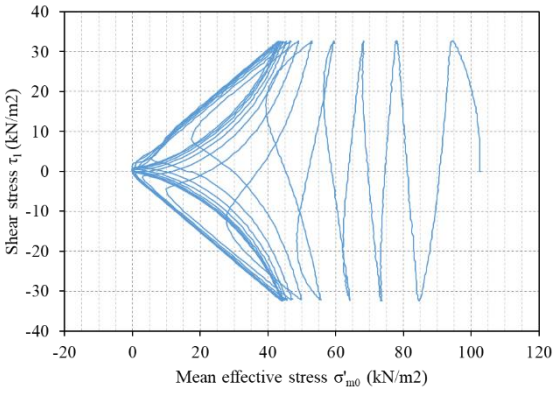

(d)

Figure A22 (a) Time History of Shear Stress - Model Dr70-2-3 (b) Time History of EPWP ratio development - Model Dr70-2-3 (c) Stress-Strain curve - Model Dr70-2-3 (d) Stress path - Model Dr70-2-3

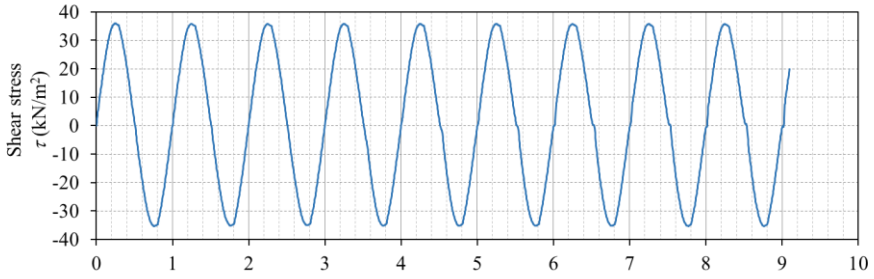

(a)

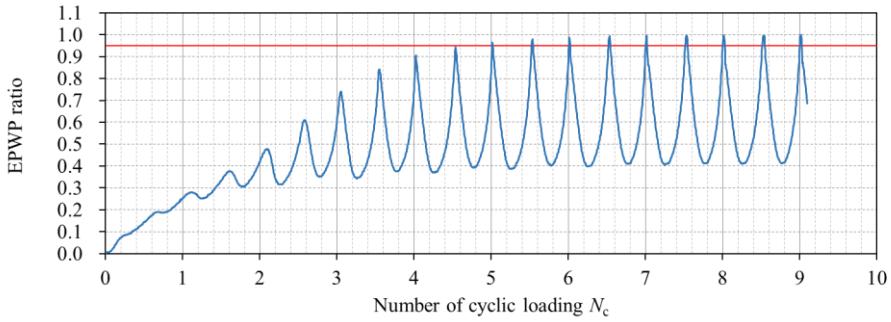

(b)

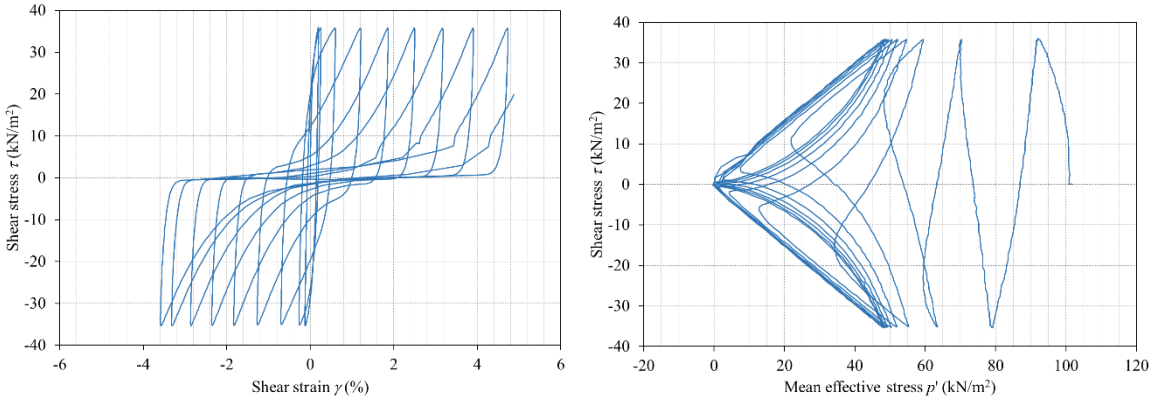

(c) (d)

Figure A23 (a) Time History of Shear Stress - Model Dr70-2-4 (b) Time History of EPWP ratio development - Model Dr70-2-4 (c) Stress-Strain curve - Model Dr70-2-4 (d) Stress path - Model Dr70-2-4

A3. Stress Space Multiple Mechanism Model - Governing equations, finite element formulation, and model formulation

This section provides a description of the governing equations and the finite element formulation, based on documentation from the FLIP Consortium [153], and the model formulation, based on the paper written by Iai et. al [16].

A3-1 Governing Equations and FE Formulation

A3-1.1 Basic equations

As introduced in Section 2.3.1, the porous media theory is based on a representation of two or more elements occupying the same space at the same time. In the case of a fully saturated ground, the elements are the soil skeleton, and water.

Following Zienkiewicz et al. [154], the equations of motion and water flow balance equations for a fully saturated porous media are given by using the total stress tensor $\boldsymbol{\sigma}$ as follows (u-p formulation).

$$\mathrm{div}\boldsymbol{\sigma} + \rho\boldsymbol{g} = \rho\ddot{\boldsymbol{u}} \tag{A3-1}$$

$$\mathrm{div}(\boldsymbol{k}\,\mathrm{grad}p) - \mathrm{div}\dot{\boldsymbol{u}} - \mathrm{div}\left(\boldsymbol{k}\rho_f\boldsymbol{g}\right) = -\mathrm{div}\left(\boldsymbol{k}\rho_f\ddot{\boldsymbol{u}}\right) + n\dot{p}/K_f \tag{A3-2}$$

Where:

- ρ : Overall density of the soil/water mixture
- $\boldsymbol{g}$ **:** Gravitational acceleration vector
- $\boldsymbol{u}$ **:** Soil skeleton displacement vector
- $\boldsymbol{k}$ **:** Permeability (symmetric tensor)
- p : Pore water pressure
- ρ_f : Pore water density
- n : Volume fraction (porosity)
- K_f : Volumetric elastic modulus of water

Regarding the sign convention of stress/strain, in this formulation, compression is assigned to take negative values, and tension is assigned to take positive values; however, for pore water pressure, compression is assigned to be positive.

The following four conditions are considered as boundary conditions for Eq. (A3-1) and (A3-2).

$$\boldsymbol{u} = \overline{\boldsymbol{u}} \text{ on } \partial\Omega_{\boldsymbol{u}} \tag{A3-3}$$

$$\boldsymbol{T} = \boldsymbol{\sigma n} = \overline{\boldsymbol{T}} \text{ on } \partial\Omega_{\boldsymbol{\sigma}} \tag{A3-4}$$

$$p = \bar{p} \text{ on } \partial\Omega_{p} \tag{A3-5}$$

$$\boldsymbol{q} = \boldsymbol{k}\left(\text{grad}p - \rho_f \boldsymbol{g} + \rho_f \ddot{\boldsymbol{u}}\right)\boldsymbol{n} = \overline{\boldsymbol{q}} \text{ on } \partial\Omega_{\boldsymbol{q}} \tag{A3-6}$$

Where:

- $\overline{\boldsymbol{u}}$: Displacement defined on the $\partial\Omega_{\boldsymbol{u}}$ boundary
- $\overline{\boldsymbol{T}}$ **:** Surface forces defined on the $\partial\Omega_{\boldsymbol{\sigma}}$ boundary
- $\bar{p}$ **:** Pore water pressure forces defined on the $\partial\Omega_{p}$ boundary
- $\overline{\boldsymbol{q}}$ **:** Pore water inflow forces defined on the $\partial\Omega_{\boldsymbol{q}}$ boundary

The $\partial\Omega_{\boldsymbol{u}}$ boundary and the $\partial\Omega_{\boldsymbol{\sigma}}$ boundary combined are equal to the entire surface of the target area, and there is no common area between $\partial\Omega_{\boldsymbol{u}}$ and $\partial\Omega_{\boldsymbol{\sigma}}$ boundaries. This also holds true for $\partial\Omega_{p}$ and $\partial\Omega_{\boldsymbol{q}}$ boundaries.

The initial conditions on the target area are given as follows.

$$\boldsymbol{u} = \dot{\boldsymbol{u}} = \ddot{\boldsymbol{u}} = 0 \tag{A3-7}$$

$$\boldsymbol{\sigma} = \boldsymbol{\sigma}_0 \tag{A3-8}$$

$$p = p_0 \tag{A3-9}$$

$$\dot{p} = 0 \tag{A3-10}$$

Also, the initial conditions on the boundary are given as:

$$\boldsymbol{u} = \overline{\boldsymbol{u}}_0 \text{ on } \partial\Omega_{\boldsymbol{u}} \tag{A3-11}$$

$$\boldsymbol{T} = \boldsymbol{\sigma}_0\boldsymbol{n} = \overline{\boldsymbol{T}}_0 \text{ on } \partial\Omega_{\boldsymbol{\sigma}} \tag{A3-12}$$

$$p = \bar{p}_0 \text{ on } \partial\Omega_{p} \tag{A3-13}$$

$$\boldsymbol{q} = \boldsymbol{k}\left(\text{grad}p_0 - \rho_f \boldsymbol{g}\right)\boldsymbol{n} = \overline{\boldsymbol{q}}_0 \text{ on } \partial\Omega_{\boldsymbol{q}} \tag{A3-14}$$

A3-1.2 Discretization of the equations of motion

By considering the effective stress principle, Eq. (A3-15), the equation of motion of the porous media, expressed in Eq. (A3-1), can be expressed as shown in Eq. (A3-16):

$$\boldsymbol{\sigma} = \boldsymbol{\sigma}' - p\boldsymbol{I} \tag{A3-15}$$

$$\text{div}(\boldsymbol{\sigma}' - p\boldsymbol{I}) + \rho\boldsymbol{g} = \rho\ddot{\boldsymbol{u}} \tag{A3-16}$$

Where:

- $\boldsymbol{I}$: Second-order unit tensor, expressed in Eq. (A3-17) using the unitary vector $\boldsymbol{e_i}$ in the dimension under consideration.

$$\boldsymbol{I} = \delta_{ij}\boldsymbol{e_i} \otimes \boldsymbol{e_j} \tag{A3-17}$$

By applying the principle of virtual work to the equation of motion in Eq. (A3-16), the following equation is obtained.

$$\int_{\boldsymbol{\Omega}} [(\boldsymbol{\sigma}' - p\boldsymbol{I}) : \delta\boldsymbol{\varepsilon} - (\rho\boldsymbol{g} - \rho\ddot{\boldsymbol{u}}) \cdot \delta\boldsymbol{u}]\, dV - \int_{\Omega_{\boldsymbol{\sigma}}} \overline{\boldsymbol{T}} \cdot \delta\boldsymbol{u}\, dS = 0 \tag{A3-18}$$

Where:

- $\boldsymbol{\varepsilon}$: Strain tensor

Furthermore, by using interpolation functions, nodal displacements, etc.; in order to apply the Finite Element Method, the soil skeleton displacements, and pore water pressure are discretized as follows:

$$\boldsymbol{u} = \boldsymbol{H}\underline{\boldsymbol{u}} \tag{A3-19}$$

$$\ddot{\boldsymbol{u}} = \boldsymbol{H}\underline{\ddot{\boldsymbol{u}}} \tag{A3-20}$$

$$p = \widehat{\boldsymbol{H}}\underline{\boldsymbol{p}} \tag{A3-21}$$

$$\boldsymbol{g} = -\boldsymbol{H}g\underline{\boldsymbol{I_V}} \tag{A3-22}$$

Where:

- $\boldsymbol{H}$: Interpolation function for displacements
- $\widehat{\boldsymbol{H}}$: Interpolation function for water pressure
- $\underline{\boldsymbol{u}}$: Nodal displacement
- $\underline{\ddot{\boldsymbol{u}}}$: Nodal acceleration
- $\underline{\boldsymbol{p}}$: Nodal pore water pressure
- g : Acceleration of gravity

For a 2-dimensional case, the values are expressed as follows:

$$\boldsymbol{H} = \begin{bmatrix} h_1\ 0\ h_2\ 0\ h_3\ 0 \cdots h_N\ 0 \\ 0\ h_1\ 0\ h_2\ 0\ h_3 \cdots\ 0\ h_N \end{bmatrix} \tag{A3-23}$$

$$\widehat{\boldsymbol{H}} = [\hat{h}_1 \quad \hat{h}_2 \quad \hat{h}_3 \quad \cdots \quad \hat{h}_N] \tag{A3-24}$$

$$\underline{\boldsymbol{u}}^T = [u_1^1 \quad u_2^1 \quad u_1^2 \quad u_2^2 \quad u_1^3 \quad u_2^3 \quad \cdots \quad u_1^N \quad u_2^N] \tag{A3-25}$$

$$\underline{\boldsymbol{p}}^T = [p_1 \quad p_2 \quad p_3 \quad \cdots \quad p_N] \tag{A3-26}$$

$$\underline{\boldsymbol{I_V}}^T = [0 \quad 1 \quad 0 \quad 1 \quad 0 \quad 1 \quad \cdots \quad 0 \quad 1] \tag{A3-27}$$

Where:

- N : Number of nodal points per element (usually N=4 for a 2D analysis)

The above equations are used to discretize the equation of motion in a 2D analysis.

First, the virtual strain corresponding to the stress and virtual displacement produces the virtual work $\delta \boldsymbol{W}$, as follows.

$$\delta \boldsymbol{W} = \int_\Omega \boldsymbol{\sigma} : \delta \boldsymbol{\varepsilon} \, dV = \int_\Omega \boldsymbol{\sigma} : sym(grad \, \delta \boldsymbol{u}) \, dV \tag{A3-28}$$

Here, using Eq. (A3-19), the virtual strain in Eq. (A3-28) can be written as follows:

$$\delta \boldsymbol{\varepsilon} = sym(grad \, \delta \boldsymbol{u}) = sym\left(\begin{bmatrix} \sum_{k=1}^N \frac{\partial h_k}{\partial x_1} \delta u_1^k & \sum_{k=1}^N \frac{\partial h_k}{\partial x_2} \delta u_1^k \\ \sum_{k=1}^N \frac{\partial h_k}{\partial x_1} \delta u_2^k & \sum_{k=1}^N \frac{\partial h_k}{\partial x_2} \delta u_2^k \end{bmatrix}\right) \tag{A3-29}$$

This equation can be rewritten in vector representation as follows:

$$\delta \hat{\boldsymbol{\varepsilon}} = \begin{bmatrix} \sum_{k=1}^N \frac{\partial h_k}{\partial x_1} \delta u_1^k \\ \sum_{k=1}^N \frac{\partial h_k}{\partial x_2} \delta u_2^k \\ \sum_{k=1}^N \frac{\partial h_k}{\partial x_2} \delta u_1^k + \sum_{k=1}^N \frac{\partial h_k}{\partial x_1} \delta u_2^k \end{bmatrix} = \boldsymbol{B} \delta \boldsymbol{u} \tag{A3-30}$$

Where:

$$\boldsymbol{B} = \begin{bmatrix} \frac{\partial h_1}{\partial x_1} & \boldsymbol{0} & \frac{\partial h_2}{\partial x_1} & \boldsymbol{0} & \frac{\partial h_3}{\partial x_1} & \boldsymbol{0} & \cdots & \frac{\partial h_N}{\partial x_2} & \boldsymbol{0} \\ \boldsymbol{0} & \frac{\partial h_1}{\partial x_2} & \boldsymbol{0} & \frac{\partial h_2}{\partial x_2} & \boldsymbol{0} & \frac{\partial h_3}{\partial x_2} & \cdots & \boldsymbol{0} & \frac{\partial h_N}{\partial x_2} \\ \frac{\partial h_1}{\partial x_2} & \frac{\partial h_1}{\partial x_1} & \frac{\partial h_2}{\partial x_2} & \frac{\partial h_2}{\partial x_1} & \frac{\partial h_3}{\partial x_2} & \frac{\partial h_3}{\partial x_1} & \cdots & \frac{\partial h_N}{\partial x_2} & \frac{\partial h_N}{\partial x_1} \end{bmatrix} \tag{A3-31}$$

By using Eq. (A3-31) into Eq. (A3-18), and further considering Eq. (A3-20) and (A3-22), the following discretized equations of motion are obtained:

$$\int_\Omega \boldsymbol{B}^T (\widehat{\boldsymbol{\sigma}'} - p\widehat{\boldsymbol{m}}) \, dV + \boldsymbol{M}\left(g\underline{\boldsymbol{I_V}} + \underline{\ddot{\boldsymbol{u}}}\right) - \int_{\partial\Omega_\sigma} \boldsymbol{H}^T \overline{T} \, dS = 0 \tag{A3-32}$$

Here:

$$\widehat{\boldsymbol{\sigma}'}^{T} = [\sigma'_{11} \quad \sigma'_{22} \quad \sigma'_{12}] \tag{A3-33}$$

$$\widehat{\boldsymbol{m}}^{T} = [1 \quad 1 \quad 0] \tag{A3-34}$$

$$\boldsymbol{M} = \int_{\Omega} \rho \boldsymbol{H}^{T} \boldsymbol{H}\, dV \tag{A3-35}$$

Additionally, by substituting Eq. (A3-21) into Eq. (A3-32) and applying the interpolation function for pore water pressure, the following equation is obtained

$$\int_{\Omega} \boldsymbol{B}^{T} \widehat{\boldsymbol{\sigma}'}\, dV - \boldsymbol{Q}\underline{\boldsymbol{p}} + \boldsymbol{M}\left(g\underline{\boldsymbol{I_V}} + \underline{\ddot{\boldsymbol{u}}}\right) - \int_{\partial\Omega_{\sigma}} \boldsymbol{H}^{T}\overline{T}\, dS = 0 \tag{A3-36}$$

Where:

$$\boldsymbol{Q} = \int_{\Omega} \boldsymbol{B}^{T} \widehat{\boldsymbol{m}} \widehat{\boldsymbol{H}}\, dV \tag{A3-37}$$

Note that the equation of motion for the undrained case is given by using the excess pore water pressure p in Eq. (A3-36) as follows:

$$\int_{\Omega} \boldsymbol{B}^{T} \widehat{\boldsymbol{\sigma}'}\, dV - \int_{\Omega} \boldsymbol{B}^{T} p^{*} \widehat{\boldsymbol{m}}\, dV + \boldsymbol{M}\left(g\underline{\boldsymbol{I_V}} + \underline{\ddot{\boldsymbol{u}}}\right) - \int_{\partial\Omega_{\sigma}} \boldsymbol{H}^{T}\overline{T}\, dS = 0 \tag{A3-38}$$

A3-1.3 Discretization of the water flow balance equation

First, the balance equation expressed in Eq. (A3-2) is integrated following the Galerkin method using an arbitrary function $\hat{h}$ that becomes zero at the hydraulic-pressure constraint boundary $\partial\Omega_p$, leading to the following equation.

$$\begin{aligned}\int_{\Omega} \hat{h}\mathrm{div}(\boldsymbol{k}\mathrm{grad}p)dV - \int_{\Omega} \hat{h}\mathrm{div}\dot{\boldsymbol{u}}dV - \int_{\Omega} \hat{h}\mathrm{div}\left(\boldsymbol{k}\rho_f(\boldsymbol{g} - \ddot{\boldsymbol{u}})\right)dV - \\ \int_{\Omega} \hat{h}n\dot{p}/K_f\, dV + \int_{\partial\Omega} \hat{h}(\overline{\boldsymbol{q}} - \boldsymbol{q})dS = 0\end{aligned} \tag{A3-39}$$

Where, for any scalar field, and vector field, the following relationship stands [155]:

$$\mathrm{div}(\Phi\mathbf{v}) = \Phi\mathrm{div}(\mathbf{v}) + \mathbf{v}\cdot\mathrm{grad}(\Phi) \tag{A3-40}$$

By applying Eq. (A3-40), the first and third terms of Eq. (A3-39) can be expressed as follows:

$$\int_{\Omega} \hat{h}\mathrm{div}(\boldsymbol{k}\mathrm{grad}p)dV = \int_{\Omega} \mathrm{div}(\hat{h}\boldsymbol{k}\mathrm{grad}p)dV - \int_{\Omega} \boldsymbol{k}\mathrm{grad}p\cdot\mathrm{grad}(\hat{h})dV \tag{A3-41}$$

$$\int_\Omega \hat{h}\mathrm{div}\left(\boldsymbol{k}\rho_f(\boldsymbol{g}-\ddot{\boldsymbol{u}})\right)dV = \int_\Omega \mathrm{div}\left(\hat{h}\boldsymbol{k}\rho_f(\boldsymbol{g}-\ddot{\boldsymbol{u}})\right)dV - \int_\Omega \boldsymbol{k}\rho_f(\boldsymbol{g}-\ddot{\boldsymbol{u}})\cdot\mathrm{grad}(\hat{h})dV \quad \text{(A3-42)}$$

Then, applying the Gauss theorem, the previous equations are expressed as follows:

$$\int_\Omega \hat{h}\mathrm{div}(\boldsymbol{k}\mathrm{grad}p)dV = \int_{\partial\Omega}\hat{h}\boldsymbol{k}(\mathrm{grad}p)\cdot\mathbf{n}dS - \int_\Omega \boldsymbol{k}\mathrm{grad}p\cdot\mathrm{grad}(\hat{h})dV \quad \text{(A3-43)}$$

$$\int_\Omega \hat{h}\mathrm{div}\left(\boldsymbol{k}\rho_f(\boldsymbol{g}-\ddot{\boldsymbol{u}})\right)dV = \int_{\partial\Omega}\hat{h}\boldsymbol{k}\rho_f(\boldsymbol{g}-\ddot{\boldsymbol{u}})\cdot\mathbf{n}dS - \int_\Omega \boldsymbol{k}\rho_f(\boldsymbol{g}-\ddot{\boldsymbol{u}})\cdot\mathrm{grad}(\hat{h})dV \quad \text{(A3-44)}$$

Then, substituting Eq. (A3-43), and (A3-44) into Eq. (A3-39), and by considering that $\hat{h}$ on $\partial\Omega_p$ and $\boldsymbol{q} = \boldsymbol{k}\left(\mathrm{grad}p - \rho_f\boldsymbol{g} + \rho_f\ddot{\boldsymbol{u}}\right)\boldsymbol{n}$ (from Eq. (A3-6)), the integral term with respect to $\boldsymbol{q}$ in the area component is cancelled, and the following equation is obtained.

$$\int_\Omega (\mathrm{grad}\hat{h})^T\boldsymbol{k}(\mathrm{grad}p)dV + \int_\Omega \hat{h}\mathrm{div}\dot{\boldsymbol{u}}dV - \int_\Omega \left(\mathrm{grad}\hat{h}\right)^T\left(\boldsymbol{k}\rho_f(\boldsymbol{g}-\ddot{\boldsymbol{u}})\right)dV + \int_\Omega \hat{h}n\dot{p}/K_f\,dV - \int_{\partial\Omega_q}\hat{h}\bar{\boldsymbol{q}}dS = 0 \quad \text{(A3-45)}$$

It shall be noted that that the integration range of the area of the last term of the above equation is an integral over only $\partial\Omega_{\boldsymbol{q}}$, based on the condition that $\partial\Omega_p \cap \partial\Omega_{\boldsymbol{q}} = \emptyset$.

Next, using Eq. (A3-21), (A3-24), and (A3-26), the hydraulic gradient is discretized as follows:

$$\mathrm{grad}p = \begin{bmatrix}\sum_{k=1}^{N}\frac{\partial\widehat{h_k}}{\partial x_1}p_k \\ \sum_{k=1}^{N}\frac{\partial\widehat{h_k}}{\partial x_2}p_k\end{bmatrix} = \hat{\boldsymbol{b}}\underline{\boldsymbol{p}} \quad \text{(A3-46)}$$

Where:

$$\hat{\boldsymbol{b}} = \begin{bmatrix}\frac{\partial\widehat{h_1}}{\partial x_1} & \frac{\partial\widehat{h_2}}{\partial x_1} & \frac{\partial\widehat{h_3}}{\partial x_1}\cdots & \frac{\partial\widehat{h_N}}{\partial x_1} \\ \frac{\partial\widehat{h_1}}{\partial x_2} & \frac{\partial\widehat{h_2}}{\partial x_2} & \frac{\partial\widehat{h_3}}{\partial x_2}\cdots & \frac{\partial\widehat{h_N}}{\partial x_2}\end{bmatrix} \quad \text{(A3-47)}$$

Thus, by using Eq. (A3-46), and adopting the interpolation function $\widehat{h_k}$ of the water pressure as an arbitrary function $\hat{h}$ (however setting it to zero at the at the hydraulic-pressure constraint boundary $\partial\Omega_p$), Eq. (A3-45) is discretized

as follows:

$$\boldsymbol{G}\underline{\boldsymbol{p}} + \boldsymbol{R}\underline{\dot{\boldsymbol{p}}} = \int_{\partial\Omega_q} \widehat{\boldsymbol{H}}^T \bar{\boldsymbol{q}} dS - \boldsymbol{Q}^T \underline{\dot{\boldsymbol{u}}} - \widehat{\boldsymbol{M}}(g\underline{\boldsymbol{I_V}} + \underline{\ddot{\boldsymbol{u}}}) \quad \text{(A3-48)}$$

Where:

$$\boldsymbol{G} = \int_\Omega \widehat{\boldsymbol{b}}^T \boldsymbol{k} \widehat{\boldsymbol{b}} dV \quad \text{(A3-49)}$$

$$\boldsymbol{R} = \int_\Omega \frac{n}{K_f} \widehat{\boldsymbol{H}}^T \widehat{\boldsymbol{H}} dV \quad \text{(A3-50)}$$

$$\boldsymbol{Q}^T = \int_\Omega \widehat{\boldsymbol{H}}^T \widehat{\boldsymbol{m}}^T \boldsymbol{B} dV = \left(\int_\Omega \boldsymbol{B}^T \widehat{\boldsymbol{m}} \widehat{\boldsymbol{H}} dV \right)^T \quad \text{(A3-51)}$$

$$\boldsymbol{R} = \int_\Omega \rho_f \widehat{\boldsymbol{b}}^T \boldsymbol{k} \boldsymbol{H} dV \quad \text{(A3-52)}$$

A3-1.4 Self-weight analysis

For the seismic-induced liquefaction analysis of ground deposits in FLIP ROSE, as a minimum, the following two steps are required:

- Initial self-weight analysis; which consists in a static analysis that aims to define/estimate the initial stress distribution of the deposit under study.
- Dynamic analysis, which consists in a dynamic analysis that aims to estimate the ground response of the deposit under seismic loading.

This section describes the governing equations (and its solution methodology) used in the self-weight analysis, and section A3-1.5 describes the governing equations (and its solution methodology) used in the dynamic analysis.

Self-weight analysis - Ground deformation governing equations

For the ground self-weight analysis, the discretized equation of motion, given by Eq. (A3-36) can be expressed as follows:

$$\int_\Omega \boldsymbol{B}^T \widehat{\boldsymbol{\sigma}'} \, dV - \boldsymbol{Q}\underline{\boldsymbol{p}} = \Re \quad \text{(A3-53)}$$

$$\Re = -\boldsymbol{M} g \underline{\boldsymbol{I_V}} + \int_{\partial\Omega_\sigma} \boldsymbol{H}^T \overline{T} \, dS \quad \text{(A3-54)}$$

In these equations, the terms for the degrees of freedom on the displacement-constrained boundary $\partial\Omega_q$ are assumed to be removed, and the solution of the steady seepage flow analysis given in the next section is used to obtain the water pressure p.

The equations expressed in Eq. (A3-53) and (A3-54) are divided into several steps and solved by increasing the load step by step. Assuming that the solutions up to the n-th loading step are known, Eq. (A3-53) for the n+1-th

loading step is expressed as follows:

$$\int_{\Omega} \boldsymbol{B}^T \widehat{\boldsymbol{\sigma}'}_{n+1}\, dV - \boldsymbol{Q}\underline{\boldsymbol{p}}_{n+1} = \Re_{n+1} \tag{A3-55}$$

Here $\underline{\boldsymbol{u}}^i{}_{n+1}$ and $\widehat{\boldsymbol{\sigma}'}^i{}_{n+1}$ denote the i-th trial value of the nodal displacement vector $\underline{\boldsymbol{u}}_{n+1}$ and the effective stress vector $\widehat{\boldsymbol{\sigma}'}_{n+1}$ calculated from the strain vector $\hat{\boldsymbol{\varepsilon}}_{n+1}$, respectively.

By including $\boldsymbol{\varphi}^i{}_{n+1}$ as the unbalanced force for the i-th trial value, the above equations are expressed as follows:

$$\boldsymbol{\varphi}^i{}_{n+1} = -\int_{\Omega} \boldsymbol{B}^T \widehat{\boldsymbol{\sigma}'}^i{}_{n+1}\, dV - \boldsymbol{Q}\underline{\boldsymbol{p}}_n + \Re_{n+1} \tag{A3-56}$$

$$\Re_{n+1} = -\boldsymbol{M} g_{n+1} \underline{\boldsymbol{I}_V} + \int_{\partial\Omega_\sigma} \boldsymbol{H}^T \overline{T}_{n+1}\, dS \tag{A3-57}$$

If the i+1-th trial value $\underline{\boldsymbol{u}}^{i+1}{}_{n+1}$ of the nodal displacement vector is determined by Eq. (A3-58), the unbalanced force for the i+1-th trial value is approximately given by Eq. (A3-59), following Newton's method.

$$\underline{\boldsymbol{u}}^{i+1}{}_{n+1} = \underline{\boldsymbol{u}}^i{}_{n+1} + \Delta\underline{\boldsymbol{u}}^i{}_{n+1} \tag{A3-58}$$

$$\boldsymbol{\varphi}^{i+1}{}_{n+1} = \boldsymbol{\varphi}^i{}_{n+1} + \left(\frac{\partial \boldsymbol{\varphi}}{\partial \underline{\boldsymbol{u}}}\right)^i_{n+1} \Delta\underline{\boldsymbol{u}}^i{}_{n+1} \tag{A3-59}$$

Here:

$$\left(\frac{\partial \boldsymbol{\varphi}}{\partial \underline{\boldsymbol{u}}}\right)^i_{n+1} = -(\boldsymbol{K}_L)^i_{n+1} \tag{A3-60}$$

$$(\boldsymbol{K}_L)^i_{n+1} = \int_{\Omega} \boldsymbol{B}^T \left(\frac{\partial \widehat{\boldsymbol{\sigma}'}}{\partial \underline{\boldsymbol{u}}}\right)^i_{n+1} dV = \int_{\Omega} \boldsymbol{B}^T \boldsymbol{D}^i_{n+1} dV \tag{A3-61}$$

Note that $\boldsymbol{D}$ represents the stiffness of the geomaterial in Vector/Matrix representation.

If the stresses (and other values) calculated by the self-weight analysis are displayed using the subscript "st" the initial load vector for dynamic analysis is given as follows:

$$-\boldsymbol{M} g \underline{\boldsymbol{I}_V} = \int_{\Omega} \boldsymbol{B}^T \widehat{\boldsymbol{\sigma}'}_{st} dV - \boldsymbol{Q}\underline{\boldsymbol{p}}_{st} - \int_{\partial\Omega_\sigma} \boldsymbol{H}^T \overline{\boldsymbol{T}}_{st}\, dS \tag{A3-62}$$

Self-weight analysis - Steady-state seepage flow analysis

In the steady-state seepage flow analysis (i.e., the self-weight analysis of water pressure without considering time dependence), Eq. (A3-48) is solved by not considering the time-dependent term, as follows.

$$\boldsymbol{G}\underline{\boldsymbol{p}} = \int_{\partial\Omega_q} \widehat{\boldsymbol{H}}^T \bar{\boldsymbol{q}} dS - \widehat{\boldsymbol{M}} g \underline{\boldsymbol{I_V}} \tag{A3-63}$$

Where the nodal pore water pressure vector $\underline{\boldsymbol{p}}$ is decomposed into an unconstrained degree of freedom $\underline{\boldsymbol{p}}^f$, and a constrained degree of freedom $\underline{\boldsymbol{p}}^c$ (on the water pressure boundary $\partial\Omega_{0p}$). Also, the matrix G over the nodal water pressure is also decomposed and expressed accordingly.

$$\underline{\boldsymbol{p}} = \begin{bmatrix} \underline{\boldsymbol{p}}^f \\ \underline{\boldsymbol{p}}^c \end{bmatrix}, \boldsymbol{G} = [\boldsymbol{G}^f \quad \boldsymbol{G}^c] \tag{A3-64}$$

It shall be noted that, for the sake of notational brevity, the unconstrained degree of freedom water pressure $\underline{\boldsymbol{p}}^f$ is re-written as $\underline{\boldsymbol{p}}$; the corresponding matrix is also re-written by omitting the superscript.

Then, Eq. (A3-63) can be re-written as follows.

$$\boldsymbol{G}\underline{\boldsymbol{p}} = \int_{\partial\Omega_q} \widehat{\boldsymbol{H}}^T \bar{\boldsymbol{q}} dS - \widehat{\boldsymbol{M}} g \underline{\boldsymbol{I_V}} - \boldsymbol{G}^c \underline{\boldsymbol{p}}^c \tag{A3-65}$$

Here, $\boldsymbol{G}\underline{\boldsymbol{p}}$ is expressed as follows:

$$\boldsymbol{G}\underline{\boldsymbol{p}} = \Re^p \tag{A3-66}$$

Then,

$$\Re^p = \int_{\partial\Omega_q} \widehat{\boldsymbol{H}}^T \bar{\boldsymbol{q}} dS - \widehat{\boldsymbol{M}} g \underline{\boldsymbol{I_V}} - \boldsymbol{G}^c \underline{\boldsymbol{p}}^c \tag{A3-67}$$

As in the case of the ground's self-weight analysis, Eq. (A3-66) is divided into several steps and solved by increasing the load step by step.

Assuming that the solution up to the n-th load step is known, Eq. (A3-66) is expressed as follows in the n+1-th step.

$$\boldsymbol{G}\underline{\boldsymbol{p}}_{n+1} = \Re^p{}_{n+1} \tag{A3-68}$$

If the water pressure obtained by the steady-state seepage flow analysis is displayed using the subscript "st", Eq. (A3-63) can be written as follows.

$$\widehat{\boldsymbol{M}} g \underline{\boldsymbol{I_V}} = \int_{\partial\Omega_q} \widehat{\boldsymbol{H}}^T \overline{\boldsymbol{q}}_{st} dS - \boldsymbol{G}\underline{\boldsymbol{p}}_{st} \tag{A3-69}$$

Static Coupled Self-Weight Analysis of Ground Deformation and Water Pressure

When coupling the self-weight analysis of the ground with the steady seepage flow analysis, the coupled equations Eq. (A3-53), and (A3-66) are solved. Here, following Eq. (A3-64) the nodal relative displacement vector $\underline{\boldsymbol{u}}$ is decomposed into an unconstrained degree of freedom $\boldsymbol{u}^f$, and a constrained degree of freedom $\underline{\boldsymbol{u}}^c$ (on the water pressure boundary $\partial\Omega_{0\boldsymbol{u}}$). Also, the mass matrix M is also decomposed and expressed accordingly.

$$\underline{\boldsymbol{u}} = \begin{bmatrix} \underline{\boldsymbol{u}}^f \\ \underline{\boldsymbol{u}}^c \end{bmatrix}, \boldsymbol{M} = [\boldsymbol{M}^f \quad \boldsymbol{M}^c] \tag{A3-70}$$

For the sake of notational brevity, the unconstrained degree of freedom displacement $\underline{\boldsymbol{u}}^f$ is re-written as $\underline{\boldsymbol{u}}$; the corresponding mass matrix is also re-written by omitting the superscript ($\boldsymbol{M}$ instead of $\boldsymbol{M}^f$). Furthermore, the matrix $\boldsymbol{Q}$ representing the coupled ground and water pressure terms, is divided as follows:

$$\boldsymbol{Q} = \begin{bmatrix} \boldsymbol{Q}^{ff} & \boldsymbol{Q}^{fc} \\ \boldsymbol{Q}^{cf} & \boldsymbol{Q}^{cc} \end{bmatrix} \tag{A3-71}$$

Here:

- ff : Unconstrained degrees of freedom at both the displacement boundary, and the water pressure boundary.
- fc : Unconstrained degrees of freedom at the displacement boundary, and constrained degrees of freedom at the water pressure boundary.
- cf : Unconstrained degrees of freedom at the displacement boundary, and unconstrained degrees of freedom at the water pressure boundary.
- cc : Constrained degrees of freedom at both the displacement boundary, and the water pressure boundary.

Additionally, to simplify the notation, $\boldsymbol{Q}^{ff}$ is written simply as $\boldsymbol{Q}$.

Using these, the coupled equations in the self-weight analysis are given as follows:

$$\int_{\Omega} \boldsymbol{B}^T \widehat{\boldsymbol{\sigma}}' \, dV - \boldsymbol{Q}\underline{\boldsymbol{p}} = \Re \tag{A3-72}$$

$$\boldsymbol{G}\underline{\boldsymbol{p}} = \Re^p \tag{A3-73}$$

Where:

$$\Re = \boldsymbol{Q}^{fc}\underline{\boldsymbol{p}}^c - \boldsymbol{M}g\underline{\boldsymbol{I_V}} + \int_{\partial\Omega_\sigma} \boldsymbol{H}^T\overline{T} \, dS \tag{A3-74}$$

$$\Re^p = -\boldsymbol{G}^c\underline{\boldsymbol{p}}^c + \int_{\partial\Omega_q} \widehat{\boldsymbol{H}}^T\overline{\boldsymbol{q}}dS - \widehat{\boldsymbol{M}}g\underline{\boldsymbol{I_V}} \tag{A3-75}$$

These are solved by dividing the load into several steps, and increasing the load step by step.

Assuming that the n-th loading step is known and considering the balancing at the n+1-th loading step, Eq. (A3-72) and (A3-73) can be expressed as follows:

$$\int_{\Omega} \boldsymbol{B}^T \widehat{\boldsymbol{\sigma}'}_{n+1} dV - \boldsymbol{Q}\underline{\boldsymbol{p}}_{n+1} = \Re_{n+1} \tag{A3-76}$$

$$\boldsymbol{G}\underline{\boldsymbol{p}}_{n+1} = \Re^p{}_{n+1} \tag{A3-77}$$

By considering $\boldsymbol{\varphi}^i{}_{n+1}$ as the unbalanced force for the i-th trial value, it could be expressed in the following form for Eq. (A3-76) and (A3-77) as follows:

$$\boldsymbol{\varphi}^i{}_{n+1} = \begin{bmatrix} (\boldsymbol{\varphi}^{\boldsymbol{u}})^i_{n+1} \\ (\boldsymbol{\varphi}^p)^i_{n+1} \end{bmatrix} \tag{A3-78}$$

Where:

$$(\boldsymbol{\varphi}^{\boldsymbol{u}})^i_{n+1} = -\int_{\Omega} \boldsymbol{B}^T \widehat{\boldsymbol{\sigma}}'^i_{n+1} dV + \boldsymbol{Q}\underline{\boldsymbol{p}}^i_{n+1} + \Re^i_{n+1} \tag{A3-79}$$

$$(\boldsymbol{\varphi}^p)^i_{n+1} = \boldsymbol{G}\underline{\boldsymbol{p}}_{n+1} - \Re^{p\,i}_{n+1} \tag{A3-80}$$

Furthermore, the vector composed by the nodal displacement vector $\underline{\boldsymbol{u}}$ and the nodal pore water pressure vector $\underline{\boldsymbol{p}}$ is defined as follows:

$$\underline{\boldsymbol{\zeta}} = \begin{bmatrix} \underline{\boldsymbol{u}} \\ \underline{\boldsymbol{p}} \end{bmatrix} \tag{A3-81}$$

Assuming that the i+1-th trial value $\underline{\boldsymbol{\zeta}}^{i+1}{}_{n+1}$ is determined by Eq. (A3-82), the unbalanced force for the i+1-th trial value is approximated by linearization in Eq. (A3-83).

$$\underline{\boldsymbol{\zeta}}^{i+1}{}_{n+1} = \underline{\boldsymbol{\zeta}}^{i}{}_{n+1} + \Delta\underline{\boldsymbol{\zeta}}^{i}{}_{n+1} \tag{A3-82}$$

$$\boldsymbol{\varphi}^{i+1}{}_{n+1} = \boldsymbol{\varphi}^{i}{}_{n+1} + \left(\frac{\partial \boldsymbol{\varphi}}{\partial \underline{\boldsymbol{\zeta}}}\right)^{i}_{n+1} \Delta\underline{\boldsymbol{\zeta}}^{i}{}_{n+1} \tag{A3-83}$$

Where:

$$\left(\frac{\partial \boldsymbol{\varphi}}{\partial \underline{\boldsymbol{\zeta}}}\right)^{i}_{n+1} = \begin{bmatrix} \left(\frac{\partial \boldsymbol{\varphi}^{u}}{\partial \underline{\boldsymbol{u}}}\right)^{i}_{n+1} & \left(\frac{\partial \boldsymbol{\varphi}^{u}}{\partial \underline{\boldsymbol{p}}}\right)^{i}_{n+1} \\ \left(\frac{\partial \boldsymbol{\varphi}^{p}}{\partial \underline{\boldsymbol{u}}}\right)^{i}_{n+1} & \left(\frac{\partial \boldsymbol{\varphi}^{p}}{\partial \underline{\boldsymbol{p}}}\right)^{i}_{n+1} \end{bmatrix} = \begin{bmatrix} (\boldsymbol{K}_L)^{i}_{n+1} & \boldsymbol{Q} \\ 0 & \boldsymbol{G} \end{bmatrix} \tag{A3-84}$$

Therefore, the nodal displacement and the increment of water pressure could be determined by the following equation so that the i+1-th unbalanced force in Eq. (A3-83) becomes zero.

$$\begin{bmatrix} (\boldsymbol{K}_L)^{i}_{n+1} & \boldsymbol{Q} \\ 0 & \boldsymbol{G} \end{bmatrix} = \boldsymbol{\varphi}^{i}{}_{n+1} \tag{A3-85}$$

A3-1.5 Dynamic Analysis

The following sections, will be focused on the dynamic analysis that takes into account inertial forces caused by the motion of objects, and formulate the necessary equations/expressions for introducing them into the numerical analysis.

In the dynamic analysis, the stresses obtained from the self-weight analysis are considered as the initial state, and the relative displacements are considered based on the nodal displacements at the end of the self-weight analysis. Also, in the case of a dynamic analysis of a soil-structure system during an earthquake, it is necessary to determine the response to the earthquake acceleration $\ddot{u}_g$ applied uniformly on the base. Therefore, the relative displacement to the base is given as a new definition of relative displacement to the previous relative displacement.

<u>Dynamic Analysis of Ground Deformation</u>

The equation of motion expressed in Eq. (A3-36) is rewritten as follows

$$\int_{\Omega} \boldsymbol{B}^{T}\widehat{\boldsymbol{\sigma}}'\, dV - \boldsymbol{Q}\underline{\boldsymbol{p}} + \boldsymbol{C}\underline{\dot{\boldsymbol{u}}} + \boldsymbol{M}\underline{\ddot{\boldsymbol{u}}} = -\ddot{u}_g \boldsymbol{M}\underline{\boldsymbol{I}} - \boldsymbol{M}g\underline{\boldsymbol{I}_{\boldsymbol{V}}} + \int_{\partial\Omega_{0\sigma}} \boldsymbol{H}^{T}\overline{T}\, dS \tag{A3-86}$$

Here $\underline{\boldsymbol{I}}$ is a vector where, for each nodal displacement, 1 is assigned to the component of freedom equal to the direction of excitation at the base, and 0 to the others. A viscous damping term proportional to velocity ($\boldsymbol{C}$ is the

viscosity matrix) is added.

Substituting Eq. (A3-62) obtained from the ground self-weight analysis, the following is obtained:

$$\int_{\Omega} \boldsymbol{B}^T \widehat{\boldsymbol{\sigma}}' \, dV - \boldsymbol{Q}\underline{\boldsymbol{p}}^* + \boldsymbol{C}\underline{\dot{\boldsymbol{u}}} + \boldsymbol{M}\underline{\ddot{\boldsymbol{u}}} = -\ddot{u}_g \boldsymbol{M}\underline{\boldsymbol{I}} + \int_{\Omega} \boldsymbol{B}^T \widehat{\boldsymbol{\sigma}}'_{st} dV + \int_{\partial\Omega_\sigma} \boldsymbol{H}^T \overline{\boldsymbol{T}}^* \, dS \qquad \text{(A3-87)}$$

Here, the nodal water pressure and boundary stresses in the dynamic analysis are given relative to the nodal water pressure and boundary stresses in the self-weight analysis as follows:

$$\underline{\boldsymbol{p}}^* = \underline{\boldsymbol{p}} - \underline{\boldsymbol{p}}_{st} \qquad \text{(A3-88)}$$

$$\overline{\boldsymbol{T}}^* = \overline{\boldsymbol{T}} - \overline{\boldsymbol{T}}_{st} \qquad \text{(A3-89)}$$

Following Eq. (A3-70), the viscosity matrix $\boldsymbol{C}$ is also divided as follows:

$$\boldsymbol{C} = [\boldsymbol{C}^f \quad \boldsymbol{C}^c] \qquad \text{(A3-90)}$$

Additionally, by omitting the superscript f representing the unbounded degrees of freedom (for the sake of notational simplicity), the discretized equation of motion (Eq. (A3-87)) is rewritten using equations (A3-70) and (A3-90) as follows:

$$\int_{\Omega} \boldsymbol{B}^T \widehat{\boldsymbol{\sigma}}' \, dV - \boldsymbol{Q}\underline{\boldsymbol{p}}^* + \boldsymbol{C}\underline{\dot{\boldsymbol{u}}} + \boldsymbol{M}\underline{\ddot{\boldsymbol{u}}} = \Re \qquad \text{(A3-91)}$$

Here:

$$\Re = -\ddot{u}_g \boldsymbol{M}\underline{\boldsymbol{I}} - \boldsymbol{C}^c \underline{\dot{\boldsymbol{u}}}^c + \int_{\Omega} \boldsymbol{B}^T \widehat{\boldsymbol{\sigma}}'_{st} dV + \int_{\partial\Omega_\sigma} \boldsymbol{H}^T \overline{\boldsymbol{T}}^* \, dS \qquad \text{(A3-92)}$$

The overall concept of the time integration in the equation of motion is similar to the treatment of load steps in the static analysis, where the displacement up to the n-th time step is known, and the displacement at the n+1-th time step is obtained by Eq. (A3-91).

Several methods for the time integration of the equations of motion are available, however, in liquefaction analysis for undrained conditions using the "Strain Space Multiple Mechanism Model", the Newmark's method and the Wilson's θ method are commonly used. These methods are described as follows:

(a) Newmark Method

In the Newmark method, the displacement, velocity, and acceleration at the n-th time step are assumed to be known, and the displacement $\underline{\boldsymbol{u}}_{n+1}$(and other variables) at the n+1-th time step are obtained by nonlinear iteration. Since Eq. (A3-91) holds at the n+1-th time step, it can be written as follows:

$$\int_{\Omega} \boldsymbol{B}^T \widehat{\boldsymbol{\sigma}'}\, dV - \boldsymbol{Q}\underline{\boldsymbol{p}^*}_{n+1} + \boldsymbol{C}\underline{\dot{\boldsymbol{u}}}_{n+1} + \boldsymbol{M}\underline{\ddot{\boldsymbol{u}}}_{n+1} = \Re_{n+1} \tag{A3-93}$$

$\boldsymbol{\varphi}^i{}_{n+1}$ is considered to be the unbalanced force for the i-th trial value, which is given by:

$$\begin{aligned} \boldsymbol{\varphi}^i{}_{n+1} &= -\int_{\Omega} \boldsymbol{B}^T \widehat{\boldsymbol{\sigma}'}^i{}_{n+1} dV + \boldsymbol{Q}\underline{\boldsymbol{p}^{*i}}_{n+1} - \boldsymbol{C}\underline{\dot{\boldsymbol{u}}}^i_{n+1} - \boldsymbol{M}\underline{\ddot{\boldsymbol{u}}}^i_{n+1} + \Re_{n+1} \\ &= \boldsymbol{\psi}_{n+1} + \boldsymbol{\chi}_{n+1} \end{aligned} \tag{A3-94}$$

Where:

$$\boldsymbol{\psi}_{n+1} = -\int_{\Omega} \boldsymbol{B}^T \widehat{\boldsymbol{\sigma}'}^i_{n+1} dV + \boldsymbol{Q}\underline{\boldsymbol{p}^{*i}}_{n+1} + \Re_{n+1} \tag{A3-95}$$

$$\boldsymbol{\chi}_{n+1} = -\boldsymbol{C}\underline{\dot{\boldsymbol{u}}}^i_{n+1} - \boldsymbol{M}\underline{\ddot{\boldsymbol{u}}}^i_{n+1} \tag{A3-96}$$

$$\Re_{n+1} = -\ddot{u}_{g\,n+1}\boldsymbol{M}\underline{\boldsymbol{I}} - \boldsymbol{C}^c\underline{\dot{\boldsymbol{u}}}^c_{n+1} - \boldsymbol{M}^c\underline{\ddot{\boldsymbol{u}}}^c_{n+1} + \int_{\Omega} \boldsymbol{B}^T \widehat{\boldsymbol{\sigma}'}_{st} dV + \int_{\partial\Omega_\sigma} \boldsymbol{H}^T \overline{\boldsymbol{T}}^*_{n+1}\, dS \tag{A3-97}$$

The i+1-th trial value is given by:

$$\underline{\boldsymbol{u}}^{i+1}_{n+1} = \underline{\boldsymbol{u}}^i_{n+1} + \Delta\underline{\boldsymbol{u}}^i_{n+1} \tag{A3-98}$$

Then, the unbalanced force for the n+1-th trial value is, as in the case of the self-weight analysis shown in Eq. (A3-59), approximately expressed by:

$$\boldsymbol{\varphi}^{i+1}{}_{n+1} = \boldsymbol{\psi}^i_{n+1} + \left(\frac{\partial \boldsymbol{\psi}}{\partial \underline{\boldsymbol{u}}}\right)^i_{n+1} \Delta\underline{\boldsymbol{u}}^i_{n+1} + \boldsymbol{\chi}_{n+1} \tag{A3-99}$$

Where:

$$\left(\frac{\partial \boldsymbol{\psi}}{\partial \underline{\boldsymbol{u}}}\right)^i_{n+1} = -(\boldsymbol{K}_L)^i_{n+1} \tag{A3-100}$$

In the Newmark method, $\underline{\ddot{\boldsymbol{u}}}^{i+1}_{n+1}$ and $\underline{\dot{\boldsymbol{u}}}^{i+1}_{n+1}$ are represented by $\underline{\boldsymbol{u}}^{i+1}_{n+1}$ as follows:

$$\underline{\ddot{\boldsymbol{u}}}^{i+1}_{n+1} = a_0\underline{\boldsymbol{u}}^{i+1}_{n+1} - (a_0\underline{\boldsymbol{u}}_{\boldsymbol{n}} + a_2\underline{\dot{\boldsymbol{u}}}_{\boldsymbol{n}} + a_3\underline{\ddot{\boldsymbol{u}}}_{\boldsymbol{n}}) \tag{A3-101}$$

$$\underline{\dot{\boldsymbol{u}}}^{i+1}_{n+1} = a_1\underline{\boldsymbol{u}}^{i+1}_{n+1} - (a_1\underline{\boldsymbol{u}}_{\boldsymbol{n}} + a_4\underline{\dot{\boldsymbol{u}}}_{\boldsymbol{n}} + a_5\underline{\ddot{\boldsymbol{u}}}_{\boldsymbol{n}}) \tag{A3-102}$$

Where:

$$a_0 = \frac{1}{\alpha \Delta t^2}, a_1 = \frac{\delta}{\alpha \Delta t}, a_2 = \frac{1}{\alpha \Delta t}, a_3 = \frac{1}{2\alpha} - 1, a_4 = \frac{\delta}{\alpha} - 1, \\ a_5 = \frac{\Delta t}{2}\left(\frac{\delta}{\alpha} - 2\right) \tag{A3-103}$$

Therefore, applying Eq. (A3-98), (A3-101) and (A3-102) to Eq. (A3-99), and setting the unbalanced force for the n+1-th trial value to zero, the following equation is obtained:

$$\left[(\boldsymbol{K}_L)^i_{n+1} + a_1\boldsymbol{C} + a_0\boldsymbol{M}\right]\Delta\underline{\boldsymbol{u}}^i_{n+1} = \boldsymbol{\psi}^i_{n+1} - (a_1\boldsymbol{C} + a_0\boldsymbol{M})\underline{\boldsymbol{u}}^i_{n+1} + \\ \boldsymbol{C}\left(a_1\underline{\boldsymbol{u}}_{\boldsymbol{n}} + a_4\dot{\underline{\boldsymbol{u}}}_{\boldsymbol{n}} + a_5\ddot{\underline{\boldsymbol{u}}}_{\boldsymbol{n}}\right) + \boldsymbol{M}(a_0\underline{\boldsymbol{u}}_{\boldsymbol{n}} + a_2\dot{\underline{\boldsymbol{u}}}_{\boldsymbol{n}} + a_3\ddot{\underline{\boldsymbol{u}}}_{\boldsymbol{n}}) \tag{A3-104}$$

This equation is solved for $\Delta\underline{\boldsymbol{u}}^i_{n+1}$, and obtain the i+1-th trial value $\underline{\boldsymbol{u}}^{i+1}_{n+1}$ from Eq. (A3-98). Then, the increments of strain and stress with respect to $\Delta\underline{\boldsymbol{u}}^i_{n+1}$ can be obtained.

(b) Wilson's θ method

While the Newmark method described earlier considers the equilibrium condition at the n+1-th time step, the Wilson's θ method performs a nonlinear iterative calculation to satisfy the equilibrium condition at $t + \theta\Delta\mathrm{t}$ ($\theta > 1$), where t is the time at the n-th time step.

Replacing the subscript n+1 in Eq. (A3-99) with $t + \theta\Delta\mathrm{t}$, the unbalanced forces for the i+1-th trial value are given by:

$$\boldsymbol{\varphi}^{i+1}{}_{t+\theta\Delta\mathrm{t}} = \boldsymbol{\psi}^i_{t+\theta\Delta\mathrm{t}} + \left(\frac{\partial\boldsymbol{\psi}}{\partial\underline{\boldsymbol{u}}}\right)^i_{t+\theta\Delta\mathrm{t}} \Delta\underline{\boldsymbol{u}}^i_{t+\theta\Delta\mathrm{t}} + \boldsymbol{\chi}_{t+\theta\Delta\mathrm{t}} \tag{A3-105}$$

Each term on the right-hand side of Eq. (A3-99) is defined by replacing the subscript n+1 with $t + \theta\Delta\mathrm{t}$ in equations (A3-95), (A3-100), and (A3-96), respectively.

Also, the 1+i-th trial value $\underline{\boldsymbol{u}}^{i+1}_{t+\theta\Delta\mathrm{t}}$ is expressed as follows:

$$\underline{\boldsymbol{u}}^{i+1}_{t+\theta\Delta\mathrm{t}} = \underline{\boldsymbol{u}}^i_{t+\theta\Delta\mathrm{t}} + \Delta\underline{\boldsymbol{u}}^i_{t+\theta\Delta\mathrm{t}} \tag{A3-106}$$

In the Wilson's θ method, $\ddot{\underline{\boldsymbol{u}}}^{i+1}_{t+\theta\Delta\mathrm{t}}$ and $\dot{\underline{\boldsymbol{u}}}^{i+1}_{t+\theta\Delta\mathrm{t}}$ are expressed as follows:

$$\ddot{\underline{\boldsymbol{u}}}^{i+1}_{t+\theta\Delta\mathrm{t}} = a_0\underline{\boldsymbol{u}}^{i+1}_{t+\theta\Delta\mathrm{t}} - (a_0\underline{\boldsymbol{u}}_{\boldsymbol{n}} + a_2\dot{\underline{\boldsymbol{u}}}_{\boldsymbol{n}} + 2\ddot{\underline{\boldsymbol{u}}}_{\boldsymbol{n}}) \tag{A3-107}$$

$$\dot{\underline{\boldsymbol{u}}}^{i+1}_{t+\theta\Delta\mathrm{t}} = a_1\underline{\boldsymbol{u}}^{i+1}_{t+\theta\Delta\mathrm{t}} - (a_1\underline{\boldsymbol{u}}_{\boldsymbol{n}} + 2\dot{\underline{\boldsymbol{u}}}_{\boldsymbol{n}} + a_3\ddot{\underline{\boldsymbol{u}}}_{\boldsymbol{n}}) \tag{A3-108}$$

Here:

$$a_0 = \frac{6}{(\theta\Delta t)^2}, a_1 = \frac{3}{\theta\Delta t}, a_2 = 2a_1, a_3 = \frac{\theta\Delta t}{2} \quad \text{(A3-109)}$$

Therefore, applying Eq. (A3-107) and (A3-108) to Eq. (A3-105) and setting the unbalanced force for the i+1-th trial to zero, the following equation is obtained:

$$\begin{aligned}\left[(\boldsymbol{K}_L)^i_{t+\theta\Delta\mathrm{t}} + a_1\boldsymbol{C} + a_0\boldsymbol{M}\right]\Delta\underline{\boldsymbol{u}}^i_{t+\theta\Delta\mathrm{t}} = \boldsymbol{\psi}^i_{t+\theta\Delta\mathrm{t}} - (a_1\boldsymbol{C} + a_0\boldsymbol{M})\underline{\boldsymbol{u}}^i_{t+\theta\Delta\mathrm{t}} + \\ \boldsymbol{C}\left(a_1\underline{\boldsymbol{u}}_{\boldsymbol{n}} + 2\underline{\dot{\boldsymbol{u}}}_{\boldsymbol{n}} + a_3\underline{\ddot{\boldsymbol{u}}}_{\boldsymbol{n}}\right) + \boldsymbol{M}(a_0\underline{\boldsymbol{u}}_{\boldsymbol{n}} + a_2\underline{\dot{\boldsymbol{u}}}_{\boldsymbol{n}} + 2\underline{\ddot{\boldsymbol{u}}}_{\boldsymbol{n}})\end{aligned} \quad \text{(A3-110)}$$

Solving Eq. (A3-110) for $\Delta\underline{\boldsymbol{u}}^i_{t+\theta\Delta\mathrm{t}}$, the trial value for the i+1-th step $\underline{\boldsymbol{u}}^{i+1}_{t+\theta\Delta\mathrm{t}}$ could be obtained using Eq. (A3-106).

Dynamic Analysis - Hydraulic Pressure

Substituting Eq. (A3-69) obtained from the steady-state seepage flow analysis into Eq. (A3-48), the discretized water flow balance equation can be expressed as follows

$$\boldsymbol{G}\underline{\boldsymbol{p}} + \boldsymbol{R}\underline{\dot{\boldsymbol{p}}} = \int_{\partial\Omega_q}\widehat{\boldsymbol{H}}^T\overline{\boldsymbol{q}}^* dS - \boldsymbol{Q}^T\underline{\dot{\boldsymbol{u}}} - \widehat{\boldsymbol{M}}\underline{\ddot{\boldsymbol{u}}} - \boldsymbol{G}\underline{\boldsymbol{p}}_{st} \quad \text{(A3-111)}$$

Here, the porewater inflow at the boundary in the dynamic analysis is given relative to the porewater inflow in the self-weight analysis as follows:

$$\overline{\boldsymbol{q}}^* = \overline{\boldsymbol{q}} - \overline{\boldsymbol{q}}_{st} \quad \text{(A3-112)}$$

In the dynamic analysis of water pressure, the time derivative of the left term of Eq. (A3-111) is solved by the difference approximation. Note that since Eq. (A3-111) includes nodal velocity and acceleration on the right term, it is common to solve it coupled with the ground displacement, as shown in the next section. Therefore, the details of the difference approximation are described in the next section.

Coupled Dynamic Analysis of Ground Deformation and Water Pressure

In this section, the method for solving Eq. (A3-91) and (A3-111) (coupled analysis) using the SSpj method (Zienkiewicz et al., 2000) is introduced. This method is commonly employed for liquefaction analysis under drained conditions when utilizing the "Strain Space Multiple Mechanism Model".

The simultaneous equations to be solved are listed as follows:

$$\int_{\Omega} \boldsymbol{B}^T \widehat{\boldsymbol{\sigma}'}\, dV + \boldsymbol{C}\dot{\underline{\boldsymbol{u}}} + \boldsymbol{M}\ddot{\underline{\boldsymbol{u}}} - \boldsymbol{Q}\underline{\boldsymbol{p}}^* = \Re \tag{A3-113}$$

$$\boldsymbol{G}\underline{\boldsymbol{p}} + \boldsymbol{R}\dot{\underline{\boldsymbol{p}}} + \boldsymbol{Q}^T\dot{\underline{\boldsymbol{u}}} + \widehat{\boldsymbol{M}}\ddot{\underline{\boldsymbol{u}}} = \Re^p \tag{A3-114}$$

Where:

$$\Re = -\ddot{u}_g \boldsymbol{M}\underline{\boldsymbol{I}} - \boldsymbol{C}^c\dot{\underline{\boldsymbol{u}}}^c - \boldsymbol{M}^c\ddot{\underline{\boldsymbol{u}}}^c + \int_{\Omega} \boldsymbol{B}^T \widehat{\boldsymbol{\sigma}'}_{st} dV + \int_{\partial\Omega_{\sigma}} \boldsymbol{H}^T \overline{\boldsymbol{T}}^*\, dS \tag{A3-115}$$

$$\Re^p = \int_{\partial\Omega_q} \widehat{\boldsymbol{H}}^T \underline{\boldsymbol{q}}^* dS + \boldsymbol{G}\underline{\boldsymbol{p}}_{st} \tag{A3-116}$$

Here, as in the coupled self-weight analysis, the nodal relative displacement vector $\underline{\boldsymbol{u}}$ is decomposed into an unconstrained degree of freedom $\boldsymbol{u}^f$, and a constrained degree of freedom $\underline{\boldsymbol{u}}^c$ (on the water pressure boundary $\partial\Omega_{0\boldsymbol{u}}$); the related matrices are also expressed as in Eq. (A3-70) and (A3-90). The nodal pore water pressure vector $\underline{\boldsymbol{p}}$ is also decomposed into an unconstrained degree of freedom $\underline{\boldsymbol{p}}^f$, and a constrained degree of freedom $\underline{\boldsymbol{p}}^c$ (on the water pressure boundary $\partial\Omega_{0p}$); the related matrices are also expressed as in Eq. (A3-64) and (A3-117). For the sake of notational brevity, the superscript f for the unconstrained degrees of freedom is omitted.

$$\boldsymbol{R} = [\boldsymbol{R}^f \quad \boldsymbol{R}^c] \tag{A3-117}$$

Similarly, for the matrices $\boldsymbol{Q}$, and that represent the coupled terms of ground displacement and water pressure, the partitioning is performed as in Eq. (A3-71) and (A3-118).

$$\widehat{\boldsymbol{M}} = \begin{bmatrix} \widehat{\boldsymbol{M}}^{ff} & \widehat{\boldsymbol{M}}^{fc} \\ \widehat{\boldsymbol{M}}^{cf} & \widehat{\boldsymbol{M}}^{cc} \end{bmatrix} \tag{A3-118}$$

Also, for the sake of notational brevity, ff is omitted from the superscripts.

Using these, Eq. (A3-113) and (A3-114) could be expressed as follows:

$$\int_{\Omega} \boldsymbol{B}^T \widehat{\boldsymbol{\sigma}'}\, dV + \boldsymbol{C}\dot{\underline{\boldsymbol{u}}} + \boldsymbol{M}\ddot{\underline{\boldsymbol{u}}} - \boldsymbol{Q}\underline{\boldsymbol{p}}^* = \Re \tag{A3-119}$$

$$\boldsymbol{G}\underline{\boldsymbol{p}} + \boldsymbol{R}\dot{\underline{\boldsymbol{p}}} + \boldsymbol{Q}^T\dot{\underline{\boldsymbol{u}}} + \widehat{\boldsymbol{M}}\ddot{\underline{\boldsymbol{u}}} = \Re^p \tag{A3-120}$$

Where:

$$\Re = -\ddot{u}_g \boldsymbol{M}\underline{\boldsymbol{I}} - \boldsymbol{C}^c\dot{\underline{\boldsymbol{u}}}^c - \boldsymbol{M}^c\ddot{\underline{\boldsymbol{u}}}^c + \boldsymbol{Q}^{fc}\underline{\boldsymbol{p}}^c + \int_{\Omega} \boldsymbol{B}^T \widehat{\boldsymbol{\sigma}'}_{st} dV + \int_{\partial\Omega_{\sigma}} \boldsymbol{H}^T \overline{\boldsymbol{T}}^*\, dS \tag{A3-121}$$

$$\Re^p = -\boldsymbol{G}^c\underline{\boldsymbol{p}}^c - \boldsymbol{R}^c\dot{\underline{\boldsymbol{p}}}^c - \boldsymbol{Q}^{cf^T}\dot{\underline{\boldsymbol{u}}}^c - \widehat{\boldsymbol{M}}^{cf}\ddot{\underline{\boldsymbol{u}}}^c + \int_{\partial\Omega_q} \widehat{\boldsymbol{H}}^T \underline{\boldsymbol{q}}^* dS + \boldsymbol{G}\underline{\boldsymbol{p}}_{st} \tag{A3-122}$$

The SSpj method assumes the following relationship between time steps t_n to $t_{n+1}(=t_n+\Delta t)$.

$$\underline{\boldsymbol{u}}=\underline{\boldsymbol{u}}_n+\underline{\dot{\boldsymbol{u}}}_n\tau+\cdots+\frac{\underline{\boldsymbol{u}}_n^{p-1}}{(p-1)!}\tau^{p-1}+\frac{\boldsymbol{\alpha}}{p!}\tau^p=\sum_{k=0}^{p-1}\frac{\underline{\boldsymbol{u}}_n^{k}}{k!}\tau^k+\frac{\boldsymbol{\alpha}}{p!}\tau^p \tag{A3-123}$$

$$\underline{\dot{\boldsymbol{u}}}=\sum_{k=1}^{p-1}\frac{\underline{\boldsymbol{u}}_n^{k}}{(k-1)!}\tau^{k-1}+\frac{\boldsymbol{\alpha}}{(p-1)!}\tau^{(p-1)} \tag{A3-124}$$

$$\underline{\ddot{\boldsymbol{u}}}=\sum_{k=2}^{p-1}\frac{\underline{\boldsymbol{u}}_n^{k}}{(k-2)!}\tau^{k-2}+\frac{\boldsymbol{\alpha}}{(p-2)!}\tau^{(p-2)} \tag{A3-125}$$

$$\underline{\boldsymbol{p}}=\underline{\boldsymbol{p}}_n+\underline{\dot{\boldsymbol{p}}}_n\tau+\cdots+\frac{\underline{\boldsymbol{p}}_n^{q-1}}{(q-1)!}\tau^{q-1}+\frac{\boldsymbol{\beta}}{q!}\tau^q=\sum_{k=0}^{q-1}\frac{\underline{\boldsymbol{p}}_n^{k}}{k!}\tau^k+\frac{\boldsymbol{\beta}}{q!}\tau^q \tag{A3-126}$$

$$\underline{\dot{\boldsymbol{p}}}=\sum_{k=1}^{q-1}\frac{\underline{\boldsymbol{p}}_n^{k}}{(k-1)!}\tau^{k-1}+\frac{\boldsymbol{\beta}}{(q-1)!}\tau^{q-1} \tag{A3-127}$$

Where τ is represented as $\tau=t-t_n$ by the present time t. Also, $\boldsymbol{\alpha}$ and $\boldsymbol{\beta}$ are unknown vectors related to nodal displacements and water pressure.

Additionally, it is assumed that the forced displacements and boundary stresses vary linearly during the relevant time step, as follows.

$$\underline{\boldsymbol{u}}^c=\underline{\boldsymbol{u}}_n^c+\frac{\underline{\boldsymbol{u}}_{n+1}^c-\underline{\boldsymbol{u}}_n^c}{\Delta t}\tau \tag{A3-128}$$

$$\underline{\dot{\boldsymbol{u}}}^c=\underline{\dot{\boldsymbol{u}}}_n^c+\frac{\underline{\dot{\boldsymbol{u}}}_{n+1}^c-\underline{\dot{\boldsymbol{u}}}_n^c}{\Delta t}\tau \tag{A3-129}$$

$$\underline{\ddot{\boldsymbol{u}}}^c=\underline{\ddot{\boldsymbol{u}}}_n^c+\frac{\underline{\ddot{\boldsymbol{u}}}_{n+1}^c-\underline{\ddot{\boldsymbol{u}}}_n^c}{\Delta t}\tau \tag{A3-130}$$

$$\underline{\boldsymbol{p}}^c=\underline{\boldsymbol{p}}_n^c+\frac{\underline{\boldsymbol{p}}_{n+1}^c-\underline{\boldsymbol{p}}_n^c}{\Delta t}\tau \tag{A3-131}$$

$$\underline{\dot{\boldsymbol{p}}}^c=\underline{\dot{\boldsymbol{p}}}_n^c+\frac{\underline{\dot{\boldsymbol{p}}}_{n+1}^c-\underline{\dot{\boldsymbol{p}}}_n^c}{\Delta t}\tau \tag{A3-132}$$

$$\overline{\boldsymbol{T}}^*=\overline{\boldsymbol{T}}^*{}_n+\frac{\overline{\boldsymbol{T}}^*{}_{n+1}-\overline{\boldsymbol{T}}^*{}_n}{\Delta t}\tau \tag{A3-133}$$

$$\overline{\boldsymbol{q}}^*=\overline{\boldsymbol{q}}^*{}_n+\frac{\overline{\boldsymbol{q}}^*{}_{n+1}-\overline{\boldsymbol{q}}^*{}_n}{\Delta t}\tau \tag{A3-134}$$

Furthermore, it is assumed that the changes in stress during the time step in under analysis varies linearly with the displacement. The above assumptions are applied to Eq. (A3-119) and (A3-120), and both sides are multiplied by the weight function W and integrated over the interval 0∼Δt. Furthermore, dividing both sides by $\int_0^{\Delta t}W\,dt$, the following equations could be obtained.

$$\widetilde{\Re}-\int_\Omega \boldsymbol{B}^T\widetilde{\boldsymbol{\sigma}'}\,dV+\boldsymbol{C}\underline{\tilde{\boldsymbol{u}}}+\boldsymbol{M}\underline{\tilde{\ddot{\boldsymbol{u}}}}-\boldsymbol{Q}\underline{\tilde{\boldsymbol{p}}}^*=0 \tag{A3-135}$$

$$\boldsymbol{G}\underline{\tilde{\boldsymbol{p}}}+\boldsymbol{R}\underline{\tilde{\dot{\boldsymbol{p}}}}+\boldsymbol{Q}^T\underline{\tilde{\boldsymbol{u}}}+\widehat{\boldsymbol{M}}\underline{\tilde{\ddot{\boldsymbol{u}}}}-\widetilde{\Re}^p=0 \tag{A3-136}$$

Where:

$$\widetilde{\widehat{\boldsymbol{\sigma}'}} = \widehat{\boldsymbol{\sigma}'}\,(\widetilde{\underline{\boldsymbol{u}}}) \tag{A3-137}$$

$$\widetilde{\underline{\boldsymbol{u}}} = \sum_{k=0}^{p-1} \frac{\overset{k}{\underline{\boldsymbol{u}}_n}}{k!}\theta_k \Delta\tau^k + \frac{\boldsymbol{\alpha}}{p!}\theta_p \Delta\tau^p \tag{A3-138}$$

$$\widetilde{\dot{\underline{\boldsymbol{u}}}} = \sum_{k=1}^{p-1} \frac{\overset{k}{\underline{\boldsymbol{u}}_n}}{(k-1)!}\theta_{k-1} \Delta\tau^{k-1} + \frac{\boldsymbol{\alpha}}{(p-1)!}\theta_{p-1} \Delta\tau^{(p-1)} \tag{A3-139}$$

$$\widetilde{\ddot{\underline{\boldsymbol{u}}}} = \sum_{k=2}^{p-1} \frac{\overset{k}{\underline{\boldsymbol{u}}_n}}{(k-2)!}\theta_{k-2} \Delta\tau^{k-2} + \frac{\boldsymbol{\alpha}}{(p-2)!}\theta_{p-2} \Delta\tau^{(p-2)} \tag{A3-140}$$

$$\widetilde{\underline{\boldsymbol{p}}} = \sum_{k=0}^{q-1} \frac{\overset{k}{\underline{\boldsymbol{p}}_n}}{k!}\theta_k \Delta\tau^k + \frac{\boldsymbol{\beta}}{q!}\tau^q \tag{A3-141}$$

$$\widetilde{\dot{\underline{\boldsymbol{p}}}} = \sum_{k=1}^{q-1} \frac{\overset{k}{\underline{\boldsymbol{p}}_n}}{(k-1)!}\theta_{k-1} \Delta\tau^{k-1} + \frac{\boldsymbol{\beta}}{(q-1)!}\theta_{k-1} \Delta\tau^{q-1} \tag{A3-142}$$

$$\theta_k \Delta\tau^k = \int_0^{\Delta t} W\tau^k d\tau \,/\, \int_0^{\Delta t} W d\tau \tag{A3-143}$$

Similarly, the constrained displacements, pore water pressure, boundary stresses, and boundary pore water inflow, on the boundary are given by linear relationships as follows

$$\widetilde{\underline{\boldsymbol{u}}}^c = \underline{\boldsymbol{u}}_n^c + \theta_1(\underline{\boldsymbol{u}}_{n+1}^c - \underline{\boldsymbol{u}}_n^c) \tag{A3-144}$$

$$\widetilde{\dot{\underline{\boldsymbol{u}}}}^c = \dot{\underline{\boldsymbol{u}}}_n^c + \theta_1(\dot{\underline{\boldsymbol{u}}}_{n+1}^c - \dot{\underline{\boldsymbol{u}}}_n^c) \tag{A3-145}$$

$$\widetilde{\ddot{\underline{\boldsymbol{u}}}}^c = \ddot{\underline{\boldsymbol{u}}}_n^c + \theta_1(\ddot{\underline{\boldsymbol{u}}}_{n+1}^c - \ddot{\underline{\boldsymbol{u}}}_n^c) \tag{A3-146}$$

$$\widetilde{\underline{\boldsymbol{p}}}^c = \underline{\boldsymbol{p}}_n^c + \theta_1(\underline{\boldsymbol{p}}_{n+1}^c - \underline{\boldsymbol{p}}_n^c) \tag{A3-147}$$

$$\widetilde{\dot{\underline{\boldsymbol{p}}}}^c = \dot{\underline{\boldsymbol{p}}}_n^c + \theta_1(\dot{\underline{\boldsymbol{p}}}_{n+1}^c - \dot{\underline{\boldsymbol{p}}}_n^c) \tag{A3-148}$$

$$\widetilde{\overline{\boldsymbol{T}}}^* = \overline{\boldsymbol{T}}^*{}_n + \theta_1(\overline{\boldsymbol{T}}^*{}_{n+1} - \overline{\boldsymbol{T}}^*{}_n) \tag{A3-149}$$

$$\widetilde{\overline{\boldsymbol{q}}}^* = \overline{\boldsymbol{q}}^*{}_n + \theta_1(\overline{\boldsymbol{q}}^*{}_{n+1} - \overline{\boldsymbol{q}}^*{}_n) \tag{A3-150}$$

$\widetilde{\Re}$ and $\widetilde{\Re}^p$ are obtained by substituting these equations into Eq. (A3-121) and (A3-122).

When solving the simultaneous Eq. (A3-135) and (A3-136) using the SSpj method, the unknown vector indicated in Eq. (A3-151), which appears in Eq. (A3-138) - (A3-142) shall be obtained by an iterative method. First, the unbalanced force $\boldsymbol{\varphi}^i$ for the i-th trial value is written expressed as shown in Eq. (A3-152):

$$\boldsymbol{\gamma} = \begin{bmatrix} \boldsymbol{\alpha} \\ \boldsymbol{\beta} \end{bmatrix} \tag{A3-151}$$

$$\boldsymbol{\varphi}^i = \begin{bmatrix} \boldsymbol{\varphi}^{ui} \\ \boldsymbol{\varphi}^{pi} \end{bmatrix} \tag{A3-152}$$

Where:

$$\boldsymbol{\varphi}^{\boldsymbol{u}i} = \int_{\Omega} \boldsymbol{B}^T \widetilde{\boldsymbol{\sigma}'^i}\, dV - \boldsymbol{C}\widetilde{\underline{\boldsymbol{u}}}^i - \boldsymbol{M}\widetilde{\underline{\ddot{\boldsymbol{u}}}}^i + \boldsymbol{Q}\widetilde{\underline{\boldsymbol{p}}}^{*i} + \widetilde{\Re}^i \tag{A3-153}$$

$$\boldsymbol{\varphi}^{pi} = \boldsymbol{G}\widetilde{\underline{\boldsymbol{p}}}^i + \boldsymbol{R}\widetilde{\underline{\dot{\boldsymbol{p}}}}^i + \boldsymbol{Q}^T\widetilde{\underline{\boldsymbol{u}}}^i + \widehat{\boldsymbol{M}}\widetilde{\underline{\ddot{\boldsymbol{u}}}}^i - \widetilde{\Re}^{pi} \tag{A3-154}$$

Assuming that the i+1-th trial value $\boldsymbol{\gamma}^{i+1}$ is obtained by Eq. (A3-155), the unbalanced force for the i+1-th trial value can be approximated by Eq. (A3-156).

$$\boldsymbol{\gamma}^{i+1} = \boldsymbol{\gamma}^i + \Delta\boldsymbol{\gamma}^i \tag{A3-155}$$

$$\boldsymbol{\varphi}^{i+1} = \boldsymbol{\varphi}^i + \left(\frac{\partial \boldsymbol{\varphi}}{\partial \boldsymbol{\gamma}}\right)^i \Delta\boldsymbol{\gamma}^i \tag{A3-156}$$

Where:

$$\left(\frac{\partial \boldsymbol{\varphi}}{\partial \boldsymbol{\gamma}}\right)^i = \begin{bmatrix} \left(\frac{\partial \boldsymbol{\varphi}^{\boldsymbol{u}}}{\partial \boldsymbol{\alpha}}\right)^i & \left(\frac{\partial \boldsymbol{\varphi}^{\boldsymbol{u}}}{\partial \boldsymbol{\beta}}\right)^i \\ \left(\frac{\partial \boldsymbol{\varphi}^{p}}{\partial \boldsymbol{\alpha}}\right)^i & \left(\frac{\partial \boldsymbol{\varphi}^{p}}{\partial \boldsymbol{\beta}}\right)^i \end{bmatrix} \tag{A3-157}$$

$$\left(\frac{\partial \boldsymbol{\varphi}^{\boldsymbol{u}}}{\partial \boldsymbol{\alpha}}\right)^i = -(\boldsymbol{K}_L)^i \theta_p \frac{\Delta t^p}{p!} - \boldsymbol{C}\theta_{p-1}\frac{\Delta t^{p-1}}{(p-1)!} - \boldsymbol{M}\theta_{p-2}\frac{\Delta t^{p-1}}{(p-2)!} \tag{A3-158}$$

$$\left(\frac{\partial \boldsymbol{\varphi}^{\boldsymbol{u}}}{\partial \boldsymbol{\beta}}\right)^i = \boldsymbol{Q}\theta_q\frac{\Delta t^q}{q!} \tag{A3-159}$$

$$\left(\frac{\partial \boldsymbol{\varphi}^{p}}{\partial \boldsymbol{\beta}}\right)^i = \boldsymbol{G}\theta_{\boldsymbol{q}}\frac{\Delta t^q}{q!} + \boldsymbol{R}\theta_{q-1}\frac{\Delta t^{q-1}}{(q-1)!} \tag{A3-160}$$

$$\left(\frac{\partial \boldsymbol{\varphi}^{p}}{\partial \boldsymbol{\alpha}}\right)^i = \boldsymbol{Q}^T\theta_{p-1}\frac{\Delta t^{p-1}}{(p-1)!} + \widehat{\boldsymbol{M}}\theta_{p-2}\frac{\Delta t^{p-2}}{(p-2)!} \tag{A3-161}$$

From the above, in the coupled analysis of ground deformation and water pressure when the SSpj method is applied, the incremental values of nodal displacement and water pressure shall be obtained by the following equation, so that the i+1-th unbalanced force in Eq. (A3-156) becomes zero.

$$\begin{bmatrix} -\left(\frac{\partial \boldsymbol{\varphi}^{\boldsymbol{u}}}{\partial \boldsymbol{\alpha}}\right)^i & -\left(\frac{\partial \boldsymbol{\varphi}^{\boldsymbol{u}}}{\partial \boldsymbol{\beta}}\right)^i \\ -\left(\frac{\partial \boldsymbol{\varphi}^{p}}{\partial \boldsymbol{\alpha}}\right)^i & -\left(\frac{\partial \boldsymbol{\varphi}^{p}}{\partial \boldsymbol{\beta}}\right)^i \end{bmatrix} \Delta\boldsymbol{\gamma}^i = \boldsymbol{\varphi}^i \tag{A3-162}$$

Furthermore, the obtained nodal displacements and water pressure increments allow the estimation of the i+1th trial value $\boldsymbol{\gamma}^{i+1}$ using Eq. (A3-155).

A-3-2 Formulation of the "Strain Space Multiple Mechanism Model"

The formulation of the dilatancy in the strain space multiple mechanism is based on the following postulates [16]:

- From a micromechanical point of view, granular materials consist of an assemblage of particles in contact with each other; the pattern of contacts (i.e. the micromechanical structure) changes during macroscopic deformations.
- The "Strain Space Multiple Mechanism Model" idealizes the structures as a twofold structure consisting of a multitude of virtual two-dimension mechanisms.
- A second-order fabric tensor describes the direct macroscopic stress-strain relationship, and a fourth-order fabric tensor describes the incremental relationship
- In order to establish a bridge between the micromechanical and macroscopic dilative component of dilatancy, the mechanism of interlocking was defined as the energy less component of the macroscopic strain. On the other hand, as for the contractive component of dilatancy, a bridge is established by assuming that the macroscopic component is given from those of microscopic counterparts associated with the virtual simple shear strain rate.
- The dilatancy along the stress path beyond a line slightly above the phase transformation line is only due to the mechanism of interlocking, and the increment on dilatancy due to this interlocking eventually vanishes for a large shear strain.

A3-2.1 Multiple mechanism idealized through fabric tensors

Stress in granular materials can be defined by a certain average of the contact forces between particles; for 2D plane strain conditions, the contact force (**P**) can be decomposed into normal (**n**) and tangential (**t**) contact forces; if we define **I** as the second-order identity tensor, p as the effective confining pressure (compression positive), and q as the micromechanical stress contributions to the macroscopic deviator stress (due to the contact forces), the twofold structure that describes the macroscopic effective stress through a second-order fabric tensor is defined in Eq. (A3-163):

$$\boldsymbol{\sigma}' = -p\boldsymbol{I} + \frac{1}{4\pi}\iint q\langle \boldsymbol{t}\otimes\boldsymbol{n}\rangle d\omega d\Omega \qquad \text{(A3-163)}$$

The integrated form (i.e. stress-strain relationship) was derived by relating the macroscopic strain tensor **ε** to the macroscopic effective stress **σ'** (Eq. (A3-163)). In this sense, the volumetric strain ε and the virtual shear strains γ were defined as the projections of the macroscopic through Eq. (A3-164) and (A3-165).

$$\varepsilon = \boldsymbol{I}:\boldsymbol{\varepsilon} \tag{A3-164}$$

$$\gamma = \langle \boldsymbol{t}\otimes\boldsymbol{n}\rangle:\boldsymbol{\varepsilon} \tag{A3-165}$$

To take into account the volumetric strain due to dilatancy ε_d, the effective volumetric strain ε' is defined in Eq. (A3-166). It is important to mention that the rate of volumetric strain due to dilatancy is given by the projection of the strain rate field to a second-order tensor $\mathbf{I_d}$.

$$\varepsilon' = \varepsilon - \varepsilon_d \tag{A3-166}$$

The scalar variables defined in Eq. (A3-165) and (A3-166) are used to define the isotropic stress p and the virtual simple shear stress q through path-dependent functions, as shown in Eq. (A3-167) and (A3-168), respectively.

$$p = p(\varepsilon') \tag{A3-167}$$

$$q = q(\gamma) \tag{A3-168}$$

Additionally, the virtual simple shear mechanism is formulated as a hysteretic function, where a backbone curve is given by the hyperbolic function shown in Eq. (A3-169).

$$q(\gamma) = \frac{\gamma/\gamma_v}{1 + |\gamma/\gamma_v|} q_v \tag{A3-169}$$

Where the parameters q_v and γ_v are the shear strength and the reference strain of the virtual simple shear mechanism, respectively.

The incremental form of the constitutive equation was derived by taking the time derivative of both sides of Eq. (A3-163); and by substituting the values of Eq. (A3-164), (A3-165) and (A3-166), the incremental form of the constitutive equation can be expressed as shown by Eq. (A3-170) and (A3-171):

$$\dot{\boldsymbol{\sigma}}' = \mathbb{C}:\dot{\boldsymbol{\varepsilon}} \tag{A3-170}$$

$$\mathbb{C} = K_{L/U}\boldsymbol{I}\otimes\boldsymbol{I} + \frac{1}{4\pi}\iint G_{L/U}\langle \boldsymbol{t}\otimes\boldsymbol{n}\rangle\otimes\langle \boldsymbol{t}\otimes\boldsymbol{n}\rangle d\omega d\Omega - K_{L/U}\boldsymbol{I}\otimes\boldsymbol{I_d} \tag{A3-171}$$

Where $\mathbb{C}$ is a fourth-order tensor with strain-induced anisotropy. It worth to mention that the first and second members of Eq. (A3-171) represent the volumetric and deviator relationships (being major symmetric), meanwhile, the third component represents the effect of dilatancy that is formulated as a coupling between the volumetric and deviator mechanisms (being major asymmetric).

The terms of the tangential stiffness $K_{L/U}$ and $G_{L/U}$ are defined by Eq. (A3-172) and (A3-173).

$$K_{L/U} = -\frac{dp}{d\varepsilon'} \tag{A3-172}$$

$$G_{L/U} = \frac{\partial q}{\partial \gamma} \tag{A3-173}$$

A3-2.2 Generalized multiple mechanism

The fundamental form of the constitutive equations reviewed above can be generalized by decomposing the dilatancy (Eq. (A3-166)) into contractive ε_d^c and dilative ε_d^d components, and considering Eq. (A3-163), (A3-164), and (A3-165) as being the same.

By using the contractive component, the virtual effective volumetric strain ε'' is defined in Eq. (A3-174).

$$\varepsilon'' = \varepsilon - \varepsilon_d^c \tag{A3-174}$$

Assuming Eq. (A3-167) as being the same, Eq. (A3-168) can be generalized to take into account various failure criteria defined for the three-dimensional model [156], and the effects of effective stress and state of liquefaction by introducing additional variables, as shown in Eq. (A3-175).

$$\mathrm{q} = \mathrm{q}(\gamma, \varepsilon', \varepsilon'', J_2, \theta) \tag{A3-175}$$

Where J_2 and θ represent the second invariant of the stress tensor, and the Lode angle, respectively.

Based on Eq. (A3-174) and (A3-175), the generalized incremental constitutive equation can be expressed as shown by Eq. (A3-176), (A3-177), and (A3-178):

$$\dot{\boldsymbol{\sigma}}' = \mathbb{C} : \dot{\boldsymbol{\varepsilon}} + \mathbb{Q} : \dot{\boldsymbol{\sigma}}' \tag{A3-176}$$

$$\begin{aligned}\mathbb{C} = K_{L/U}\boldsymbol{I}\otimes\boldsymbol{I} + \frac{1}{4\pi}\iint G_{L/U}\langle \boldsymbol{t}\otimes\boldsymbol{n}\rangle\otimes\langle \boldsymbol{t}\otimes\boldsymbol{n}\rangle d\omega d\Omega - K_{L/U}\boldsymbol{I}\otimes\boldsymbol{I_d} \\ + \frac{1}{4\pi}\iint H\langle \boldsymbol{t}\otimes\boldsymbol{n}\rangle d\omega d\Omega \otimes (\boldsymbol{I} - \boldsymbol{I_d}) + \frac{1}{4\pi}\iint L\langle \boldsymbol{t}\otimes\boldsymbol{n}\rangle d\omega d\Omega \otimes (\boldsymbol{I} - \boldsymbol{I_d^c})\end{aligned} \tag{A3-177}$$

$$\mathbb{Q} = -\boldsymbol{K}_{L/U}\boldsymbol{I}\otimes\boldsymbol{J_d} - \frac{\boldsymbol{1}}{\boldsymbol{4\pi}}\iint H\langle \boldsymbol{t}\otimes\boldsymbol{n}\rangle d\omega d\Omega \otimes \boldsymbol{J_d} + \frac{\boldsymbol{1}}{\boldsymbol{4\pi}}\iint \langle \boldsymbol{t}\otimes\boldsymbol{n}\rangle \otimes \boldsymbol{J_q} d\omega d\Omega \tag{A3-178}$$

Where:

$$H = \frac{\partial q}{\partial \varepsilon'} \tag{A3-179}$$

$$L = \frac{\partial q}{\partial \varepsilon''} \tag{A3-180}$$

$$\boldsymbol{J_q} = \frac{\partial q}{\partial J_2}\frac{\partial J_2}{\partial \boldsymbol{\sigma'}} + \frac{\partial q}{\partial \theta}\frac{\partial \theta}{\partial \boldsymbol{\sigma'}} \tag{A3-181}$$

The first three terms on the right side of Eq. (A3-177) are the same as those appearing in the fundamental form (Eq. (A3-171)); the generalized form includes the fourth term representing the dependency of shear mechanism on effective stress and the fifth term on the state of liquefaction. Additionally, Eq. (A3-178) includes the effect of the second invariant of stress tensor J_2 and the Lode angle θ on the shear dilatancy.

A3-2.3 Strain energy and dilatancy

The rate of strain energy in the strain space multiple mechanism model $\dot{W}$ is computed by means of Eq. (A3-163), (A3-164) and (A3-165), and is shown in Eq. (A3-182).

$$\dot{W} = \boldsymbol{\sigma'}:\boldsymbol{\dot{\varepsilon}} = \dot{W}_p + \frac{1}{4\pi}\iint \dot{W_{qv}} d\omega d\Omega \tag{A3-182}$$

Where $\dot{W}_p = -p\dot{\varepsilon}$, and $\dot{W_{qv}} = q\dot{\gamma}$.

Eq. (A3-182) defines the fundamental relationship between the macroscopic strain energy rate $\dot{W}$ and the microscopic strain energy rate $\dot{W_{qv}}$. Based on Eq. (A3-166) and the fact that the dilatancy can be decomposed into contractive ε_d^c and dilative ε_d^d components of dilatancy, the volumetric strain rate can be expressed as shown in Eq. (A3-183).

$$\dot{\varepsilon} = \dot{\varepsilon}' + \dot{\varepsilon}_d^c + \dot{\varepsilon}_d^d \tag{A3-183}$$

By substituting Eq. (A3-183) into (A3-182), we obtain Eq. (A3-184).

$$\dot{W} = \boldsymbol{\sigma'}:\boldsymbol{\dot{\varepsilon}} = \dot{W'}_p + \dot{W}_p^{dc} + \dot{W}_p^{dd} + \frac{1}{4\pi}\iint \dot{W_{qv}} d\omega d\Omega \tag{A3-184}$$

Where $\dot{W'}_p = -p\dot{\varepsilon}'$, $\dot{W}_p^{dc} = -p\dot{\varepsilon}_d^c$, and $\dot{W}_p^{dd} = -p\dot{\varepsilon}_d^d$

A3-2.3.1 Dilative component of dilatancy

One of the important hypotheses made in this model is that the fraction of the shear strain energy is consumed in the mechanism of interlocking, as shown in Eq. (A3-185).

$$\dot{W}_p^{dd} + \frac{1}{4\pi}\iint \dot{W}_{qv}^{dd} d\omega d\Omega = 0 \tag{A3-185}$$

Where, by using the parameter r_{ε_d}, the fraction of the shear strain energy rate is given by Eq. (A3-186).

$$\dot{W}_{qv}^{dd} = r_{\varepsilon_d} \dot{W}_{qv} = r_{\varepsilon_d} q\dot{\gamma} \tag{A3-186}$$

In this model, it is also assumed that the shear stress contribution to the interlocking in Eq. (A3-186), refers to the backbone curve in Equation (A3-169).

Based on the previously mentioned hypothesis, and by defining $M_{fv} = q_v/p$, the dilative component of dilatancy is given by Eq. (A3-187).

$$\dot{\varepsilon}_d^d = \frac{1}{4\pi} r_{\varepsilon_d} \iint \frac{\gamma/\gamma_v}{1 + |\gamma/\gamma_v|} M_{fv} \dot{\gamma} d\omega d\Omega \tag{A3-187}$$

Eq. (A3-187) represents the fundamental form of the dilative component of dilatancy; the formulation can be extended for describing the steady-state of the soil by introducing an upper limit to the dilative component of dilatancy, by introducing a parameter γ_{vus} representing an asymptote limit state. The incremental form is shown in Eq. (A3-188) and (A3-189).

$$\dot{\varepsilon}_d^d = \boldsymbol{I_d^d} : \dot{\boldsymbol{\varepsilon}} \tag{A3-188}$$

$$\boldsymbol{I_d^d} = \frac{1}{4\pi} r_{\varepsilon_d} \iint \frac{\tilde{\gamma}/\gamma_v}{1 + |\tilde{\gamma}/\gamma_v|} sgn(\gamma) \exp(-\frac{|\gamma|}{\gamma_{vus}}) M_{fv} \langle \boldsymbol{t} \otimes \boldsymbol{n} \rangle d\omega d\Omega \tag{A3-189}$$

A3-2.3.2 Contractive component of dilatancy

The contractive component of dilatancy is given by assuming that the macroscopic component is given from those of microscopic counterparts associated with the virtual simple shear strain rate, as shown in Eq. (A3-190).

$$\dot{\varepsilon}_d^c = -\frac{1}{4\pi} \iint M_v |\dot{\gamma}_p| d\omega d\Omega \tag{A3-190}$$

Where, $\dot{\gamma}_p$ denotes the plastic portion of virtual simple shear strain, defined by $\dot{\gamma}_p = \dot{\gamma} - c_1 \dot{\gamma}_e$; in which, the parameter c_1 controls the elastic range.

By applying Eq. (A3-169) and (A3-173), and by defining $G_{L0} = q_v/\gamma_v$, the contractive component of dilatancy is formulated through another second-order fabric tensor $\boldsymbol{I_d^c}$, as shown in Eq. (A3-191) and (A3-192).

$$\dot{\varepsilon}_d^c = \boldsymbol{I_d^c} : \dot{\boldsymbol{\varepsilon}} \tag{A3-191}$$

$$\boldsymbol{I_d^c} = -\frac{1}{4\pi} \iint M_v (1 - c_1 (\frac{G_{L/U}}{G_{L0}})) |\boldsymbol{t} \otimes \boldsymbol{n}|^* d\omega d\Omega \tag{A3-192}$$

This formulation of dilatancy postulates that no increase is allowed for contractive component of dilatancy along the stress path beyond a limiting line that is defined between the failure line and the phase transformation line; Figure A3-1 shows the position of this line relative to the phase transformation and failure lines in a stress plane defined by the effective confining pressure p and the shear stress $\tau = \sqrt{J_2}cos\theta$; it worth to mention that the shaded area allows only dilative component of dilatancy due to interlocking, so, the steady-state cannot be reached without going through this zone.

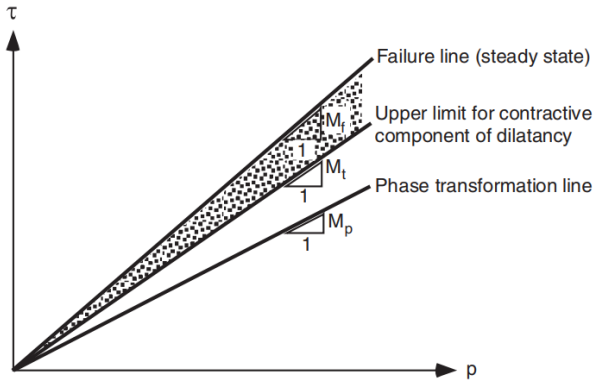

Figure A3-1 Zoning of stress plane with respect to dilatancy [16]

References

[1] M. Manzari, B. Kutter, M. Zeghal, S. Iai, T. Tobita, S. Madabhushi, S. Haigh, L. Mejia, D. Gutierrez, R. Armstrong, M. Sharp, Y. Chen and Y. Zhou, "LEAP projects: Concept and challenges," *Geotechnics for Catastrophic Flooding Events*, pp. 109-116, 2015.

[2] American Society of Mechanical Engineers, Standard for Verification and Validation in Computational Solid Mechanics V V 10 - 2019, 2020.

[3] S. Schlesinger, "Terminology for Model Credibility," *Simulation*, vol. 32, no. 3, pp. 103-104, 1979.

[4] L. Schewer, "Verification and validation in computational solid mechanics and the ASME Standards Committee," in *Fluid Structure Interaction and Moving Boundary Problems*, WIT Press, 2005, pp. 109-117.

[5] American Society of Mechanical Engineers, Standard for Verification and Validation in Computational Fluid Dynamics and Heat Transfer, 2009(R2021).

[6] Institute of Electrical and Electronics Engineers, IEEE Approved Draft Standard for Validation of Computational Electromagnetics Computer Modeling and Simulations, IEEE Standards Association, 2022.

[7] W. Oberkampf and T. Trucano, "Verification and validation in computational fluid dynamics," *Progress in Aerospace Sciences*, vol. 38, no. 3, pp. 209-272, 2002.

[8] K. Ziotopoulou and R. Boulanger, "Validation Protocols for Constitutive Modeling of Liquefaction," *Proceedings of the 6th International Conference on Earthquake Geotechnical Engineering*, 2015.

[9] B. Thacker, S. Doebling, F. Hernandez, M. Anderson, J. Pepin and E. Rodriguez, "Concepts of Model Verification and Validation," Los Alamos National Laboratory, 2004.

[10] T. Carey and B. Kutter, "Validation of models used to predict the effects of lateral spreading by comparison of experimental and numerical response surfaces," *Soil Dynamics and Earthquake Engineering*, vol. 163, 2022.

[11] R. Jauregui and F. Silva, "Numerical Validation Methods," in *Numerical Analysis Theory and Application*, InTech, 2011, pp. 155-174.

[12] A. Drozd, "Selected methods for validating computational electromagnetic modeling techniques," in *International Symposium on Electromagnetic Compatibility*, 2005.

[13] L. Godoy and P. Dardati, "Validación de modelos en mecánica computacional (in Spanish)," *Mecanica Computacional*, vol. 20, pp. 663-670, 2001.

[14] Japanese Society of Civil Engineers, Verification and Validation Methods for Nonlinear Ground/Structures Simulations - Guidelines and Practical Examples (in Japanese), Japanese Society of Civil Engineers, 2022.

[15] Atomic Energy Society of Japan, Guide for the Assessment of Nuclear Simulation Credibility, AESJ, 2015.

[16] S. Iai, T. Tobita, O. Ozutsumi and K. Ueda, "Dilatancy of granular materials in a strain space multiple mechanism model," *International Journal for Numerical and Analytical Methods in Geomechanics*, vol. 35(3), pp. 360-392, 2011.

[17] American Society of Mechanical Engineers, An Illustration of the Concepts of Verification and Validation in Computational Solid Mechanics, ASME Standard V&V 10.1-2016, 2012.

[18] L. Eca, K. Dowding and P. Roache, "On the interpretation and scope of the V&V 20 Standard for Verification and Validation in Computational Fluid Dynamics and Heat Transfer," in *Proceedings of V&V Verification and Validation Symposium V&V 2020*, Baltimore, USA, 2020.

[19] K. Ueda and S. Iai, "Numerical Predictions for Centrifuge Model Tests of a Liquefiable Sloping Ground Using a Strain Space Multiple Mechanism Model Based on the Finite Strain Theory," *Soil*

Dynamics and Earthquake Engineering, vol. 113, pp. 771-792, 2018.

[20] K. Ueda and Y. Murano, "Analytical Evaluation of Input Loss of Pile Foundation by Using 2-Dimensional Finite Element Method," *14th Japan Earthquake Engineering Symposium (in Japanese),* 2014.

[21] K. Ueda, "Dynamics of Poroelastic Media Based on Multiple Shear Mechanism at Finite Strain," *20th Applied Mechanics Symposium – Japanese Society of Civil Engineers (in Japanese),* 2017.

[22] S. Iai, T. Morita, T. Kameoka, Y. Matsunaga and K. Abiko, "Response of a dense sand deposit during 1993 Kushiro-oki earthquake," *Soils and Foundations,* vol. 35(1), pp. 115-131, 1995.

[23] O. Ozutsumi, S. Sawada, S. Iai, Y. Takeshima, W. Sugiyama and T. Shimizu, "Effective stress analyses of liquefaction-induced deformation in river dikes," *Soil Dynamics and Earthquake Engineering,* vol. 22 (9～12), pp. 1075-1082, 2002.

[24] B. Kutter, T. Carey, N. Stone, M. Bonab, M. Manzari, M. Zeghal, S. Escoffier, S. Haigh, S. Madabhushi, W. Hung, D. Kim, N. Kim, M. Okamura, T. Tobita, K. Ueda and Y. Zhou, "LEAP-UCD-2017 V. 1.01 model specifications," *Model Tests and Numerical Simulations of Liquefaction and Lateral Spreading,* 2019.

[25] T. Tobita, K. Ichii and K. Ueda, "LEAP-ASIA-2019 Experiments (Liquefaction Experiments and Analysis Projects) - Dataset," DesignSafe-CI, 2022.

[26] R. Vargas, K. Ueda and K. Uemura, "Influence of the relative density and K0 effects in the cyclic response of Ottawa F-65 sand - cyclic Torsional Hollow-Cylinder shear tests for LEAP-ASIA-2019," *Soil Dynamics and Earthquake Engineering,* vol. 133, 2020.

[27] I. Idriss and R. Boulanger, Soil Liquefaction During Earthquakes, MNO-12, Earthquake Engineering Research Institute, 2008.

[28] K. Ishihara, Soil behaviour in earthquake geotechnics, Oxford University Press, 1996.

[29] H. Seed and K. Lee, "Liquefaction of saturated sands during cyclic loading," *Journal of ASCE,* vol. 92, 1966.

[30] T. Youd, I. Idriss, R. Andrus, I. Arango, G. Castro, J. Christian, R. Dobry, W. Finn, L. Harder, M. Hynes, K. Ishihara, J. Koester, S. Liao, W. Marcuson, G. Martin, J. Mitchell, Y. Moriwaki, M. Power, P. Robertson, R. Seed and K. Stokoe, "Liquefaction Resistance of Soils: Summary Report from the 1996 NCEER and 1998 NCEER/NSF Workshops on Evaluation of Liquefaction Resistance of Soils," *Journal of Geotechnical and Geoenvironmental Engineering,* vol. 127, no. 10, 2001.

[31] H. Seed and I. Idriss, "Simplified Procedure for Evaluating Soil Liquefaction Potential," *Journal of the Soil Mechanics and Foundations Division,* vol. 97, no. 9, 1971.

[32] R. Boulanger and I. Idriss, CPT and SPT Based Liquefaction Triggering Procedures, University of California at Davis, 2014.

[33] Japanese Road Association JRA, Road Bridge Specifications and Commentary: Seismic Design (in Japanese), 2019.

[34] P. Robertson, "Evaluation of flow liquefaction and liquefied strength using the cone penetration test: an update," *Canadian Geotechnical Journal* , vol. Note, 2021.

[35] R. Andrus and K. Stokoe, "Liquefaction Resistance of Soils from Shear-Wave Velocity," *Journal of Geotechnical and Geoenvironmental Engineering,* vol. 126, no. 11, 2000.

[36] S. Madabhushi, Centrifuge Modelling for Civil Engineers, CRC Press, 2015.

[37] S. Bartlett and T. Youd, "Empirical Prediction of Liquefaction-Induced Lateral Spread," *Journal of Geotechnical Engineering,* vol. 121, 1995.

[38] S. Kramer, "Lateral Spreading," in *Bobrowsky, P.T. (eds) Encyclopedia of Natural Hazards. Encyclopedia of Earth Sciences Series*, Springer, Dordrecht, 2013.

[39] A. Rauch, "EPOLLS: An Empirical Method for Prediciting Surface Displacements Due to Liquefaction-Induced Lateral Spreading in Earthquakes," Ph.D. dissertation - Virginia Polytechnic Institute and State University, VA, 1997.

[40] G. Zhang, P. Robertson and R. Brachman, "Estimating Liquefaction-Induced Lateral Displacements Using the Standard Penetration Test or Cone Penetration Test," *Journal of Geotechnical and Geoenvironmental Engineering,* vol. 130, no. 8, 2004.

[41] H. Woldesellasse and S. Tesfamariam, "Prediction of lateral spreading displacement using conditional Generative Adversarial Network (cGAN)," *Soil Dynamics and Earthquake Engineering,* vol. 156, 2022.

[42] M. Durante and E. Rathje, "An exploration of the use of machine learning to predict lateral spreading," *Earthquake Spectra,* vol. 37, no. 4, 2021.

[43] Z. Chen, Y. Chen, Y. Zhang, X. Liu, P. Xiao and P. Samui, "Assessment of liquefaction-induced lateral spread using soft computing approaches," *Gondwana Research,* 2022.

[44] A. Schofield, "Cambridge geotechnical centrifuge operations," *Geotechnique,* vol. 30, pp. 227-268, 1980.

[45] UC Davis - Center for Geotechnical Modeling, "Principles of Centrifuge Modeling," [Online]. Available: https://cgm.engr.ucdavis.edu/principles/. [Accessed 25 April 2023].

[46] P. Cundall and O. Strack, "A discrete numerical model for granular assemblies," *Geotechnique ,* vol. 29(1), pp. 47-65, 1979.

[47] M. Otsubo, S. Chitravel, R. Kuwano, H. Kyokawa and J. Koseki, "Liquefaction characteristics in triaxial tests under various gravity environments – DEM analyses," *Computers and Geotechnics,* vol. 156, 2023.

[48] F. Oka and S. Kimoto, Computational Modeling of Multiphase Geomaterials, New York: Taylor & Francis Group, 2013.

[49] R. Uzuoka and R. Borja, "Dynamics of unsaturated poroelastic solids at," *International Journal for Numerical and Analytical Methods in Geomechanics,* vol. 36, 2002.

[50] M. Biot, "Mechanics of deformation and acoustic propagation in porous media," *Journal of Applied Physics,* vol. 33, no. 4, pp. 1482-1498, 1962.

[51] O. Zienkiewicz and T. Shiomi, "Dynamic behavior of saturated porous media: The generalized Biot formulation and its numerical solution," *International Journal for Numerical and Analytical Method in Geomechanics,* vol. 8, pp. 71-96, 1984.

[52] O. Zienkiewicz, C. Chang and P. Bettes, "Drained, undrained, consolidating and dynamic behavior assumptions in soils, limits of validity," *Geotechnique,* vol. 30, no. 4, pp. 385-395, 1980 .

[53] A. Elgamal, Z. Yang, E. Parra and A. Ragheb, "Modeling of Cyclic Mobility in Saturated Cohesionless Soils," *International Journal of Plasticity,* vol. 19(6), pp. 883-905, 2003.

[54] H. Ling and S. Yang, "A Unified Sand Model Based on Critical State and Generalized Plasticity," *Journal of Engineering Mechanics,* vol. 132(12), pp. 1380-1391, 2006.

[55] M. Manzari and Y. Dafalias, "A Critical State Two-Surface Plasticity Model for Sands," *Geotechnique,* vol. 19(2), pp. 255-272, 1997.

[56] M. Cubrinovski and K. Ishihara, "State Concept and Modified Elastoplasticity for Sand Modeling," *Soils and Foundations,* vol. 38(4), pp. 213-225, 1998.

[57] M. Taiebat, Advanced Elastic-Plastic Constitutive and Numerical Modeling in Geomechanics, LAP Lambert Academic Publishing, 2009.

[58] F. Oka, R. Uzuoka, A. Tateishi and A. Yashima, "A cyclic elasto-plastic model for sand and its application to liquefaction analysis," *Constitutive modelings of geomaterials, selected contributions from the Frank L. DiMaggio Symposium,* pp. 75-99, 2002.

[59] S. Iai, T. Sugano, K. Ichii and T. Morita, "Seismic Performance of Quay Walls - Kobe Earthquake," in *Proceedings of Earthquake Criteria Workshop - Recent Developments in Seismic Hazard and Risk Assessments for Port, Harbor, and Offshore Structures,* Yokohama, 1997.

[60] K. Ueda, S. Iai and T. Tobita, "Centrifuge model tests and large deformation analyses of a breakwater subject to combined effects of tsunami," *Soil Dynamics and Earthquake Engineering,* vol. 91, pp.

294-303, 2016.

[61] K. Ueda, T. Wada and R. Uzuoka, "Centrifuge model tests and effective stress analyses for higher-accuracy prediction of the seismic behavior of liquefiable sloping ground," *Journal of Japan Society of Civil Engineers A1 (Structural and Earthquake Engineering),* vol. 75, no. 4, pp. 494-505, 2019.

[62] NAFEMS, SAFESA Technical Manual, R0041, 1995.

[63] J. Smith, Engineering Simulation Quality Management Standard, NAFEMS, 2020.

[64] Japan Society for Computational Engineering and Science, The Application Examples for Quality Management of Engineering Simulation (HQC001) & A Model Procedure for Engineering Simulation (HQC002) (in Japanese), JSCES, 2015.

[65] Japan Society for Computational Engineering and Science, Quality Management of Engineering Simulation (in Japanese), JSCES, 2017.

[66] American Institute of Aeronautics and Astronautics, "Guide for the Verification and Validation of Computational Fluid Dynamics Simulations," AIAA, 1998.

[67] American Society of Mechanical Engineers, Assessing Credibility of Computational Modeling through Verification and Validation: Application to Medical Devices, 2018.

[68] S. Lopez-Querol and R. Blazquez, "Validation of a new endochronic liquefaction model for granular soil by using centrifuge test data," *Soil Dynamics and Earthquake Engineering,* vol. 27(10), pp. 920-937, 2007.

[69] S. Gobbi, M. Santisi d'Avila, L. Lenti, J. Semblat and P. Reiffsteck, "Liquefaction assessment of silty sands: Experimental characterization and numerical calibration," *Soil Dynamics and Earthquake Engineering,* vol. 159, 2022.

[70] K. Kassas, O. Adamidis and I. Anastasopoulos, "Shallow strip foundations subjected to earthquake-induced soil liquefaction: Validation, modelling uncertainties, and boundary effects," *Soil Dynamics and Earthquake Engineering,* vol. 147, 2021.

[71] G. Tsinidis, K. Pitilakis and A. Trikalioti, "Numerical simulation of round robin numerical test on tunnels using a simplified kinematic hardening model," *Acta Geotechnica,* vol. 9, pp. 641-659, 2014.

[72] A. Cibelli, M. Pathirage, G. Cusatis, L. Ferrara and G. Di Luzio, "A discrete numerical model for the effects of crack healing on the behaviour of ordinary plain concrete: Implementation, calibration, and validation," *Engineering Fracture Mechanics,* vol. 263, 2022.

[73] E. Watanabe and M. Kurumatani, "Code verification and calculation verification for non-linear finite element analysis of reinforced concrete beam," *Proceedings of the Japan Society for Computational Engineering and Science (in Japanese),* p. 20220011, 2022.

[74] M. Kurumatani, T. Saka, Y. Yamamoto, N. Ueda, S. Okazaki and H. Ogura, "A nonlinear computational model for predicting flexural fracture behavior of reinforced concrete beam based on beam theory and its verification and validation," *Proceedings of the Japan Society for Computational Engineering and Science (in Japanese),* p. 20210020, 2021.

[75] M. Kurumatani, T. Saka, T. Yamamoto, N. Ueda, M. Ryuto and M. Kobayashi, "A surrogate model for nonlinear finite element analysis of reinforced concrete beam and its validation," *Journal of Japan Society of Civil Engineers A2 (Applied Mechanics) (in Japanese),* vol. 77, no. 2, pp. 403-412, 2021.

[76] L. Duarte, G. Dellinger, N. Dellinger, A. Ghenaim and A. Terfous, "Implementation and validation of a strongly coupled numerical model of a fully passive flapping foil turbine," *Journal of Fluids and Structures,* vol. 102, 2021.

[77] E. Botero, M. Clarke, R. Erhard, J. Smart, J. Alonso and A. Blaufox, "Aerodynamic Verification and Validation of SUAVE," *AIAA SCITECH 2022 Forum,* 2022.

[78] M. Jayathilake, S. Rudra and L. Rosendahl, "Numerical modeling and validation of hydrothermal liquefaction of a lignin particle for biocrude production," *Fuel,* vol. 305, 2021.

[79] X. Gao and W. Gu, "Verification of a Numerical Model for Simulating Intervertebral Disc Pathophysiology," *Proceedings of the ASME 2020 Verification and Validation Symposium VVS2020,* 2020.

[80] A. Widuch, K. Myöhänen, M. Nikku, M. Nowak, A. Klimanek and W. Adamczyk, "Data set generation at novel test-rig for validation of numerical models for modeling granular flows," *International Journal of Multiphase Flow,* vol. 142, 2021.

[81] J. Grove, A. Coleman, C. Johnson and R. Menikoff, "A verification and validation study of the Cyclops I PBX 9502 Experiment," *Proceedings of the ASME 2020 Verification and Validation Symposium,* 2020.

[82] S. Eshraghi, M. Carolan, B. Perlman and F. Gonzales, "Comparison of methodologies for finite element model validation of railroad tank car side impact tests," *Proceedings of the ASME 2020 Verification and Validation Symposium,* 2020.

[83] D. Hizen, K. Ueno and R. Uzuoka, "Verification and validation of numerical analysis for consolidation of clay," *Journal of Japan Society of Civil Engineers A2 (Applied Mechanics) (in Japanese),* vol. 75, no. 2, pp. 351-359, 2019.

[84] M. Kurumatani, H. Ogura and H. Sakurai, "An example of the verification and validation for non-linear finit element analysis of concrete," *Proceedings of the Japan Society for Computational Engineering and Science,* p. 20220005, 2022.

[85] J. Thompson and C. Boyd, "CFD verification and validation exercise: Turbulent mixing of stratified layer," *Proceedings of the ASME 2020 Verification and Validation Symposium,* 2020.

[86] M. Kurumatani, S. Okazaki, Y. Yamamoto, N. Ueda and H. Ogura, "Simultaneous experiments of RC beams for the quantification of uncertainty," *Journal of Japan Society of Civil Engineers A2 (Applied Mechanics) (in Japanese),* vol. 75, no. 2, pp. 411-420, 2019.

[87] K. Arulanandan and R. Scott, "Verification of Numerical Procedures for the Analysis of Soil Liquefaction Problems," *Proceedings of the International Conference on the Verification of Numerical Procedures for the Analysis of Soil Liquefaction Problems,* vol. Vol. 1 and 2, 1993.

[88] R. Popescu and J. Prevost, "Centrifuge validation of a numerical model for dynamic soil liquefaction," *Soil Dynamics and Earthquake Engineering,* vol. 12(2), pp. 73-90, 1993.

[89] L. Lucy, "A numerical approach to the testing of the fission hypothesis," *Astronomical Journal,* vol. 82, pp. 1013-1024, 1977.

[90] J. Monaghan, "Smoothed particle hydrodynamics," *Annual Rev. Astron. Astrophys,* vol. 30, pp. 543-574, 1992.

[91] S. Koshizuka and Y. Oka, "Moving-particle semi-implicit method for fragmentation of incompressible fluid," *Nuclear Science and Engineering,* vol. 123(3), pp. 421-434, 1996.

[92] B. Kutter, M. Manzari, M. Zeghal, Y. Zhou and R. Armstron, "Proposed outline for LEAP verification and validation processes," *Geotechnics for Catastrophic Flooding Events,* pp. 99-108, 2015.

[93] T. Tobita, T. Ashino, J. Ren and S. Iai, "Kyoto University LEAP-GWU-2015 tests and the importance of curving the ground surface in centrifuge modelling," *Soil Dynamics and Earthquake Engineering,* vol. 113, pp. 650-662, 2018.

[94] B. Kutter, T. Carey, T. Hashimoto, M. Zeghal, T. Abdoun, P. Kokkali, S. Madabhushi, S. Haigh, F. Burali d'Arezzo, S. Madabhushi, W. Hung, C. Lee, S. Iai, T. Tobita, Y. Zhou, Y. Chen and M. Manzari, "LEAP-GWU-2015 experiment specifications, results, and comparisons," *Soil Dynamics and Earthquake Engineering,* vol. 113, pp. 616-628, 2018.

[95] B. Kutter, T. Carey, N. Stone, B. Zheng, A. Gavras, M. Manzari, M. Zeghal, T. Abdoun, E. Korre, S. Escoffier, S. Haigh, G. Madabhushi, S. Madabhushi, W. Hung, T. Liao, D. Kim, S. Kim, J. Ha, N. Kim, M. Okamura, A. Sjafuddin, T. Tobita, K. Ueda, R. Vargas, Y. Zhou and K. Liu, "LEAP-UCD-2017 comparison of centrifuge test results," *Model Tests and Numerical Simulations of Liquefaction and Lateral Spreading,* 2019.

[96] T. Tobita, K. Ueda, R. Vargas, K. Ichii, M. Okamura, A. Sjafruddin, J. Takemura, L. Hang, R. Uzuoka, S. Iai, J. Boksmati, A. Fusco, S. Torres-Garcia, S. Haigh, G. Madabhushi, M. Manzari, S. Escoffier, Z. Li, D. Kim, S. Manandhar, W. Hung, J. Huang, T. Pham, M. Zeghal, T. Abdoun, E.

Korre, B. Kutter, T. Carey, N. Stone, Y. Zhou, K. Liu and Q. Ma, "LEAP-ASIA-2019: Validation of centrifuge experiments and the generalized scaling law on liquefaction-induced lateral spreading," *Soil Dynamics and Earthquake Engineering,* vol. 157, 2022.

[97] T. Carey, N. Stone and B. Kutter, "Grain Size Analysis and Maximum and Minimum Dry Density of Ottawa F-65 Sand for LEAP-UCD-2017," *Model Tests and Numerical Simulations of Liquefaction and Lateral Spreading,* 2019.

[98] M. El Ghoraiby, H. Park and M. Manzari, "Physical and Mechanical Properties of Ottawa F65 Sand," *Model Tests and Numerical Simulations of Liquefaction and Lateral Spreading,* 2019.

[99] S. Iai, T. Tobita and T. Nakahara, "Generalized scaling relations for dynamic centrifuge tests," *Geotechnique,* vol. 55(5), pp. 355-362, 2005.

[100] B. Kutter, T. Carey, B. Zheng, A. Gavras, N. Stone, M. Zeghal, T. Abdoun, E. Korre, M. Manzari, S. Madabhushi, S. Haigh, S. Madabhushi, M. Okamura, A. Sjafuddin, S. Escoffier, D. Kim, S. Kim, J. Ha, T. Tobita, H. Yatsugi, K. Ueda, R. Vargas, W. Hung, T. Liao, Y. Zhou and K. Liu, "Twenty-Four Centrifuge Tests to Quantify Sensitivity of Lateral Spreading to Dr and PGA," *Geotechnical Earthquake Engineering and Soil Dynamics V : Slope Stability and Landslides, Laboratory Testing, and In Situ Testing,* 2018.

[101] R. Vargas, K. Ueda and T. Tobita, "Centrifuge modeling of the dynamic response of a sloping ground – LEAP-UCD-2017 and LEAP-ASIA-2019 tests at Kyoto University," *Soil Dynamics and Earthquake Engineering,* vol. 140, 2021.

[102] N. Izumo, "Physical Quantity Measured by a Vibration Viscometer," *Proc. 23th Sensing Forum,* 2006.

[103] M. Okamura and T. Inoue, "Preparation of fully saturated models for liquefaction study," *International Journal of Physical Modeling in Geotechnics,* vol. 12(1), p. 39–46, 2012.

[104] T. Carey, A. Gavras, B. Kutter, G. Madabhushi, S. Haigh, M. Okamura, D. Kim, K. Ueda, W. Hung, Y. Zhou, Y. Chen, M. Zeghal, T. Abdoun, S. Escoffier and M. Manzari, "A new shared miniature cone penetrometer for centrifuge testing," *Proceedings of 9th International Conference on Physical Modelling in Geotechnics,* 2018.

[105] B. Kutter, M. Zeghal and M. Manzari, "LEAP-UCD-2017 Experiments (Liquefaction Experiments and Analysis Projects) - Dataset," DesignSafe-CI, 2018.

[106] R. Vargas, T. Tobita, K. Ueda and H. Yatsugi, "LEAP-UCD-2017 Centrifuge Test at Kyoto University," *Model Tests and Numerical Simulations of Liquefaction and Lateral Spreading,* 2019.

[107] B. Kutter and D. Wilson, "De-liquefaction shock waves," *Proceedings of the Seventh US-Japan Workshop on Earthquake Resistant Design of Lifeline Facilities and Countermeasures Against Liquefaction,* 1999.

[108] R. Vargas, K. Ueda and S. Iai, "Effects of Soil Spatial Variability on Liquefaction Behavior of Horizontally Layered Ground," *JSCE Journal of Earthquake Engineering,* vol. 74(4), pp. I_16-I_24, 2018.

[109] T. Carey, A. Gavras and B. Kutter, "Comparison of LEAP-UCD-2017 CPT results," *Model Tests and Numerical Simulations of Liquefaction and Lateral Spreading,* 2019.

[110] M. Yoshimine, H. Nishizaki, K. Amano and Y. Hosono, "Flow deformation of liquefied sand under constant shear load and its application to analysis of flow slide in infinite slope," *Soil Dynamics and Earthquake Engineering,* Vols. 26(2-4), pp. 253-264, 2006.

[111] R. Vargas, Validation of numerical predictions of laterial spreading based on "hollow-cylinder torsional tests" and "a large centrifuge-models database", Master Thesis submitted to the Department of Civil and Earth Resources Engineering - Kyoto University, 2020.

[112] J. Ching and K. Phoon, "Constructing Site-Specific Multivariate Probability Distribution Model Using Bayesian Machine Learning," *Journal of Engineering Mechanics,* vol. 145(1), 2019.

[113] A. Gelman, J. Carlin, H. Stern, D. Dunson, A. Vehtari and D. Rubin, Bayesian Data Analysis, Third Edition, Taylor & Francis, 2013.

[114] R. Vargas, Z. Tang, K. Ueda and R. Uzuoka, "Validation of numerical predictions for liquefaction phenomenon – Lateral spreading in clean sands," *Soils and Foundations,* vol. 62(1), 2022.

[115] A. Ang and W. Tang, Probability concepts in engineering emphasis on applications to civil and environmental engineering, 2nd ed. Vol 1, Wiley, 2007.

[116] V. Barnett, "The Study of Outliers: Purpose and Model," *Journal of the Royal Statistical Society. Series C (Applied Statistics),* vol. 27(3), pp. 242-250, 1978.

[117] A. Smith, "Bayesian approaches to outliers and robustness," *Specifying Statistical Models (Lecture Notes in Statistics),* vol. 16, pp. 13-35, 1983.

[118] I. Verdinelli and L. Wasserman, "Bayesian analysis of outlier problems using the Gibbs sampler," *Statistics and Computing,* vol. 1, pp. 105-117, 1991.

[119] A. Gelman, "Prior distributions for variance parameters in hierarchical models," *Bayesian Analysis,* vol. 1(3), pp. 515-533, 2006.

[120] N. Polson and J. Scott, "On the Half-Cauchy Prior for a Global Scale Parameter," *Bayesian Analysis,* vol. 7(4), pp. 887-902, 2012.

[121] M. El Ghoraiby and M. Manzari, "LEAP-2018 - Stress-strain response of Ottawa F65 sand in Cyclic Simple Shear - Dataset," DesignSafe-CI, 2018.

[122] A. Parra Bastidas, "Ottawa F-65 Sand Characterization," PhD Dissertation, University of California, Davis, 2016.

[123] A. Vasko, "An Investigation into the Behavior of Ottawa Sand through Monotonic and Cyclic Shear Tests," MS Thesis. George Washington University, 2015.

[124] K. Ishihara and S. Yasuda, "Sand liquefaction in hollow cylinder torsion under irregular excitation," *Soils and Foundations,* vol. 15(1), 1975.

[125] K. Ishihara, A. Yamazaki and K. Haga, "Liquefaction of Ko-consolidated sand under cyclic rotation of principal principal stress direction with lateral constraint," *Soils and Foundations,* vol. 25(4), 1985.

[126] J. Koseki, T. Yoshida and T. Sato, "Liquefaction Properties of Toyoura Sand in Cyclic Torsional Shear Tests Under Low Confining Stress," *Soils and Foundations,* vol. 45(5), pp. 103-113, 2005.

[127] Japanese Geotechnical Society Standards, " Practice for preparing hollow cylindrical specimens of soils for torsional shear test – JGS-0550-2009.," *Laboratory Testing Standards of Geomaterials,* vol. 3, 2018.

[128] Japanese Geotechnical Society Standards, "Method for torsional shear test on hollow cylindrical specimens of soils - JGS-0551-2009," *Laboratory Testing Standards of Geomaterials,* vol. 3, 2018.

[129] Japanese Geotechnical Society Standards, "Method for cyclic triaxial test on soils - JGS-0541-2009," *Laboratory Testing Standards of Geomaterials,* vol. 2, 2016.

[130] S. Sawada, R. Sakuraba, N. Ohmukai and T. Mikami, "Effect of K0 on liquefaction strength of silty sand," *Fourth international conference on recent advances in geotechnical earthquake engineering and soil dynamics. Missouri: EEUU,* 2001.

[131] I. Towhata, Geotechnical earthquake engineering, Springer-Verlag Berlin Heidelberg, 2008.

[132] K. Been and G. Jefferies, "A state parameter for sands," *Geotechnique,* vol. 15(2), 1985.

[133] K. Ishihara, S. Iwamoto, S. Yasuda and H. Takatsu, "Liquefaction of anisotropically consolidated sand," *Proc. 9th international conference on soil mechanics and foundation engineering, vol. 2,* 1977.

[134] Public Works Research Institute - Japan, "Soil dynamics group – report No. 70 (in Japanese)," 1992.

[135] K. Ishihara and M. Yoshimine, "Evaluation of settlements in sand deposits following liquefaction during earthquakes," *Soils and Foundations,* vol. 32(1), 1992.

[136] N. Sento, M. Kazama and R. Uzuoka, "xperimental and idealization of the volumetric compression characteristics of clean sand after undrained cyclic shear (in Japanese)," *Japanese Society of Civil Engineers,* vol. 764, pp. 307-317, 2004.

[137] F. Tatsuoka, S. Yasuda, T. Iwasaki and K. Tokida, "Normalized Dynamic Undrained Strength of Sands Subjected to Cyclic and Random Loading," *Soils and Foundations,* vol. 20(3), pp. 1-16, 1980.

[138] S. Iai, Y. Matsunaga and T. Kameoka, "Strain space plasticity model for cyclic mobility," *Soils and Foundations,* vol. 32(2), p. 1–15, 1992.

[139] M. ElGhoraiby and M. Manzari, "The effects of base motion variability and soil heterogeneity on lateral spreading of mildly sloping ground," *Soil Dynamics and Earthquake Engineering,* vol. 135, 2020.

[140] R. Alford, K. Kelly and D. Boore, "Accuracy of finite difference modeling of the acoustic wave equation," *Geophysics,* vol. 39(6), p. 834–842, 1974.

[141] M. Okamura, T. Abdoun, R. Dobry, M. Sharp and V. Taboada, "Effects of Sand Permeability and Weak Aftershocks on Earthquake-Induced Lateral Spreading," *Soils and Foundations,* vol. 41(6), pp. 63-77, 2001.

[142] R. Popescu, J. Prevost and G. Deodatis, "Effects of Spatial Variability on Soil Liquefaction: Some Design Recommendations," *Geotechnique,* vol. 47(5), pp. 1019-1036, 1997.

[143] R. Popescu, J. Prevost and G. Deodatis, "3D Effects in Seismic Liquefaction of Stochastically Variable Soil Deposits," *Geotechnique,* vol. 55(1), pp. 21-31, 2005.

[144] J. Montgomery and R. Boulanger, "Effects of Spatial Variability on Liquefaction-Induced Settlement and Lateral Spreading," *Journal of Geotechnical and Geoenvironmental Engineering,* vol. 143(1), 2017.

[145] S. Iai, K. Ichii, H. Liu and T. Morita, "Effective Stress Analyses of Port Structures," *Soils and Foundations - Special Issue on Geotechnical Aspects of the January 17 1995 Hyogoken-Nambu Earthquake,* vol. 2, pp. 97-114, 1998.

[146] K. Kanda and M. Motosaka, "The Evaluation of Effects of Spatial Variability of Soil Properties, Surface Topography and Spatial Coherency of Incident Wave on Ground Motion Amplification –The Case of Kushiro J.M.A. Site (in Japanese)," *J. Struct. Constr. Eng., AIJ,* vol. 476, pp. 85-94, 1995.

[147] T. Mikami, O. Ozutsumi, T. Nakahara, S. Iai, K. Ichii and T. Kawasaki, "Easy method for setting parameters of liquefaction analysis program FLIP (in Japanese)," *46th Japan National Conference on Geotechnical Engineering, Kobe, Japan* , pp. 1627-1628, 2011.

[148] E. Vanmarcke, Random Fields, MIT Press, Cambridge, 1984.

[149] F. Nadim, H. Einstein and W. Roberds, "Probabilistic Stability Analysis for Individual Slope in Soil and Rock," *Proc. Int. Conf. on Landslide Risk Management,* pp. 63-98, 2005.

[150] M. Shinozuka and G. Deodatis, "Simulation of Multi-dimensional Gaussian Fields by Spectral Representation," *Applied Mechanics Reviews, ASME,* vol. 49(1), pp. 29-53, 1996.

[151] T. Morita, S. Iai, H. Liu, K. Ichii and Y. Sato, "Simplified Method to Determine Parameter of FLIP (in Japanese)," *Technical Note of the Port and Airport Research Institute, No. 869,* 1997.

[152] S. Kramer, Geotechnical Earthquake Engineering, Prentice Hall, USA, 1996.

[153] FLIP Consortium, Inc., "FLIP ROSE/TULIP analysis techniques, Analysis Theory and Setting of Analysis Conditions," FLIP Consortium, Inc., 2021.

[154] O. Zienkiewicz and P. Bettess, "Soils and other saturated porous media under transient, dynamic conditions. General formulation and the validity of various simplifying assumptions," in *Soil Mechanics –Transient and Cyclic Loads*, John Wiley & Sons, 1982, pp. 1-16.

[155] G. Holzapfel, Nonlinear Solid Mechanics, John Wiley&Sons, 2001.

[156] S. Iai and O. Ozutsumi, "Yield and cyclic behaviour of a strain space multiple mechanism model for granular materials," *International Journal for Numerical and Analytical Methods in Geomechanics,* vol. 29(4), p. 417–442, 2005.